Development of Non-linear Two-Terminal Mass Components for Application to Vehicle Suspension Systems

A thesis submitted to
the Faculty of Engineering
in partial fulfillment of the requirements for the
degree of Doctor of Philosophy in
Mechanical Engineering

by
Shuai Yang

Ottawa-Carleton Institute for Mechanical and Aerospace Engineering
University of Ottawa

Abstract

To achieve passive vibration control, an adaptive flywheel design is proposed and fabricated from two different materials. The corresponding mathematical models for the adaptive flywheels are developed. A two-terminal hydraulic device and a two-terminal inverse screw device are introduced to analyze the two adaptive flywheels. Experiments are carried out to identify key parameters for both the two-terminal hydraulic system and the inverse screw system. The performance of three different suspension systems are evaluated; these are the traditional suspension system, the suspension system consisting of an ideal two-terminal device with constant flywheel and the suspension system consisting of an ideal two-terminal device with an adaptive flywheel (AFW suspension system). Results show that the AFW suspension system can outperform the other two suspension systems under certain conditions. The performance of a suspension system with the adaptive flywheel under different changing ratio is evaluated, and an optimal changing ratio is identified under certain circumstances.

To obtain the steady-state response of the two-terminal device with adaptive flywheel, three different methods have been applied in this thesis. These methods are the single harmonic balance method, the multi-harmonic balance method and the scanning iterative multi-harmonic balance method, respectively. Compared to the single harmonic balance method, the multi-harmonic balance method provides a much more accurate system response. However, the proposed scanning iterative multi-harmonic balance method provides more accurate system response than the single harmonic balance method with much less computational effort.

Acknowledgements

My deep appreciation is presented to Dr. Ming Liang, my supervisor, for his comprehensive and continuous guidance, as well as partial financial support during the work. I also would like to thank Dr. Natalie Baddour, my co-supervisor, for her patience and professional advice, which provided the opportunity to prove myself. I would like to express my appreciation to Dr. Chuang Li for providing his lab equipment. At last, my grateful thanks to my parents, wife and parents in law for their endless help and support.

Table of contents

Abstract ii

Acknowledgements iii

Table of contents iv

List of figures viii

List of tables xv

Nomenclature xvii

1. Introduction 1

    1.1. Background 1

    1.2. Motivation 7

    1.3. Objectives of the thesis 8

    1.4. Contributions 8

    1.5. Thesis organization 10

2. Literature Review 11

    2.1. Literature review of active and passive vibration control 11

        2.1.1. Active vibration control 11

        2.1.2. Passive vibration control 17

    2.2. Literature Review of Two-terminal vibration control system 25

        2.2.1. Electrical passive network 25

        2.2.2. Mechanical passive networks 26

        2.2.3. Two-terminal vibration control system 27

3. Design and theoretical analysis of nonlinear two-terminal mass mechanisms 32

    3.1. Design motivation and proposed designs 32

        3.1.1. Design motivation 32

        3.1.2. Proposed designs 33

    3.2. Theoretical analysis for two-terminal hydraulic device with metal adaptive flywheel 34

3.2.1. Mathematical calculation of metal adaptive flywheel...............34

3.2.2. Relationship between flywheel angular velocity and slider location...37

3.2.3. Ideal model of the two-terminal hydraulic device 40

3.2.4. Mathematical model of the two-terminal hydraulic system 42

3.3. Theoretical analysis for two-terminal hydraulic device with nylon adaptive flywheel..44

3.3.1. Design of nylon adaptive flywheel 45

3.3.2. Moment of inertia of the nylon adaptive flywheel.....................46

3.3.3. The mechanism of the inverse screw system 49

3.3.4. Mathematical model of the inverse screw system with nylon adaptive flywheel..52

3.4. Design strategy...55

3.4.1. The design of the metal adaptive flywheel................................55

3.4.2. The design of the spring 55

3.5. Conclusion...57

4. Application of ideal two-terminal device with adaptive flywheel to suspension system 58

4.1. Mathematical model for a quarter car with different suspension systems 58

4.2. Performance evaluation for each suspension system 64

4.2.1. Riding comfort 64

4.2.2. Tire grip 70

4.2.3. Vehicle body deflection 76

4.3. Performance evaluation for different changing ratio 81

4.3.1. First situation: zero input..82

4.3.2. Second situation: impulse input 85

4.3.3. Third situation: sinusoidal excitation 88

4.3.4. Optimal changing ratio for adaptive flywheel 91

4.4. Conclusion..100
5. Experimental identification..102
5.1. Experimental identification for two-terminal hydraulic system.........102
5.1.1. Experimental setup for two-terminal hydraulic system...........102
5.1.2. Experimental validation of the inaccurate transmission ratio caused by pressure loss and friction..106
5.1.3. Parameter identification..107
5.1.4. Experimental validation of the mathematical model...............115
5.2. Experimental identification for the inverse screw system with nylon adaptive flywheel..117
5.2.1. Experimental Set-up...117
5.2.2. Identification of key parameters 118
5.2.3. Comparison between calculated and actual forces 121
5.3. Two-terminal hydraulic system with rectifier....................................124
5.4. Conclusion 130
6. Application of hydraulic two-terminal device with adaptive flywheel to suspension system 131
6.1. Mathematical models for the suspension systems...........................131
6.2. Performance evaluation..134
6.2.1. Riding comfort 134
6.2.2. Tire grip 139
6.2.3. Vehicle body deflection..144
6.3. Performance evaluation under different changing ratio..................149
6.3.1. Zero input...149
6.3.2. Impulse input 153
6.3.3. Sinusoidal input..156
6.3.4. Optimal changing ratio for adaptive flywheel.........................159
6.4. Conclusion...162
7. Steady state frequency response of two-terminal device with adaptive

flywheel 165

7.1. Differential equation of motion for two-terminal device with adaptive flywheel 165

7.2. Steady state harmonic response analysis by single harmonic balance method 167

7.3. Numerical solution for the system response 169

7.4. Multi-harmonic balance method for steady state harmonic response analysis 175

7.5. Scanning iterative multi-harmonic balance method 180

7.6. Conclusions 190

8. Conclusion 192

8.1. Concluding remarks 192

8.2. Future work 193

References 195

Appendix A – Signals used in Model Validation 213

Appendix B - Code 219

Appendix C – Accepted Manuscripts 228

List of figures

Figure 1.1 Tacoma Narrow Bridge in 1940 [2] 1
Figure 1.2 Typical car shock absorber [11] 2
Figure 1.3 Strategy of vibration control 3
Figure 2.1 Diagram of closed loop control system 11
Figure 2.2 Prototype device: Inerter (a) Prototype of inerter, and (b) schematic of inerter[171] 29
Figure 2.3 Prototype of inverse screw two-terminal system (a) prototype of inverse screw two-terminal system, and (b) schematic of inverse screw two-terminal system [38] 29
Figure 2.4 Prototype of electro-hydraulic variable two-terminal mass device (a) Prototype of electro-hydraulic variable two-terminal mass device, and (b) schematic of electro-hydraulic variable two-terminal mass device [37] 30
Figure 3.1 The metal adaptive flywheel: a) schematic diagram, and b) prototype (note: 1-spring, 2-inner hole for the shaft, 3-slot, 4-slider, and 5-frame) 34
Figure 3.2 Slot of the metal adaptive flywheel 35
Figure 3.3 The relationship between flywheel angular velocity and slider location 39
Figure 3.4 The two-terminal hydraulic device (note: 1-terminal 1, 2-release valve, 3-hydraulic cylinder, 4-hydraulic motor, 5-pressure gauge, 6-holding shaft of the flywheel, 7-terminal 2) (Fabricated by the Engineering Laboratory For Detection, Control and Integrated System, Chongqing Technology and Business University, China) 40
Figure 3.5 Schematic diagram of the two-terminal hydraulic device with a mounted variable flywheel 41
Figure 3.6 Mechanical model of the two-terminal hydraulic system 43
Figure 3.7 Schematic diagram of nylon adaptive flywheel (top view and side view without springs and sliders) 45
Figure 3.8 The relationship between l_n and I_{afn} 49
Figure 3.9 Inverse screw system with adaptive nylon flywheel (fabricated by the Engineering Laboratory For Detection, Control and Integrated System, Chongqing Technology and Business University, China) 49

Figure 3.10 Structural diagram of the inverse screw [173].................................50
Figure 3.11 Schematic diagram of inverse screw system 53
Figure 3.12 Dynamic model of inverse screw system with nylon flywheel 54
Figure 4.1 Quarter car model with traditional suspension system......................59
Figure 4.2 Suspension system of two-terminal device with constant flywheel ..61
Figure 4.3 Suspension system of two-terminal device with adaptive flywheel ..63
Figure 4.4 Weighted root mean square acceleration with zero input..................67
Figure 4.5 Weighted root mean square acceleration with impulse input 68
Figure 4.6 Weighted root mean square acceleration with sinusoidal input.........70
Figure 4.7 Weighted root mean square tire grip index with zero input...............73
Figure 4.8 Weighted root mean square tire grip index with impulse input.........74
Figure 4.9 Weighted root mean square tire grip index with sinusoidal input 75
Figure 4.10 Weighted root mean square vehicle body deflection with zero input 78
Figure 4.11 Weighted root mean square vehicle body deflection with impulse input 79
Figure 4.12 Weighted root mean square vehicle body deflection with sinusoidal input 81
Figure 4.13 Weighted accelerations of AFW suspension system with different changing ratios under zero input..83
Figure 4.14 Weighted tire grip index of AFW suspension system with different changing ratios under zero input..84
Figure 4.15 Weighted suspension deflections of AFW suspension system with different changing ratios under zero input 84
Figure 4.16 Weighted accelerations of AFW suspension system with different changing ratios under impulse input..86
Figure 4.17 Weighted tire grip index of AFW suspension system with different changing ratios under impulse input..87
Figure 4.18 Weighted vehicle body deflections of AFW suspension system with different changing ratios under impulse input 87
Figure 4.19 Weighted accelerations of AFW suspension system with different changing ratios under sinusoidal input 89
Figure 4.20 Weighted tire grip index of AFW suspension system with different changing ratios under sinusoidal input 90

Figure 4.21 Weighted vehicle body deflections of AFW suspension system with different changing ratios under sinusoidal input..90

Figure 5.1 Test rig for the adaptive flywheel (Note: 1-force cell, 2- two-terminal hydraulic system, 3–computer, 4-actuator, 5-controller)..........................103

Figure 5.2 Comparison of adaptive flywheel under different configurations. (a), (b) and (c) are force–time diagrams of three adaptive flywheels under frequency 0.2 Hz, amplitude 0.01 m/s, frequency 1Hz, amplitude 0.01 m/s and frequency 2 Hz, amplitude 0.02 m/s respectively..............................105

Figure 5.3 The relationship between actual fitted and theoretical flywheel angular velocities: (a) and (c) compare the actual and fitted flywheel angular displacements in response to the triangular command (linear) displacement inputs (amplitudes = 0.005 m and 0.01 m respectively) applied to the two terminals of the hydraulic device, (b) and (d) compare the actual fitted and theoretical flywheel angular velocities obtained from (a) and (c), respectively. 107

Figure 5.4 Rectangular velocity inputs and corresponding measured forces. (a), (c) and (e) present the velocity inputs with different frequencies and amplitudes ((0.2Hz 0.005m/s), (0.5Hz, 0.0075m/s) and (1Hz, 0.015m/s)) respectively. (b), (d) and (f) are the measured forces corresponding to the velocity inputs shown in (a), (c) and (e), respectively..109

Figure 5.5 Comparison of the measured forces and calculated forces based on the estimated b_{ah} and F_{fh}. (a) Velocity input (frequency = 0.5 Hz, amplitude = 0.005 m/s), (b) measured and calculated forces corresponding to the velocity input in (a), (c) velocity input (frequency = 1 Hz, amplitude = 0.01 m/s), and (d) measured and calculated forces corresponding to the velocity input in (c). 110

Figure 5.6 The variable behavior of the flywheel moment of inertia and equivalent mass: (a) sinusoidal velocity input (frequency = 0.1 Hz, amplitude = 0.0314 m/s), (b) slider location (i.e., the distance between slider centroid and flywheel rotational center) that varies in response to the velocity input in (a), (c) the variable moment of inertia of the flywheel associated with the slider location presented in (b), and (d) the variable equivalent mass of the flywheel due to the location change of the sliders..112

Figure 5.7 Sinusoidal velocity inputs and corresponding measured forces. (a), (c) and (e) are sinusoidal velocity inputs associated with frequency-amplitude combinations of (0.1Hz, 0.0019m/s), (0.5Hz, 0.016m/s) and (2Hz, 0.1m/s), respectively. (b), (d) and (f) are measured forces corresponding to the inputs in (a), (c) and (e), respectively. 114

Figure 5.8 Comparison of the measured forces and calculated forces based on the estimated k_h. (a) Velocity input (frequency = 0.4 Hz, amplitude = 0.012 m/s), (b) measured and calculated forces corresponding to the velocity input in (a), (c) velocity input (frequency = 2 Hz, amplitude = 0.063 m/s), and (d) measured and calculated forces corresponding to the velocity input in (c) 115

Figure 5.9 The comparison of measured forces and calculated forces using the mathematical model. (a) comparison between measured and calculated forces with a velocity input of low frequency and amplitude (0.4 Hz, 0.012 m/s), (b) comparison between measured and calculated forces with an input of middle frequency and amplitude (1 Hz, 0.0314m/s), and (c) comparison between measured and calculated forces with an input of high frequency and amplitude (2Hz, 0.126 m/s). 116

Figure 5.10 Experimental rig of inverse screw system with nylon flywheel.... 117

Figure 5.11 Theoretical input (a) and corresponding calculated equivalent mass (b) 119

Figure 5.12. Comparison of the measured and calculated force based on the estimated *f*, *c* and *k*. (a) displacement input (frequency 0.1Hz, amplitude 0.005m), (b) measured and calculated forces corresponding to the displacement input in (a), (c) displacement input (frequency 0.5Hz, amplitude 0.01m), (d) measured and calculated forces corresponding to the displacement input in (c), (e) displacement input (frequency 2Hz, amplitude 0.05m), (f) measured and calculated forces corresponding to the displacement input in (e)... 121

Figure 5.13. Comparison between the actual and calculated force, based on the mathematical model: (a) sinusoidal input with frequency 0.5Hz and amplitude 0.015m, (b) comparison between actual and calculated force corresponding to the sinusoidal input in (a), (c) sinusoidal input with

frequency 2Hz and amplitude 0.01m, (d) comparison of the actual and calculated force corresponding to the sinusoidal input in (c) 122

Figure 5.14 The comparison of three situations: variable, maximum, and minimum slider position 123

Figure 5.15 Comparison between nylon adaptive flywheel with and without sliders 123

Figure 5.16 prototype of two-terminal hydraulic system with rectifier (Note: 1-terminal one 2- hydraulic motor 3-flywheel 4-terminal two 5-hydraulic rectifier).. 125

Figure 5.17 Schematic diagram of new nylon adaptive flywheel 126

Figure 5.18 Experimental rig of two-terminal hydraulic system with rectifier 127

Figure 5.19 Comparison of two-terminal hydraulic system with and without rectifier: (a) Sinusoidal input (frequency = 0.4Hz, and amplitude = 0.05m), and (b) Measured force of two-terminal hydraulic system with and without rectifier. 128

Figure 5.20 Comparison between actual measured force and theoretically calculated force: (a) Force corresponding to sinusoidal inputs with frequency 1Hz, amplitude 0.05m, and (b) Force corresponding to sinusoidal inputs with frequency 0.2Hz, amplitude 0.15m. 130

Figure 6.1 Suspension system A 132

Figure 6.2 Suspension system B 133

Figure 6.3 Weighted root mean square acceleration with zero input 135

Figure 6.4 Weighted root mean square acceleration with impulse input 137

Figure 6.5 Weighted root mean square acceleration with sinusoidal input 138

Figure 6.6 Weighted root mean square tire grip index with zero input 140

Figure 6.7 Weighted root mean square tire grip index with impulse input 142

Figure 6.8 Weighted root mean square tire grip index with sinusoidal input ... 143

Figure 6.9 Weighted root mean square vehicle body deflection with zero input 145

Figure 6.10 Weighted root mean square vehicle body deflection with impulse input 147

Figure 6.11 Weighted root mean square vehicle body deflection with sinusoidal input 148

Figure 6.12 Weighted accelerations of suspension system B with different changing ratio under zero input 151
Figure 6.13 Weighted tire grip index of suspension system B with different changing ratio under zero input 151
Figure 6.14 Weighted vehicle body deflections of suspension system B with different changing ratio under zero input...152
Figure 6.15 Weighted accelerations of suspension system B with different changing ratio under impulse input...154
Figure 6.16 Weighted tire grip index of suspension system B with different changing ratio under impulse input...154
Figure 6.17 Weighted vehicle body deflections of suspension system B with different changing ratio under impulse input...155
Figure 6.18 Weighted accelerations of suspension system B with different changing ratio under sinusoidal input..157
Figure 6.19 Weighted tire grip index of suspension system B with different changing ratio under sinusoidal input..157
Figure 6.20 Weighted vehicle body deflections of suspension system B with different changing ratio under sinusoidal input 158
Figure 7.1 two-terminal device with adaptive flywheel 166
Figure 7.2 Comparisons between simulation solution and single harmonic balance method frequency response under different amplitude inputs a) $B_s = 1cm$. b) $B_s = 3cm$. c) $B_s = 5cm$. d) $B_s = 7cm$. e) $B_s = 10cm$. f) $B_s = 20cm$. 171
Figure 7.3 Enlarged view of super-harmonic responses under different inputs 173
Figure 7.4 Comparisons between simulation solution and multi-harmonic balance method under different amplitude inputs a) $B_s = 1cm$. b) $B_s = 3cm$. c) $B_s = 5cm$. d) $B_s = 7cm$. e) $B_s = 10cm$. f) $B_s = 20cm$. 178
Figure 7.5 Enlarged view of super-harmonic responses comparison between numerical simulation and multi-harmonic balance method under different inputs...179
Figure 7.6 Flow diagram of the scanning iterative multi-harmonic balance method 184

Figure 7.7 Comparison between simulation solution and single harmonic balance method for different amplitude inputs a) $B_s = 1cm$. b) $B_s = 3cm$. c) $B_s = 5cm$. d) $B_s = 7cm$. e) $B_s = 10cm$. f) $B_s = 20cm$ 186

Figure 7.8 Enlarged view of super-harmonic responses comparison between numerical simulation and scanning iterative multi-harmonic balance method under different inputs 187

Figure 7.9 Comparison between the traditional suspension system and suspension system of two-terminal device with adaptive flywheel under different amplitude inputs: a) $B_s = 1cm$, b) $B_s = 5cm$, c) $B_s = 10cm$, and d) $B_s = 20cm$ 189

List of tables

Table 1.1 Comparisons between active and passive vibration control..................5

Table 2.1 Analogy between electrical system and mechanical system[167] 27

Table 2.2 Analogy between mass element and grounded capacitor[32]...........28

Table 3.1 Parameters of the metal adaptive flywheel prototype 36

Table 3.2 Parameters of the two-terminal hydraulic device (provided by the manufacturer)...41

Table 3.3 Specific parameters of the nylon adaptive flywheel...........................47

Table 3.4 Parameters of the inverse screw system (provided by manufacturer).52

Table 4.1 Weighted root mean square acceleration with zero input....................66

Table 4.2 Weighted root mean square acceleration with impulse input..............68

Table 4.3 Weighted root mean square acceleration with sinusoidal input 69

Table 4.4 Weighted root mean square tire grip index with zero input.................72

Table 4.5 Weighted root mean square tire grip index with impulse input...........73

Table 4.6 Weighted root mean square tire grip index with sinusoidal input 75

Table 4.7 Weighted root mean square vehicle body deflection with zero input..77

Table 4.8 Weighted root mean square vehicle body deflection with impulse input 79

Table 4.9 Weighted root mean square vehicle body deflectionwith sinusoidal input 80

Table 4.10 Performance with different changing ratio under zero input............82

Table 4.11 Performance with different changing ratio under impulse input.......85

Table 4.12 Performance with different changing ratio under sinusoidal input ...88

Table 4.13 performance of AFW suspension system with different input under optimal changing ratio 98

Table 4.14 Optimal changing ratio with different performance proportion........99

Table 4.15 Relationship between optimal changing ratio and proportion of inputs 100

Table 5.1 Parameters of NI USB-6212..103

Table 5.2 Parameters of Letry PLN-20 electro hydraulic servo fatigue test machine...118

Table 5.3 Specific parameters of the new two-terminal hydraulic system........125

Table 5.4 Specific parameters of the new nylon adaptive flywheel..................126
Table 6.1 Weighted root mean square acceleration with zero input................135
Table 6.2 Weighted root mean square acceleration with impulse input............136
Table 6.3 Weighted root mean square acceleration with sinusoidal input.........138
Table 6.4 Weighted root mean square tire grip index with zero input..............139
Table 6.5 Weighted root mean square tire grip index with impulse input.........141
Table 6.6 Weighted root mean square tire grip index with sinusoidal input.....142
Table 6.7 Weighted root mean square vehicle body deflection with zero input 144
Table 6.8 Weighted root mean square vehicle body deflection with impulse input 146
Table 6.9 Weighted root mean square vehicle body deflection with sinusoidal input 147
Table 6.10 Performance with different changing ratio under zero input...........150
Table 6.11 Performance with different changing ratio under impulse input.....153
Table 6.12 Performance with different changing ratio under sinusoidal input .156
Table 6.13 Performance of suspension system B with different input under optimal changing ratio 160
Table 6.14 Optimal changing ratio with different performance proportion......161
Table 6.15 Relationship between optimal changing ratio and proportion of inputs 162
Table 7.1 Resonance frequency and max amplitude of response under inputs with different amplitudes 172
Table 7.2 Normalized root mean square errors between numerical simulation and single harmonic balance method..174
Table 7.3 Normalized root mean square errors between numerical simulation and multi-harmonic balance method..180
Table 7.4 Normalized root mean square errors between numerical simulation and scanning iterative multi-harmonic balance method..................................188

Nomenclature

O_m	Rotation center of the flywheel
l_m	Distance from rotation center of flywheel and centroid of the slider
P_m	Centroid of a slider
m_{sm}	Mass of slider
d_m	Diameter of slider
l_{sm}	Length of slider
I_{szm}	Moment of inertia of the slider
I_{afm}	Moment of inertia of the metal adaptive flywheel
r_m	Radius of inner hole
R_m	Outer radius of the flywheel
a_m	Length of slot
k_{sm}	Stiffness of spring
m_{fm}	Mass of flywheel(including slots)
m_{om}	Mass of the removed slot material
I_{fzm}	Moment of inertia of the circular disk (before removal of slot)
I_{ozm}	Moment of inertia of the removed slot material
a_{sm}	Radial acceleration caused by rotation
$l_{m,\min}$	Minimum travel of the slider
ω_m	Rotation speed of flywheel
A	Cross-section area of the cylinder
h	Displacement of the motor
F	Force applied to the terminal
M	Flow rate from one chamber to another
T_1	Torque of the variable flywheel

m_{em}	Equivalent inertia mass
P_l	Oil pressure loss
F_{fh}	Friction between piston and cylinder
k_h	Stiffness of two-terminal hydraulic system
x_k	Elastic deformation
b_h	Pressure loss coefficient
b_{ah}	Equivalent damper with a damping ratio
v_a	Relative velocity between the two terminals
$M_{em}(s)$	Laplace transform of m_{em}
$\mathrm{sgn}(v_a)$	Direction of velocity
I_{fn}	Moment inertia of the nylon disk
m_{fn}	Mass of the nylon disk
R_n	Outer radius of nylon flywheel
r_{1n}	Inner radius of nylon flywheel
T_n	Thickness of nylon flywheel
P	Density of PA66
m_{on}	Mass of each slot of nylon flywheel
I_{on}	Moment inertia of the slots of nylon flywheel
d_{1n}	Width of slot of nylon flywheel
l_{1n}	Length of slot of nylon flywheel
m_{hn}	Mass of each hole of nylon flywheel
I_{hn}	Moment of inertia of each hole of nylon flywheel
r_{2n}	Radius of each hole of nylon flywheel
L_n	Distance from center of hole from the axis of rotation of nylon flywheel
m_{sn}	The mass of the slider of nylon flywheel

l_n	Distance from centroid of each slider to rotation center of nylon flywheel
l_{2n}	Length of slider of nylon flywheel
r_{3n}	Radius of slider of nylon flywheel
I_{afn}	Total moment of inertia of the of nylon flywheel
k_{sn}	Stiffness of spring of nylon flywheel
$I_{afn,\max}$	Maximum moment of inertia of the nylon flywheel
$I_{afn,\min}$	Minimum moment of inertia of the nylon flywheel
$\ddot{x}$	Vertical acceleration
d	Diameter of the ball screw
α	Helix angle of the ball screw
$\ddot{\theta}$	Angular acceleration of the flywheel
F	Axial force
F_c	Centrifugal force
$l_{n,\min}$	Minimum distance between the centroid of slider and the rotation center
ρ_1 ρ_2	Backlashes of inverse screw system
k_i	Stiffness of inverse system
c_i	Viscous damping ratio of inverse system
$F_{mh}(t)$	Measured force
$F_{ch}(t)$	Theoretically calculated force
$F_{mh}(n)$	Measured force
$F_{ch}(n)$	Theoretically calculated force
n_{eh}	Last sampling point of a dataset
n	Sampling point
$F_{mi}(t)$	Measured force,

$F_{ci}(t)$	Theoretically calculated force
$F_{mi}(n)$	Measured force
$F_{ci}(n)$	Theoretically calculated force
n_{ei}	Last sampling point of a dataset
R_r	Outer radius of flywheel
T_r	Thickness of nylon disk
L_r	Distance between hole and rotation center
r_{r1}	Radius of inner circle
r_{r2}	Radius of holes in flywheel
d_r	Diameter of slots in flywheel
l_{r1}	Length of slots
r_{r3}	Radius of sliders
l_{r2}	Length of sliders
m_{sr}	Mass of slider
I_{afr}	Inertia of new adaptive nylon flywheel
m_{er}	Equivalent mass of the new adaptive nylon flywheel
f_r	Force of friction of two-terminal hydraulic system
c_r	Damping ratio
k_r	Stiffness of whole system
$F_{mr}(t)$	Measured force
$F_{cr}(t)$	Theoretically calculated force
t_{sr}	Start time of data recording
t_{er}	End time of data recording
$F_{mr}(n)$	Measured force

$F_{cr}(n)$	Theoretically calculated force
M	Quarter-car combined mass of car and passenger
M_t	Mass of one tire
K	Stiffness of the quarter-car suspension system
C	Damping coefficient
K_t	Stiffness of the tire
C_t	Damping coefficient of the tire
X_1	Road vertical displacement
X_2	Displacement of unsprung mass (mass not supported by the suspension),
X_3	Displacement of the sprung mass
ω_t	Tire natural frequency
ω_b	Body natural frequency
ζ	Suspension damping ratio
α	Tire-body mass ratio
M_e	Equivalent mass generated by the adaptive flywheel
$G_q(n_0)$	Road roughness parameters
a_w	Weighted root mean square acceleration
M_{tg}	Tire grip index
M_{wtg}	Weighted root mean square tire grip index
D_f	Vehicle body deflection
D_{fw}	Weighted root mean square vehicle body deflection
α_{zw}	Weighted accelerations under zero input
M_{ztgw}	Weighted tire grip index with zero input

α_{iw}	Weighted accelerations under impulse input
M_{itgw}	Weighted tire grip index with impulse input
α_{sw}	Weighted accelerations with sinusoidal input and
M_{stgw}	Weighted tire grip index with sinusoidal input
$f_{zp}(x)$	Performance function with zero input
α_{szw}	Weighted accelerations of traditional suspension system with zero input
M_{sztgw}	Weighted tire grip index with zero input
x_1	Performance proportion of riding comfort while
x_2	Performance proportion of safety
$f_{ip}(x)$	Performance function with impulse input
α_{siw}	Weighted acceleration - traditional suspension system with impulse input
M_{sitgw}	Weighted tire grip index with impulse input
$f_{sp}(x)$	Performance function with sinusoidal input
α_{ssw}	Weighted acceleration of traditional suspension system with sinusoidal input
M_{sstgw}	Weighted tire grip index with sinusoidal input
$f_p(x)$	Overall performance function
x_3	Proportion of zero input
x_4	Proportion of impulse input
x_5	Proportion of sinusoidal input
$X_0(t)$	Simple harmonic motion
B_s	Amplitude of input

f_s	Frequency of input
B_{sa}	Amplitude of system response
$A_1(f(0.005i))$	Amplitude of numerical solution, 0.005 is the frequency interval
B_{m0}	Coefficient of constant
N_m	Highest order harmonic of the system response
B_{m1i}, B_{m2i}	Coefficients of each order harmonic of the system response
B_{h0}	Constant coefficient
B_{h1i}, B_{h2i}	Coefficients for the different order harmonic
N_h	Highest order of harmonic
E_{h1i}, E_{h2i}	Coefficients for the different order harmonic
T_h	Time vector
N_{hf}	Number of time points
E_h	Error vector

1. Introduction

1.1. Background

Vibration as a phenomenon has been studied by many researchers from different fields. This phenomenon exists in both mechanical systems and various civil structures. Vibration in civil structures can cause health problems for humans such as dizziness, nausea and anxiety [1]. If the amplitude of vibration is large enough, it may lead to catastrophic consequence. For example, the Tacoma Narrows Bridge (**Figure 1.1**) was destroyed only four months after its opening in 1940 due to vibrations caused by wind [2].

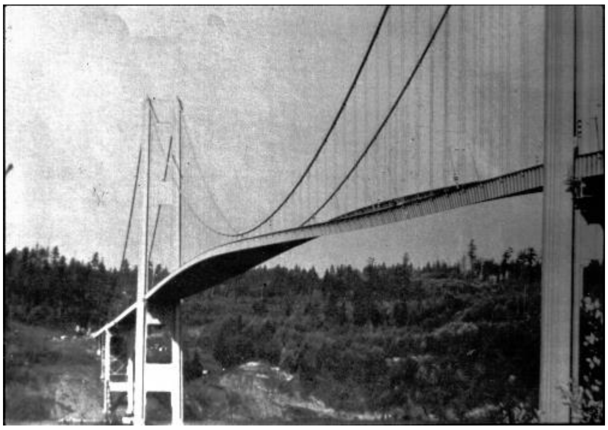

Figure 1.1 Tacoma Narrow Bridge in 1940 [2]

Compared to vibration in civil structures, vibrations within mechanical systems are far more common, and also cause tremendous problems such as shortened machine life span, reduced manufacturing precision, poor product quality, and noise [3]. In particular for modern transportation devices, the existence of vibration causes more severe problems than simply the discomfort of passengers. In some extreme cases, such vibrations will cause the malfunction of the device, which may inevitably lead to fatal accidents [4].

Based on all the above reasons, vibration control in civil structures and mechanical systems is extremely important. In the last several decades, researchers have been achieving remarkable progress in these fields, especially for mechanical vibration control. The classical vibration control of mechanical systems can be further divided into vibration isolation and vibration absorption by methods of application.

Vibration isolation is often applied to a system which is fixed at one point. By minimizing the vibration at the attaching point to the excitation source, this approach usually yields good performance. However, when this system is subjected to multiple excitation sources, the control strategy of vibration isolation may become very complicated [5,6].

Compared to vibration isolation, vibration absorption achieves the goal of vibration control by using vibration absorbers. In most cases, the vibration absorber is a secondary system which consists of a mass, spring and damper [7,8]. For example, the common vibration absorber, a car shock absorber, dissipates vibration energy to suppress the vibration of the vehicle body, which in turn provides improved ride comfort for the driver and passengers [9,10]. A typical car vibration absorber is shown in **Figure 1.2**.

Figure 1.2 Typical car shock absorber [11]

With the development of simulation and analysis tools, system design can be optimized by modeling and simulation. The application of modern control theory explores many new ways to achieve effective vibration control [1]. The general development of strategies for vibration control is shown in **Figure 1.3**. From **Figure 1.3**, it can be seen that there are three major ways to achieve vibration control: traditional design optimization which occurs at the system design stage, an additional vibration control system that is added to the structure (extra control system) and design of a self-adaptive structure. As a popular control method, the addition of an extra control system has been attracting much attention. Specifically, passive vibration control and active vibration control are two major approaches to the extra vibration control system. By combining these two vibration control concepts, combination vibration control, hybrid vibration control, often also referred to as semi-active vibration control, has been proposed.

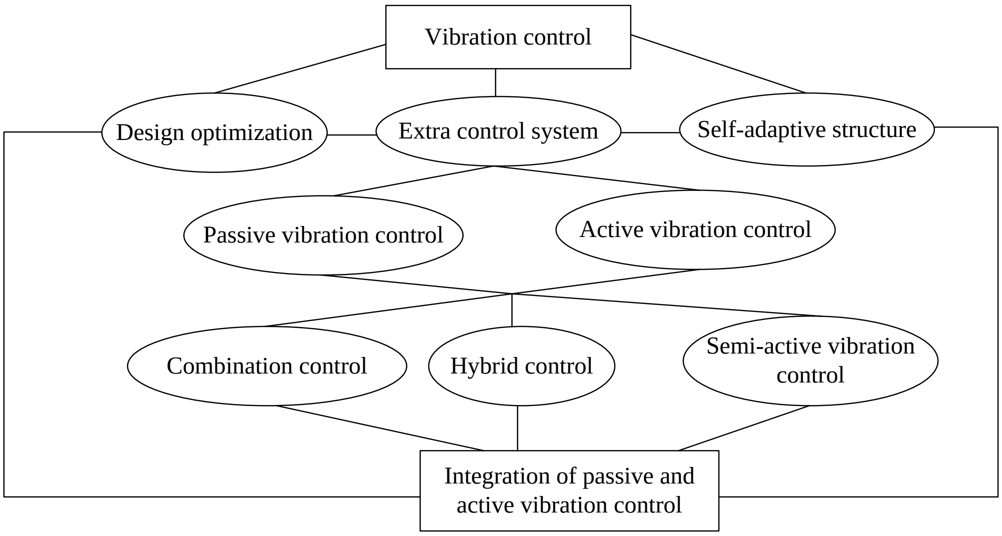

Figure 1.3 Strategy of vibration control

Vibration control can be further classified into passive vibration control and active vibration control. Due to its high reliability and low cost, passive vibration control has wide industrial application [12,13]. Usually, passive vibration control is related to the movement of a target system which requires vibration control. By dissipating vibration energy and isolating the transmission of vibration, the intent is for the whole system to eventually trend towards stability [14] .

On the other hand, active vibration control may be either related to the target system, or independent from the system, depending on the excitation [15,16]. Since there is an actuator that is powered by an outside energy source, an active vibration control system can not only cause the decay of vibrations, but may also cause amplification of vibration, potentially leading to system instability. In order to build a feasible active control system, the determination of controller parameters is critical to the whole design. In most cases, a close-loop feedback control system is chosen and the input excitation of the actuator will be a function of system state [17,18]. The most important feature of active vibration control is high controllability, but due to high cost and low reliability, widespread application of active vibration control is still limited [19]. A comparison between passive and active vibration control is shown in **Table 1.1**.

Table 1.1 Comparisons between active and passive vibration control

Objective / Classification	Working principle	Controllability	Robustness	Stability	Reliability	Extra mass	Energy source required	cost
Passive vibration control	Simple	Low	Good	Good	High	Small	None	Low
Active vibration control	Complicated	High	Depends on controller	Depends on controller	Low	Large	High	High

In the past several decades, researchers have achieved impressive progress in active vibration control [20–23]. Nakano even proposed a self-powered active vibration control system using a piezoelectric actuator [24]. Concomitantly, many researchers have focused on semi-active vibration control by developing variable damping ratio or variable stiffness systems [25–27].

Recently, research on passive vibration control has evolved in many directions [28]. For instance, Behrens et al. presented a design for passive vibration control via electromagnetic shunt damping [13]. By designing an appropriate electrical shunt, a transducer was shown to be capable of significantly reducing mechanical vibrations. Another design adjusts the natural frequency of the system to suppress vibration by adding a large mass. This concept is referred to as a tuned mass damper (TMD) [29–31]. However, both designs require extra components to achieve passive vibration control, which eventually lead to higher cost.

In a related theme, many researchers have focused on using flywheels to achieve passive vibration control. Smith [32] proposed a new device named the inerter, and Rivin [33] also developed a spiral flywheel. Both devices transfer linear motion into the rotation of a flywheel, which in turn generates equivalent inertial mass equal to as much as 400 times that of the gravitational mass of the flywheel. Wang and Wu [34] applied this inerter to vibration control of an optical table, and experimental results were promising. Based on the same theory, Li et al. [35–38] proposed several two-terminal devices to achieve passive vibration control, such as a two-terminal inverse screw transmission system and a two-terminal hydraulic system. One of these designs was shown capable of obtaining a variable two-terminal mass by adjusting an electro-hydraulic proportional valve. Experiments were carried out, and the results agreed with the design requirements. Despite all this progress, none of these approaches can passively generate variable equivalent mass and industrial applications are still rare. Xu investigates a different design for the flywheel, which led to the creation of variable mass [39]. However, in his design, the maximum change in the moment of inertia was limited to 11.67% due to the large mass of the flywheel base relative to that of the sliders.

1.2. Motivation

As mentioned above, researchers have been making progress with vibration control, particularly, in structural and mechanical vibration control. Active and semi-active vibration controls have attracted much attention in the last few decades. However, due to high cost, low reliability and robustness, real-world implementations of active and semi-active vibration control are rare. Passive vibration control still dominates industrial applications due to low cost, high robustness and high reliability. However, in the case of passive vibration control, once key system parameters (stiffness, damping ratio and mass) have been chosen, the characteristics of the system are then fixed. This implies that the ability of a passive vibration control system to deal with a variety of situations is limited. Therefore, the design must always make compromises, favoring the conditions that the passive system is most likely to encounter at the expense of other conditions which are expected to occur less frequently.

With the invention of the inerter, there was increased interest in two-terminal mass vibration control systems - a new and effective method of passive vibration control which is achieved by using a two-terminal mass device. By achieving much larger equivalent mass through the flywheel in the system, a two-terminal mass vibration control system can change the natural frequency of the whole system, which can lead to the suppression of vibrations. However, most of these two-terminal mass vibration control systems can only generate a constant equivalent mass. The generation of a variable equivalent mass would make it possible to change the system parameters during operation. However as mentioned earlier, this usually requires a complicated mechanism at high cost. Moreover, the flywheel would also cause an increase in the overall weight of the system, which implies higher energy consumption.

1.3. Objectives of the thesis

The goal of this thesis is the design, development and evaluation of a new passive vibration control component. For most passive vibration control systems, once the key parameters are chosen, the characteristic of the system are fixed. The passive vibration control device proposed in this thesis is a two-terminal device with an adaptive flywheel that can passively generate variable inertial mass under different excitations. The proposed system is non-linear. To evaluate the performance of the newly proposed component, a mathematical model must be derived and experimentally validated. The newly proposed component can then be applied to a car suspension system, and performance will be evaluated via numerical simulations. The relationship between suspension performance and changing ratio of the adaptive flywheel will be discussed under both ideal and real situations, and the optimal changing ratio will be determined under certain conditions. The changing ratio is defined as the ratio between the minimum moment of inertia of this flywheel and its maximum moment of inertia. Finally, the non-linearity of the system implies difficulties in the calculation of the system's frequency response, which is a key analysis tool used in engineering design. Therefore, to enable the analysis of the new system component within the context of an engineering design, an efficient mathematical method will be proposed to analyze the steady state response of this non-linear system.

1.4. Contributions

The contributions of this thesis are as follows:

1. Two adaptive flywheels made of different materials are proposed and corresponding mathematical models are derived.
2. Two different types of two-terminal devices are applied to analyze the two different adaptive flywheels of different materials. Experiments are carried out to identify the key parameters of the two-terminal devices. To obtain a more accurate mathematical

model, a hydraulic rectifier is introduced to eliminate backlash in the two-terminal hydraulic system. Close agreement between theoretical and experimental results has verified the accuracy of the mathematical models.

3. To evaluate the performance of the proposed system as a suspension component, an ideal two-terminal hydraulic system with nylon adaptive flywheel is applied to a quarter car model. The new quarter car model is evaluated with three performance criteria - riding comfort, tire grip and vehicle body suspension deflection. The quarter car model with the new suspension components out-performs the traditional quarter car model under most circumstances. The relationship between the changing ratio of the adaptive flywheel and the performance of the suspension system is discussed, and the optimal changing ratio is determined under certain conditions. Under different conditions, the optimal changing ratio will also change.

4. In order to analyze the application of the adaptive flywheel, a real two-terminal hydraulic system with nylon adaptive flywheel is applied to a quarter car model, and all the key parameters are identified from the previous experiments performed in this thesis. The same performance evaluation and discussion about changing ratio are carried out. The results show, based on the same conditions, that the optimal changing ratio of a real two-terminal hydraulic system is higher than for an ideal one.

5. The steady state response of a two-terminal device with adaptive flywheel is discussed. The single harmonic balance method and multi-harmonic balance method are applied, and it is found that the results of multi-harmonic balance method are more accurate than those of the single harmonic balance method. Due to the complicated calculation process of the multi-harmonic balance method, a new optimal iterative multi-harmonic balance method is proposed and evaluated. It is found that the results of the optimal iterative multi-harmonic balance method are as accurate as those of the multi-harmonic balance method.

1.5. Thesis organization

The thesis is organized as follows. Chapter 2 is the literature review, which gives an overview of current research. In Chapter 3, two different adaptive flywheels (different materials) and two-terminal devices are proposed, and the corresponding mathematical models are developed. In Chapter 4, an ideal two-terminal hydraulic device is applied to a quarter model car, and the performance of this new suspension system is evaluated. Experiments are carried out to identify the key parameters for each two-terminal device in Chapter 5. In Chapter 6, a real two-terminal hydraulic device with nylon adaptive flywheel is applied to a traditional suspension system; performance evaluation and a discussion of changing ratio are also carried out. Chapter 7 presents the single harmonic balance method and multi-harmonic balance method to find the steady state response of a two-terminal device with adaptive flywheel. Due to the low accuracy of the single harmonic balance method and complexity of the multi-harmonic balance method, a new optimal iterative multi-harmonic balance method is proposed. Conclusions are drawn in Chapter 8, in which future research directions are also suggested.

2. Literature Review

In the last century, vibration control has attracted the attention of many researchers. Two major control methods were proposed, active and passive vibration control. Due to high cost, poor stability and low robustness, real world applications of active vibration control are rare. On the other hand, passive vibration control is widely used in industry, because of its high stability, good robustness and low cost. With the invention of two-terminal system, a brand new passive vibration control concept was proposed, which shows promising performance for vibration control. In the following sections, the literature on active, passive and two-terminal vibration control is reviewed.

2.1. Literature review of active and passive vibration control

2.1.1. Active vibration control

As was mentioned in the introduction, closed-loop control is used in most applications of active vibration control. The goal of active vibration control is to actively change the placement of pole-zero points or other control parameters for the objective system, which eventually leads to achieving the dynamical requirements of the system. In order to achieve this goal, knowledge of the proper state of a system and its feedback is the key factor. The basic structure of a closed-loop control system is shown in **Figure 2.1**.

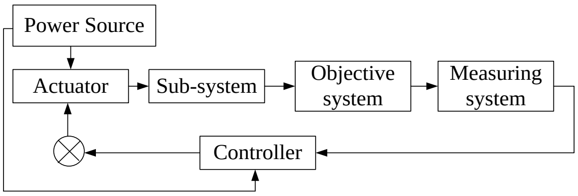

Figure 2.1 Diagram of closed loop control system

There are six major control strategies: (i) independent modal space control, (ii) pole-placement, (iii) optimal control, (iv) self-adaptive control, (v) robust control and

(vi) intelligent control. Each of them will be briefly reviewed in the following.

2.1.1.1. Independent Modal Space Control (IMSC)

By separating the vibration system into mode sequences, this method focuses on controlling the active mode to control the whole vibration system [40]. Baz and Poh [41] proposed an experimental implementation of Modified Independent Modal Space Control (MIMSC), by using a piezo-electric actuator to control several vibration modes. Experimental results showed that with maximum modal energy ranking, MIMSC is an efficient approach to damping the vibration of the objective system.

However, the modes of vibration of a system often cannot be easily calculated due to the coupling between them. An optimal modal coupling control algorithm usually presents a large computational burden, even for a supercomputer, which is the main limitation of this approach to vibration control [42].

2.1.1.2. Pole-placement

This approach includes choosing different eigenvalues and eigenvectors to control the vibration system. It is well known that system eigenvalues will affect the dynamic characteristics of the system, and eigenvectors will affect its stability [43–45]. Through state feedback or output feedback, the location of system poles can be relocated to meet the criteria of the target system.

Bueno and Zanetta [46] presented a new pole placement method by using the system matrix transfer function and sparsity, and experimental results indicate that this method can be applied to different conditions with small signal stability analysis of large system. However, it is extremely difficult to adjust the pole into a proper location via a pole placement method in industrial applications due to their complexity [47].

2.1.1.3. Optimal control method

By using mathematical algorithms such as the extremism principle, optimal filtering and dynamic programming, the theory of optimal control can be used to determine the optimal control input which will meet the system requirements. For linear systems with a quadratic performance index, the optimal feedback control can be presented in analytical form. Software for these calculations already exists [48,49].

In the last two decades, optimal control has been applied to many fields[50–52]. For example, constrained layer damping as an effective vibration suppression approach has been applied to many industrial problems [53–55]. Xie et al.[56] proposed a new optimal vibration control method for a rotating plate with self-sensing active constrained layer damping, which demonstrated the potential for more efficient vibration control. Optimal control has also been used in tracked vehicle suspension systems, where simulation also demonstrated the possibility for efficient, real-time and robust control [57]. However, for systems of higher order than two, the determination of optimal control is complicated, and it is also extremely difficult to present in analytical form [58].

2.1.1.4. Self-adaptive control

A Self-adaptive control system is one which can automatically monitor the changing of system parameters, and maintain an optimum system performance index in real-time [59]. It can be classified into three different types: self-adaptive feed-forward control, self-correction control and model reference self-adaptive control. When it is assumed that the disturbance is measurable, self-adaptive feed-forward control can be applied [60]. Self-correction control integrates real-time identified parameters of a vibration system with parameters of the actuator, which eventually achieves self-correction control [61]. The main theory of model reference self-adaptive control is that the vibration system will be driven by the self-adaptive system, which requires that the output of a vibration system follow the output of a model reference [62]. Self-adaptive control usually shows high performance for system control, because it can change the system parameters in real-time.

Valoor et al. applied self-adaptive control method to smart composite beams using recurrent neural architecture. By developing a finite element model, simulations were carried out and the results indicated high efficiency and good robustness of the implementation [63]. However, self-adaptive control usually requires a good model of the vibration system, which may not always be feasible. Additionally, in order to achieve real-time control, sensors and actuators with high precision are also required, which implies an increase in the cost of implementing the control system [64].

2.1.1.5. Robust control

Through linear feedback, robust control can provide a certain capacity for resisting disturbances for a closed-loop system. Although self-adaptive control can also be applied to a vibration system with uncertainty, there is still a major difference between the two control approaches. Robust control uses excessive controllers to ensure that the state of the target system will move to a stable configuration. If the changing rate of system parameters stays at the design requirements of the controller, this system will always be stable [65].

Based on robust control, Sun et al. [66] proposed an adaptive robust vibration control of a full-car active suspensions with electro-hydraulic actuators. By testing on different road conditions, the high stability of this control system was demonstrated through a Lyapunov framework. Since robust control requires excessive control, which inevitably leads to chattering, a decrease in the precision of the system-tracking and also an increase to the abrasion of the actuator [67].

2.1.1.6. Intelligent control

As one of most popular methods of vibration control, the development of intelligent control presents a whole new field for active vibration control. Fuzzy control is a major branch of intelligent control, which provides an effective approach to solve complicated control system problems[68]. Models of many systems cannot be easily developed. However, fuzzy control not only provides objective information of the target system, but can also embed the experiences and intuition of human intelligence into the control system [69]. Neural network control is another approach to intelligent control. The neural network based intelligent control uses massively parallel processing to simulate the structure and function of a human neural network for application to nonlinear dynamical systems. For some situations, these two methods can also be combined into a fuzzy neural network control approach [70].

Aliki et al. [71] applied fuzzy control to vibration suppression of a smart elastic rectangular plate. A comparison was carried out between fuzzy control and a more traditional proportional integral derivative (PID) controller. The results indicated better vibration suppression with the fuzzy control approach. Another self-learning system was proposed by Gordon, which has been applied to optimize the vehicle suspension. This self-learning system can be used for real-time control [72].

Because intelligent control usually requires pre-description of a system function, this implies that sample data with sufficient precision are necessary. If intelligent control cannot achieve the control function as predicted, trouble-shooting is usually difficult [73].

2.1.1.7. Semi-active vibration control

In the last several decades, researchers have been focusing on semi-active vibration control [74,75]. Semi-active vibration control can be considered as a branch of passive vibration control, since in many cases there is no direct mechanical energy input into the control system. However, in order to achieve semi-active vibration control, a minor outside energy source is needed to control the actuator and actively adjust semi-active vibration control devices. Moreover, feedback control is applied in most cases of semi-active vibration control, which makes semi-active vibration control more similar to active vibration control.

Semi-active vibration control devices are usually combined control systems consisting of devices with passive stiffness or damping and a mechanical active actuator [76]. Active variable stiffness systems (AVS) and active variable damping systems (AVD) are classic examples of semi-active vibration control devices [25,77]. Since the main feature of a semi-active vibration control system is providing an optimum control force, active control theory is fundamental for semi-active vibration control. Furthermore, because the control force of a semi-active vibration control system is limited, the active control algorithm which drives the semi-active vibration control to output the optimum control force must be related to the semi-active vibration control force. In 1990, the Kajima research center firstly applied the AVS system to a three-story office building, which resulted in high performance under low or medium level earthquakes[78]. In 1997, a bridge with an AVD system was first built in America, which resulted in vibrations caused by heavy-loading vehicles to be effectively suppressed [79].

The most important application of semi-active vibration control is semi-active suspensions for vehicles. This theory was proposed by Crosby and Karnopp in 1970s, but applications started at the beginning of the 1980s [80–82]. Different from a passive or active suspension, a semi-active suspension system consists of a constant stiffness spring and variable damping shock absorber, which is also called a no source active suspension due to the minor energy input. In a semi-active suspension system, there is no actuator to generate the control force. Instead, the controller calculates the control force based on data from the sensors and then adjusts the damping of the shock absorber to produce the needed control force, which in turn finally achieves vibration suppression [83].

There are three major types of shock absorber used to achieve semi-active vibration control: hydraulic shock absorber [84], electro-rheological (ER) fluid vibration damper [85] and magneto-rheological (MR) fluid damper [86]. All these shock absorbers usually consist of a small accumulator with a damping valve and a hydraulic control system, which will make the damping force generated by the hydraulic shock absorber proportional to the absolute velocity of the vehicle. In particular, the magneto-rheological fluid damper has been widely used in many vibration systems due to its high damping ratio and low energy cost.

For example, in 1999, Suh and Yeo proposed a theory by using the Binghan-plastic model of ER fluid to estimate the damping force of an ER fluid damper. Through this, the main parameters of the ER damper can be accurately determined and experimental results indicate the actual damping force is in good agreement with the estimated damping force [87]. With the invention of the MR damper, more and more researchers have focused on this specific area, in particular for high-mobility multi-purpose wheeled vehicle [88,89]. Karakas et al. used experiments with a quarter car model to investigate the performance difference between the MR damper and original equipment manufacturer damper. Through skyhook control algorithms, the experimental results indicate that the MR damper can help to achieve highly-efficient vibration suppression [90].

2.1.2. Passive vibration control

As mentioned above, active vibration control usually requires an outside energy source to generate the force required to suppress vibrations. Due to the high cost and low reliability of active controllers, industrial application of active vibration control is limited. On the other hand, passive vibration control due to its associated low cost and high reliability is widely used for vibration control. Passive vibration control can often be realized by structural design [91,92] and has been applied to two major fields: structural vibration control and mechanical passive vibration control.

2.1.2.1. Passive vibration control by structural design

In many mechanical or civil engineering applications, a machine or structure will experience vibration. If this is known in advance, the vibration level may be effectively minimized through optimal design. In particular for some customized structures, this will usually involve calculation, testing, modification, re-calculation and re-testing. However, with the development of Computer Aided Design (CAD), optimal design of a structure is much easier. Instead of a manual design process, design and modification of the prototype can be performed with a computer, and additionally the reliability can also be analyzed through computer simulation [93].

There are several methods of structural design approaches to achieve passive vibration control. These are: de-tuning, reducing the number of responding modes, de-coupling, structure stiffening, optimizing the structural geometry and selecting the best material, respectively [91,92,94]

When there are spectral spikes at certain frequencies in the excitation, the method of de-tuning can be applied [95]. The basic theory of de-tuning design is that the design and modification of the structure will eventually avoid the near proximity of the resonance frequencies and spectral spikes. The approach of reducing the number of responding modes usually can be applied when the structure is under finite-band random excitation [96]. Since the total response of the structure depends on the number of modes, reducing the number of modes results in effective vibration suppression.

De-coupling has been used to describe many procedures, but in structural design, there are two types of de-coupling which can lead to vibration control. The first one is de-coupling the different types of motion at the design state, implying that one type of vibration (e.g. linear) should not excite a different type of vibration (e.g. rotational). The other one is separating the natural frequencies of different components of a structure [97]. By de-coupling the natural frequencies, the whole structure will not resonate under excitation with one fixed frequency.

There are only a few cases of passive vibration control that involve structural stiffening [98]. This follows because an increase in stiffness of a structure will inevitably change its natural frequencies, which may lead to resonance frequencies becoming closer to possible excitation frequencies [99].

When the type of excitation is known, optimization of the structural geometry can lead to vibration suppression. The last method of vibration suppression by structural design is through the selection of the best material under different situations. With the development of material engineering in last several decades, many new compound materials are being discovered or designed, and these have shown high performance in suppression of vibration [100].

2.1.2.2. Structural passive vibration control

In vibration control of structures, passive control can be classified into three basic types: seismic isolation control, energy dissipation control and energy absorption control [101].

Seismic isolation control: By applying an isolation layer at the bottom of the structure above ground, the structure can be separated from the top surface of the foundation. In this way, the seismic energy will be blocked from the main structure, which eventually leads to the reduction in vibrations [102]. Seismic isolation control usually requires variable horizontal stiffness. Under strong winds or low-level earthquakes, the displacement of the upper structure can be made to be extremely small by using a sufficiently high horizontal stiffness [103]. This in turn ensures that the main structure is not affected. When the earthquake is of medium strength, the upper structure will lightly slide in the horizontal direction due to the small stiffness, which will transform the rigid seismic structure into flexible seismic structure. The natural period of vibration will be obviously extended, and separated from the natural period of the lower structure and characteristic period of the ground [104]. Through this, the vibration of the ground can be effectively isolated, which reduces the seismic reaction of the upper structure.

Seismic isolation control is one of oldest passive vibration control methods, and it is also the most popular due to its high reliability and straightforward application. However, this method cannot be applied to high rise buildings or to the control of vibrations caused by strong winds.

Energy dissipation control: There are two ways to achieve energy dissipation control [105,106], one is via no-load-bearing components (such as a supporting wall, shear wall and connector) of the structure that have been designed as energy dissipation devices. The other approach is through dampers that are located at some specific locations (such as interbedded space, nodes and connection space) of the structure. Under the situation of low-level seismic forces or winds, the initial stiffness of the energy dissipation components is sufficient to make them stay in an elastic state, which has enough lateral rigidity to satisfy the application requirements of the main structure[107]. When the earthquake is of a higher magnitude, the energy dissipation components will stay in an inelastic state, which eventually keeps the main structure and all components from seismic destruction.

Energy dissipation devices can be classified as damping, energy dissipation supporting device and energy dissipation wall [108]. To be more specific, the dampers can be listed as a metal damper, friction damper, viscous damper, viscoelastic damper, composite damper and so forth. For energy dissipation supporting, there are three types including eccentric energy dissipation supporting, friction energy dissipation supporting and cycle energy dissipation supporting [109]. The major types of energy dissipation wall can be summarized as band seam energy dissipation wall, horizontal seam roof energy dissipation wall and damper energy dissipation wall [110].

Energy absorption control: By adding an additional sub-structure, energy absorption control will transfer the vibration of the main structure to the sub-structure. The vibration energy of the main structure will be distributed into the main structure and sub-structure, which leads to the reduction of vibrations [111,112]. Most of the extra sub-structures consist of mass, damper and stiffness elements. Through adjusting these three components, the natural frequency of vibration of the sub-structure can also be changed. This will be adjusted to be as close as possible to the excitation vibration frequency of the main structure. When there is excitation of the main structure, the sub-structure will generate inertia forces with opposite direction of the vibration of the main structure, which eventually achieves the reduction and control of vibration [113].

The types of energy absorption passive control devices include tuned mass dampers (TMD) [114], tuned liquid dampers (TLD) [115], pendulum mass dampers[116], air dampers and hydraulic-mass vibration control systems [117]. Of all these devices, the TMD is the most widely used in industry [118]. By using the inertia of the mass, the TMD can increase the damping ratio of the main structure to achieve vibration control. In order to achieve the best results, TMD is usually located at the point where the vibration reaches the maximum amplitude. However, modern architecture adds various equipment or hanging gardens on the top of many buildings, which often makes the installation of a TMD impossible[119]. In particular, in the case of a television tower, a TMD is impossible to install due to the presence of the satellite antenna. Finding the optimum location for a TMD is also extremely important for energy absorption control [120].

2.1.2.3. Mechanical passive vibration control

As mentioned above, the vibration of mechanical systems is a universal phenomenon. Tremendous progress has been made with vibration control in mechanical systems. In particular, passive vibration control, due to its low cost, high reliability and high robustness, has been widely applied in industry [12,91,92]. Within the realm of passive vibration control, vibration control for rotating systems and vehicle passive suspension are two major applications of mechanical passive vibration control.

Rotation system passive vibration control: Rotating systems are the most common device within a mechanical system, and can be found in many industrial applications [28,121]. Due to manufacturing defects, the centroid of each micro-segment of a rotor generally has a small deviation from the axis of rotation. Due to this deviation, centrifugal forces will cause the vibration of the rotor when it is rotating. The vibration of the rotor will not only cause noise and shorten the service life, but also in extreme cases will cause the failure of the whole system.

In the past several decades, researchers have been achieving huge progress in rotating system vibration control [122,123], in particular with respect to reliability, cost, robustness and simplicity. In general, the vibration of a rotating system can be classified into four different types: steady-state oscillation, unstable vibration, self-excited oscillation and torsional vibration. Each of these will be discussed in turn.

Steady-state oscillation: In a rotating system, the static and dynamic balance of the rotor is extremely important. If the rotor is unbalanced, when the rotation frequency reaches the natural frequency of the rotor, vibration caused by harmonic resonance will occur [124]. For this situation, Tatara proposed a bearing with rubber to support the rotor, which can be used for damping by friction [125]. However, for some machines, e.g., a laundry machine, the unbalance of the rotor changes as the operations change. Theale proposed an automatic ball balancer, by locating two balls in the cavity with appropriate angles on the opposite side to the unbalance, which will eventually balance the rotor automatically in the post-critical speed range [126].

Unstable vibration: In a rotating system, the rotor is usually connected with some transmission components, such as a shaft. When the geometric structure of this shaft is asymmetric, unstable vibration will occur if the rotation speed is close to the critical speed of the rotor. The main strategy for this circumstance is to make dummy slots on the shaft, which can eliminate the asymmetry [127,128]. In 2010, Ishida and Liu proposed a method to suppress such an unstable vibration by using discontinuous spring characteristics [129]. With this method, the range of rotation speeds for unstable vibration can be adjusted above the major critical speed.

Self-excited oscillation: internal friction or internal damping in a rotating system are caused by friction between the rotation components, which inevitably leads to vibration of the system in the post critical speed range [130]. By using leaf springs to support the outer ring of the bearing that is mounted on the shaft, a new method was proposed to dissipate energy to suppress the self-excited oscillation. The damping intensity can be adjusted by changing the preload on the leaf spring [131].

Torsional vibration: The driving torque in multi-cylinder reciprocating engines changes at certain periods due to complicated processes such as combustion, intake, exhaust strokes and compression [132,133]. This vibration not only causes problems for the rotating mechanics system, but also imposes an unhealthy work environment on the operator of the machinery. Many devices have been invented to suppress torsional vibration, a centrifugal pendulum vibration absorber being one of the most famous [134–136]. By using the idea of an anti-resonance point for a two-degree freedom system, this damper can effectively achieve vibration control.

2.1.2.4. Vehicle passive suspension

As mentioned above, vehicle suspension is one of the most successful and popular applications of passive vibration control. Researchers have been achieving impressive progress with vehicle passive suspensions in the last several decades. Due to high reliability, good robustness and low cost, passive suspensions still play a major role in vehicle vibration control. Most vehicle passive suspensions can be classified into two different types: non-independent suspension and independent suspension [82,83,137].

Non-independent suspension: The defining structural characteristic of a non-independent suspension is that both sides of the wheels are connected by a wheel axle, and that the wheels and wheel axles are suspended under the car body by an elastic suspension. There are many advantages to a non-independent suspension, namely simplicity, low cost, high strength, easy maintenance and small changes in the orientation of the front wheels on the road. However, due to poor ride comfort and handling stability, this kind of suspension is now mainly used for trucks and buses instead of passenger cars [138].

There are four kinds of springs for non-independent suspensions [139], leaf spring [140], coil spring [141], air spring [142] and oil-gas spring. As indicated by their names, leaf, coil, air and oil-gas spring non-independent suspensions use leaf springs, coil springs, air springs and oil-gas springs as their elastic components, respectively. The type of spring used represents the major difference between these non-independent suspensions [138].

Independent suspension: unlike non-independent suspensions, the defining structural characteristic of an independent suspension is that each side of the wheel is individually suspended under the car body through an elastic suspension [142]. Compared to a non-independent suspension, there are four advantages to an independent suspension. First, the reduction in weight reduces the impact on the car body and increases adhesion between the wheel and the road. Second, a spring of relatively low stiffness can be used for this suspension, which improves the ride comfort. Third, the location of the engine can be lower, which leads to a lower center of gravity of the car and thus increased stability. Lastly, the vibration between the two sides of the vehicle are uncoupled, which eventually causes a reduction of inclination and vibration of the vehicle [82,83,143].

Despite the complicated structure, high cost and inconvenient maintenance, independent suspensions are still the preferred design choice for most modern passenger vehicles. Independent suspensions can be classified as (i) wishbone suspension, (ii) multi-link suspension, (iii) trailing arm suspension, (iv) sliding pillar suspension, and (v) McPherson suspension [144–146].

A wishbone independent suspension implies that the wheels of the car can only swing in the transverse plane. Wishbone suspensions can be separated into single wishbone and double wishbone suspensions, according to the number of transversal arms [147,148]. The application of a single wishbone independent suspension is rare in modern car design, because this suspension will cause the rear part of the car to swing when the car is under high speed [149]. Double wishbone independent suspension can be specified as isometric wishbone or long-short wishbone independent suspension. An isometric wishbone independent suspension has the same disadvantage of a single wishbone independent suspension. However, a long-short wishbone independent suspension can be optimized in the length of the long and short wishbones and the location of the two wishbones. This suspension can also provide high ride stability [150–152].

A multi-link independent suspension is a combination of three to five control rods, which leads to location changes of the wheels. This suspension will make the car turn smoothly, following the driver’s intention; however, there will be shaft swing when the car is running at a high speed [154]. A trailing arm independent suspension is similar to a wishbone independent suspension, the wheels of the car only swing in the vertical plane. It can also be classified as single and double trailing arm independent suspension. This suspension is usually applied to a steering wheel [153,154].

The structural characteristic of a sliding pillar independent suspension is that the wheels are moving up and down along the kingpin axis, which is rigidly fixed to the car frame. There are only a few applications about this suspension, because the kingpin will take most of the lateral force during driving, which increases the abrasion of the kingpin and shortens its service life [155]. The wheels of a McPherson independent suspension still move along with the kingpin. However, unlike sliding pillar independent suspensions, the kingpin can swing instead of being rigidly fixed. A McPherson independent suspension is a combination of a wishbone and sliding pillar independent suspensions [156]. Compared to wishbone independent suspensions, McPherson suspensions have a compact structure, small changes of front wheel orientation on the road and high handling stability [157]. The lateral force on the kingpin is also much smaller than with a sliding pillar independent suspension. This suspension has been widely used for medium or small size cars [158]. However, with the advancement of technology, more attention is paid to the controllability rather than the cost, which is a challenge for passive vibration control.

2.2. Literature Review of Two-terminal vibration control system

2.2.1. Electrical passive network

The main research on electrical passive networks uses a limited number of resistors, inductors, capacitors and transformers to describe a function within a given network. There are two main features of electrical passive networks. First, before an excitation is applied there are no voltages or currents between any two terminals. The second feature is that for any arbitrary excitation, there is no negative energy delivery in the network [159]. In 1931, Brune first defined the electrical passive network and proved that the resistance or admittance function is a positive-real function for all passive networks [160]. Brune also proposed a general method named the Brune

Comprehensive Method, which is used to describe any positive-real function by using a limited number of resistors, inductors, capacitors and transformers.

In the past several decades, much research has been done on electrical passive networks[161,162]. However, the redundancy of components in passive networks is still the main obstacle to its development. Especially for multi-terminal passive networks, a non-transformer solution is still impossible[159]. In the 1970s, with the development of the integrated circuit, interest in research on electrical passive networks started to wane [163].

2.2.2. Mechanical passive networks

In many industrial mechanical control systems, passive components are applied, for example, to vehicle suspension systems and mechanical vibration control systems [164]. Compared to mechanical active networks, passive networks are valued due to their high reliability and low cost. However, structural design and selection of components for a mechanical device is extremely complicated and is usually achieved by trial and error [163].

In order to describe a mechanical system accurately, many researchers attempt to analogize a mechanical system with an electrical system by using a force–current analogy [165]. With the analogy of force-current and velocity-voltage, the system consisting of passive mechanical components can be considered as a passive mechanical network. In a mechanical system, if all the components can be made to correspond to resistors, inductors, capacitors and transformers in an electrical system, the theory of electrical passive network can be applied to the mechanical passive network. According to the kinetic equation, resistors, inductors and transformers in electrical systems can be analogized in the mechanical system as dampers, springs and shafts respectively [142]. The specific analogies between electrical and mechanical systems are shown in **Table 2.1**.

Table 2.1 Analogy between electrical system and mechanical system [167]

Electrical System	Mechanical System
Current (*i*)	Force (*F*)
Voltage (*u*)	Velocity (*v*)
Electrical zero point (Voltage=0)	Mechanical zero point (Velocity=0)
Resistor (*R* = resistance) 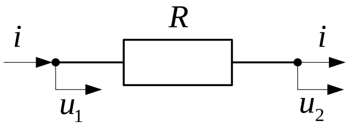 $u = Ri$	Damper (*c* = damping constant) 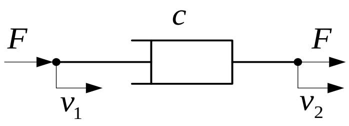 $cv = F$
Inductor (*L* = inductance) 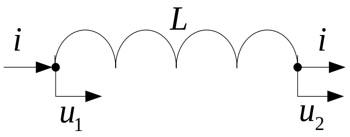 $u = L\frac{di}{dt}$	Spring (*k*= stiffness) 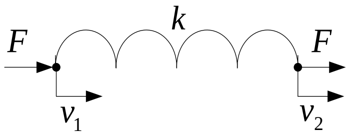 $v = \frac{1}{k}\frac{dF}{dt}$
Transformer	Lever
Capacitor 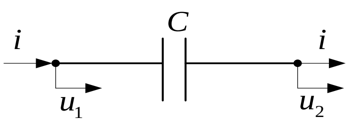 $C\frac{du}{dt} = i$	Mass 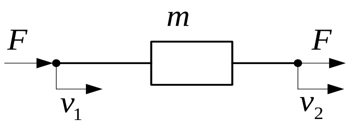 $m\frac{dv}{dt} = F$
Electrical connectors	Mechanical connectors

2.2.3. Two-terminal vibration control system

2.2.3.1. Two-terminal mass system

As mentioned above, the theory of electrical passive networks can be applied to mechanical passive networks if all the corresponding components are matched. However, for the analogy between capacitance and mass, the two terminals of the mass element need to be defined to match the two terminals of the capacitor. According to Newton's second law, one terminal of the mass element is the center of mass, and the other one should be a fixed point in the inertial frame [164]. Therefore, the mass element is analogous to a grounded capacitor, as shown in **Table 2.2**.

Table 2.2 Analogy between mass element and grounded capacitor[32]

Capacitor(Grounded)	Mass(Grounded)
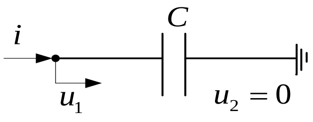	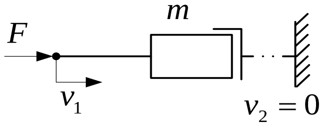
$C\frac{du}{dt} = i$	$m\frac{dv}{dt} = F$

Based on **Table 2.2**, the mass element can be analogized as a grounded capacitor. However, there are still two major problems about this analogue. First, there is the possibility that unreasonably large masses may be required. Second, if the capacitor is not grounded, there is no direct mechanical component which can be analogized [168].

2.2.3.2. Two-terminal mass devices

(1) Inerter: In 2002, Smith proposed a new two-terminal mass device named inerter, which resolves the capacitor analogy difficulty mentioned above [32]. This inerter can not only be used for analogizing the capacitor in electrical networks, but can also generate as high as several hundred times equivalent mass even if the real mass (gravitational) of this system is small [169,170]. The prototype of inerter is shown in **Figure 2.2**.

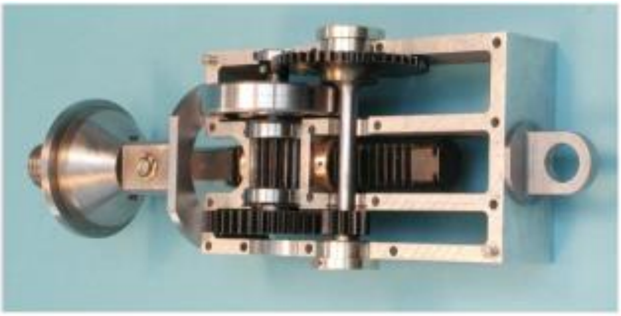

(a)

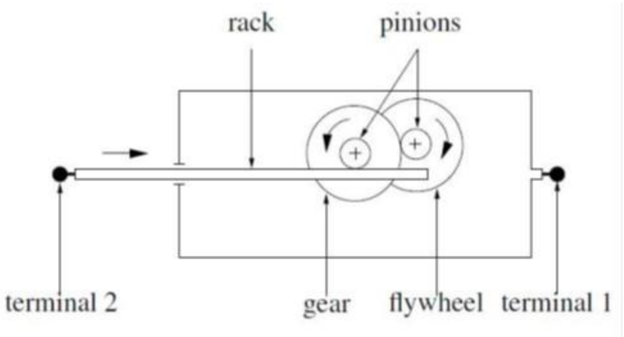

(b)

Figure 2.2 Prototype device: Inerter (a) Prototype of inerter, and (b) schematic of inerter[171]

(2) **Inverse screw two-terminal system:** Inverse screw two-terminal system is a combination of flywheel and inverse screw transmission system [35]. Through the inverse screw transmission system, the inverse screw two-terminal system can transfer vertical or horizontal movement into rotation, which eventually leads to the generation of large equivalent mass. The prototype is shown in **Figure 2.3.**

(a)

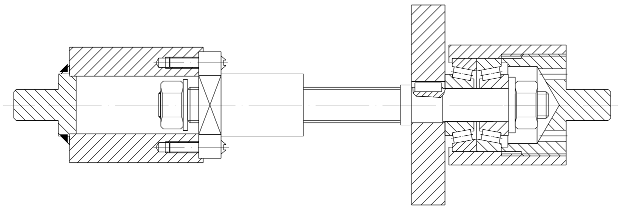

(b)

Figure 2.3 Prototype of inverse screw two-terminal system (a) prototype of inverse screw two-terminal system, and (b) schematic of inverse screw two-terminal system [38]

(3) **Electro-hydraulic variable two-terminal mass device:** In 2011, Li and Liang proposed an electro-hydraulic variable two-terminal mass device, which can generate variable equivalent mass [37]. By changing the voltage of the electrical valve, the transmission ratio will also change, which will in turn cause the generation of different equivalent mass. The prototype of the electro-hydraulic variable two-terminal mass device is shown in **Figure 2.4**.

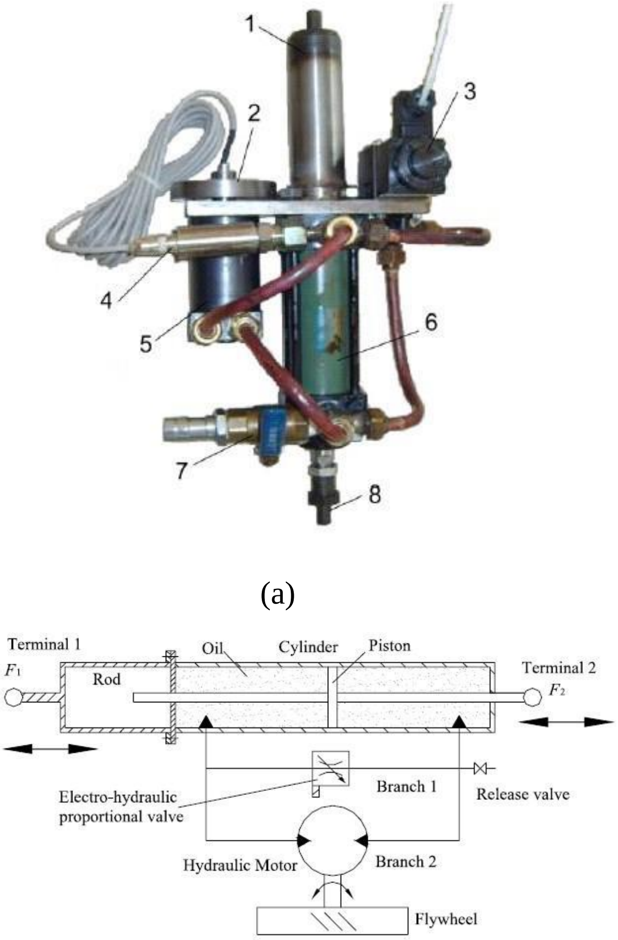

(a)

(b)

Figure 2.4 Prototype of electro-hydraulic variable two-terminal mass device (a) Prototype of electro-hydraulic variable two-terminal mass device, and (b) schematic of electro-hydraulic variable two-terminal mass device [37]

All these two-terminal mass devices have been used for vibration control by many researchers [169], [171], [172]. Chen et al. combined the inerter with a conventional semi-active control system. The experimental results indicated that compared to traditional semi-active control, semi-active control with inerter has shown better vibration suppression performance [172]. Li and Liang also applied a two-terminal hydraulic system to a vehicle suspension [36]. Compared to conventional passive suspension, this two-terminal hydraulic system demonstrated better performance on passenger comfort and tire grip [36]. However, most of these two-terminal mass vibration control systems can only generate constant equivalent mass, because the moment of inertia of the flywheel is constant. Even if they can generate variable equivalent mass, this usually requires a complicated structure and associated high cost. Moreover, a flywheel with fixed moment of inertia will also add more weight to a car, which means more energy consumption.

3. Design and theoretical analysis of nonlinear two-terminal mass mechanisms

In this chapter, two different adaptive flywheel designs are proposed, and the corresponding mathematical models for the adaptive flywheels are derived. The first proposed flywheel is made of metal and the second is made of nylon. Compared to the metal adaptive flywheel, the nylon adaptive flywheel can generate less equivalent mass, but the changing ratio of the nylon adaptive flywheel is much higher. To analyze these adaptive flywheels, a two-terminal hydraulic device and a two-terminal inverse screw device are introduced. The mathematical models for both two-terminal devices are also derived. At the end of this chapter, the design strategy for an adaptive flywheel is discussed. The reasons for choosing certain specific parameters for the adaptive flywheel are illustrated.

3.1. Design motivation and proposed designs

3.1.1. Design motivation

As mentioned in the literature review, researchers have been making progress with vibration control, particularly in structural and mechanical vibration control. Active and semi-active vibration controls have attracted much attention in the last few decades. However, due to high cost, low reliability and robustness, real-world implementations of active and semi-active vibration control are still rare. Passive vibration control still dominates industrial applications because of low cost, high robustness and high reliability. However, in the case of passive vibration control, once key system parameters (stiffness, damping ratio and mass) have been chosen, the characteristics of the system are then fixed. This implies that the ability of a passive vibration control system to deal with a variety of situations is limited. Therefore, the design must always make compromises, favoring the conditions that the passive system is most likely to encounter at the expense of other conditions which are expected to occur less frequently.

With the invention of the inerter, there was increased interest in two-terminal mass vibration control [36,173] - a new and effective method of passive vibration control. By achieving a much larger equivalent mass through the flywheel in the system, a two-terminal mass vibration control system can change the natural frequency of the whole system, which in turn can lead to the suppression of vibrations. However, most of these two-terminal mass vibration control systems can only generate a constant equivalent mass. The generation of variable equivalent mass would make it possible to change system parameters ‘on the fly’. However, as mentioned earlier, this usually requires complicated mechanisms at high cost. Moreover, the flywheel would also cause an increase in the overall weight of the system, which implies higher energy consumption.

3.1.2. Proposed designs

For all the reasons mentioned above, a new type of adaptive two-terminal mass system is therefore proposed in this thesis. In place of a constant flywheel fixed on a two-terminal mass system, a new type of adaptive flywheel will be added and evaluated. There are three features of this new adaptive flywheel that are pertinent. First, the proposed adaptive flywheel can generate the same equivalent mass as a traditional non-adaptive flywheel, but with less weight. Second, this flywheel can passively generate different equivalent mass, and the change in equivalent mass is large enough to be significant. Finally, with the adaptive flywheel, the whole two-terminal vibration control system exhibits nonlinearity in vibration control. Compared to a linear vibration control system, a nonlinear system may offer a better ability to suppress vibrations [174–176].

Since the intended application of the proposed adaptive flywheel is mainly for vehicle suspension systems, there are two design requirements that need to be satisfied.

First, the size of the flywheel must be small enough to fit into the vehicle suspension system rattle space. Second, three performance criteria must be considered for the new adaptive two-terminal mass system: passenger comfort, tire grip and suspension deflection.

Two adaptive flywheels with different materials are proposed, designed and manufactured. Subsequent to the designs of the new adaptive flywheel, two traditional two-terminal systems (i.e., the two-terminal hydraulic transmission system and the two-terminal inverse screw transmission system) connected to the new adaptive flywheels are also proposed and analyzed. Mathematical models of the two different two-terminal systems with adaptive flywheels will also be developed in the thesis.

3.2. Theoretical analysis for two-terminal hydraulic device with metal adaptive flywheel

3.2.1. Mathematical calculation of metal adaptive flywheel

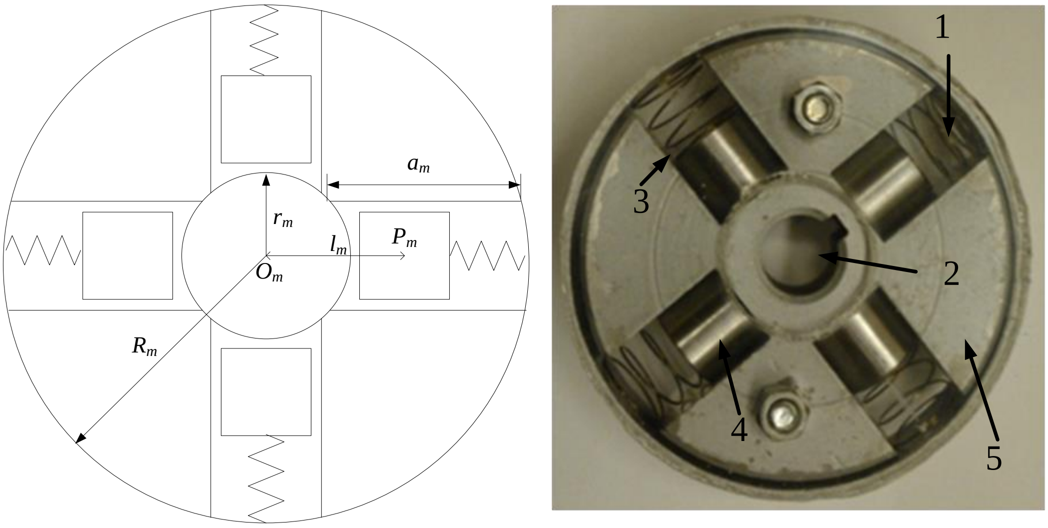

(a) (b)

Figure 3.1 The metal adaptive flywheel: a) schematic diagram, and b) prototype (note: 1-spring, 2-inner hole for the shaft, 3-slot, 4-slider, and 5-frame)

The prototype of the metal adaptive flywheel is shown in **Figure 3.1**. There are four slots in the circular plate. In each slot, there is a slider and spring. The rotation of the flywheel will cause slider motion along the slot. The moving sliders will compress the springs to a certain extent, depending on the rotational speed of the flywheel. The variable location of the sliders in the slot leads to variable moment of inertia of the flywheel. The parameters of this prototype are shown in **Table 3.1**.

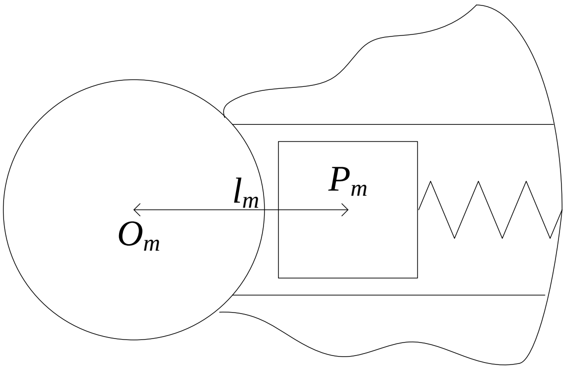

Figure 3.2 Slot of the metal adaptive flywheel

To analyze the variation in the moment of inertia of the metal adaptive flywheel, consider one slot shown in **Figure 3.2**. Point O_m in the figure is the rotation center of the flywheel, point P_m is the centroid of a slider, and l_m is the distance between the rotation center of the flywheel and the centroid of the slider. Denote the mass, diameter, and length of the slider as m_{sm}, d_m and l_{sm}, respectively. The moment of inertia of the slider can then be calculated as:

$$I_{szm} = \frac{1}{12} m_{sm} \left(\frac{3}{4} d_m{}^2 + l_{sm}{}^2 \right) + m_{sm} l_m{}^2 \tag{3.1}$$

Equation (3.1) indicates that the moment of inertia of the slider varies with the distance between the rotation center of the flywheel and the centroid of the slider. In this equation, the moment of inertia of the spring is neglected due to its relatively small weight. To maximize the range in the variation of the moment of inertia of the flywheel, the weights of the frame and other support components should be as light as possible. In an ideal case, if the weights of the frame and other support components are negligible, and the distance l_m is much larger than diameter d_m and length l_{sm}, then the moment of inertia of the metal adaptive flywheel I_{afm} can be written as

$$I_{afm} = 4I_{szm} = 4m_{sm}{l_m}^2 \tag{3.2}$$

Equation (3.2) shows that in the ideal case, the moment of inertia of the adaptive flywheel I_{afm} depends on the distance between the rotation center of the flywheel and the centroid of the slider.

Table 3.1 Parameters of the metal adaptive flywheel prototype

No	Name	Notation	Specification
1	Radius of inner hole	r_m	0.01 m
2	Outer radius of the flywheel	R_m	0.047 m
3	Length of slot	a_m	0.03 m
4	Width of slot /Diameter of slider	d_m	0.02 m
5	Length of slider	l_{sm}	0.015 m
6	Stiffness of spring	k_{sm}	90 N/m
7	Mass of slider	m_{sm}	0.035 kg
8	Mass of flywheel (including slots)	m_{fm}	1 kg
9	Mass of the removed slot material	m_{om}	0.079 kg

Parameters in **Table 3.1** will be discussed at end of this chapter. To model the proposed variable flywheel, its moment of inertia must be calculated. The schematic diagram of the variable flywheel is shown in **Figure 3.1(a)**. The moment of inertia of the variable flywheel is given by

$$I_{afm} = I_{fzm} - 4I_{ozm} + 4I_{szm} \tag{3.3}$$

where I_{fzm} , I_{ozm}, and I_{szm} are the moments of inertia of the circular disk (before removal of the slot), the removed slot material, and one slider, respectively. The moment of inertia of the solid circular disk I_{fzm} (including the slot material) is given by

$$I_{fzm} = \frac{1}{2} m_{fm} ({r_m}^2 + {R_m}^2) \tag{3.4}$$

where m_{fm} is the mass of flywheel (including slots), r_m is the radius of inner hole and R_m is the outer radius of the flywheel. As the distance between the rotation center of the flywheel and the centroid of a slot is given by $R_m - \frac{1}{2} a_m$, the moment of inertia of one slot, I_{ozm}, can be obtained from

$$I_{ozm} = \frac{1}{12} m_{om} \left({d_m}^2 + {a_m}^2 \right) + m_{om} \left(R_m - \frac{1}{2} a_m \right)^2 \tag{3.5}$$

where m_{om} is the mass of the removed slot material. The moment of inertia of one slider I_{szm} can be obtained from Equation (3.1).

Based on the data in **Table 3.1**, the moment of inertia of the adaptive flywheel assembly is

$$I_{afm} = (8.83 \times 10^{-4} + 0.14 {l_m}^2) kg.m^2 \tag{3.6}$$

Since the travel of the slider is in the range of [0.0225m, 0.0375m], the minimum and maximum moment of inertia can be calculated as $I_{afm,\min} = 9.54 \times 10^{-4} kg.m^2$ and $I_{afm,\max} = 1.08 \times 10^{-3} kg.m^2$. The range of the moment of inertia is therefore from $(I_{afm,\max} - I_{afm,\max}) / I_{afm,\max}$ to $(I_{afm,\max} - I_{afm,\min}) / I_{afm,\max}$, or equivalently 0% to 11.67%, for this particular prototype.

3.2.2. Relationship between flywheel angular velocity and slider location

Figure 3.1(a) shows that the distance l_m between the slider centroid and the center of the flywheel depends on the acceleration of the slider. The direction of acceleration is along the slot either toward or away from the rotational center. The acceleration of the slider is mainly caused by the rotation of the flywheel. This can be represented mathematically as

$$m_{sm}a_{sm} = k_{sm}(l_m - l_{m,\min}) \tag{3.7}$$

where a_{sm} is the radial acceleration caused by rotation, $l_{m,\min}$ is the minimum travel of the slider and k_{sm} represents the stiffness of spring. As is shown in equation (3.7), the friction between sliders and slots is neglected. The sliders and slots have been polished during the process of manufacture, and surfaces of both sliders and slots are covered with lubricant oil. Therefore, the friction between sliders and slots is small enough to be neglected. Since $a_{sm} = l_m\omega_m{}^2$, where ω_m is the rotation speed of flywheel, equation (3.7) can be rewritten as

$$m_{sm}l_m\omega_m{}^2 = k_{sm}(l_m - l_{m,\min}) \tag{3.8}$$

Therefore, it follows that

$$l_m = \frac{k_{sm}l_{m,\min}}{k_{sm} - m_{sm}\omega_m{}^2} \tag{3.9}$$

In our design, the minimum and maximum travel distances of the sliders are respectively 0.0225 m and 0.0375 m. Hence, the relationship between flywheel slider angular velocity and slider location can be plotted as shown in **Figure 3.3**. It should be noted that according to equation (3.7), l_m can theoretically be infinity when $k_{sm} = m_{sm}\omega_m{}^2$. However, the actual maximum travel of l_m is limited to 0.0375 m because of the outer ring restriction in the design. Therefore, even if the angular velocity exceeds a certain limit, the slider will remain 0.0375 m from the rotational center no matter how much faster the flywheel rotates and hence there will be no further increase in the equivalent inertial mass.

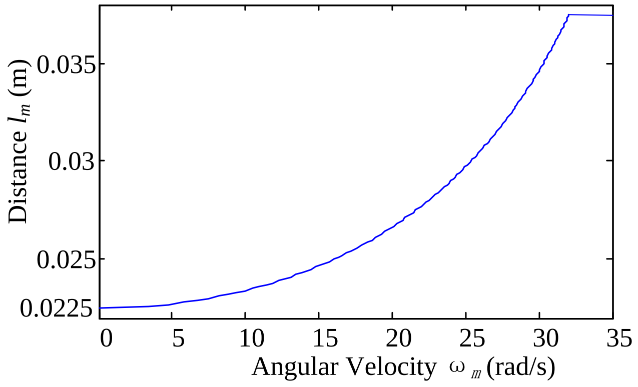

Figure 3.3 The relationship between flywheel angular velocity and slider location

From **Figure 3.3**, the relationship between flywheel angular velocity and slider location is shown, which also indicates the relationship between the angular velocity and the moment of inertia of the flywheel. When the angular speed is zero, the distance between rotation center and centroid of slider, l_m, is minimum, which means the moment inertia of flywheel is also minimum. The increase in angular velocity will lead to increased l_m, and hence the increased moment of inertia. However, when the angular velocity reaches 32 rad/s, l_m also reaches its maximum value. Further increasing the angular velocity will not cause additional increase of the distance between the rotational center and centroid of slider, and thus the moment of inertia will not further increase either because the slider has reached the end wall of the slot.

3.2.3. Ideal model of the two-terminal hydraulic device

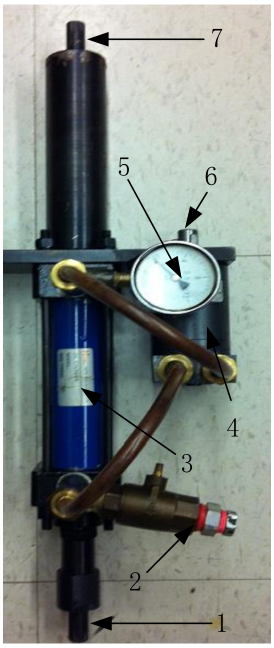

Figure 3.4 The two-terminal hydraulic device (note: 1-terminal 1, 2-release valve, 3-hydraulic cylinder, 4-hydraulic motor, 5-pressure gauge, 6-holding shaft of the flywheel, 7-terminal 2) (Fabricated by the Engineering Laboratory For Detection, Control and Integrated System, Chongqing Technology and Business University, China)

The two-terminal hydraulic device (**Figure 3.4**) is used to test the performance of the variable flywheel because is easy to operate. The structure and main elements of the two-terminal hydraulic device are shown in **Figure 3.4**. Before the tests, the variable flywheel is mounted on the shaft displayed in **Figure 3.4**. When the device is experiencing an excitation input through its two terminals, the oil flow will drive the hydraulic motor and hence transfer the linear motion of the two terminals into the rotation of the variable flywheel. The main parameters of this two-terminal hydraulic device are listed in **Table 3.2**.

Table 3.2 Parameters of the two-terminal hydraulic device (provided by the manufacturer)

No	Name	Notation	Specification
1	Travel of the piston		0.1 m
2	Maximum pressure		7 MPa
3	Cross-section area of the cylinder	A	0.001256 m^2
4	Displacement of the motor	h	1.30607 × 10^{-6} m^3/rad

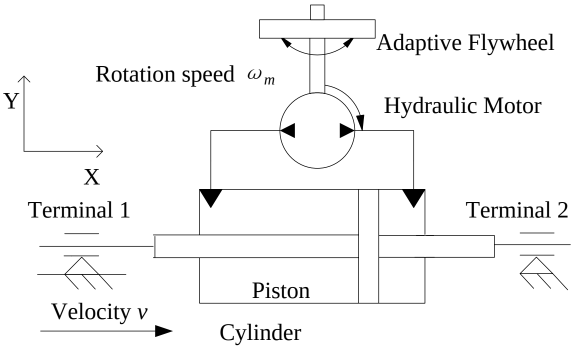

Figure 3.5 Schematic diagram of the two-terminal hydraulic device with a mounted variable flywheel

The two-terminal hydraulic device is schematically shown in **Figure 3.5**. According to the energy conservation principle, the input power must be equal to the output power. This relationship can be expressed as

$$F\Delta R / A = T_1\omega_m \tag{3.10}$$

where F is the force applied to the terminal, ΔR is the flow rate from one chamber to another, A represents the inner cross-sectional area of the cylinder (excluding the cross-sectional area of the rods on both sides of the piston), T_1 is the torque of the variable flywheel, and ω_m is the rotational speed of the variable flywheel. Since $\omega_m = vA/h$, where h is the ratio of displacement of the motor (in m^3/radian), then

$\Delta R = h\omega_m$ and $T_1 = I_{afm}\dot{\omega}_m$, equation (3.10) can be rewritten as:

$$F = I_{afm}\frac{A^2}{h^2}\dot{v} \tag{3.11}$$

where I_{afm} is the moment of inertia of the variable flywheel. Based on Equation (3.11), the equivalent inertia mass of the variable flywheel can be calculated by:

$$m_{em} = I_{afm}\frac{A^2}{h^2} \tag{3.12}$$

3.2.4. Mathematical model of the two-terminal hydraulic system

In the mathematical modeling of this system, four factors will affect this prototype. These are (i) the oil pressure loss P_l in the system (including any leak between the two chambers and friction of the oil with pipe and cylinder), (ii) the friction F_{fh} between piston and cylinder, (iii) the stiffness k_h of this system, and (iv) the compressibility of the hydraulic oil. The compressibility of the hydraulic oil under laminar flow used in this research is 1.023×10^{-7} /Pa, which means that a pressure of 6.895MPa can only cause a 0.5% oil volume change. Hence, this hydraulic oil can be considered as incompressible. The model of the system can therefore be expressed as:

$$F = m_{em}\dot{v} + P_l A + F_{fh} = k_h x_k \tag{3.13}$$

where k_h is the stiffness of the system, and x_k is the elastic deformation of the system. The relationship between pressure loss and flow rate can be formulated as:

$$P_l = b_h \Delta R \tag{3.14}$$

where b_h is a pressure loss coefficient. Since $\Delta R = h\omega_m$ and $\omega_m = vA/h$, the pressure loss can be obtained from $P_l = b_h vA$ and the associated reduction in force by $F_l = b_h vA^2$. In this hydraulic system, the pressure loss P_l can be transferred into energy loss. In a mechanical system, this can be modeled by an equivalent damper with a damping ratio of b_{ah} ($=b_h A^2$) and the same characteristic energy loss. As such, the two-terminal hydraulic system can be represented by the model shown in **Figure 3.6**.

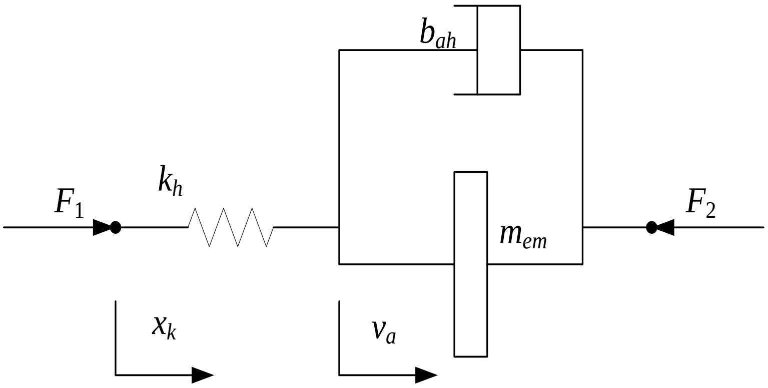

Figure 3.6 Mechanical model of the two-terminal hydraulic system

The mathematical model corresponding to **Figure 3.6** with the consideration of friction is therefore

$$\begin{cases} F = k_h x_k \\ v = \dot{x}_k + v_a \\ F = m_{em}\dot{v}_a + b_{ah}v_a + F_{fh} \\ F_{fh} = \left|F_{fh}\right| \mathrm{sgn}(v_a) \end{cases} \tag{3.15}$$

where $F = F_1 - F_2$, v_a is the relative velocity between the two terminals and can be considered as the input velocity, and b_{ah} is the damping ratio which is equal to $b_h A^2$. The direction of the friction force F_{fh} is opposite to that of v_a. Using the Laplace transform with zero initial conditions, equation (3.15) can be rewritten as:

$$\begin{cases} F(s) = k_h x_k(s) \\ v(s) = x_k(s)s + v_a(s) \\ F(s) = M_{em}(s)v_a(s)s + b_{ah}v_a(s) + F_{fh}(s) \\ F_{fh}(s) = \left|F_{fh}(s)\right| \mathrm{sgn}(v_a) \end{cases} \tag{3.16}$$

where $M_{em}(s)$ is the Laplace transform of m_{em} and $\mathrm{sgn}(v_a)$ represents the direction of velocity. From equation (3.15), a new equation can be formulated as:

$$\frac{1}{k_h}\left(F(s)-F_{fh}(s)\right)\left(k_h+M_{em}(s)s^2+b_{ah}s\right)=M_{em}(s)v(s)s+b_{ah}v(s)- \left(M_{em}(s)\frac{F_{fh}(s)}{k_h}s^2+b_{ah}\frac{F_{fh}(s)}{k_h}s\right) \tag{3.17}$$

For this system, the stiffness $k_h >> F_{fh}$. Therefore, $M_{em}(s)\frac{F_{fh}(s)}{k_h}s^2+b_{ah}\frac{F_{fh}(s)}{k_h}s \approx 0$.

To analyze this system, $F(s)-F_{fh}(s)$ will be considered to be the output signal, and $v(s)$ to be the input signal. As m_{em} is a nonlinear function of time t, one cannot obtain a closed-form expression of the transfer function based on equation (3.17). Therefore, the transfer function is simply written as follows:

$$G(s)=\frac{F(s)-F_{fh}(s)}{v(s)}=\frac{k_h(m_{em}s+b_{ah})}{k_h+m_{em}s^2+b_{ah}s} \tag{3.18}$$

Equations (3.17) and (3.18) clearly show that the transfer function and hence the system behavior are affected by four parameters, i.e., b_{ah}, F_{fh}, k_h and m_{em}. To examine the performance of the system, parameters b_{ah}, F_{fh}, and k_h will be experimentally identified and m_{em} will be calculated using equation (3.12), as described in other chapter. It should be noted that the purpose of presenting equation (3.18) is to show that the system behavior is affected by the above-mentioned four parameters, but not to find a mathematical solution.

3.3. Theoretical analysis for two-terminal hydraulic device with nylon adaptive flywheel

As mentioned in equation (3.2), if the weights of the frame and other support components are negligible, and the distance l_m is much larger than diameter d_m and length l_{sm}, then the moment of inertia of the metal adaptive flywheel I_{afm} will only depend on the distance l_m. However, this is only the ideal condition. In real applications, the proposed metal adaptive flywheel, the maximum changing ratio defined as

$(I_{afm,\max} - I_{afm,\min}) / I_{afm,\max}$ is 11.67%. While this changing ratio is likely to be sufficient for some applications, it is anticipated that larger changing ratios may also be required for other applications.

In order to achieve a higher changing ratio, another structure design and materials are required. In last several decades, due to its light weight and high strength, nylon materials have been widely using in industry of manufacture, which is also ideal materials for a new design.

3.3.1. Design of nylon adaptive flywheel

In view of the physical strength of the adaptive flywheel and the manufacturing properties of nylon materials, the schematic diagram of a proposed nylon adaptive flywheel is shown in **Figure 3.7**. The flywheel can be fixed on a rotation shaft through the inner circle. Four drilled slots are evenly distributed in the nylon disk, which are polished after drilling. In this way, the friction forces between sliders and slots can be neglected.

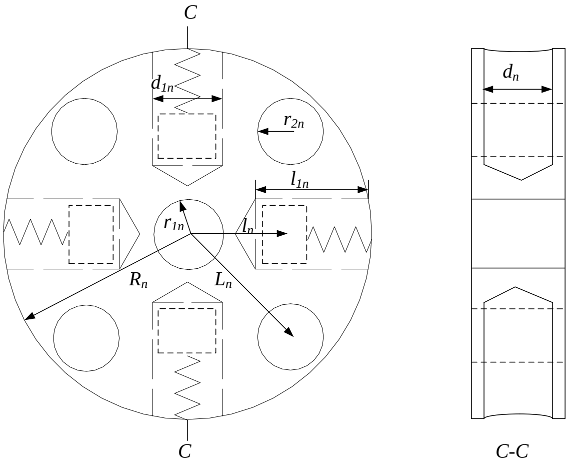

Figure 3.7 Schematic diagram of nylon adaptive flywheel (top view and side view without springs and sliders)

It is well known that the moment of inertia of an object will change with the distance between the object and the center of rotation. Four circular holes are evenly located near the edge of the nylon disk to further reduce the moment of inertia of the flywheel. Due to the small moment of inertia of the flywheel, the changing ratio of moment of inertia caused by the change in position of the sliders will be higher.

A slider and a spring are located in each slot. The centrifugal force caused by the rotation of the flywheel will drive the slider to compress the spring, where the extent of the spring compression depends on the rotational speed of the flywheel. The changing location of the sliders in their slot eventually leads to a variable moment of inertia of the flywheel.

3.3.2. Moment of inertia of the nylon adaptive flywheel

As shown in **Figure 3.7**, the total moment of inertia of the flywheel is divided into four parts: nylon disk (with 4 slots and 4 holes), slots (removed material), sliders and holes (removed material). The moment of inertia of the springs is neglected because of their light weight. The density of polyamide 66 is used for calculating the mass of the slots and holes. The moment inertia of the nylon disc I_{fn} can be represented as

$$I_{fn} = \frac{1}{2} m_{fn} (R_n^2 + r_{1n}^2) \tag{3.19}$$

where the m_{fn} is the mass of the nylon disc, R_n is its outer radius and r_{1n} is its inner radius. For a flywheel of thickness T_n, and density ρ, the mass of the flywheel can be determined from the density of polyamide 66 as

$$m_{fn} = \rho\pi (R_n^2 - r_{1n}^2) T_n \tag{3.20}$$

Based on the same method, the mass of each slot, m_{on}, and the moment inertia of the slots, I_{on}, can be calculated as

$$\begin{cases} m_{on} = \pi \dfrac{{d_{1n}}^2}{4} l_{1n}\rho \\ I_{on} = \dfrac{1}{3} m_{on} \left(\dfrac{3}{4} {d_{1n}}^2 + {l_{1n}}^2 \right) + 4m_{on} \left(R_n - \dfrac{1}{2} l_{1n} \right)^2 \end{cases} \tag{3.21}$$

where d_{1n} and l_{1n} are the width and length of each slot. The mass of each hole m_{hn} and the moment of inertia of each hole I_{hn} are presented

$$\begin{cases} m_{hn} = \pi {r_{2n}}^2 \rho T_n \\ I_{hn} = 2m_{hn} {r_{2n}}^2 + 4m_{hn} {L_n}^2 \end{cases} \tag{3.22}$$

where r_{2n} is the radius of each hole, and L_n is the distance of the center of the hole from the axis of rotation. The mass of the slider, m_{sn}, is measured with an electrical scale, and the moment of inertia of each slider is then calculated as

$$I_{sn} = \frac{m_{sn}}{3}(3{r_{3n}}^2 + {l_{2n}}^2) + 4m_{sn} {l_n}^2 \tag{3.23}$$

where l_n is the distance between the centroid of each slider and the rotation center, l_{2n} is the length of slider and r_{3n} is the radius of slider. By calculating the moment of inertia of the four parts separately, the total moment of inertia of the flywheel I_{afn} can be written as

$$I_{afn} = I_{fn} - I_{on} - I_{hn} + I_{sn} \tag{3.24}$$

Table 3.3 Specific parameters of the nylon adaptive flywheel

Name	**Notation**	**Specification**
Outer radius of flywheel	R_n	0.05m
Thickness of nylon disk	T_n	0.022m
Distance between hole and rotation center	L_n	0.0375m
Radius of inner circle	r_{1n}	0.01m
Radius of holes in flywheel	r_{2n}	0.0085m
Diameter of slots in flywheel	d_{1n}	0.017m

Length of slots	l_{1n}	0.035m
Radius of sliders	r_{3n}	0.008m
Length of sliders	l_{2n}	0.015m
Mass of slider	m_{sn}	0.0237kg
Density of PA66	ρ	1150kg/m^3
Stiffness of spring	k_{sn}	120N/m

The specific parameters for the flywheel are shown in **Table 3.3** (these parameters will be further discussed at the end of this chapter), from which the accurate moment inertia of the adaptive flywheel can be calculated as

$$I_{afn} = (1.75 \times 10^{-4} + 0.0948 l_n{}^2) kg.m^2 \tag{3.25}$$

As shown in Equation (3.25), the moment of inertia of the adaptive flywheel is a function of variable l_n, which implies that the moment of inertia is determined by the distance between the centroid of the sliders and the rotation center. In this design, the travel distance of the sliders ranges from 0.0225m to 0.038m, after taking into consideration that the springs still occupy some space after full compression. The corresponding maximum and minimum moment of inertia are therefore $I_{afn,\max} = 3.12 \times 10^{-4} kg.m^2$ and $I_{afn,\min} = 2.231 \times 10^{-4} kg.m^2$, respectively. The range of the moment of inertia is therefore from $(I_{afn,\max} - I_{afn,\max}) / I_{afn,\max}$ to $(I_{afn,\max} - I_{afn,\min}) / I_{afn,\max}$, or equivalently 0% to 28.5%, for this particular prototype. This range is much wider than that of the metal flywheel (i.e., 0% to 11.67%), as discussed in section 3.2.1.

The relationship between l_n and I_{afn} is shown in **Figure 3.8**.

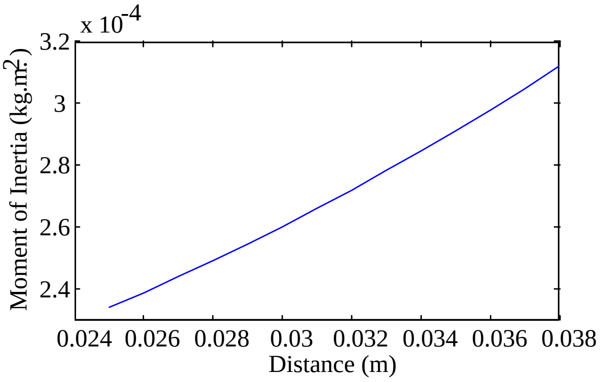

Figure 3.8 The relationship between l_n and I_{afn}

3.3.3. The mechanism of the inverse screw system

As mentioned in section 3.3.2, the changing ratio of the nylon adaptive flywheel is 28.5%, which is much higher than for the metal adaptive flywheel, which has a changing ratio of 11.67%. However, due to the light weight of nylon material, the maximum moment of inertia of the nylon adaptive flywheel is much less than the maximum moment of inertia of the metal adaptive flywheel. If the same two-terminal hydraulic system is applied to analyze this nylon adaptive flywheel, the equivalent mass will be much smaller than for the metal adaptive flywheel, which will eventually lead to an insufficient inertial force in future applications.

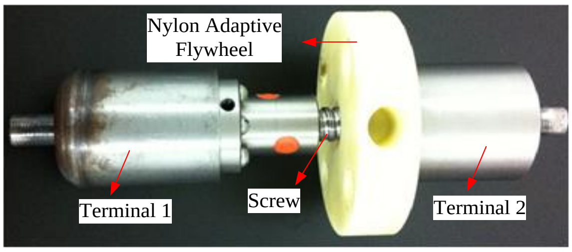

Figure 3.9 Inverse screw system with adaptive nylon flywheel (fabricated by the Engineering Laboratory For Detection, Control and Integrated System, Chongqing Technology and Business University, China)

Therefore, a new two-terminal device needs to be applied. In order to achieve higher equivalent mass and to analyze the characteristics of the nylon adaptive flywheel, it is fixed onto an inverse screw system, as shown in **Figure 3.9**. If one of the terminals is fixed, application of an input to the other terminal results in the transformation of vertical movement into rotation by the inverse screw.

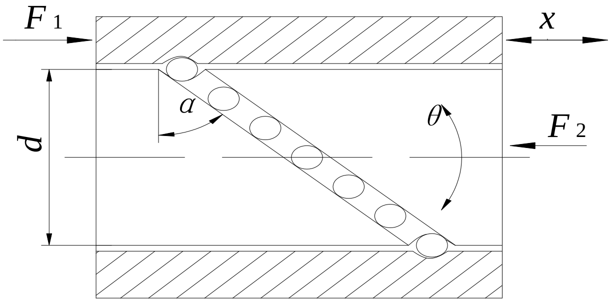

Figure 3.10 Structural diagram of the inverse screw [173]

The structural diagram of the inverse screw is presented in **Figure 3.10**. The transmission relationship between vertical acceleration and angular acceleration is given by [173]

$$\ddot{\theta} = \frac{2\ddot{x}}{d\tan\alpha} \tag{3.26}$$

where $\ddot{x}$ is the vertical acceleration, d is the diameter of the ball screw, α is the helix angle of the ball screw, and $\ddot{\theta}$ is the angular acceleration of the flywheel. Based on Newton's laws of motion, the torque on the ball screw should be equal to the torque on the nylon adaptive flywheel, which leads to [173]

$$\frac{Fd\tan\alpha}{2} = I_{afn}\ddot{\theta} \tag{3.27}$$

where I_{afn} is the moment inertia of adaptive flywheel, and F is the axial force. Combining equation (3.26) with (3.27), the axial force is calculated as [173]

$$F = I_{afn}\ddot{x}\left(\frac{2}{d\tan\alpha}\right)^2 \tag{3.28}$$

According to Newton's second Law, $F = m_{en}\ddot{x}$, where m_{en} represents the equivalent mass generated by the nylon flywheel, therefore the equivalent mass m_{en} is given by

$$m_{en} = I_{afn}\left(\frac{2}{d\tan\alpha}\right)^2 \tag{3.29}$$

From equation (3.25), it is clear that the moment of inertia of the adaptive flywheel, I_{afn}, is determined by the distance between the centroid of the sliders and the rotation center, l_n. Assuming that the flywheel is rotating in **Figure 3.7**, the centrifugal force can be written as

$$F_c = m_{sn} l_n \dot{\theta}^2 \tag{3.30}$$

where F_c is the centrifugal force, m_{sn} is the mass of the slider, l_n is the distance between the centroid of each slider and the rotation center, $\dot{\theta}$ is the angular velocity of the flywheel. The centrifugal force can also be described by the stiffness of spring k_{sn} as

$$F_c = k_{sn}(l_n - l_{n,\min}) \tag{3.31}$$

where $l_{n,\min}$ is the minimum distance between the centroid of the slider and the rotation center. From the above two equations, the distance l_n can be represented by both the angular velocity of the flywheel and the stiffness of the spring. Combining equations (3.26), (3.30) and (3.31), the relationship between distance l_n and the other variables is given by

$$l_n = \frac{0.0225 k_{sn}}{k_{sn} - m_{sn} 4\dot{x}^2 / (d\tan\alpha)^2} \tag{3.32}$$

Furthermore, by combination of equations (3.25), (3.29) and (3.32), the equivalent mass m_{en} is given by

$$m_{en} = \left(1.75\times10^{-4} + 0.0948 \left(\frac{0.0225 k_{sn}}{k_{sn} - m_{sn} 4\dot{x}^2 / (d\tan\alpha)^2} \right)^2 \right) \left(\frac{2}{d\tan\alpha} \right)^2 \qquad (3.33)$$

The key specifications of the inverse screw system are shown in **Table 3.4**.

Table 3.4 Parameters of the inverse screw system (provided by manufacturer)

Name	Notation	Specification
Diameter of ball screw	d	16mm
Helix angle of ball screw	α	14°
Maximum working travel distance		-35mm~35mm

3.3.4. Mathematical model of the inverse screw system with nylon adaptive flywheel

In section 3.3.1, the inverse screw system was shown to lead to the creation of an equivalent mass m_{en} which is much larger than the mass of the original nylon flywheel. In achieving an accurate dynamic model of the inverse screw system with the nylon adaptive flywheel, there are a few factors which should be taken into account.

Since the inverse screw system is based on a screw transmission mechanism, the backlash problem is a factor which cannot be ignored [173]. The existence of backlash will affect the transmission precision of a system. However, in some circumstances backlash will also reduce friction and increase the service life of the transmission system. In practical applications, there is always the presence of backlash due to many reasons, such as manufacturing error and thermal expansion.

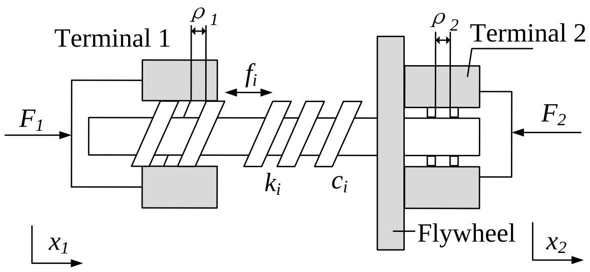

Figure 3.11 Schematic diagram of inverse screw system

As shown in **Figure 3.11**, the transmission path through terminal 1 to terminal 2 is a screw and bearing path, which is the reason why there are two backlashes ρ_1 and ρ_2, respectively. The elastic effect in this inverse screw system is another factor which needs to be considered. The force $F(t)$ which corresponds to the deformation can be represented as

$$F(t) = k_i(x_1 - x_2) + c_i(\dot{x}_1 - \dot{x}_2) \tag{3.34}$$

where k_i and c_i are the stiffness and viscous damping coefficient respectively, and $x_1 - x_2$ is the elastic deformation of the system. Under most of circumstances, the friction of a screw transmission system is negligible considering the large applied force. In obtaining a more accurate model, the friction $f_i(t)$ has also been taken into account as

$$f_i(t) = \begin{cases} -f_i & x_1 - x_2 > 0 \\ 0 & x_1 - x_2 = 0 \\ f_i & x_1 - x_2 < 0 \end{cases} \tag{3.35}$$

Three different situations regarding friction are expressed in equation (3.35). If the vertical displacement x_1 is a positive value (positive direction taken to the right), the direction of the friction force will be negative, and vice versa. In view of all these factors, the dynamic model can be developed as given in **Figure 3.12**.

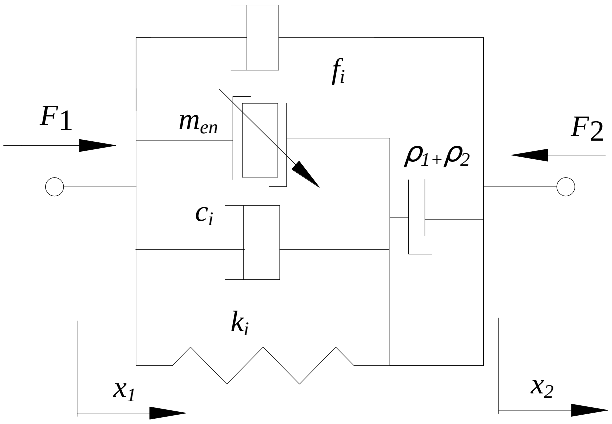

Figure 3.12 Dynamic model of inverse screw system with nylon flywheel

Two different situations will occur due to the inevitable backlash in the inverse screw system. The first condition is the condition of noncontact, which can be represented via

$$k_i(\rho_1+\rho_2) > \left|k_i(x_1-x_2)+c_i(\dot{x}_1-\dot{x}_2)\right| \tag{3.36}$$

Another condition can be described as contact and satisfies the following equation

$$k_i(\rho_1+\rho_2) \le \left|k_i(x_1-x_2)+c_i(\dot{x}_1-\dot{x}_2)\right| \tag{3.37}$$

In both equations (3.36) and (3.37), $\rho_1+\rho_2$ is the total backlash of the inverse screw system. Taking all the aforementioned factors into account, and then combining equations (3.32) to (3.37), the dynamic mathematical model of the inverse screw system with nylon adaptive flywheel can be presented as

$$\begin{cases} Noncontact: F(t)=k_i(x_1-x_2)+c_i(\dot{x}_1-\dot{x}_2)+f_i(t) \\ Contact: F(t)=k_i(x_1-x_2)+c_i(\dot{x}_1-\dot{x}_2)+m_{ei}(\ddot{x}_1-\ddot{x}_2)+f_i(t) \end{cases} \tag{3.38}$$

Based on equation (3.38), the mathematical model of this whole system can be described by four key parameters k_i, c_i, f_i and m_{en}, where x_1-x_2 is considered as an input. An accurate mathematical model of this system will be developed after the determination of the four parameters, which will be discussed in Chapter 5.

3.4. Design strategy

3.4.1. The design of the metal adaptive flywheel

As mentioned in section 3.2.1, in an ideal case the moment of inertia of the metal adaptive flywheel I_{afm} only depends on the distance between the rotation center of the flywheel and the centroid of the slider, in addition to the weight of the slider. However, in real applications, many factors need to be considered during the process of design.

Due to the different applications, the actual size of the adaptive flywheel should also be variable. In our proposed design, the major application of this adaptive flywheel is a car suspension, which implies that the size of this adaptive flywheel will need to be small due to the limited space in the suspension system of a car. According to Xu, Smith, and Li et al [39, 171,173], the outer radius of this flywheel R_m has been eventually chosen as 0.047m. Due to inner hole, the adaptive flywheel can be mounted on different devices, which means the radius of this inner hole is determined by the experimental device. In our design, the radius of the inner hole r_m is 0.005m.

Due to physical size and material strength, the size of slots should also be constrained. Larger size of the slots indicates that additional material will be removed from the flywheel, but the physical strength of the flywheel will also be reduced. Considering the reliability and physical size, the length a_m and the width d_m of the slots are chosen as 0.03m and 0.02m respectively [39].

Based on equation (3.2), the higher weight of the sliders leads to a larger moment of inertia for the adaptive flywheel. However, due to the heavy weight of the sliders, the length of the slider will also increase, leading to a shorter travel distance for the slider. Combining all the factors, the length of slider l_{sm} is chosen as 0.015m [39].

3.4.2. The design of the spring

As mentioned before, different rotational speeds of the adaptive flywheel will drive the sliders to different locations in the slots. However, other than the rotational speed of the adaptive flywheel, the location of the sliders also depends on the stiffness k_{sm} of the springs. In order to observe the behavior of the metal adaptive flywheel, an appropriate stiffness k_{sm} of the springs needs to be chosen based on experimental input. During the experiments, if the stiffness k_{sm} is too small, the sliders will reach the maximum stroke under an input with a small amplitude and frequency. On the other hand, with a high stiffness k_{sm}, the sliders cannot reach the maximum stroke even if under an input with maximum amplitude and frequency. Therefore, an appropriate stiffness k_{sm} will keep the sliders travel under maximum stroke with most inputs except those with high amplitude and frequency.

From equation (3.9), when the sliders reach the maximum stroke, the relationship between inputs and stiffness *k* can be rewritten as:

$$k_{sm} = \frac{l_{m,\max} m_{sm} \omega_m^{\ 2}}{l_{m,\max} - l_{m,\min}} \tag{3.39}$$

Since $\omega_m = vA/h$, it follows that:

$$k_{sm} = \frac{l_{m,\max} m_{sm} v^2 A^2}{\left(l_{m,\max} - l_{m,\min}\right) h^2} \tag{3.40}$$

Based on equation (3.40), with a given input, the stiffness k_{sm} can be determined. In our experiments, a sinusoidal input with amplitude 1.854m/s is chosen. From equation (3.40), the value of stiffness k_{sm} can be calculated as 90 N/m, which will keep the sliders travel under maximum stroke with most inputs.

According to the Popov's formula [142], the stiffness of spring k_{sm} can be presented as

$$k_{sm} = \frac{G d_s^{\ 4}}{8(d_m - d_s)n} \tag{3.41}$$

where d_m is the diameter of spring, d_s is the diameter of the spring wire, G represents the shear modulus of the material, n is the total circles of the spring. Since the material of the springs is steel, the shear modulus of the material G should be 83 GPa. However, there are still two unknown parameters G and n in equation (3.41). As shown in **Figure 3.1** (a), the length of the spring should be the length of slot minus the length of slider, $a_m - l_{sm}$, which is 0.015m based on **Table 3.1**. Because of this, a reasonable assumption of the value of n can be made, which is 4. According to equation (3.41), the diameter of the spring d_m can be determined as 0.00051m.

3.5. Conclusion

Two different adaptive flywheels have been proposed, and the corresponding mathematical models for the adaptive flywheels have also been developed. According to the mathematical models, the metal adaptive flywheel can generate more equivalent mass than the nylon adaptive flywheel. However, due to the light weight of the frame of the nylon adaptive flywheel, the changing ratio of the nylon adaptive flywheel is much higher than that of the metal flywheel. A two-terminal hydraulic device and two-terminal inverse screw device were introduced to analyze these adaptive flywheels. The mathematical models for both two-terminal devices were also developed. At the end of the chapter, reasonable parameters for the adaptive flywheel were chosen based on the design strategy as proposed in the chapter.

4. Application of ideal two-terminal device with adaptive flywheel to suspension system

The goal of this chapter is to compare the performance of a quarter-car suspension with three different suspensions. The three suspensions considered are the traditional suspension system (passive spring-damper combination), the suspension system consisting of an ideal two-terminal device with a constant flywheel and suspension system consisting of an ideal two-terminal device with an adaptive flywheel. Three most commonly used criteria are applied to evaluate the performance of each suspension system, namely, riding comfort, tire grip and vehicle body deflection [144,178]. To simulate the actual road situation, three different inputs are applied as excitation, which are zero input, impulse input and sinusoidal input [143,179]. At the end of this chapter, the performance of a suspension system consisting of an ideal two-terminal device with an adaptive flywheel is discussed under variable changing ratio of the adaptive flywheel. The optimal changing ratio is determined under certain conditions.

4.1. Mathematical model for a quarter car with different suspension systems

In this section, three different suspension systems will be discussed. Simulations will be carried out to verify the performance of each suspension system. The first suspension system is the traditional suspension system, which can be considered as the performance standard against which to compare the other two suspension systems. The suspension system consisting of an ideal two-terminal device with a constant flywheel is also used since this type of suspension has been analyzed by other researchers [35,36]. The last suspension system to be evaluated is a suspension system consisting of an ideal two-terminal device with an adaptive flywheel. By comparing it to the other two existing suspension systems, the reason why this system has been proposed will be clarified.

As mentioned above, an ideal two-terminal device is introduced in this chapter. However, two different materials for the adaptive flywheels and corresponding two-terminal devices were proposed in chapter 3. Unlike an inverse screw two-terminal device which transfers movement by ball-screw system, a two-terminal hydraulic device transfers movement through hydraulic oil. Due to the constant changes of the vibration direction, compared to an inverse screw two-terminal device, the reliability of a two-terminal hydraulic system is much higher. Therefore, in the simulations in this chapter, the combination of an ideal two-terminal hydraulic device with a nylon adaptive flywheel was chosen. **Figure 4.1** shows a quarter car model with traditional suspension system.

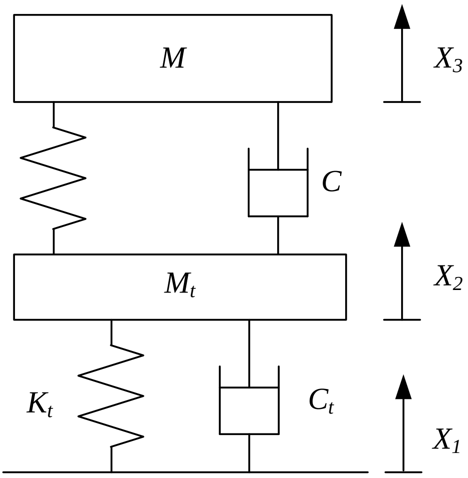

Figure 4.1 Quarter car model with traditional suspension system

The mathematical model for traditional quarter car model with a traditional suspension system can be written as [66]:

$$\begin{cases} M\ddot{X}_3 + K(X_3 - X_2) + C(\dot{X}_3 - \dot{X}_2) = 0 \\ M_t\ddot{X}_2 + K_t(X_2 - X_1) + C_t(\dot{X}_2 - \dot{X}_1) - K(X_3 - X_2) - C(\dot{X}_3 - \dot{X}_2) = 0 \end{cases} \quad (4.1)$$

In equation (4.1), M is the quarter-car combined mass of car and passenger (sprung mass), M_t represents the mass of the unspring mass of the quarter car, K is the stiffness of the quarter-car suspension system, C stands for the damping coefficient, K_t is the stiffness of the tire, C_t is the damping coefficient of the tire, X_1 is the road vertical displacement, X_2 is the displacement of the unsprung mass (mass not supported by the suspension), X_3 represents the displacement of the sprung mass (all combined masses that are supported by the suspension). By using the Laplace transform, equation (4.1) can be rewritten as:

$$\begin{cases} Ms^2X_3(\mathrm{s})+K(X_3(\mathrm{s})-X_2(\mathrm{s}))+Cs(X_3(\mathrm{s})-X_2(\mathrm{s}))=0 \\ M_ts^2X_2(\mathrm{s})+K_t(X_2(\mathrm{s})-X_1(\mathrm{s}))+C_ts(X_2(\mathrm{s})-X_1(\mathrm{s}))-K(X_3(\mathrm{s})-X_2(\mathrm{s}))-Cs(X_3(\mathrm{s})-X_2(\mathrm{s}))=0 \end{cases}$$

(4.2)

Based on equation (4.2), the tire natural frequency ω_t, body natural frequency ω_b, suspension damping ratio ζ, tire-body mass ratio α can be all determined from

$$\begin{cases} \omega_t=\sqrt{\dfrac{K_t+K}{M_t}} \\ \omega_b=\sqrt{\dfrac{KK_t}{M(K+K_t)}} \\ \zeta=\dfrac{C}{2\sqrt{KM}} \\ \alpha=\dfrac{M_t}{M} \end{cases} \qquad (4.3)$$

For conducting a comprehensive study, in addition to the traditional suspension system, the suspension system which incorporates an ideal two-terminal device with constant flywheel is also considered, this system is shown in **Figure 4.2**.

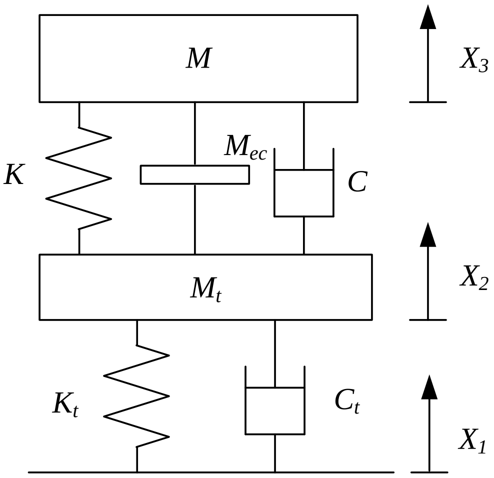

Figure 4.2 Suspension system of two-terminal device with constant flywheel

The associated mathematical model for the suspension system with a two-terminal device with a constant flywheel, as shown in **Figure 4.2**, can be represented as

$$\begin{cases} M\ddot{X}_3+M_{ec}(\ddot{X}_3-\ddot{X}_2)+K(X_3-X_2)+C(\dot{X}_3-\dot{X}_2)=0 \\ M_t\ddot{X}_2-M_{ec}(\ddot{X}_3-\ddot{X}_2)+K_t(X_2-X_1)+C_t(\dot{X}_2-\dot{X}_1)-K(X_3-X_2)-C(\dot{X}_3-\dot{X}_2)=0 \end{cases} \tag{4.4}$$

In equation (4.4), M_{ec} is the equivalent mass generated by the constant flywheel, which can be calculated as [37]

$$M_{ec}=M_{con}R_{con}{}^2A^2/(2h^2) \tag{4.5}$$

In equation (4.5), M_{con} is original weight of the constant flywheel, R_{con} is the radius of the constant flywheel. A and h are the same parameters which are defined in chapter 3.

Through Laplace transform, the equation of motion can be written in the Laplace domain as

$$\begin{cases} Ms^2X_3(s)+M_{ec}s^2(X_3(s)-X_2(s))+K(X_3(s)-X_2(s))+Cs(X_3(s)-X_2(s))=0 \\ M_ts^2X_2(s)-M_{ec}s^2(X_3(s)-X_2(s))+K_t(X_2(s)-X_1(s))+C_ts(X_2(s)+ \\ \qquad -X_1(s))-K(X_3(s)-X_2(s))-Cs(X_3(s)-X_2(s))=0 \end{cases} \tag{4.6}$$

Based on equation (4.6), the tire natural frequency ω_t, body natural frequency ω_b, suspension damping ratio ζ, tire-body mass ratio α and inertial mass ratio β can be calculated from

$$\begin{cases} \omega_t = \sqrt{\dfrac{K_t + K}{M_t}} \\ \omega_b = \sqrt{\dfrac{KK_t}{M(K + K_t)}} \\ \zeta = \dfrac{C}{2\sqrt{KM}} \\ \alpha = \dfrac{M_t}{M} \\ \beta = \dfrac{M_{ec}}{M} \end{cases} \tag{4.7}$$

In **Figure 4.3**, the suspension system of the two-terminal device with adaptive flywheel is shown. The corresponding mathematical model can be written as:

$$\begin{cases} M\ddot{X}_3 + M_e(\ddot{X}_3 - \ddot{X}_2) + K(X_3 - X_2) + C(\dot{X}_3 - \dot{X}_2) = 0 \\ M_t\ddot{X}_2 - M_e(\ddot{X}_3 - \ddot{X}_2) + K_t(X_2 - X_1) + C_t(\dot{X}_2 - \dot{X}_1) - K(X_3 - X_2) - C(\dot{X}_3 - \dot{X}_2) = 0 \end{cases}$$

(4.8)

In equation (4.8), M_e is the equivalent mass generated by the adaptive flywheel, which can be determined as:

$$M_e = I_e \frac{A^2}{h^2} \tag{4.9}$$

In equation (4.9), I_e is the moment of inertia of the adaptive flywheel. By combining equation (4.9) (3.9) and (3.25), the M_e can be rewritten as:

$$M_e = 1.75 \times 10^{-4} + 0.0948 \left(\frac{k_{sn} l_{n,\min}}{k_{sn} - m_{sn} \omega_n{}^2} \right)^2 \tag{4.10}$$

All the parameters are defined in chapter 3. Since $\omega_n = vA/h$, and $v = \dot{X}_3(t) - \dot{X}_2(t)$, equation (4.10) can also be written as:

$$M_e = (1.75 \times 10^{-4} + 0.0948 \frac{\left(k_{sn} l_{n,\min}\right)^2}{\left[k_{sn} - m_{sn} \left(\dfrac{(\dot{X}_3(t) - \dot{X}_2(t))^2 A^2}{h^2} \right) \right]^2} \tag{4.11}$$

As mentioned in chapter 3, a two-terminal device is required in order to generate equivalent mass through the flywheel. However, to study the behavior of the suspension system with the proposed adaptive flywheel, other potentially-contributing factors to the behavior of this two-terminal device need to be reduced. Therefore, in this mathematical model the two-terminal device modeled is considered to be an ideal two-terminal device, which implies that some of the characteristics of the two-terminal device (e.g. damping ratio, stiffness and friction) are neglected. The only function of this ideal two-terminal system is to convert vertical motion into the rotation of the flywheel, and it is assumed to do so perfectly. The converting ratio is based on a two-terminal hydraulic system. The same assumption is also applied to the mathematical model for the suspension system with an ideal two-terminal device with constant flywheel. By using the same conditions for both constant and adaptive flywheel, the comparison will be more reasonable due to the dynamics introduced by the two-terminal device [35,37].

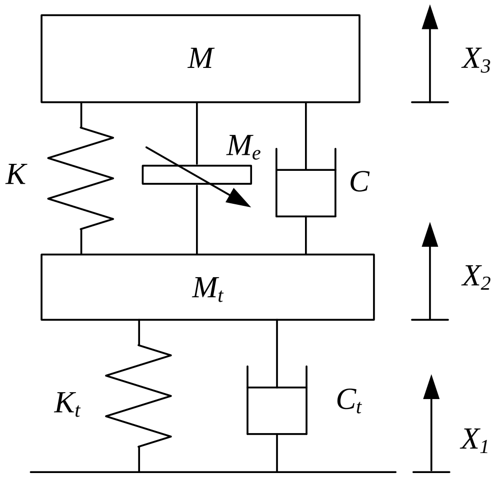

Figure 4.3 Suspension system of two-terminal device with adaptive flywheel

4.2. Performance evaluation for each suspension system

4.2.1. Riding comfort

Riding comfort as one of the most important performance criteria for a suspension system, this can be evaluated by [153,178]:

$$M_1 = \left(\frac{1}{2\pi} \int_{-\infty}^{\infty} \left| \frac{s^2 X_3(s)}{X_1(s)} \right|^2 G_q(\omega) d\omega \right)^{\frac{1}{2}} = 0.2\pi (G_q(n_0) v)^{\frac{1}{2}} \left\| H_1(s) \right\|_2 \qquad (4.12)$$

In equation (4.12), M_1 is the riding comfort coefficient, $G_q(n_0)$ represents the road roughness parameters, n_0 are the random road parameters, v is the velocity of the car, and $H_1(s) = \frac{sX_3(s)}{X_1(s)}$. Based on equation (4.12), once the road roughness is chosen and the velocity of car is fixed, the transfer function $H_1(s)$ will be the dominant factor to determine the riding comfort.

According to equation (4.2), the transfer function $H_{1t}(s)$ for the traditional suspension system can be presented as:

$$H_{1t}(s) = \frac{s\omega_t^2 (2\zeta\omega_b s + \omega_b{}^2)}{(2\zeta\omega_b^2 + \omega_b^2)(s^2 + \omega_t^2) + s^2 \left(s^2 + \frac{2\zeta\omega_b}{\alpha} s + \frac{\omega_b{}^2}{\alpha} + \omega_t^2 \right)} \qquad (4.13)$$

Based on equation (4.6), the transfer function $H_{1c}(s)$ for suspension system of two-terminal device with constant flywheel can be written as:

$$H_{1c}(s) = \frac{s\omega_t^2 (\beta s^2 + 2\zeta\omega s + \omega^2)}{(\beta s^2 + 2\zeta\omega^2 + \omega^2)(s^2 + \omega_t^2) + s^2 \left(s^2 + \frac{\beta}{\alpha} s^2 + \frac{2\zeta\omega}{\alpha} s + \frac{\omega^2}{\alpha} + \omega_t^2 \right)} \qquad (4.14)$$

As defined above, M_e is a nonlinear parameter, the Laplace transform cannot be directly applied, and the transfer function $H_{1a}(s)$ for a suspension system of a two-terminal device with adaptive flywheel cannot be obtained. This implies that there is no analytical expression for this nonlinear system. However, weighted root mean square acceleration is considered as a key index to judge the riding comfort when the velocity of the car is fixed, and this is expressed in meters per second squared (m/s^2) for translational vibrations [151]. With small weighted root mean square acceleration, the riding comfort of this suspension system is considered to be better. The weighted root mean square acceleration should be calculated in accordance with the following equation:

$$a_w = \left(\frac{1}{T} \int_0^T a(t)^2 \, dt \right)^{\frac{1}{2}} \tag{4.15}$$

where $a(t)$ is acceleration, and *T* represents the total time of the simulation. Based on equation (4.15), for this particular performance measure of riding comfort, the only relevant factor is the vertical acceleration of the vehicle body. For comparing the performance of a constant and adaptive flywheel under the same conditions, the moment of inertia of the constant flywheel should be equal to the static (or minimum) moment of inertia of the adaptive flywheel. In this simulation, the static moment of inertia of the nylon adaptive flywheel is set at $I_{afn,\min} = 2.231 \times 10^{-4} kg.m^2$, which implies that the moments of inertia of the constant and adaptive flywheels should be the same. The detailed calculation of $I_{afn,\min}$ can be found in Chapter 3. The other values chosen for key parameters are chosen to be similar to those of an actual car [180]:

$$\begin{cases} M_t = 25kg \\ M = 300kg \\ K_t = 120000\mathrm{N/m} \\ K = 90000\mathrm{N/m} \\ C_t = 1300\mathrm{Ns/m} \\ C = 5000\mathrm{Ns/m} \end{cases} \tag{4.16}$$

In our simulations, three different excitations are applied, which are zero input with an initial displacement, an impulse input and a sinusoidal input. These three excitations are applied to simulate the three most common driving situations, which are driving through a sudden drop, driving through a speed bump and driving through a bumpy road, respectively.

4.2.1.1. Zero input

An initial displacement of 0.05m is applied to the three suspension systems. By combining equation (4.15) with (4.1), (4.4) and (4.8), the numerical solution of the weighted root mean square acceleration for each suspension system in the time-domain can be calculated through Matlab. The results of this are shown in **Table 4.1** and **Figure 4.4** as the vehicle body mass is varied.

Table 4.1 Weighted root mean square acceleration with zero input

Vehicle body mass M_v (kg)	Weighted acceleration of traditional suspension system a_w(m/s^2)	Weighted acceleration of CFW (constant flywheel) suspension system a_w(m/s^2)	Weighted acceleration of AFW (adaptive flywheel) suspension system a_w(m/s^2)
340	0.4656	0.4045	0.3098
350	0.4524	0.3885	0.3064
360	0.4397	0.3744	0.3025
370	0.4288	0.3688	0.2998
380	0.4154	0.3636	0.2964
390	0.3996	0.3584	0.2928
400	0.3878	0.3497	0.2897

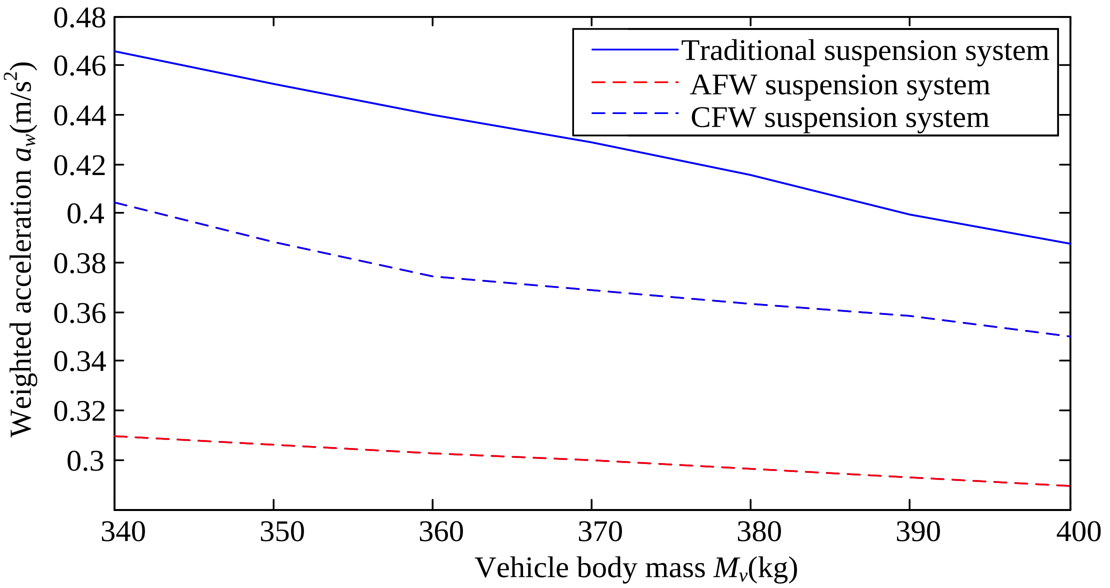

Figure 4.4 Weighted root mean square acceleration with zero input

In this simulation, four passengers of the same mass are assumed to be in the car, where the weight range of one passenger is between 40kg to 100kg. In the first column of **Table 4.1**, the vehicle body mass M_v is the combined mass of the quarter car body and one passenger. **Table 4.1** and **Figure 4.4** show the weighted root mean square acceleration of three suspension systems under zero input. With the same vehicle body mass, the weighted root mean square acceleration of adaptive flywheel suspension system is smaller than these of the other two suspension systems, which implies that the adaptive flywheel suspension system outperforms both traditional and constant flywheel in terms of ride comfort in this particular case.

4.2.1.2. Impulse input

An impulse input with amplitude of 0.05m is applied to each suspension system. This excitation simulates the condition when the car hits a bump or a pit. Using the same mathematical model, the results can be determined by Matlab and are shown in **Table 4.2** and **Figure 4.5**.

Table 4.2 Weighted root mean square acceleration with impulse input

Vehicle body mass M_v (kg)	Weighted acceleration of traditional suspension system a_w(m/s^2)	Weighted acceleration of CFW suspension system a_w(m/s^2)	Weighted acceleration of AFW suspension system a_w(m/s^2)
340	0.4878	0.3858	0.2782
350	0.4684	0.3746	0.2746
360	0.4546	0.3689	0.2715
370	0.4398	0.3625	0.2679
380	0.4264	0.3589	0.2643
390	0.4112	0.3532	0.2622
400	0.3986	0.3478	0.2598

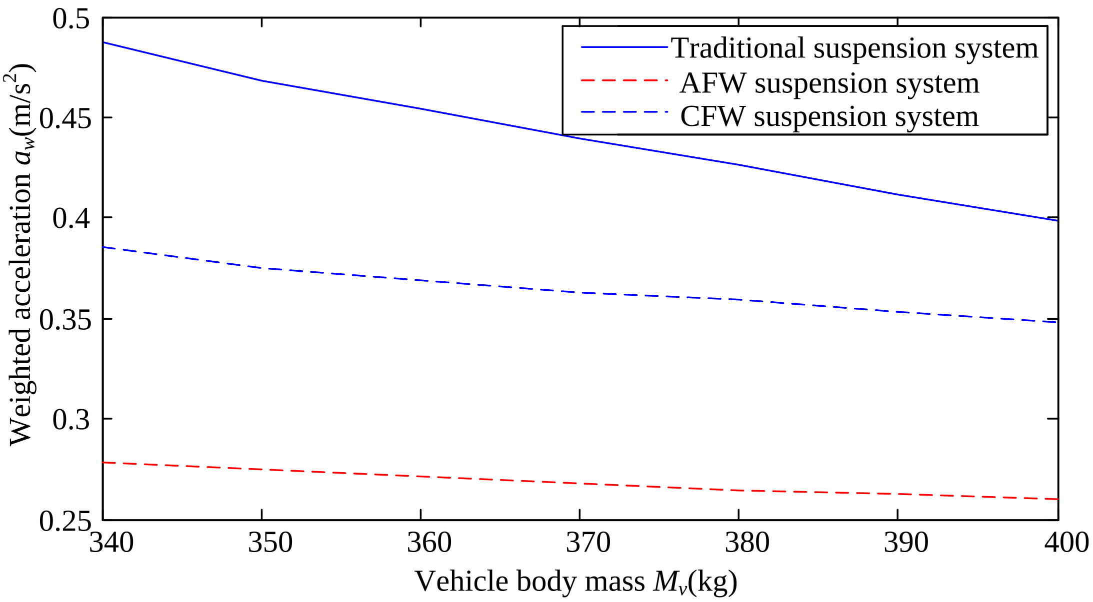

Figure 4.5 Weighted root mean square acceleration with impulse input

Table 4.2 and **Figure 4.5** show the weighted root mean square acceleration of the three suspension systems under impulse input. The weighted root mean square acceleration of adaptive flywheel suspension system is again the smallest of the three suspension system under the same vehicle body mass. This indicates that the adaptive flywheel suspension system performs better than the other two suspension system.

4.2.1.3. Sinusoidal input

A sinusoidal input with amplitude 0.05m and frequency 5Hz is applied to each suspension system. The wave length of this sinusoidal input is 4m, which indicates that the speed of the vehicle is approximately 80km/h. This excitation simulates the car running on a rough road.

Table 4.3 Weighted root mean square acceleration with sinusoidal input

Vehicle body mass M_v (kg)	Weighted acceleration of traditional suspension system	Weighted acceleration of CFW suspension system a_w(m/s^2)	Weighted acceleration of AFW suspension system a_w(m/s^2)
340	1.9786	2.8434	3.9845
350	1.8498	2.7969	3.7459
360	1.7249	2.7425	3.5315
370	1.6256	2.6998	3.3464
380	1.5143	2.6312	3.1956
390	1.3983	2.5786	3.0978
400	1.2964	2.5146	3.0364

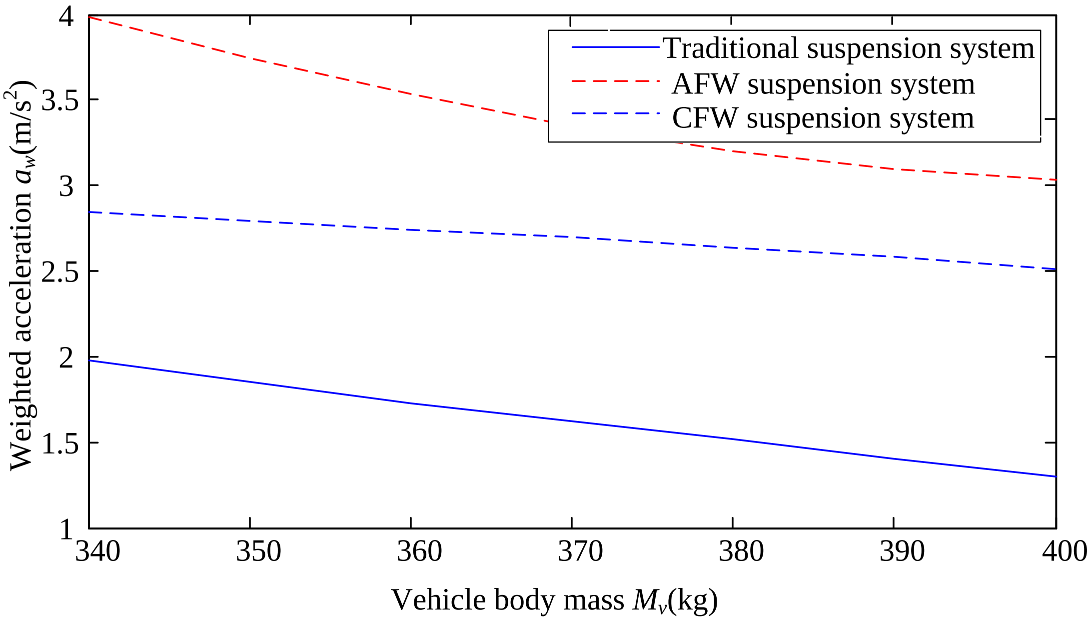

Figure 4.6 Weighted root mean square acceleration with sinusoidal input

As shown in **Table 4.3** and **Figure 4.6**, with sinusoidal input, the results of the three suspension systems are opposite to those obtained when comparing the two other inputs. Here, the weighted root mean square acceleration of the adaptive flywheel suspension system is larger than both other suspension systems, which implies that the adaptive flywheel suspension system gives the worst performance of the three chosen suspension systems under the case of a sinusoidal input. With the sinusoidal input, the adaptive flywheel will consistently generate a large inertial force. However the gravitational mass of this vehicle is constant, which eventually leads to a higher weighted root mean square acceleration.

4.2.2. Tire grip

Tire grip is another key factor to evaluate the performance of a suspension system, and can be used to characterize the ride safety of a vehicle. The tire grip can be quantified as [180,181]:

$$M_2 = 0.2\pi(G_q(n_0)v)^{\frac{1}{2}}\left\|H_2(s)\right\|_2 \tag{4.17}$$

In equation (4.17), M_2 is the tire grip index, where $H_2(s) = \frac{X_3(s) - X_2(s) - X_1(s)}{sX_1(s)}$.

As mentioned before, once the road roughness is chosen and the velocity of the car is fixed, the transfer function $H_2(s)$ will be the only factor to determine the tire grip.

Based on equation (4.2), the transfer function $H_{2t}(s)$ for a traditional suspension system can be written as:

$$H_{2t}(s) = \frac{\omega_t^2(s^2 + 2\zeta\omega_b s + \omega_b^2)}{s^3\left(s^2 + \frac{2\zeta\omega_b}{\alpha}s + \frac{\omega_b^2}{\alpha} + \omega_t^2\right) + s(s^2 + \omega_t^2)(2\zeta\omega_b s + \omega_b^2)} - 1 \tag{4.18}$$

From equation (4.6), the transfer function $H_{2c}(s)$ for a constant flywheel suspension system can be presented as:

$$H_{2c}(s) = \frac{\omega_t^2(s^2 + \beta s^2 + 2\zeta\omega_b s + \omega_b^2)}{s^3\left(s^2 + \frac{\beta}{\alpha}s^2 + \frac{2\zeta\omega_b}{\alpha}s + \frac{\omega_b^2}{\alpha} + \omega_t^2\right) + s(s^2 + \omega_t^2)(\beta s^2 + 2\zeta\omega_b s + \omega_b^2)} - 1$$

(4.19)

For the same reason mentioned in section 5.2.1, the transfer function for an adaptive flywheel cannot be obtained by Laplace transform. However, the tire grip index can also be defined as the ratio between static and dynamic loads, which can be expressed as [151]:

$$M_{tg} = \frac{K_t(X_2 - X_1)}{(M + M_T)g} \tag{4.20}$$

In equation (4.20) g is the acceleration due to gravity. As shown in equation (4.20), this performance criterion is applied under a dynamic situation; otherwise the tire grip index will reach is maximum value, which is equal to one. With a smaller tire grip index, the possibility of a tire losing contact with the road also becomes smaller, which implies improved vehicle safety. By using the weighted root mean square, an accurate tire grip index can be obtained as [182]:

$$M_{wtg} = \left(\frac{1}{T} \int_0^T M_{tg}(t)^2 \, dt \right)^{\frac{1}{2}} \tag{4.21}$$

By combining equation (4.21) with (4.1), (4.4) and (4.8), the numerical solution of the weighted root mean square tire grip index for each suspension system in the time-domain can be calculated with Matlab. The same simulation strategy is applied in this set of simulations; namely zero, impulse and sinusoidal inputs were evaluated.

4.2.2.1. Zero input

An initial displacement 0.05m is applied to the three suspension systems. The results can be found in **Table 4.4**.

Table 4.4 Weighted root mean square tire grip index with zero input

Vehicle body mass M_v (kg)	Weighted tire grip index of traditional suspension system M_{wtg}	Weighted tire grip index of CFW suspension system M_{wtg}	Weighted tire grip index of AFW suspension system M_{wtg}
340	0.3156	0.2078	0.0684
350	0.3012	0.1996	0.0669
360	0.2874	0.1922	0.0656
370	0.2756	0.1854	0.0644
380	0.2649	0.1789	0.0631
390	0.2551	0.1731	0.0619
400	0.2462	0.1680	0.0608

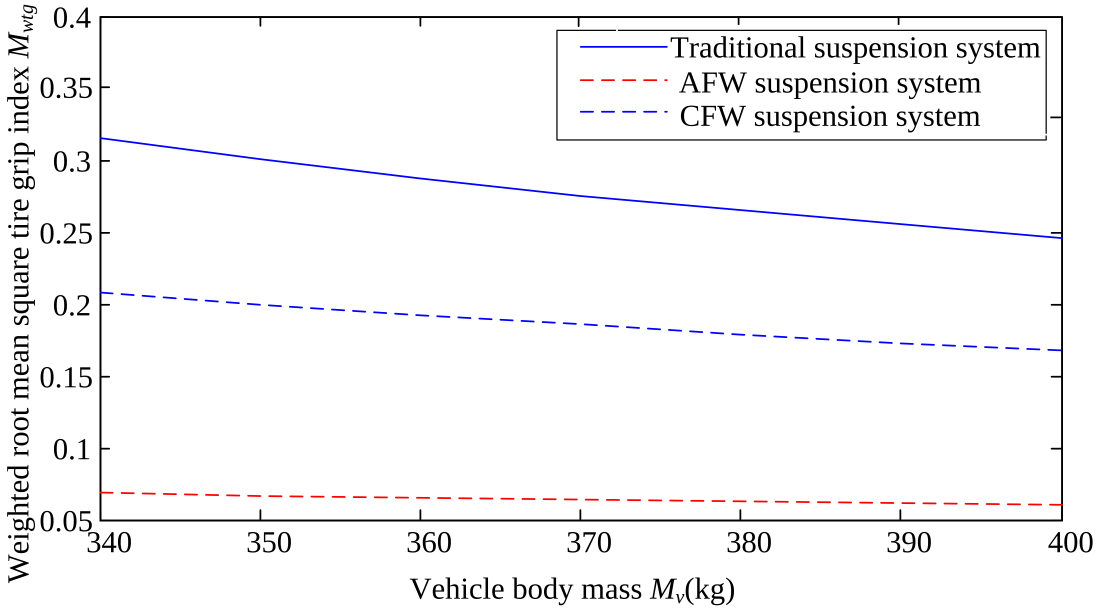

Figure 4.7 Weighted root mean square tire grip index with zero input

In **Table 4.4** and **Figure 4.7**, weighted root mean square tire grip index of the three suspension systems under zero input are shown. Compared to other two suspension systems, the weighted root mean square tire grip index of the adaptive flywheel suspension system is the smallest. Since the smaller weighted root mean square tire grip index implies higher vehicle safety, the adaptive flywheel suspension system shows better outcome than both the other suspension systems under this condition.

4.2.2.2. Impulse input

An impulse input with amplitude of 0.05m is applied to each suspension system. The results are shown in **Table 4.5** and **Figure 4.8**.

Table 4.5 Weighted root mean square tire grip index with impulse input

Vehicle body mass M_v (kg)	Weighted tire grip index of traditional	Weighted tire grip index of CFW suspension system	Weighted tire grip index of VMI suspension system

	suspension system M_{wtg}	M_{wtg}	M_{wtg}
340	0.3879	0.2216	0.1214
350	0.3624	0.2101	0.1173
360	0.3412	0.1997	0.1131
370	0.3208	0.1894	0.1094
380	0.3001	0.1798	0.1058
390	0.2814	0.1709	0.1021
400	0.2628	0.1618	0.0986

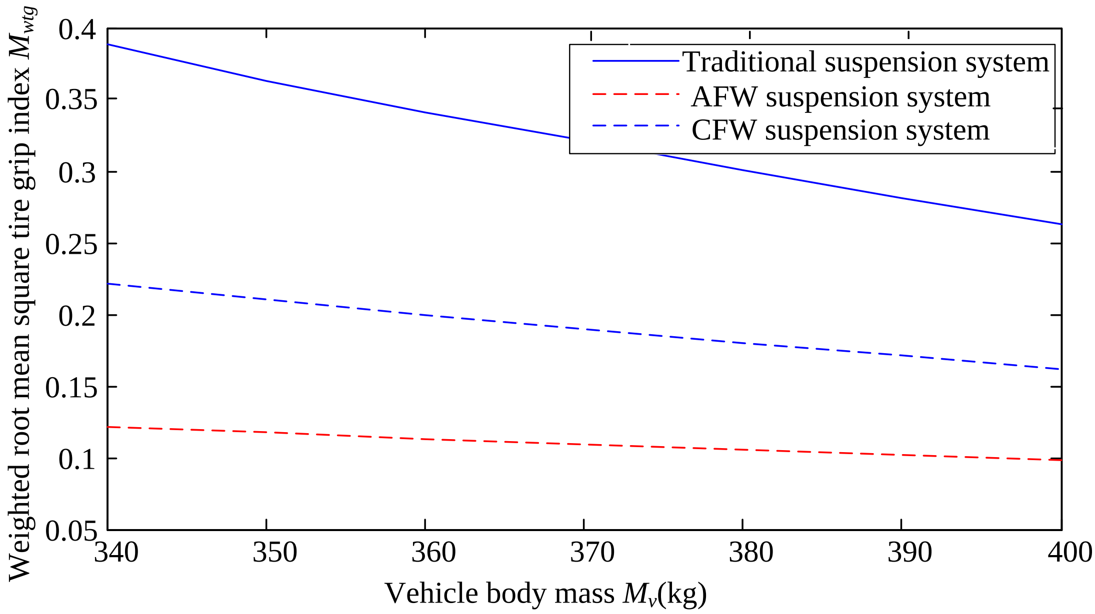

Figure 4.8 Weighted root mean square tire grip index with impulse input

Table 4.5 and **Figure 4.8** show the weighted root mean square tire grip index of three suspension systems with an impulse input. Since the weighted root mean square tire grip index of the adaptive flywheel suspension system is still the smallest of all three suspension systems under the same vehicle body mass, it follows that it out-performs the constant flywheel suspension system and the traditional suspension system.

4.2.2.3. Sinusoidal input

A sinusoidal input with wave length of 4m, amplitude of 0.05m and a frequency of 5Hz is applied to each suspension system. The results are shown in **Table 4.6** and **Figure 4.9**,

Table 4.6 Weighted root mean square tire grip index with sinusoidal input

Vehicle body mass M_v (kg)	Weighted tire grip index of traditional suspension system M_{wtg}	Weighted tire grip index of CFW suspension system M_{wtg}	Weighted tire grip index of AFW suspension system M_{wtg}
340	0.8458	0.6546	0.4516
350	0.8014	0.6234	0.4214
360	0.7624	0.5933	0.3907
370	0.7256	0.5646	0.3620
380	0.6929	0.5378	0.3346
390	0.6614	0.5116	0.3098
400	0.6319	0.4876	0.2844

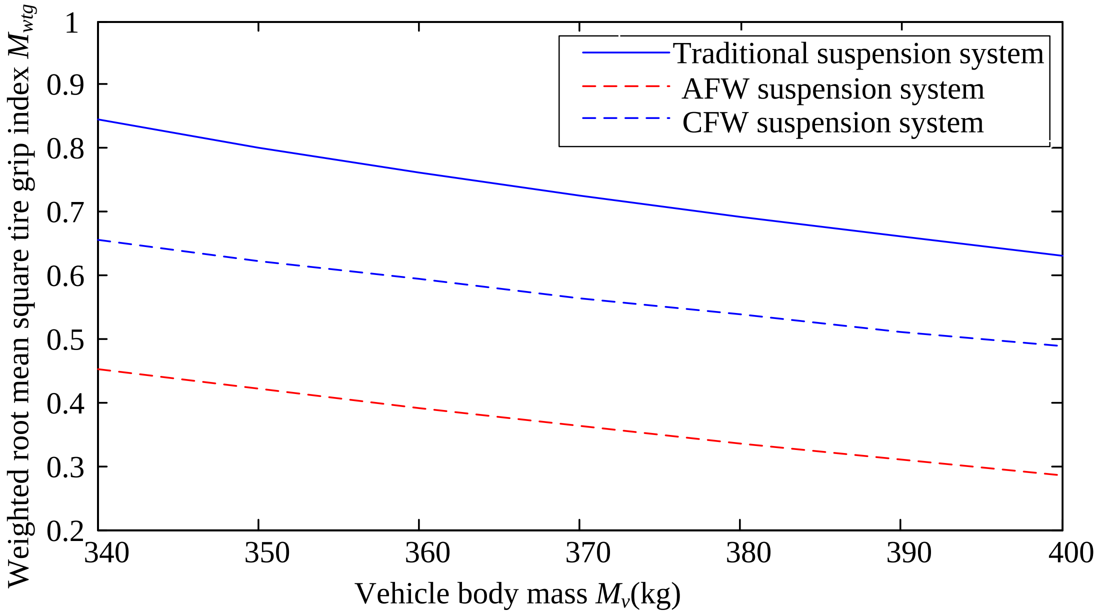

Figure 4.9 Weighted root mean square tire grip index with sinusoidal input

From **Table 4.6** and **Figure 4.9**, under the same road conditions with the same velocity, and for the same vehicle body mass, the adaptive flywheel suspension system provides the smallest weighted root mean square tire grip index. Based on this, the adaptive flywheel suspension system provides a higher safety performance than both the traditional suspension system and the constant flywheel suspension system.

4.2.3. Vehicle body deflection

The vehicle body deflection is the last important factor for evaluating the performance of a suspension system. This performance criterion corresponds to the vehicle center of gravity, which will affect the working life of a suspension system, and can be determined as [183,184]:

$$M_3 = 0.2\pi (G_q(n_0)v)^{\frac{1}{2}} \left\| H_3(s) \right\|_2 \tag{4.22}$$

In equation (4.22), M_3 is the vehicle body deflection index, and $H_3(s) = \dfrac{X_2(s)}{sX_1(s)}$. As outlined above, the vehicle body deflection is completely determined by the transfer function $H_3(s)$.

By rewriting equation (4.2), the transfer function $H_{3t}(s)$ for a traditional suspension system can be presented as:

$$H_{3t}(s) = \frac{-s\omega_t^2}{s^2\left(s^2 + \dfrac{2\zeta\omega_b}{\alpha}s + \dfrac{\omega_b^2}{\alpha} + \omega_t^2\right) + (s^2 + \omega_t^2)(2\zeta\omega_b s + \omega_b^2)} \tag{4.23}$$

From equation (4.6), the new transfer function $H_{3c}(s)$ for a constant flywheel suspension system can be rewritten as:

$$H_{3c}(s) = \frac{-s\omega_t^2}{s^2\left(s^2 + \frac{\beta}{\alpha}s^2 + \frac{2\zeta\omega_b}{\alpha}s + \frac{\omega_b^2}{\alpha} + \omega_t^2\right) + (s^2 + \omega_t^2)(\beta s^2 + 2\zeta\omega_b s + \omega_b^2)} \tag{4.24}$$

Due to the non-linearity of the adaptive flywheel, the transfer function of the adaptive flywheel cannot be acquired by Laplace transform. However, as mentioned above, the vehicle body deflection is related to the vehicle center gravity, which implies that it can be expressed as:

$$D_f = X_3 - X_2 \tag{4.25}$$

By using the same weighted root mean square method, an accurate vehicle body deflection can be calculated as [185,186]:

$$D_{fw} = \left(\frac{1}{T}\int_0^T D_f(t)^2 dt\right)^{\frac{1}{2}} \tag{4.26}$$

By combining equation (4.26) with (4.1), (4.4) and (4.8), the numerical solution of weighted root mean square vehicle body deflection for each suspension system in the time-domain can be calculated via Matlab. The same initial conditions and simulation strategy are applied in this simulation as for the simulations of riding comfort and tire grip index.

4.2.3.1. Zero input

An initial displacement 0.05m is applied on the three suspension systems. The results are shown in **Table 4.7** and **Figure 4.10**.

Table 4.7 Weighted root mean square vehicle body deflection with zero input

Vehicle body mass M_v (kg)	Weighted vehicle body deflections of traditional suspension system D_{fw}(m)	Weighted vehicle body deflections of CFW suspension system D_{fw}(m)	Weighted vehicle body deflections of AFW suspension system D_{fw}(m)

340	0.0035	0.0035	0.0035
350	0.0035	0.0035	0.0034
360	0.0035	0.0035	0.0034
370	0.0035	0.0034	0.0034
380	0.0034	0.0034	0.0033
390	0.0034	0.0034	0.0033
400	0.0034	0.0034	0.0033

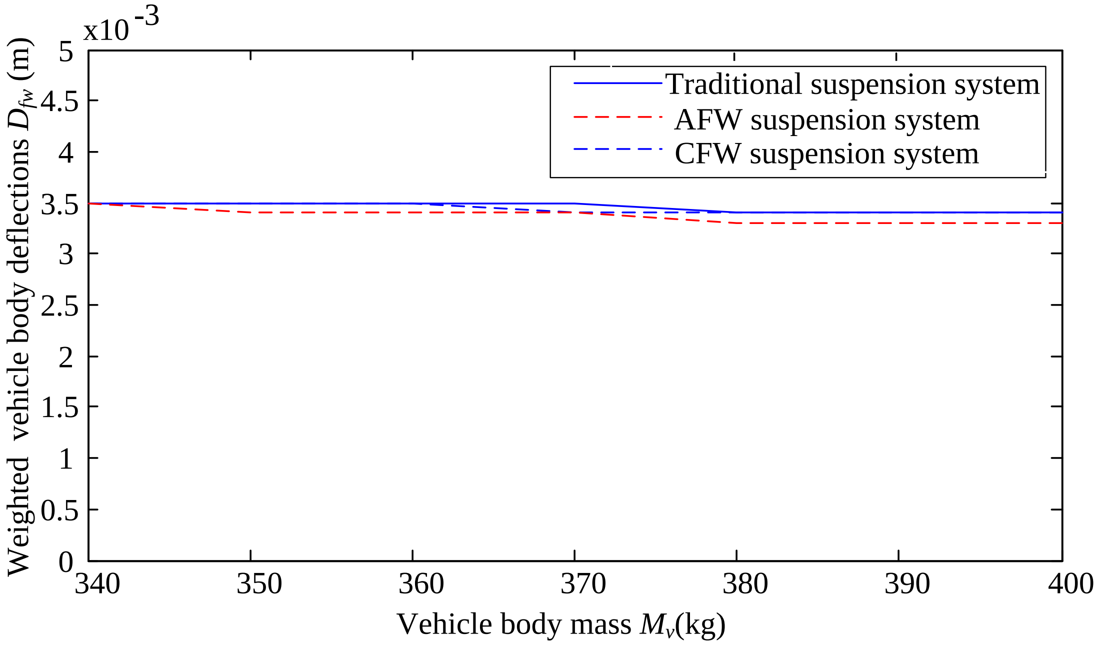

Figure 4.10 Weighted root mean square vehicle body deflection with zero input

Based on **Table 4.7**and **Figure 4.10**, the three suspension systems show almost the same weighted root mean square vehicle body deflection under zero input. This implies that the proposed adaptive flywheel suspension system shows no improvement compared to the other two suspension systems.

4.2.3.2. Impulse input

An impulse input with amplitude 0.05m is applied to each suspension system. The results are shown in **Table 4.8**.

Table 4.8 Weighted root mean square vehicle body deflection with impulse input

Vehicle body mass M_v (kg)	Weighted vehicle body deflections of traditional suspension system D_{fw}(m)	Weighted vehicle body deflections of CFW suspension system D_{fw}(m)	Weighted vehicle body deflections of AFW suspension system D_{fw}(m)
340	0.0031	0.0031	0.0030
350	0.0031	0.0031	0.0030
360	0.0031	0.0031	0.0030
370	0.0031	0.0031	0.0030
380	0.0031	0.0031	0.0030
390	0.0031	0.0031	0.0030
400	0.0031	0.0031	0.0030

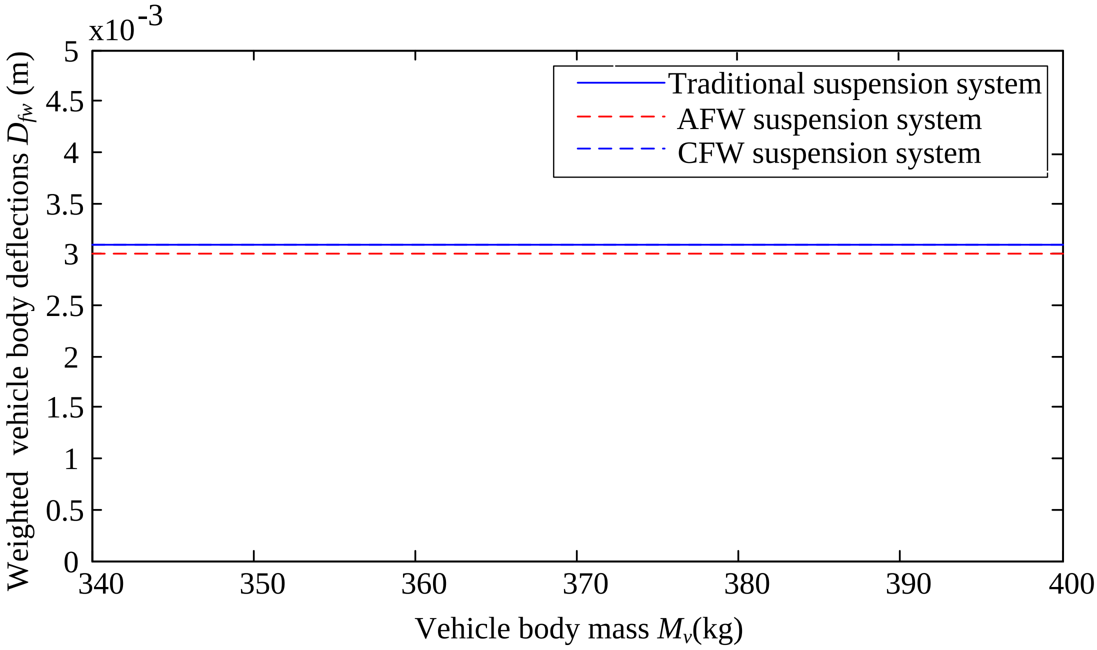

Figure 4.11 Weighted root mean square vehicle body deflection with impulse input

From **Table 4.8** and **Figure 4.11**, similar results can be found as for the case of zero input. The weighted root mean square vehicle body deflection of the three suspension systems are almost identical, which indicates there is almost no performance difference in vehicle body deflection for each suspension system.

4.2.3.3. Sinusoidal input

A sinusoidal input with wave length of 4m, amplitude 0.05m and frequency 5Hz is applied to each suspension system. The results are shown in **Table 4.9** and **Figure 4.12**.

Table 4.9 Weighted root mean square vehicle body deflectionwith sinusoidal input

Vehicle body mass M_v (kg)	Weighted vehicle body deflections of traditional suspension system D_{fw}(m)	Weighted vehicle body deflections of CFW suspension system D_{fw}(m)	Weighted vehicle body deflections of AFW suspension system D_{fw}(m)
340	0.0096	0.0096	0.0168
350	0.0095	0.0095	0.0164
360	0.0093	0.0092	0.0161
370	0.0091	0.0091	0.0157
380	0.0090	0.0090	0.0153
390	0.0088	0.00889	0.0148
400	0.0087	0.0087	0.0144

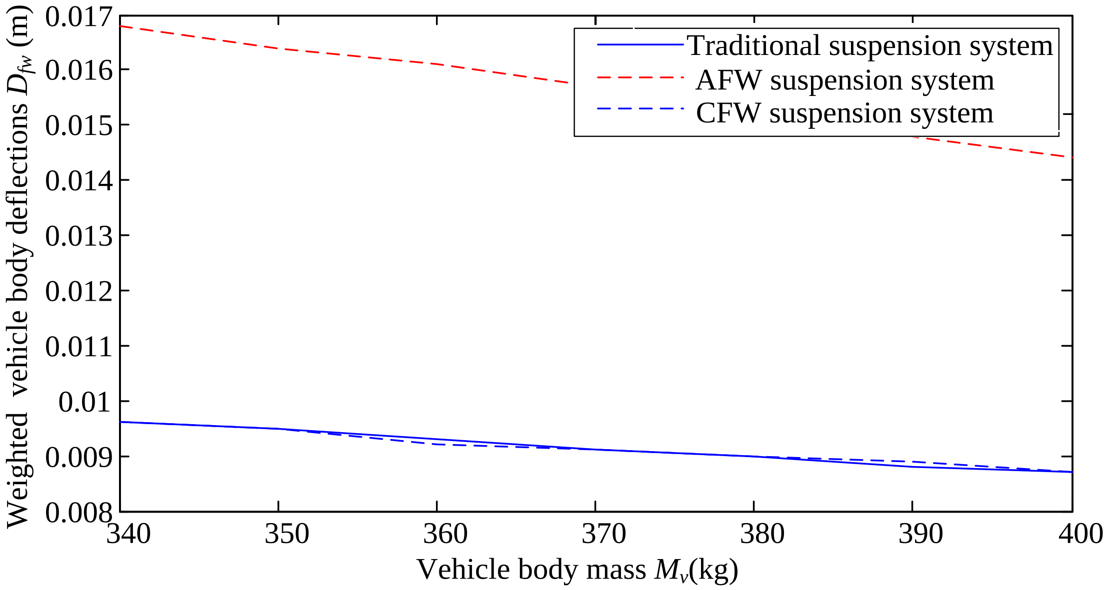

Figure 4.12 Weighted root mean square vehicle body deflection with sinusoidal input

Table 4.9 and **Figure 4.12** show the weighted root mean square vehicle body deflection of the three different suspension systems with sinusoidal input. The weighted root mean square vehicle body deflection of the adaptive flywheel is greater than the other two suspension systems, which implies that in this case, the traditional suspension system and the constant flywheel suspension system show better results than the adaptive flywheel suspension system.

4.3. Performance evaluation for different changing ratio

In the previous subsections, the three different suspension systems were evaluated by three performance criteria. The results of simulations indicate that the performance of a suspension system of a two-terminal device with adaptive flywheel is better than that of the other suspension systems under most circumstances in terms of ride comfort and tire grip. However, the suspension system of a two-terminal device with adaptive flywheel exhibits the worst performance in terms of body deflection. In order to further analyze the characteristics of the two-terminal device with an adaptive flywheel, another important simulation is also conducted in the research.

In this simulation, the only variable is the changing ratio of the adaptive flywheel, all the other parameters are kept the same. As mentioned in chapter 3, by reducing the weight of the frame, the changing ratio of the adaptive flywheel will increase. However, with the reduced weight, the frame will be more fragile, which will lead to low reliability. Moreover, the removal of additional material from the frame will not only make it difficult to manufacture, but also increase material waste, and both factors will increase cost. Therefore, in this simulation, the changing ratio is varied from 5% to 55%.

4.3.1. First situation: zero input

Assume an initial displacement 0.05m is applied to the quarter car model, the only variable is the changing ratio of the adaptive flywheel. The results of simulation are shown in **Table 4.10**. In **Table 5.10**, the index value for all three indices are the values obtained in the prior simulation results shown in **Table 4.1**, **Table 4.4** and **Table 4.7** when the vehicle body mass is 370kg.

Table 4.10 Performance with different changing ratio under zero input

Changing ratio of moment of inertia (%)	Weighted acceleration of AFW suspension system a_w(m/s^2)	Weighted tire grip index of AFW suspension system M_{wtg}	Weighted vehicle body deflection of AFW suspension system D_{fw}(m)
Index value of traditional suspension system	0.4288	0.2756	0.0035

5	0.3598	0.1681	0.0025
10	0.3486	0.1507	0.0027
15	0.3371	0.1299	0.0027
20	0.3249	0.1083	0.0026
25	0.3111	0. 0849	0.0026
30	0.2942	0.0598	0.0025
35	0.2808	0.0484	0.0025
40	0.2682	0.0417	0.0025
45	0.2579	0.0387	0.0027
50	0.2483	0.0359	0.0026
55	0.2401	0.0341	0.0026

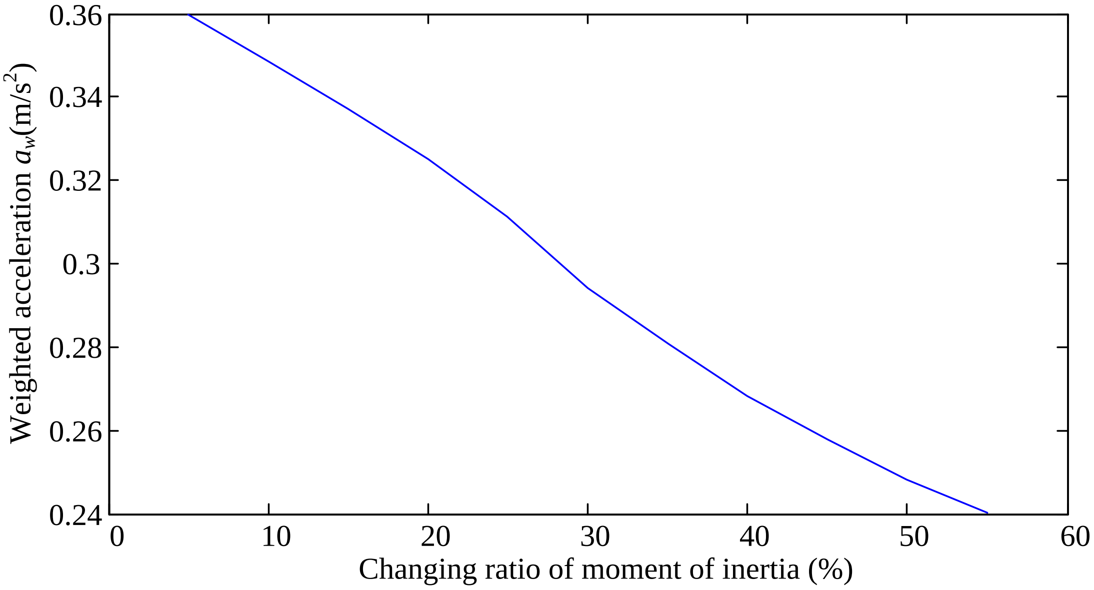

Figure 4.13 Weighted accelerations of AFW suspension system with different changing ratios under zero input

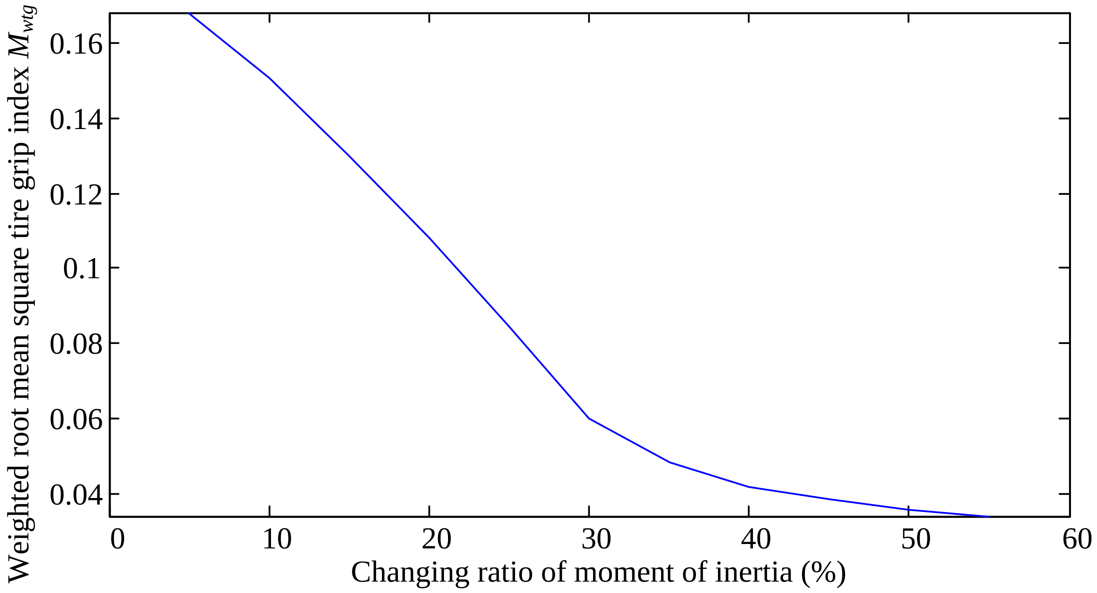

Figure 4.14 Weighted tire grip index of AFW suspension system with different changing ratios under zero input

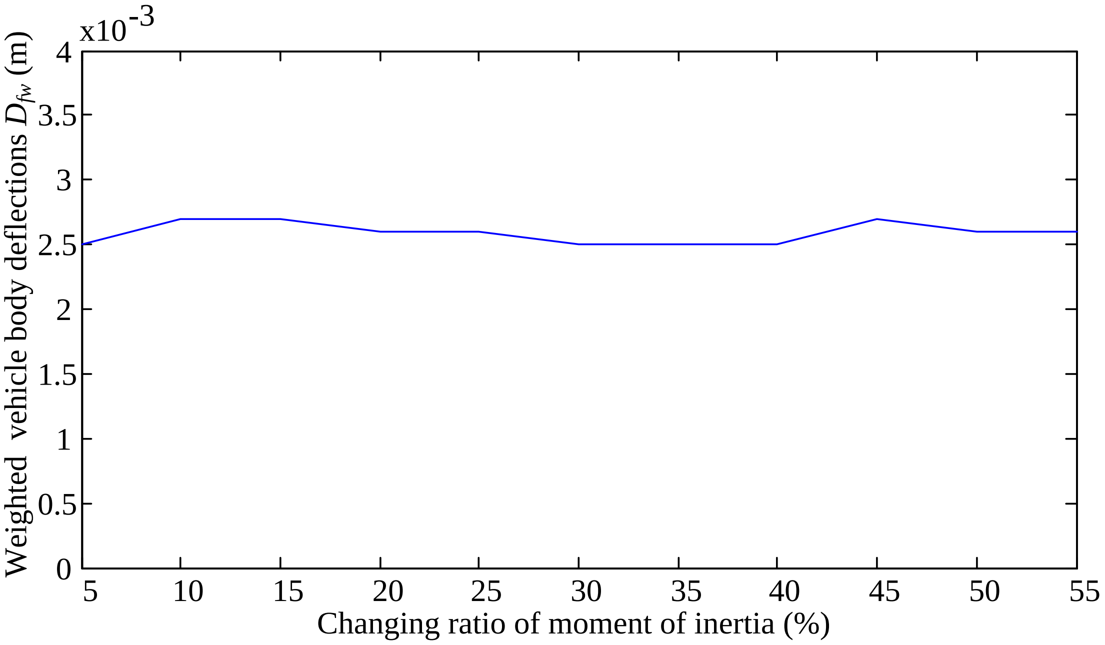

Figure 4.15 Weighted suspension deflections of AFW suspension system with different changing ratios under zero input

Figure 4.13 shows the weighted accelerations of AFW suspension system with different changing ratios under zero input and shows that the weighted accelerations will decrease when the changing ratio of the adaptive flywheel increases, which implies that with a higher changing ratio, the riding comfort will also improve. **Figure 4.14** shows the weighted tire grip index of AFW suspension system with different changing ratios under zero input. With higher changings ratio, the index will decrease, indicating improved vehicle safety. **Figure 4.15** is the weighted suspension deflections of AFW suspension system with different changing ratios under zero input. This figure shows that the weighted suspension deflections of AFW suspension system are not significantly affected by the increased changing ratio of the adaptive flywheel.

4.3.2. Second situation: impulse input

In this simulation, an impulse input with amplitude 0.05m is applied and the results of simulation are shown in **Table 4.11**.

Table 4.11 Performance with different changing ratio under impulse input

Changing ratio of moment of inertia (%)	Weighted accelerations of AFW suspension system a_w(m/s^2)	Weighted tire grip index of AFW suspension system M_{wtg}	Weighted vehicle body deflections of AFW suspension system D_{fw}(m)
Index value of traditional suspension system	0.4398	0.3208	0.0031
5	0.3496	0.1781	0.0024
10	0.3320	0.1659	0.0024
15	0.3183	0.1534	0.0024

20	0.2994	0.1387	0.0023
25	0.2803	0.1241	0.0024
30	0.2612	0.1059	0.0022
35	0.2443	0.0913	0.0023
40	0.2286	0.0789	0.0024
45	0.2134	0.0681	0.0023
50	0.2011	0.0595	0.0023
55	0.1897	0.0356	0.0022

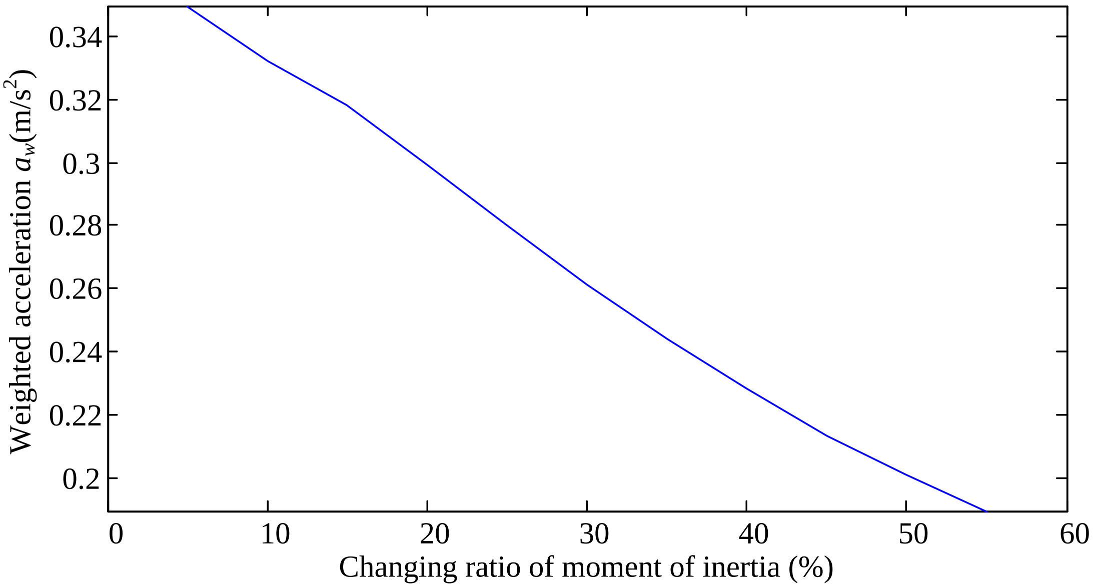

Figure 4.16 Weighted accelerations of AFW suspension system with different changing ratios under impulse input

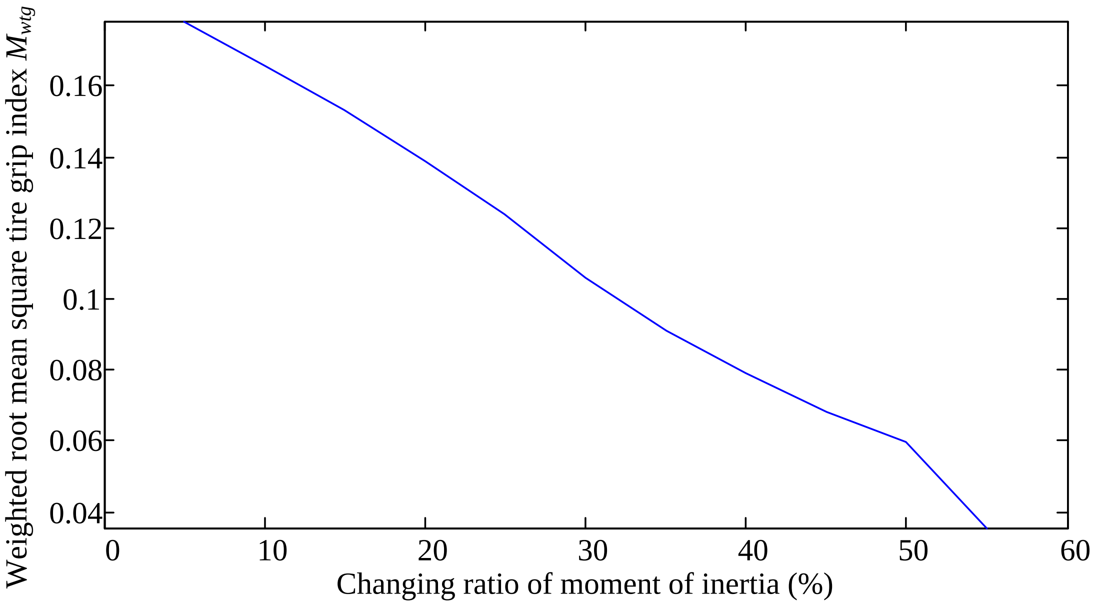

Figure 4.17 Weighted tire grip index of AFW suspension system with different changing ratios under impulse input

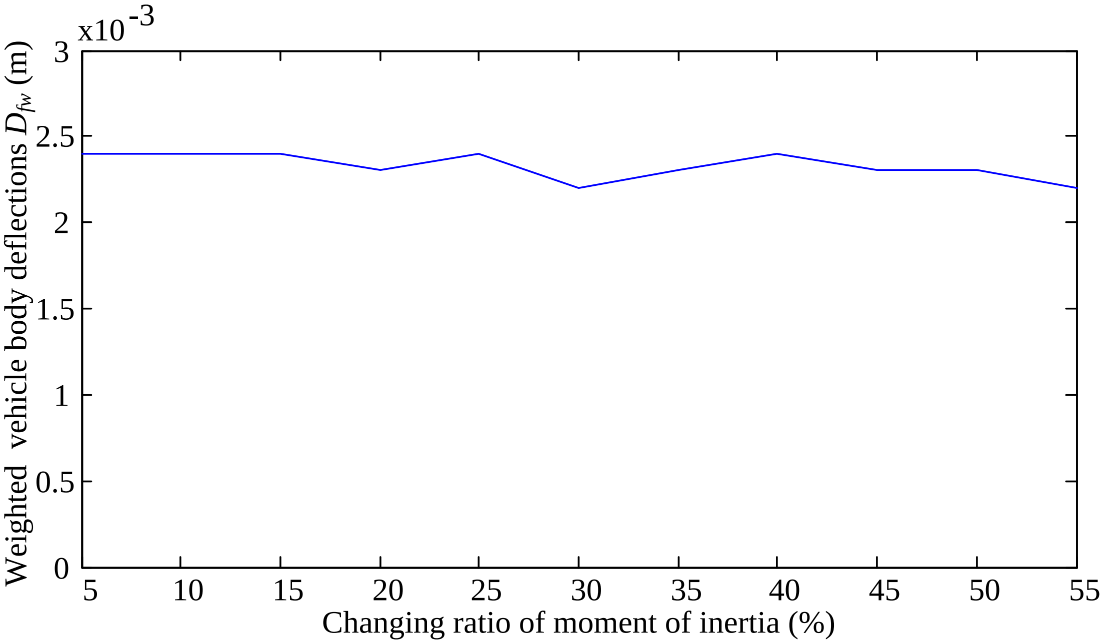

Figure 4.18 Weighted vehicle body deflections of AFW suspension system with different changing ratios under impulse input

Figure 4.16 shows the relationship between the weighted accelerations of the AFW suspension system and different changing ratios of the adaptive flywheel under impulse input. With an increase in the changing ratio of the adaptive flywheel, the weighted acceleration will decrease. This result again indicates that higher changing ratio of adaptive flywheel will improve the riding comfort. **Figure 4.17** is the weighted tire grip index of AFW suspension system with different changing ratio under impulse input. This shows that the weighted tire grip index will decrease with increasing the changing ratio, which implies the vehicle safety improves under increasing changing ratio. **Figure 4.18** is the weighted suspension deflections of AFW suspension system with different changing ratio under impulse input. With the variable changing ratio, the weighted suspension deflections of AFW suspension system almost stay the same. Therefore, the changing ratio of the adaptive flywheel does not affect the weighted suspension deflections of the AFW suspension system.

4.3.3. Third situation: sinusoidal excitation

In the final simulation, a sinusoidal input with amplitude 0.05m and frequency 5Hz is applied as excitation. Results about this simulation can be found in **Table 4.12**.

Table 4.12 Performance with different changing ratio under sinusoidal input

Changing ratio of moment of inertia (%)	Weighted accelerations of AFW suspension system a_w(m/s^2)	Weighted tire grip index of AFW suspension system M_{wtg}	Weighted vehicle body deflections of AFW suspension system D_{fw}(m)
Index value of traditional suspension system	1.6256	0.7256	0.0091

5	2.7694	0.5311	0.0156
10	2.8702	0.4899	0.0156
15	2.9798	0.4554	0.0158
20	3.1016	0.4199	0.0158
25	3.2386	0.3833	0.0157
30	3.3914	0.3449	0.0157
35	3.5219	0.2395	0.0157
40	3.6356	0.1169	0.0157
45	3.7207	0.0876	0.0156
50	3.7826	0.0659	0.0156
55	3.8303	0.0589	0.0156

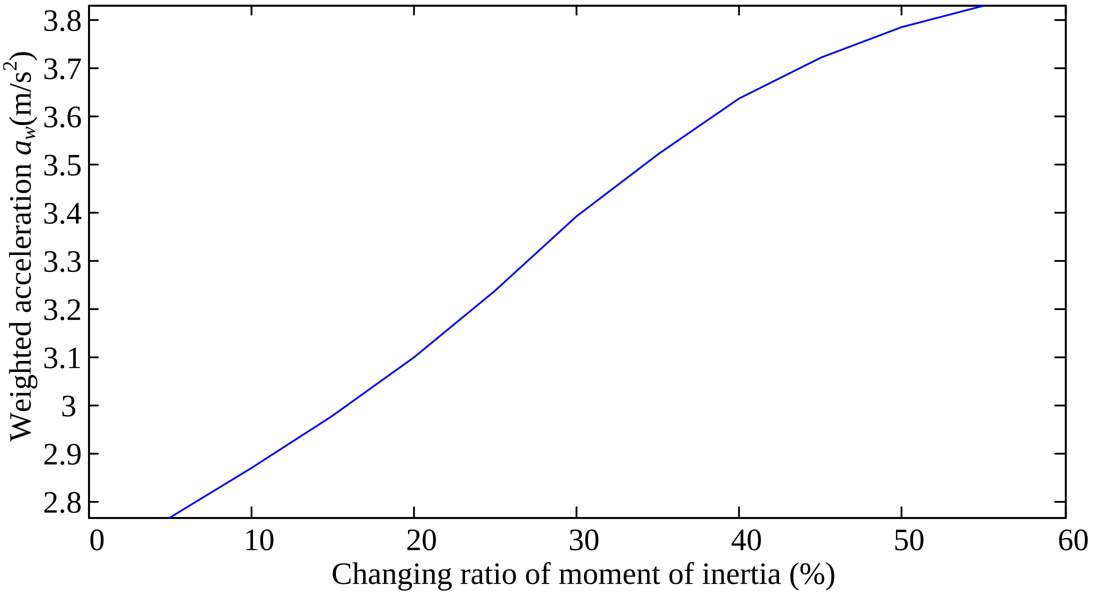

Figure 4.19 Weighted accelerations of AFW suspension system with different changing ratios under sinusoidal input

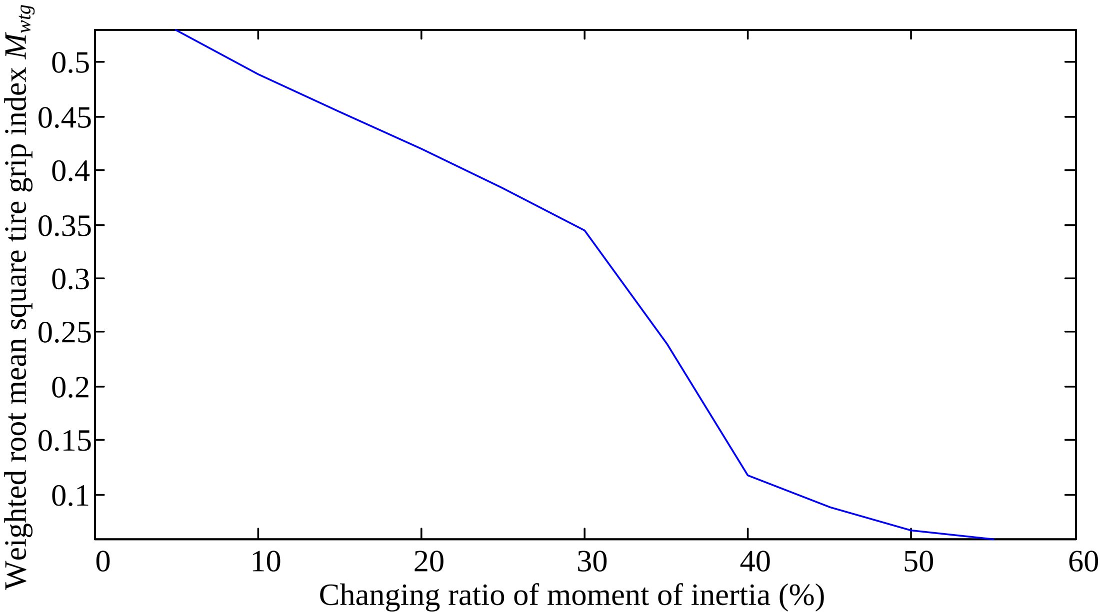

Figure 4.20 Weighted tire grip index of AFW suspension system with different changing ratios under sinusoidal input

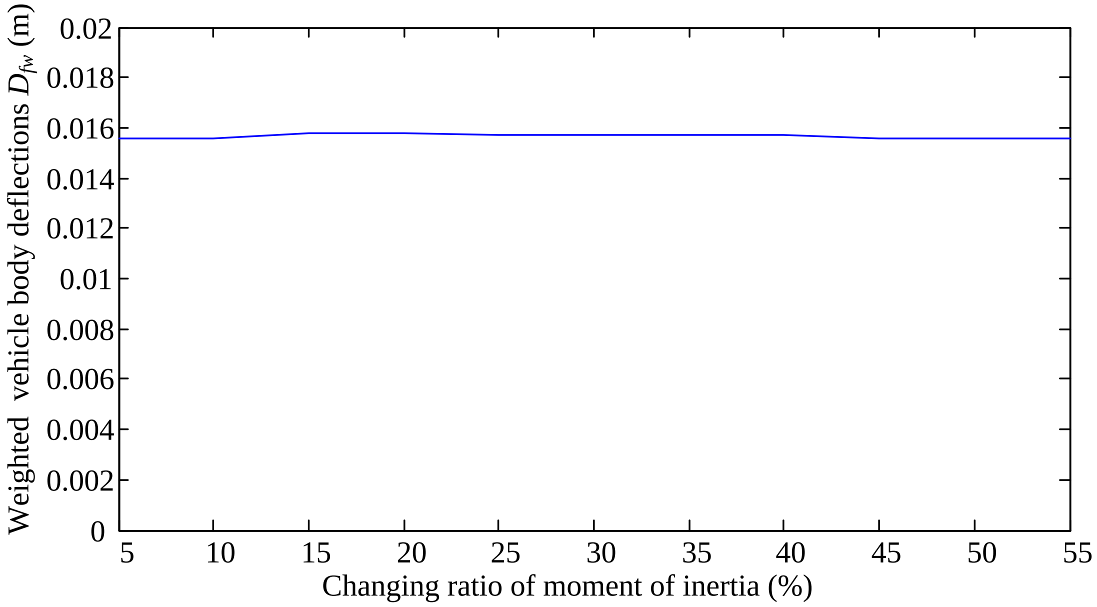

Figure 4.21 Weighted vehicle body deflections of AFW suspension system with different changing ratios under sinusoidal input

Figure 4.19 is the weighted accelerations of the AFW suspension system with different changing ratios. However, the results of simulation are different from both prior simulation results and show that with increased changing ratio of the adaptive flywheel, the weighted accelerations of AFW suspension system also increase, which implies that the riding comfort worsens. **Figure 4.20** is the weighted tire grip index of AFW suspension system with different changing ratios under sinusoidal input. The results of this simulation indicate that the weighted tire grip index of AFW suspension system will decrease when the changing ratio increases. **Figure 4.21** shows the weighted suspension deflections of AFW suspension system with different changing ratios. The results in this case are the same as the former simulation; the variable changing ratio does not affect the weighted suspension deflections of AFW suspension system.

4.3.4. Optimal changing ratio for adaptive flywheel

4.3.4.1. Determination of optimal changing ratio for adaptive flywheel

As mentioned above, with different inputs and different changing ratios of the adaptive flywheel, the performance of the AFW suspension system is quite different. In the previous simulations, three different road conditions (zero input, impulse input and sinusoidal input) and three different suspension performance criteria are introduced, and the evaluations are carried out to show the improvement of the proposed situation. However, the results show that the proposed suspension system does not always show better performance than other two suspension systems. Therefore, under the right conditions, an optimal changing ratio of adaptive flywheel for suspension system can be determined. To calculate the optimal changing ratio, three other factors need to be considered.

The first one is the proportion of road situation. At the beginning of this chapter, zero input, impulse input and sinusoidal input are introduced as three different road conditions. However, these three road conditions always appear with different proportion in a real case, the actual proportion of each road condition is critical for the calculation of optimal changing ratio [178,179].

The second factor is the proportion of performance criteria. In our simulations, riding comfort, tire grip and suspension deflection are applied to evaluate the suspension system. For the proposed suspension system, the results are conflicting under these three performance criteria. In order to find an optimal result, the important index for different performance criteria need to be classified, which will be expressed as the proportion [155,180].

The final one is the cost of manufacture of the adaptive flywheel. With the higher changing ratio, there will be more waste of materials (the cut out materials such as slots and holes). When the changing ratio reaches a certain level, the manufacture time will increase, due to the small size of this flywheel. All the reasons will cause an increase in cost [187,188]. The detailed discussions of these three factors will be introduced in a later sub-section.

According to **Figure 4.15**, **Figure 4.18** and **Figure 4.21**, the weighted suspension deflections of the AFW suspension system are independent of the variable changing ratio of the adaptive flywheel. This implies that this performance criterion can be excluded from the determination of the optimal changing ratio for the adaptive flywheel.

Assume that the relationship between the weighted accelerations of AFW suspension system and changing ratio under zero input can be presented as:

$$\alpha_{zw} = f_{za}(x) \tag{4.27}$$

where α_{zw} is the weighted acceleration under zero input, x is the changing ratio. Also assume that the relationship between the weighted tire grip index of the AFW suspension system and changing ratio under zero input can also be described as:

$$M_{ztgw} = f_{ztg}(x) \tag{4.28}$$

where M_{ztgw} is the weighted tire grip index with zero input.

The same assumptions can be made for impulse input and sinusoidal input:

$$\begin{cases} \alpha_{iw} = f_{ia}(x) \\ M_{itgw} = f_{itg}(x) \\ \alpha_{sw} = f_{sa}(x) \\ M_{stgw} = f_{stg}(x) \end{cases} \tag{4.29}$$

where α_{iw} is the weighted accelerations under impulse input, M_{itgw} is the weighted tire grip index with impulse input, α_{sw} is the weighted accelerations with sinusoidal input and M_{stgw} is the weighted tire grip index with sinusoidal input. Since there are two performance criteria, the proportion of performance between the two factors needs to be considered. New performance criteria can be written as:

$$\text{Zero input:} \quad \begin{cases} f_{zp}(x) = \dfrac{\alpha_{zw}}{\alpha_{szw}} x_1 + \dfrac{M_{ztgw}}{M_{sztgw}} x_2 \\ x_1 + x_2 = 1 \end{cases} \tag{4.30}$$

Here, $f_{zp}(x)$ is the performance function with zero input, α_{szw} is the weighted accelerations of the traditional suspension system with zero input, M_{sztgw} is the weighted tire grip index with zero input, and x_1 is the performance proportion of riding comfort while x_2 is performance proportion of tire grip. Similarly, for an impulse input, a performance function can be defined as

$$\text{Impulse input:} \begin{cases} f_{ip}(x) = \dfrac{\alpha_{iw}}{\alpha_{siw}} x_1 + \dfrac{M_{itgw}}{M_{sitgw}} x_2 \\ x_1 + x_2 = 1 \end{cases} \tag{4.31}$$

Here, $f_{ip}(x)$ is the performance function with impulse input, α_{siw} represents the weighted accelerations of the traditional suspension system with impulse input, and M_{sitgw} is the weighted tire grip index with impulse input. Finally, for a sinusoidal input

$$\text{Sinusoidal input:}\begin{cases} f_{sp}(x) = \dfrac{\alpha_{sw}}{\alpha_{ssw}} x_1 + \dfrac{M_{stgw}}{M_{sstgw}} x_2 \\ x_1 + x_2 = 1 \end{cases} \tag{4.32}$$

Here, $f_{sp}(x)$ is performance function with sinusoidal input, α_{ssw} represents the weighted accelerations of the traditional suspension system with sinusoidal input, and M_{sstgw} is weighted tire grip index with sinusoidal input.

In these simulations, zero input, impulse input and sinusoidal input are used for simulating the different road situations. However, in most cases, an actual road situation is divided into these three situations with different proportions. By combining equations (4.30), (4.31) and (4.32), a new performance equation can be determined as

$$\begin{cases} f_p(x) = f_{zp}(x)x_3 + f_{ip}(x)x_4 + f_{sp}(x)x_5 \\ x_3 + x_4 + x_5 = 1 \end{cases} \tag{4.33}$$

where $f_p(x)$ is the overall performance function, x_3 is the proportion of zero input, x_4 is the proportion of impulse input and x_5 represents the proportion of sinusoidal input.

Based on equation (4.33), when the value of $f_p(x)$ is minimum, the suspension system indicates best performance. Therefore, the determination of optimal changing ratio depends on the determination of the minimum value of $f_p(x)$. Additionally, another important factor also needs to be evaluated. As mentioned at the beginning of this sub-section, with an increase in changing ratio, the cost of the adaptive flywheel will rise. In the simulations, the cost of manufacturing adaptive flywheel is divided into two parts, waste of materials and working hours. According to China labor wage reports and Chongqing average labor cost, when the changing ratio is under 20%, the relationship between cost and changing ratio is linear. The function of cost can be written as [187,188]:

$$\begin{cases} f_c(x) = 1 + 0.8\,x & (x \le 0.2) \\ f_c(x) = 1.16 + (x+0.8)^2 & (x > 0.2) \end{cases} \tag{4.34}$$

From equation (4.33) and (4.34), the determination of the optimal changing ratio can be done minimizing two objective functions $f_p(x)$ and $f_c(x)$, i.e.,

$$\min f_p(x) + \min f_c(x) \tag{4.35}$$

subject to constraints (4.30) to (4.34).

4.3.4.2. Determination of optimal changing ratio by Chebyshev goal programming

Based on equation (4.15), the determination of optimal changing ratio can be considered as a multi-objective optimization problem. In this thesis, due to its simplicity in modelling and computation processes, Chebyshev goal programming is applied to determine the optimal changing ratio.

For single objective performance under zero input, changing ratio x_{zab} and x_{ztgb} represents the best performance for weighted accelerations f_{zab} and weighted tire grip f_{ztgb}. Similarly, the worst performance of weighted accelerations f_{zaw} and weighted tire grip f_{ztgw} correspond to changing ratio x_{zaw} and x_{ztgw}. Under impulse input, the best performance of weighted accelerations f_{iab} and weighted tire grip f_{itgb} is due to the changing ratio x_{iab} and x_{itgb}, and the worst performance of weighted accelerations f_{iaw} and weighted tire grip f_{itgw} is due to the changing ratio x_{iaw} and x_{itgw}. For sinusoidal input, best performance of weighted accelerations f_{sab} and weighted tire grip f_{stgb} is due to changing ratio x_{sab} and x_{stgb}, and the worst performance of weighted accelerations f_{saw} and weighted tire grip f_{stgw} is due to changing ratio x_{saw} and x_{stgw}. Assume there is a multi-objective optimal changing ratio x_{opt} which is related to the best performance f_{aopt} and f_{tgopt}. By using Chebyshev goal programming, the new equation can be written as:

$$\min \lambda_r \tag{4.36}$$

subject to

$$\begin{cases} \lambda_r \geq \dfrac{f_{aopt} - f_{zab}}{f_{zaw} - f_{zab}} \\ \lambda_r \geq \dfrac{f_{aopt} - f_{iab}}{f_{iaw} - f_{iab}} \\ \lambda_r \geq \dfrac{f_{aopt} - f_{sab}}{f_{saw} - f_{sab}} \\ \lambda_r \geq \dfrac{f_{tgopt} - f_{ztgb}}{f_{ztgw} - f_{ztgb}} \\ \lambda_r \geq \dfrac{f_{tgopt} - f_{itgb}}{f_{itgw} - f_{itgb}} \\ \lambda_r \geq \dfrac{f_{tgopt} - f_{stgb}}{f_{stgw} - f_{stgb}} \end{cases} \tag{4.37}$$

Through equation (4.36) and (4.37), the optimal changing ratio for the adaptive flywheel can be found. This optimal changing ratio is based on three assumptions. First, the riding comfort is as important as tire grip. The other assumption is that the proportion of inputs are identical, which implies that the road surface is equally distributed between three situations. Finally, the cost of this flywheel is excluded for this optimal changing ratio. However, for a real case, tire grip is more important than riding comfort, and the road situation is quite different.

In order to calculate the optimal changing ratio for the adaptive flywheel suspension system, the performance proportion and the proportion of inputs need to be determined. According Rath and Zhao [155,180], the performance proportion of riding comfort x_1 and safety x_2 can be taken to be 0.35 and 0.65, respectively. Based on research conducted by Wang, the proportion of zero input x_3, impulse input x_4 and sinusoidal input x_5 is chosen as 0.1, 0.5 and 0.4 respectively [178]. By considering all these factors and equation (4.30) to (4.33), a new Chebyshev goal programming model can be formulated as:

$$\min \lambda , \tag{4.38}$$

subject to

$$\begin{cases} \lambda \geq \dfrac{f_{optp} - f_{pb}}{f_{pw} - f_{pb}} \\ \lambda \geq \dfrac{f_{optc} - f_{cb}}{f_{cw} - f_{cb}} \end{cases} \tag{4.39}$$

and all other constraints are the same as for the single objective performance. In equation (4.39), f_{optp} is the multi-objective optimal best performance, f_{pb} is the single-objective best performance, f_{pw} represents the single-objective worst performance, f_{optc} is the multi-objective optimal cost, f_{cb} is the single-objective best cost, and f_{cw} is the single-objective worst cost.

By substituting equation (4.38) and (4.39) with the results of **Table 4.10**, **Table 4.11** and **Table 4.12**, the optimal changing ratio of adaptive flywheel for suspension system can be determined as $x = 0.258$. This implies that under this changing ratio, the suspension system with the adaptive flywheel shows the best performance at the lowest cost. This optimal changing ratio of adaptive flywheel for suspension system is obtained under the specific choices of x_1 to x_5 selected above, which are a function of cost, performance proportion and the proportion of inputs. Any change of these conditions, the optimal changing ratio will then also be different. By this optimal changing ratio, the performance of this suspension system with different input can be found in **Table 4.13**.

Table 4.13 performance of AFW suspension system with different inputs under optimal changing ratio

Input	Weighted accelerations of AFW suspension system a_w(m/s^2)	Weighted tire grip index of AFW suspension system M_{wtg}	Weighted vehicle body deflections of AFW suspension system D_{fw}(m)
Zero input	0.3079	0.0797	0.0026
Impulse input	0.2764	0.1203	0.0024
Sinusoidal input	3.2698	0.3757	0.0157

Table 4.13 shows the performance of the AFW suspension system with different inputs under the optimal changing ratio. Compared to the traditional suspension system:

1) Under zero input, the weighted accelerations of AFW suspension system decreases 28.2%, the weighted tire grip index of AFW suspension system decreases 71.1% and the weighted vehicle body deflections of AFW suspension system decreases 25.7%.
2) Under impulse input, the weighted accelerations of AFW suspension system decrease 37.1%, the weighted tire grip index of AFW suspension system weighted decreases 62.5% and the vehicle body deflections of AFW suspension system decreases 22.6%.
3) Under sinusoidal input, the weighted accelerations of AFW suspension system increase 101.1% (this implies that under sinusoidal input, passengers will feel more vertical acceleration than the traditional suspension system), the weighted tire grip index of AFW suspension system decreases 48.2% and the weighted vehicle body deflections of AFW suspension system increase 42%.

4.3.4.3. Optimal changing ratio for adaptive flywheel with different performance and inputs proportion

As mentioned above, with a change in the function of cost, performance proportion or proportion of inputs, the optimal changing ratio will also change. However, there are many factors which can affect the function of cost, such as different geographical areas, different factories and different workers, and it is impossible to determine one universal function of cost. Moreover, many of these factors are human factors, such as the efficiency difference between experienced and inexperienced workers, which makes some of the costs unpredictable. Therefore, in our simulations, the function of cost is always chosen as equation (4.34).

By fixing the proportion of inputs, the relationship between optimal changing ratio and performance proportion can be investigated as shown in **Table 4.14**:

Table 4.14 Optimal changing ratio with different performance proportion

Riding comfort x_1	0.2	0.4	0.5	0.6	0.8
Safety x_2	0.8	0.6	0.5	0.4	0.2
Optimal changing ratio x	0.378	0.301	0.231	0.211	0.198

Table 4.14 is the relationship between the optimal changing ratio and the performance proportion and shows that with an increasing proportion of riding comfort (or equivalently a decreasing proportion of safety), the optimal changing ratio will decrease.

The same simulations are conducted with different conditions. By fixing the performance proportion, the relationship between optimal changing ratio and proportion of inputs can also be determined by equation (4.38) and (4.39). In the proportion of inputs, there are three different types of inputs, which are zero input, impulse input and sinusoidal input, respectively. Each of these types of inputs represents a different road situation. However, in actual road situation, the proportion of zero input is quite small (meaning under 10% in most circumstances) [178,179]. Therefore, in our simulations, the proportion of zero input is fixed at 0.1, and the variables varied are the proportion of impulse input and sinusoidal input. The relationship between optimal changing ratio and proportion of inputs is shown in **Table 4.15**.

Table 4.15 Relationship between optimal changing ratio and proportion of inputs

Proportion of impulse input x_4	0.1	0.3	0.45	0.6	0.8
Proportion of sinusoidal input x_5	0.8	0.6	0.45	0.3	0.1
Optimal changing ratio x	0.201	0.219	0.241	0.297	0.389

Table 4.15 is the relationship between optimal changing ratio and proportion of inputs, and shows that a high proportion of impulse input (or equivalently low proportion of sinusoidal input), the optimal changing ratio will increase.

4.4. Conclusion

In this chapter, three different suspension systems were evaluated using three of the most commonly used performance criteria. Under zero input (initial displacement), the AFW suspension system outperforms both traditional and constant flywheel suspension system on riding comfort and tire grip, but shows no improvement on vehicle body deflection. When the excitation is an impulse input, the same results as for zero input are obtained. However, under sinusoidal input, the AFW suspension system shows the worst results on riding comfort and vehicle body deflection. For tire grip, the AFW suspension system still provides best performance.

With different changing ratio of adaptive flywheel, the performance of the AFW suspension system is variable. When the excitation is zero input, both riding comfort and tire grip are better with increasing changing ratio of the adaptive flywheel, but the weighted vehicle body deflections are not affected. Under impulse input, the same results can be found as zero input. With sinusoidal input, riding comfort decreases when the changing ratio of adaptive flywheel increases, but the tire grip becomes better. Vehicle body deflections are still not affected by the variable changing ratio of the adaptive flywheel.

This optimal changing ratio of adaptive flywheel for suspension system was obtained under specific conditions, which are a function of cost, performance proportion and the proportion of inputs. Any change of these conditions, then the optimal changing ratio will also be different. By increasing the proportion of riding comfort (or equivalently decreasing the proportion of safety), the optimal changing ratio will decrease. With a high proportion of impulse input (or equivalently low proportion of sinusoidal input), the optimal changing ratio will increase.

5. Experimental identification

In the previous chapter, an ideal two-terminal system was introduced for a new suspension system. To verify the performance of this new suspension system, actual two-terminal device parameters are needed. To identify the key parameters of two-terminal systems, experiments are required. In this chapter, experiments are carried out to identify key parameters for both the two-terminal hydraulic system and inverse screw system. After the determination of key parameters, additional experiments are applied to verify the accuracy of these parameters and the mathematical models of the systems. In order to minimize the spike forces during the experiments, which are caused by the backlash, a new experiment strategy is proposed. By adding a hydraulic rectifier, the spike forces in the two-terminal hydraulic system are reduced, which eventually leads to higher accuracy of the mathematical model.

5.1. Experimental identification for two-terminal hydraulic system

5.1.1. Experimental setup for two-terminal hydraulic system.

As mentioned in Section 3.2, to observe the behavior of the adaptive metal flywheel, a two-terminal hydraulic system is applied. From equation (3.12), it is clear that the system behavior is affected by four parameters, b_{ah}, F_{fh}, k_h and m_{em}, which implies that the identification of these four key parameters is the critical next step for analyzing the system. However, due to the complicated structure of this system, parameters b_{ah}, F_{fh}, and k_h cannot be calculated or measured directly, therefore experimental identification is required.

The experimental setup of the two-terminal hydraulic device with an adaptive flywheel is shown in **Figure 5.1**. An MTS 810 material test system is used for these tests. This system can generate sinusoidal, triangular and square input signals, with different amplitudes and frequencies. To accurately measure the rotational speed of the hydraulic motor, an encoder is added to the test rig. The sampling rate for the encoder output is set at 300Hz, the resolution of the encoder is 360/1024 degree, and the theoretical transmission ratio of the prototype is 41rads/mm. A National Instruments (NI) data acquisition board (NI USB-6212) is used to collect the rotational speed of the flywheel. The parameters of the NI data acquisition board are shown in **Table 5.1**

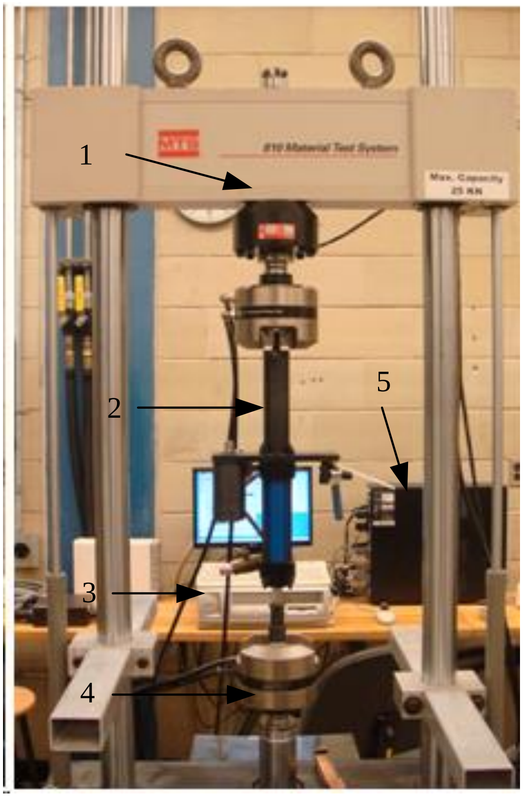

Figure 5.1 Test rig for the adaptive flywheel (Note: 1-force cell, 2- two-terminal hydraulic system, 3–computer, 4-actuator, 5-controller)

Table 5.1 Parameters of NI USB-6212

No.	Name	Specification
1	Connector	Screw/68-pin SCSI
2	Analog Iputs	16
3	Resolution(bits)	16
4	Max Rate(kS/s)	400
5	Analog Outputs	2
6	Resolution(bites)	16

7	Max Rate(kS/s)	250
8	Digital I/O	24 or 32 DIO

In order to analyze the change in the inertial force of the adaptive flywheel, three configurations are considered. The first configuration is where the sliders are allowed to move, as designed. The second two configurations are those whereby the slider are fixed at the largest and smallest allowable distance from the center of rotation. By inserting incompressible materials in the slots, the slider location can be fixed. With these three configurations, the change in the inertial force on the adaptive flywheel will be more obvious. Since foamed plastics are hard to compress and are light-weight, they were chosen to fix the slider locations in this experiment. The experimental data can be found in Appendix A.

Because of the characteristics of the two-terminal hydraulic system, three different frequency and amplitude sinusoidal signals were selected. The three sinusoidal signals are: (1) frequency 0.2 Hz and amplitude 0.01 m/s, (2) frequency 1 Hz and amplitude 0.01m/s, (3) frequency 2Hz and amplitude 0.02 m/s.

As mentioned in Chapter 3, by varying the input with different amplitudes and frequencies, the adaptive flywheel will generate different equivalent mass, which eventually causes the inertia force of the two-terminal hydraulic system to change. **Figure 5.2** shows the force-time curves of the adaptive flywheel with the sliders allowed to move and pinned at their minimum and maximum locations under frequency 0.2 Hz, amplitude 0.01 m/s, frequency 1Hz, amplitude 0.01 m/s and frequency 2 Hz, amplitude 0.02 m/s, respectively. The peaks in **Figure 5.2** are spike force caused by the air in the two-terminal hydraulic system and the hydraulic power station.

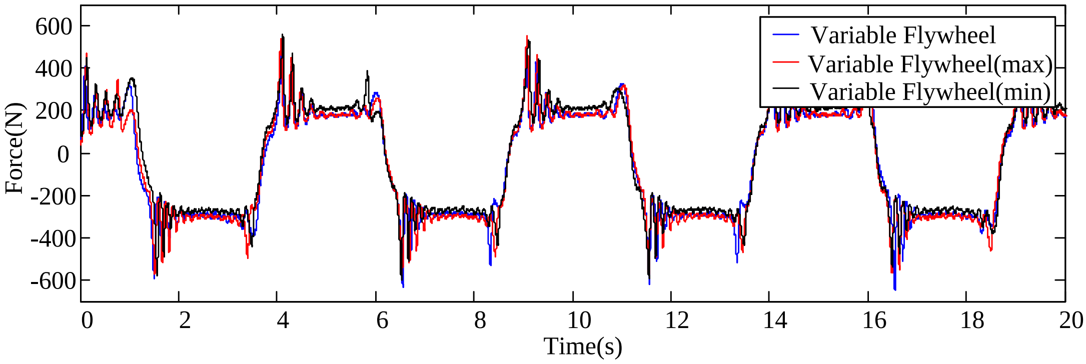

(a)

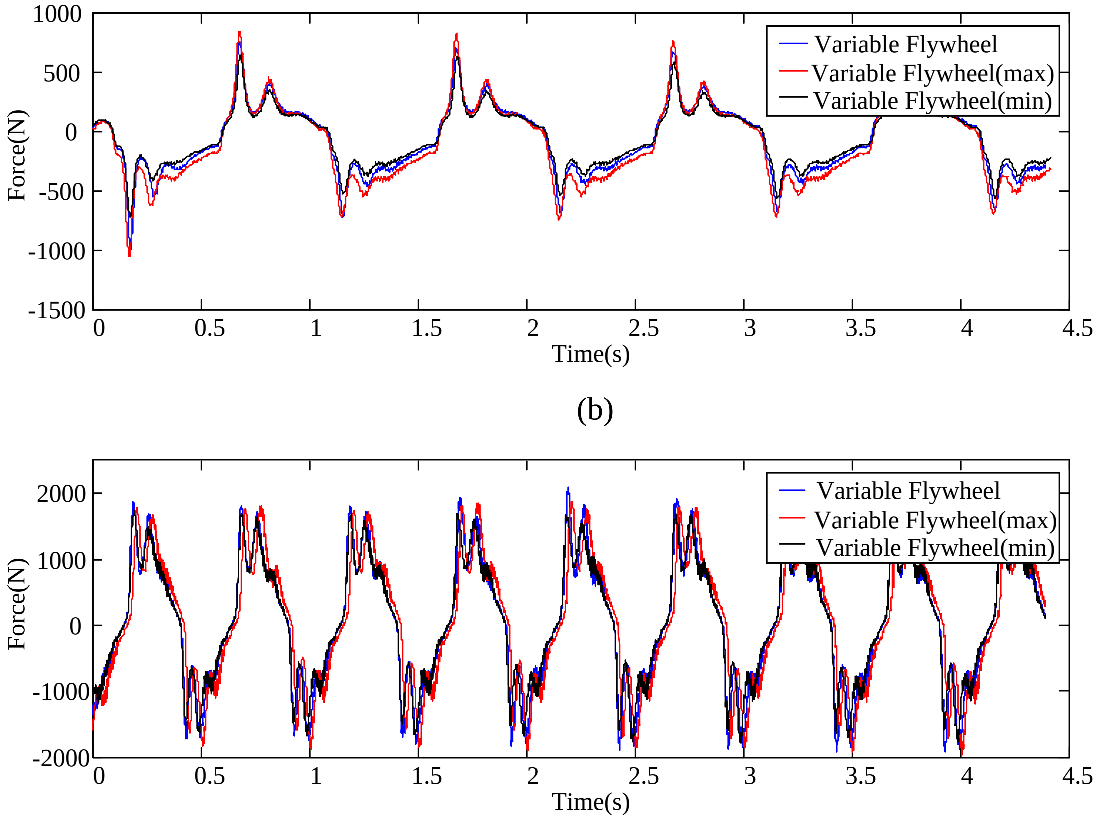

(b)

(c)

Figure 5.2 Comparison of adaptive flywheel under different configurations. (a), (b) and (c) are force–time diagrams of three adaptive flywheels under frequency 0.2 Hz, amplitude 0.01 m/s, frequency 1Hz, amplitude 0.01 m/s and frequency 2 Hz, amplitude 0.02 m/s respectively

It is expected that different equivalent masses would be generated by the adaptive flywheel with the three different configurations. In **Figure 5.2** (a), since the input sinusoidal signal with low amplitude frequency can only generate a small acceleration, this in turn leads to the changing ratio of the inertial force on the adaptive flywheel to be less than 3%. Therefore, in **Figure 5.2** (a), the three curves are almost identical, and it is difficult to distinguish the changes in the inertial force under the three different configurations.

However, as shown in **Figure 5.2** (c), the input sinusoidal signal generates a large acceleration because of high amplitude and frequency, which will cause a changing ratio of inertial force on the adaptive flywheel to be as large as 11%. However, because of the characteristics of the hydraulic system, the larger acceleration also generates larger force spikes, which in turn covers the change in the inertial force of the whole system.

For the above reasons, an excitation sinusoidal signal with a mid-range frequency and appropriate amplitude was required for this experiment. As shown in **Figure 5.2** (b), a sinusoidal input with frequency of 1Hz and amplitude of 0.01 m/s was applied, leading to an 8% changing ratio of inertial force on the adaptive flywheel. However, due to the relative lower spike force, the change of the inertial force can be clearly observed in **Figure 5.2** (b), as predicted.

5.1.2. Experimental validation of the inaccurate transmission ratio caused by pressure loss and friction

The mathematical model presented in Chapter 3 considered pressure loss and friction. Both factors will cause energy loss, which can also be presented as an inaccurate transmission ratio (smaller than theoretically expected). This concept will be validated experimentally in this sub-section. To do so, two triangular command (linear) displacement input signals with the same frequency (0.5 Hz) but different amplitudes (0.005 m and 0.010 m, respectively) were applied to the two terminals of the hydraulic device. This leads to angular motion of the hydraulic motor and flywheel. The associated flywheel angular displacements are shown as dashed lines in **Figure 5.3** (a) and (c), respectively. These results are then fitted as the solid lines in **Figure 5.3** (a) and (c). To examine the effects of pressure loss and friction, the theoretical flywheel angular velocity (calculated by $\omega = vA/h$) was compared with the actual fitted one (obtained by differentiation of the fitted angular displacement shown in **Figure 5.3** (a), and (c)). The flywheel angular velocities obtained through **Figure 5.3** (a) and (c) are presented in **Figure 5.3** (b) and (d), respectively. Flywheel angular velocities obtained using the fitted flywheel angular displacements (the solid lines in **Figure 5.3**(a) and (c)) are presented as solid lines (labeled “Actual Fitted”) in **Figure 5.3**(b) and (d), respectively. The theoretically-calculated flywheel angular velocities in response to the two linear displacement inputs are shown as dashed lines (labeled “Theoretical”) in **Figure 5.3** (b) and (d), respectively. As revealed in **Figure 5.3** (b) and (d), the actual fitted angular velocity of the flywheel (or hydraulic motor) cannot reach the theoretical angular velocity. This verifies the existence of the pressure loss and inner friction in the two-terminal hydraulic system.

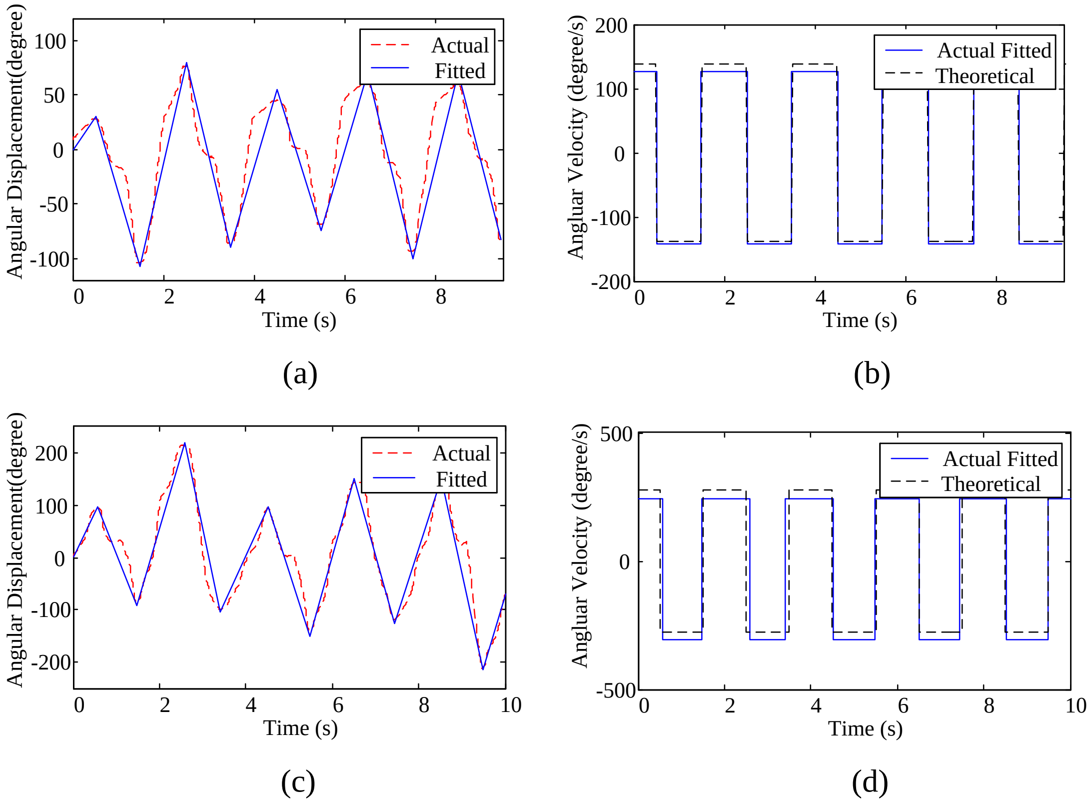

Figure 5.3 The relationship between actual fitted and theoretical flywheel angular velocities: (a) and (c) compare the actual and fitted flywheel angular displacements in response to the triangular command (linear) displacement inputs (amplitudes = 0.005 m and 0.01 m respectively) applied to the two terminals of the hydraulic device, (b) and (d) compare the actual fitted and theoretical flywheel angular velocities obtained from (a) and (c), respectively.

5.1.3. Parameter identification

As indicated earlier, to examine the system performance, the four model parameters in equation (3.15), (m_{em}, k_h, b_{ah} and F_{fh}) must be obtained first. Of these four parameters, only the equivalent mass m_{em} can be calculated, the rest have to be identified by experiment. The theory of multi-variable solutions can be applied to this problem. However, because of the characteristics of the mathematical model of this system, some of the parameters can be eliminated by different types of experimental inputs. The details are described in the following subsection.

5.1.3.1. Identification of damping ratio b_{ah} and friction force F_{fh} .

To simplify the identification process, a square command linear velocity input is applied to the two terminals of the hydraulic device. Since the associated velocity is a constant, i.e., $v(t) = q$, the acceleration is thus zero except at the direction change points. Therefore, the third equation of equation (3.14) reduces to

$$F - F_{fh} = b_{ah} v(t) = b_{ah} q \tag{5.1}$$

Since k_h is not present in equation (5.1), k_h will be identified separately whereas parameters b_{ah} and F_{fh} can be determined based on the following criterion:

$$\{F_{fh}, b_{ah}\} = \arg\min \left(\sqrt{\frac{1}{t_{eh} - t_{sh}} \sum_{t=t_{sh}}^{t_{eh}} \left(F_{mh}(t) - F_{ch}(t) \right)^2} \right) \tag{5.2}$$

In equation (5.2), $F_{mh}(t)$ is the measured force and $F_{ch}(t)$ is the theoretically-calculated force using equation (5.2), t_{sh} stands for the starting time of data recording, and t_{eh} is the end time. As the data are discrete, the above criterion can be expressed as

$$\{F_{fh}, b_{ah}\} = \arg\min \left(\sqrt{\frac{1}{n_{eh} - 1} \sum_{n=1}^{n_{eh}} \left(F_{mh}(n) - F_{ch}(n) \right)^2} \right) \tag{5.3}$$

where $F_{mh}(n)$ is the measured force, $F_{ch}(n)$ is the theoretically calculated force using equation (5.3) at sampling point n, and n_{eh} is the last sampling point of a dataset. In the experiments, 10 datasets of rectangular velocity inputs with frequency range from 0.1 Hz to 1Hz and amplitude from 0.001m/s to 0.015m/s were collected. By using Matlab to generate an iterative algorithm, different values of b_{ah} and F_{fh} can be given to calculate the force, and the minimum difference between the calculated force and actual force can be found. Therefore, parameters b_{ah} and F_{fh} are estimated as

$$b_{ah} = 8100 \pm 100 \,\text{Ns/m}, \quad F_{fh} = 190 \pm 8 \,\text{N} \tag{5.4}$$

Since the values of parameters b_{ah} and F_{fh} are estimated, the confidence interval has been included. When the difference between the calculated force and actual force is less than 5%, the value of parameters will be recorded, which eventually leads to the range of confidence interval.

Three typical datasets associated with frequency-amplitude combinations of (0.2Hz and 0.002m/s), (0.5Hz and 0.0075m/s) and (1 Hz and 0.015m/s) are shown in **Figure 5.4**.

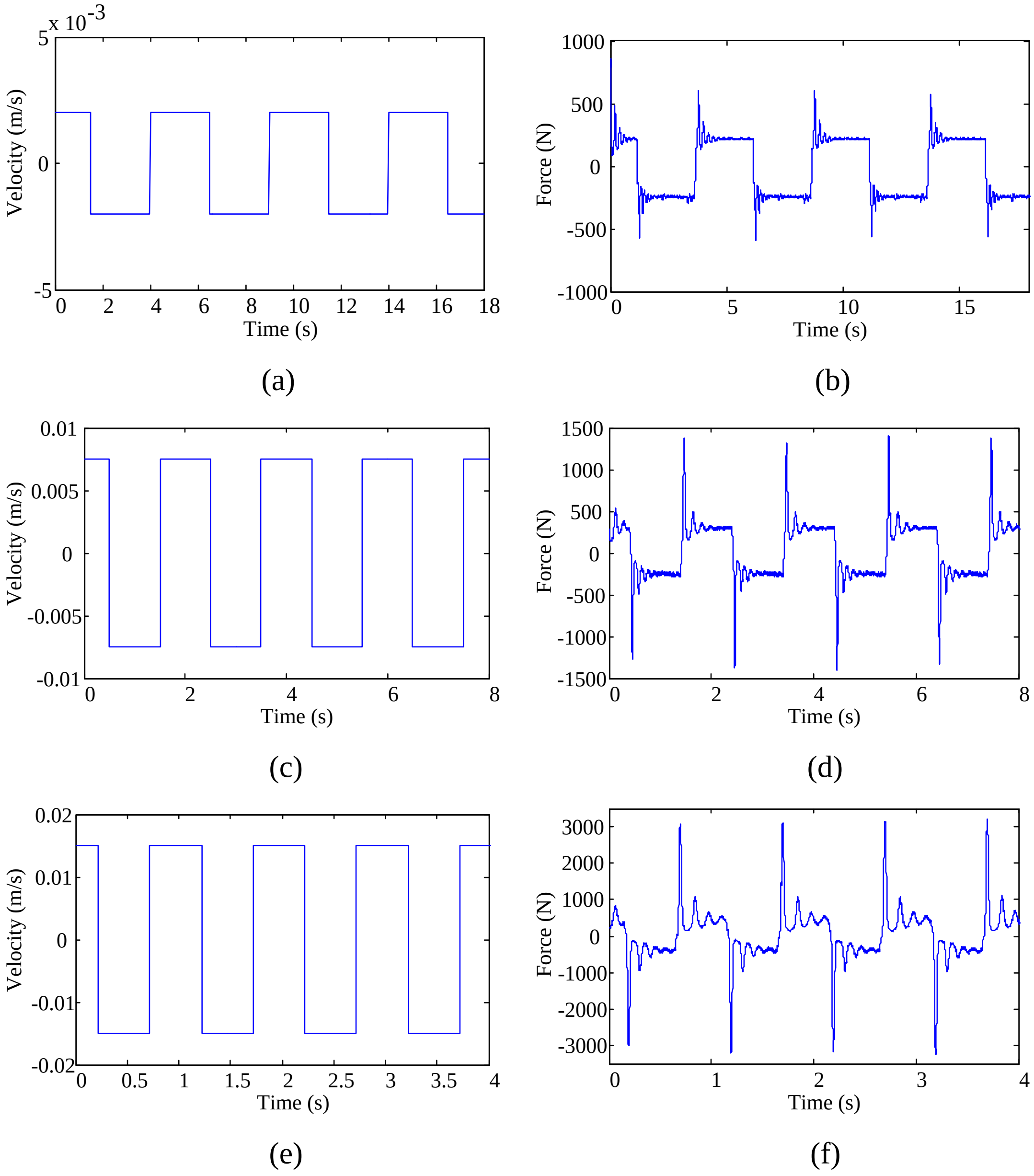

(a) (b)

(c) (d)

(e) (f)

Figure 5.4 Rectangular velocity inputs and corresponding measured forces. (a), (c) and (e) present the velocity inputs with different frequencies and amplitudes ((0.2Hz 0.005m/s), (0.5Hz, 0.0075m/s) and (1Hz, 0.015m/s)) respectively. (b), (d) and (f) are the measured forces corresponding to the velocity inputs shown in (a), (c) and (e), respectively.

With the b_{ah} and F_{fh} values obtained above, the measured and calculated forces based on another two sets of experimental data with frequency-amplitude combinations (0.5Hz, 0.005m/s) and (1Hz, 0.01m/s) are compared in **Figure 5.5**. The velocity inputs are shown in **Figure 5.5** (a) and (c), respectively. The measured forces and calculated forces based on the estimated b_{ah} and F_{fh} are presented in **Figure 5.5** (b) and (d). The close agreement between the measured and calculated forces (except at the points where the velocity change directions) validates the accuracy of the estimated b_a and F_{fh}.

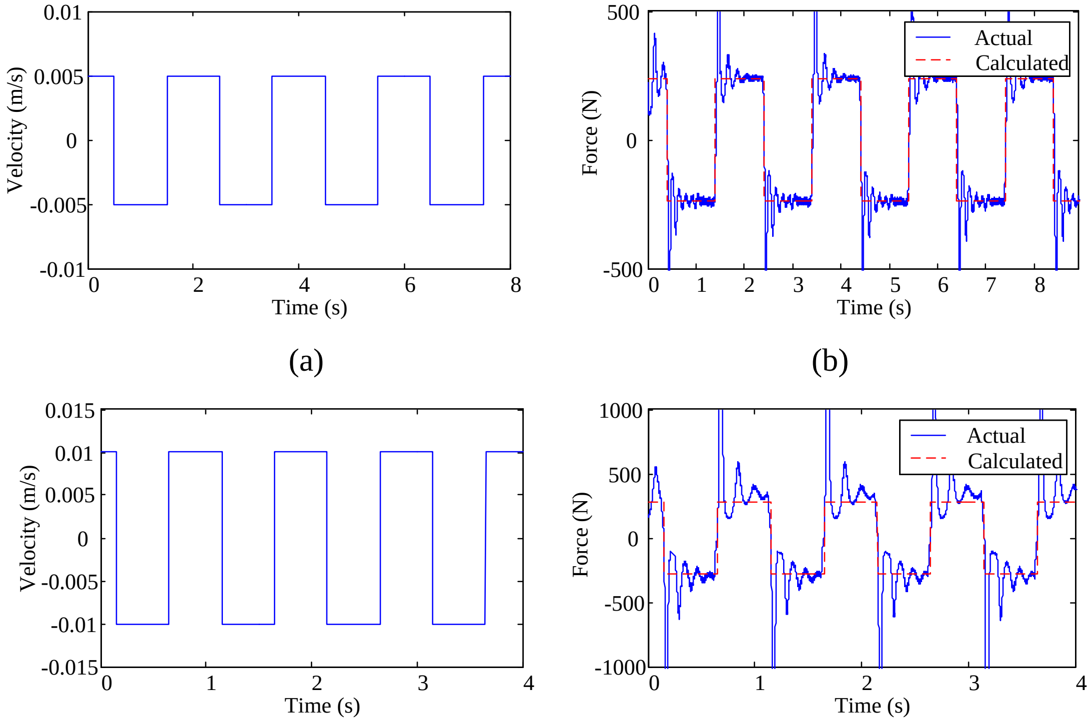

(a) (b)

(c) (d)

Figure 5.5 Comparison of the measured forces and calculated forces based on the estimated b_{ah} and F_{fh}. (a) Velocity input (frequency = 0.5 Hz, amplitude = 0.005 m/s), (b) measured and calculated forces corresponding to the velocity input in (a), (c) velocity input (frequency = 1 Hz, amplitude = 0.01 m/s), and (d) measured and calculated forces corresponding to the velocity input in (c).

5.1.3.2. The variable behavior of flywheel moment of inertia I_{afm} and equivalent mass m_{em}.

As mentioned in Section 3, the equivalent mass m_{em} will change with the input velocity. However, when the rotational speed is very low, the slider will stay at the initial location, m_{em} will be minimum, and when the rotational speed reaches a certain level, the spring in the slot will be fully compressed and m_{em} will reach its maximum value. To examine the general behavior of the flywheel, the input signal should be selected in such a way that the sliders will not stay at the two ends of the slot and hence m_{em} will be neither the minimum nor maximum value. For this reason, a sinusoidal input signal is chosen because it is less abrupt than the rectangular and triangular inputs and hence the sliders can travel between the two ends but not stay at a fixed location (i.e., one of the two ends of the slots) if the input frequency and amplitude are properly selected. In the tests, a sinusoidal velocity input with frequency 0.1Hz and amplitude 0.0314 m/s was applied to the terminals of the hydraulic device. Under the sinusoidal input of this frequency and amplitude, the sliders will not stay at the initial location and the springs will not be fully compressed either, but will travel over most of the travel range in the slots. Hence, the change of equivalent mass can be observed over a broader range.

The variable location of the sliders, the variable moment of inertia and the equivalent mass of the flywheel in response to the sinusoidal input (**Figure 5.6**(a)) can then be calculated using equations (3.6), (3.9) and (3.12) respectively. The results are presented in **Figure 5.6** (b), (c) and (d), respectively. **Figure 5.6** (c) and (d) show that the moment of inertia and equivalent mass of the flywheel vary adaptively in response to the input, however the variation frequency is doubled.

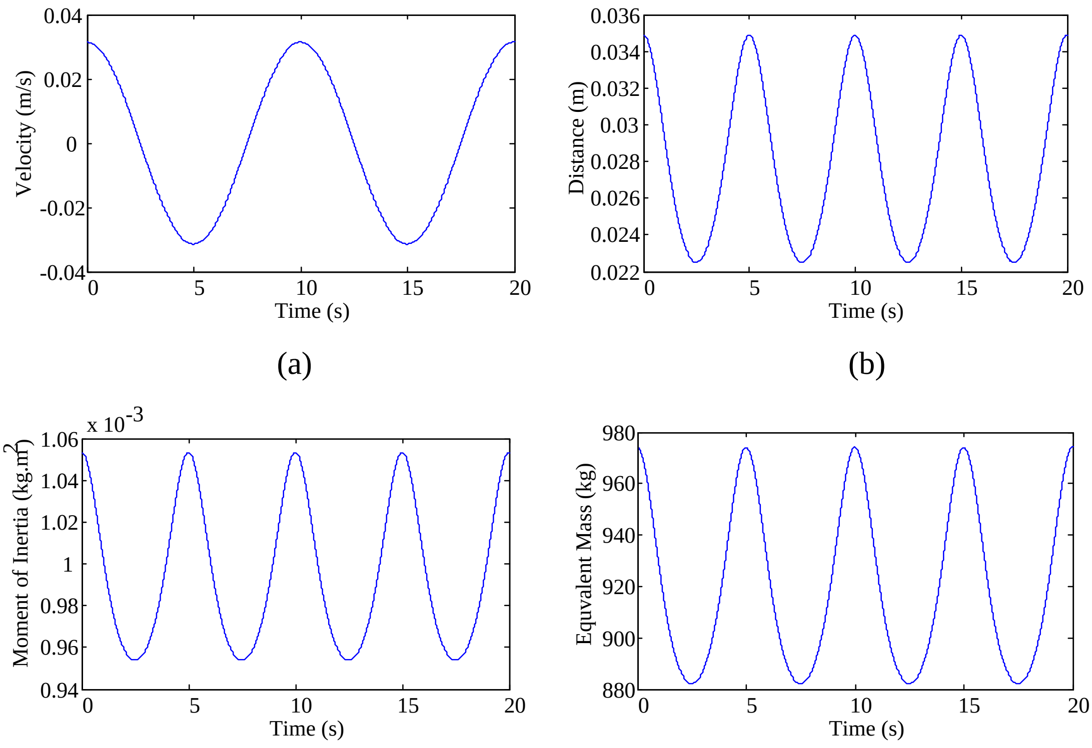

(a) (b)

(c) (d)

Figure 5.6 The variable behavior of the flywheel moment of inertia and equivalent mass: (a) sinusoidal velocity input (frequency = 0.1 Hz, amplitude = 0.0314 m/s), (b) slider location (i.e., the distance between slider centroid and flywheel rotational center) that varies in response to the velocity input in (a), (c) the variable moment of inertia of the flywheel associated with the slider location presented in (b), and (d) the variable equivalent mass of the flywheel due to the location change of the sliders.

5.1.3.3. Calculation of system stiffness k_h

After the identification of the damping ratio b_{ah}, friction force F_{fh}, and flywheel equivalent mass m_{em}, sinusoidal inputs are applied to determine the system stiffness k_h. Suppose that the velocity input signal can be expressed as

$$v(t) = a\omega\cos(\omega t) \qquad (5.5)$$

By substituting equation (5.5) into equation (3.15), the system stiffness k_h can then be determined from

$$k_h = \arg\min\left(\sqrt{\frac{1}{t_e - t_s}\sum_{t=t_s}^{t_e}\left(F_m(t) - F_c(t)\right)^2}\right) \tag{5.6}$$

The discrete version of equation (5.6) will be used in the actual calculation of k and is given by

$$k_h = \arg\min\left(\sqrt{\frac{1}{n_e - 1}\sum_{n=1}^{n_e}\left(F_m(n) - F_c(n)\right)^2}\right) \tag{5.7}$$

For this purpose, 20 experimental datasets of sinusoidal velocity inputs with frequency range from 0.1Hz to 2Hz and amplitude range from 0.0019m/s to 0.19m/s were acquired. By choosing a wide range frequency of inputs (from minimum to high frequency), more data can be extracted from the experiments. Therefore, the value of k_h based on these datasets and equation (5.7) was found to be

$$k_h = 7.76 \times 10^5 N/m \tag{5.8}$$

Three typical datasets are shown in **Figure 5.7**. Of the three datasets, one has an input with low frequency and amplitude (0.1Hz and 0.0019m/s) (**Figure 5.7** (a)), one with middle frequency and amplitude (0.5Hz and 0.016m/s) **Figure 5.7** (c)) and the other with high frequency and amplitude (2 Hz and 0.1m/s) (**Figure 5.7** (e)).

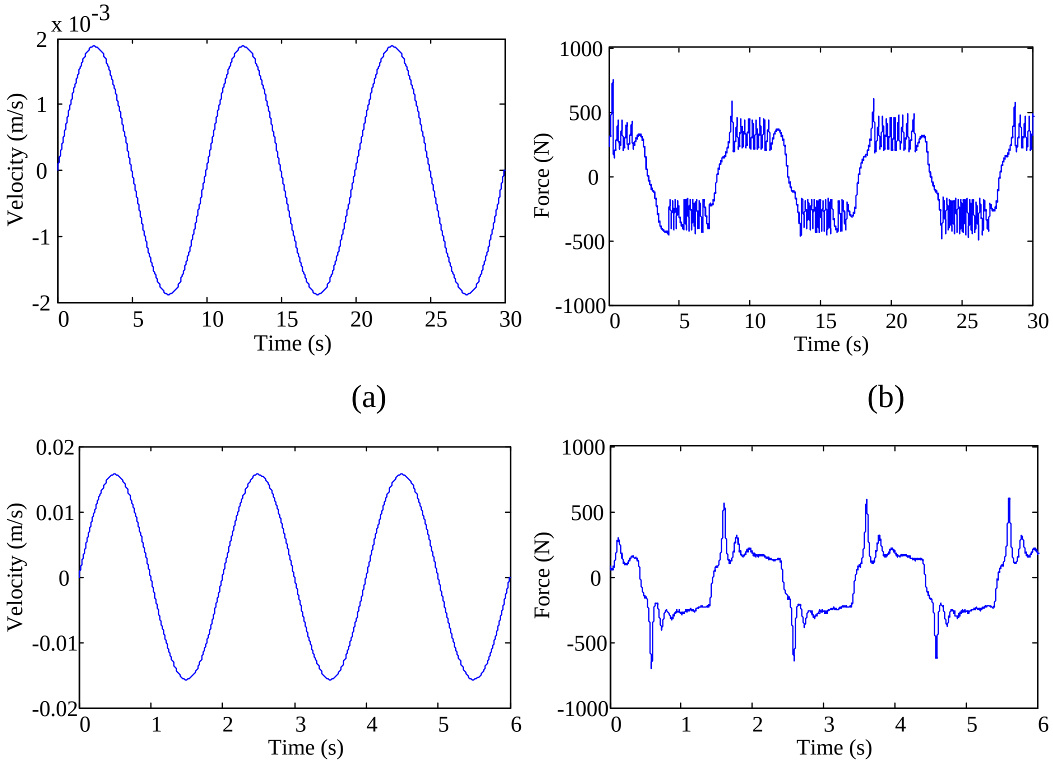

(a) (b)

(c) (d)

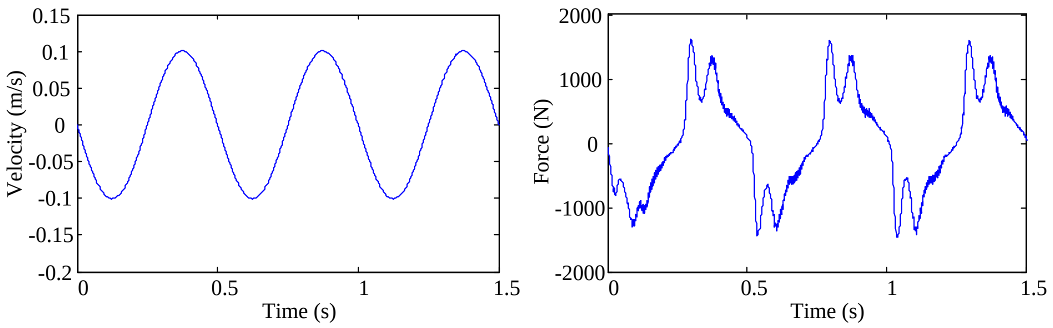

(e) (f)

Figure 5.7 Sinusoidal velocity inputs and corresponding measured forces. (a), (c) and (e) are sinusoidal velocity inputs associated with frequency-amplitude combinations of (0.1Hz, 0.0019m/s), (0.5Hz, 0.016m/s) and (2Hz, 0.1m/s), respectively. (b), (d) and (f) are measured forces corresponding to the inputs in (a), (c) and (e), respectively.

Since the value of k_h has been determined, the measured forces and calculated forces based on k_h can be compared. For this purpose, another two sets of data with velocity inputs (0.4Hz, 0.012m/s) and (2Hz, 0.063m/s) are shown in **Figure 5.8** (a) and (c) respectively. The measured forces and calculated forces corresponding to the velocity inputs in **Figure 5.8** (a) and (c) are respectively presented in **Figure 5.8** (b) and (d). With the exception of the points where the terminals of the hydraulic device experience the largest acceleration and deceleration, the measured and calculated forces are in close agreement, which shows that the system stiffness k_h has been accurately identified.

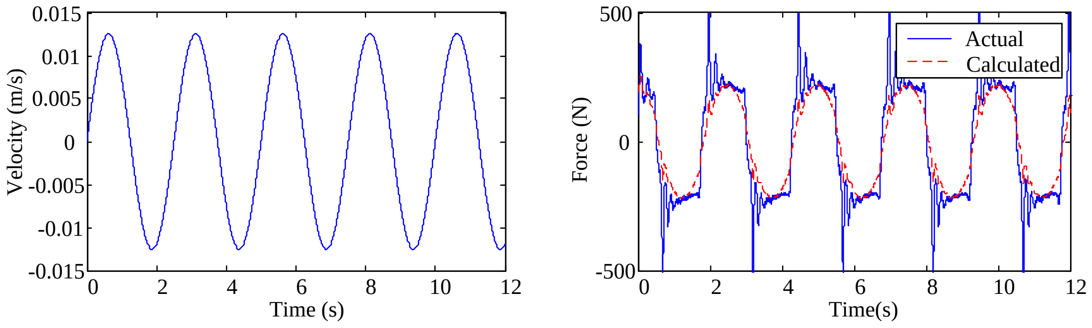

(a) (b)

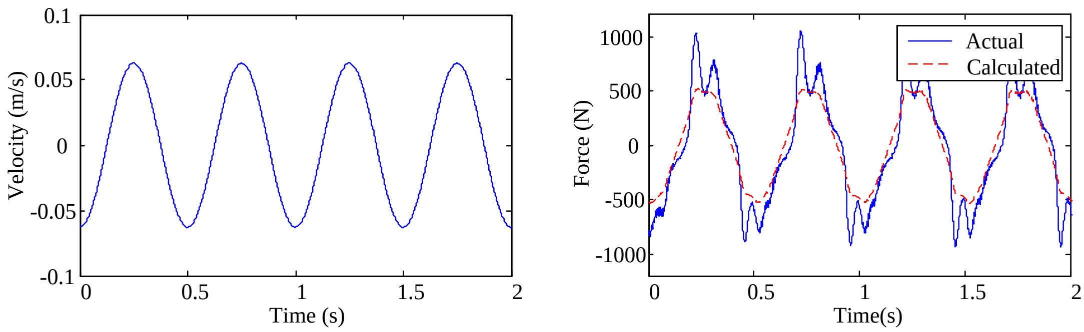

(c) (d)

Figure 5.8 Comparison of the measured forces and calculated forces based on the estimated k_h. (a) Velocity input (frequency = 0.4 Hz, amplitude = 0.012 m/s), (b) measured and calculated forces corresponding to the velocity input in (a), (c) velocity input (frequency = 2 Hz, amplitude = 0.063 m/s), and (d) measured and calculated forces corresponding to the velocity input in (c)

5.1.4. Experimental validation of the mathematical model

After identifying k_h, b_{ah}, F_{fh} and calculating m_{em}, all four key coefficients for describing the two-terminal hydraulic system are known. The accuracy of the mathematical model for this system is now examined by comparing the experimentally-measured forces to the calculated forces obtained from the mathematical model. Three typical sinusoidal velocity inputs with low frequency and amplitude (0.4 Hz, 0.012 m/s), middle frequency and amplitude (1 Hz, 0.0314m/s) and high frequency and amplitude (2Hz, 0.126 m/s) are applied to the terminals of the hydraulic device. The measured and calculated forces associated with the three inputs are respectively displayed in **Figure 5.9** (a), (b) and (c). In all the three cases, the calculated results match the measured forces very well, which validates the accuracy of the mathematical model. The spikes in the measured force are mainly caused by two reasons. The first one is the air in the hydraulic station which supplies power to the test machine. Since there is air in the power station, there will be a sudden force change when the actuator changes its moving direction. The second reason is the air in the hydraulic device; there will also be sudden force change when the rotation direction of the flywheel changes. The period of these experiments should be the time between two spike forces instead of the oscillation caused by spike forces.

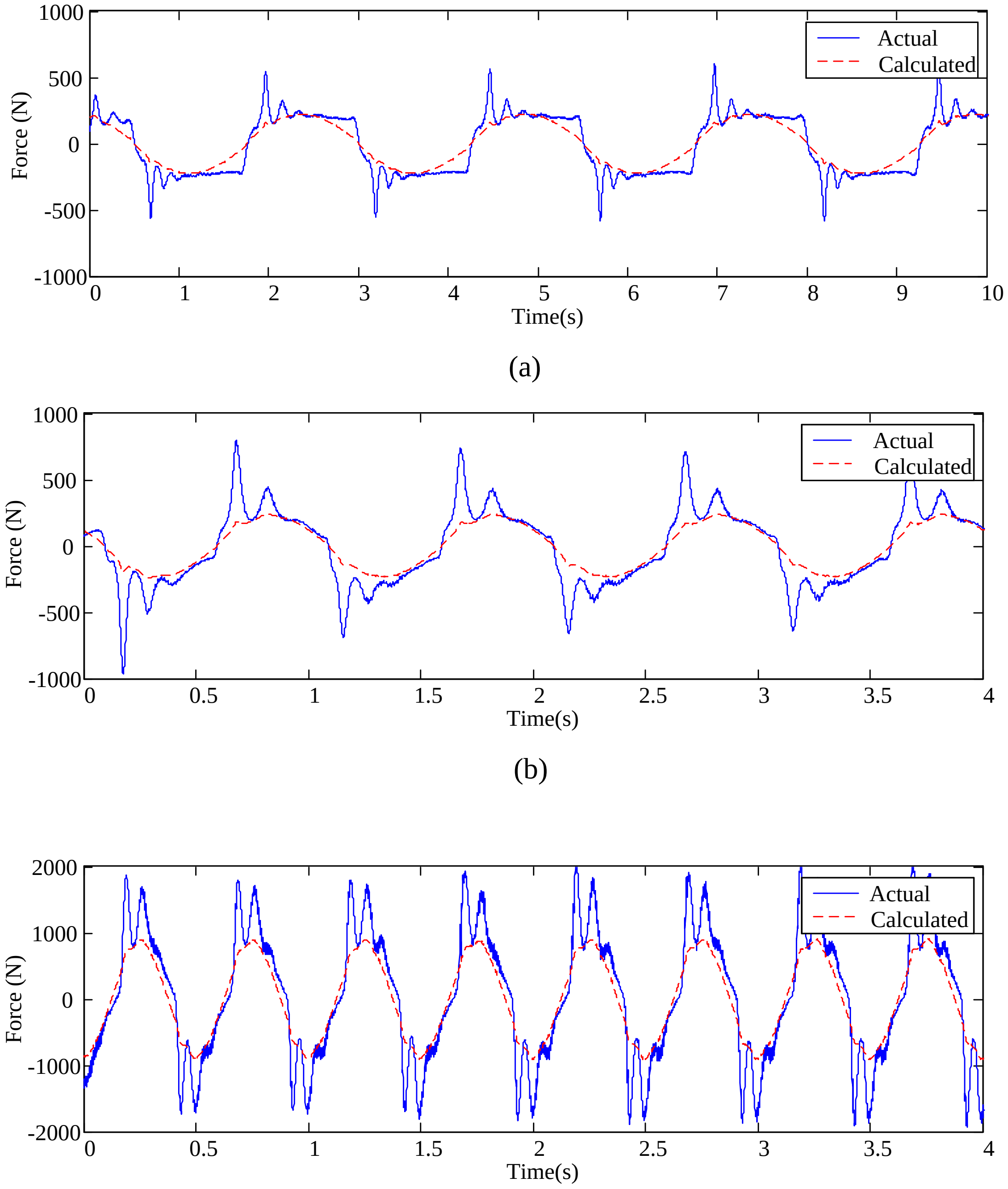

(a)

(b)

(c)

Figure 5.9 The comparison of measured forces and calculated forces using the mathematical model. (a) comparison between measured and calculated forces with a velocity input of low frequency and amplitude (0.4 Hz, 0.012 m/s), (b) comparison between measured and calculated forces with an input of middle frequency and amplitude (1 Hz, 0.0314m/s), and (c) comparison between measured and calculated forces with an input of high frequency and amplitude (2Hz, 0.126 m/s).

5.2. Experimental identification for the inverse screw system with nylon adaptive flywheel

5.2.1. Experimental Set-up

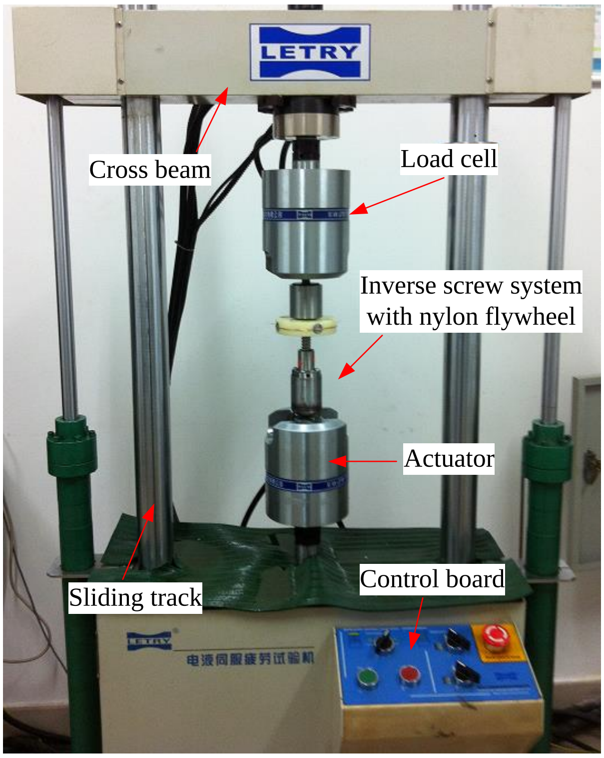

Figure 5.10 Experimental rig of inverse screw system with nylon flywheel

From equation (3.38), the mathematical model of this system can be described by four key parameters k_i, c_i, f_i and m_{en}. An accurate mathematical model of this system can be obtained after the determination of the four parameters. However, the same situation occurs as mentioned in section 5.1; parameters k_i, c_i, and f_i cannot be directly calculated or measured, which requires experimental identification.

The Letry electro hydraulic servo fatigue test machine PLN-20 was used for this experiment. The experimental rig of inverse screw system with nylon adaptive flywheel is shown in **Figure 5.10**. This test machine can generate test signals of different amplitude and frequency, such as ramp (tapped ramp), sinusoidal (tapped sinusoidal) and square signals. The key specifications of the Letry PLN-20 electro-hydraulic servo fatigue test machine are shown in **Table 5.2**.

Table 5.2 Parameters of Letry PLN-20 electro hydraulic servo fatigue test machine

Name	Specification
Maximum dynamic load	20kN
Maximum dynamic torque	-50～+50kN/m
Maximum amplitude angle	-45^{o}～+45^{o}
Maximum working travel	-100~100mm
Testing frequency	0.001~20HZ
Testing waveform	Sinusoidal wave, square wave, triangle wave, ramp, random wave, block wave

The electro-hydraulic servo controller (DSP Trier 6202) of PLN-20 can record as many as three datasets. In the experiments performed, only displacements and forces are critical, and hence there is no need for an additional data acquisition board.

5.2.2. Identification of key parameters

As previously mentioned, to develop an accurate model of the system, it is essential to identify the four key parameters k_i, c_i, f_i and m_{en}. By using equation (3.33), along with specific parameters from **Table 3.3** and **Table 3.4**, m_{en} can be calculated from a given input signal $\dot{x}$. Because of this characteristic of m_{en}, the system identification process can be divided into two parts.

First, assuming that there is a sinusoidal signal input with amplitude 0.005m and frequency 2Hz, the corresponding equivalent mass can be represented as shown in **Figure 5.11**. Additional experimental data can be found in Appendix B.

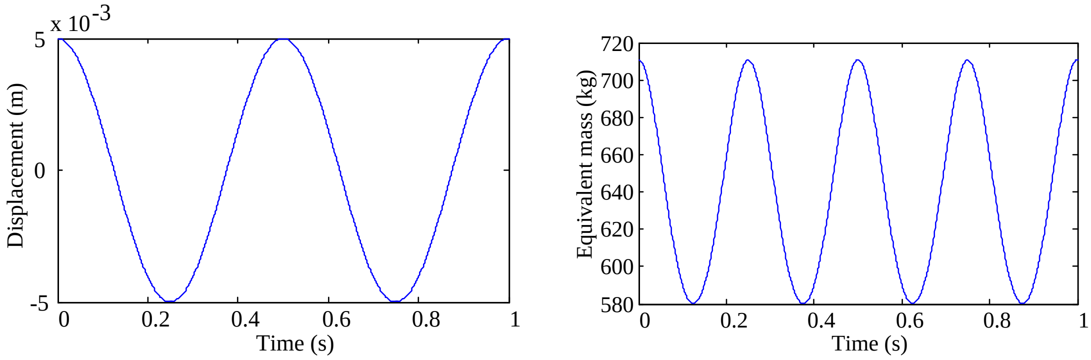

(a) (b)

Figure 5.11 Theoretical input (a) and corresponding calculated equivalent mass (b)

As shown in **Figure 5.11**, because the sinusoidal signal input generates a variable centrifugal force, this in turn changes the equivalent mass of the flywheel, as shown in **Figure 5.11** (b).

For the remaining parameter identification, many factors will affect the remaining three parameters such as the material of the inverse screw system, the set-up of experimental rig and the lubrication condition. Therefore, these three parameters cannot be accurately theoretically calculated and experimental data are needed to determine the three parameters. The most accurate values of these parameters can be determined from the following equation:

$$\{f_i, c_i, k_i\} = \arg\min\left(\sqrt{\frac{1}{t_{ei} - t_{si}} \sum_{t=t_{si}}^{t_{ei}} \left(F_{mi}(t) - F_{ti}(t)\right)^2}\right) \tag{5.9}$$

where $F_{mi}(t)$ is the measured force, $F_{ci}(t)$ is the theoretically calculated force from equation (5.9), t_{si} is the start time of data recording, and t_{ei} is the end time. Since the data are discrete, the above criterion can be rewritten as

$$\{f_i, c_i, k_i\} = \arg\min\left(\sqrt{\frac{1}{n_{ei} - 1} \sum_{n=1}^{n_{ei}} \left(F_{mi}(n) - F_{ti}(n)\right)^2}\right) \tag{5.10}$$

where $F_{mi}(n)$ is the measured force and $F_{ci}(n)$ is the theoretically calculated force using equation (5.10) at sampling point n, and n_{ei} is the last sampling point of a dataset. By using 21 datasets of sinusoidal inputs with frequency range from 0.1Hz to 5Hz and amplitude range from 0.005m to 0.015mm, parameters f_i, k_i and c_i were estimated as

$$c_i = 7600\,\text{Ns/m},\quad f_i = 80\,\text{N},\quad k_i = 1.97\times10^6\,\text{N/m} \tag{5.11}$$

The calculated forces based on the three estimated parameters and measured forces are compared in **Figure 5.12**. The sinusoidal displacement inputs are plotted in **Figure 5.12** (a), (c) and (e) with frequency 0.1Hz, amplitude 0.005m , frequency 0.5Hz, amplitude 0.01m and frequency 2Hz, amplitude 0.005m, respectively. The measured force and calculated force corresponding to inputs in **Figure 5.12** (a), (c) and (e) are presented in **Figure 5.12** (b), (d) and (f). As shown, the accuracy of the estimated c, f and k can be clearly verified by the close agreement between the measured and calculated forces.

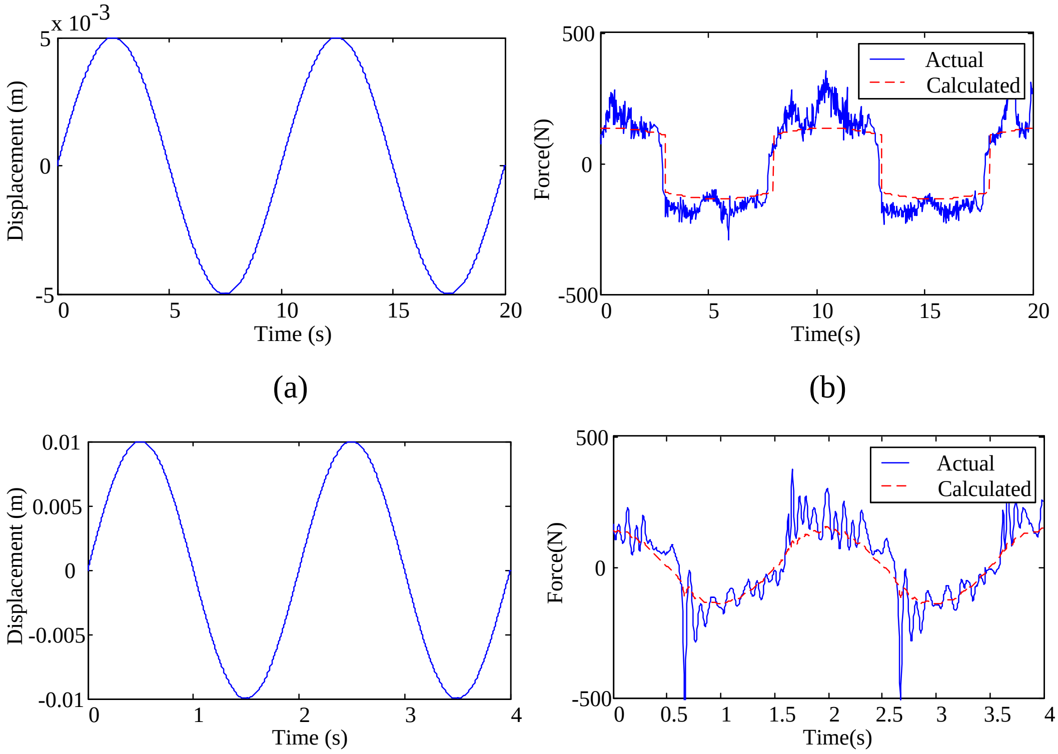

(a) (b)

(c) (d)

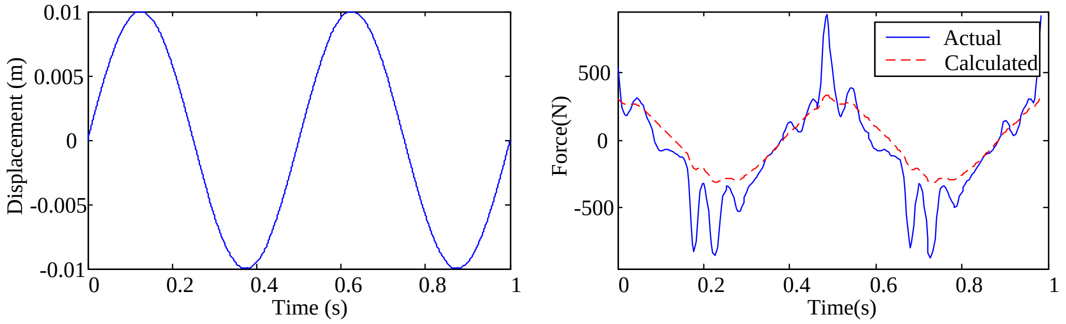

(e)

(f)

Figure 5.12. Comparison of the measured and calculated force based on the estimated *f*, *c* and *k*. (a) displacement input (frequency 0.1Hz, amplitude 0.005m), (b) measured and calculated forces corresponding to the displacement input in (a), (c) displacement input (frequency 0.5Hz, amplitude 0.01m), (d) measured and calculated forces corresponding to the displacement input in (c), (e) displacement input (frequency 2Hz, amplitude 0.05m), (f) measured and calculated forces corresponding to the displacement input in (e).

5.2.3. Comparison between calculated and actual forces

In section 5.2.2, after the determination of all the four key parameters, the behavior of the inverse screw system with nylon flywheel can be predicted. Two sinusoidal inputs with frequency 0.5Hz, amplitude 0.015m, and frequency 2Hz, amplitude 0.01m are shown in **Figure 5.13** (a) and (c), respectively. In response to inputs in **Figure 5.13** (a) and (c), comparisons between the calculated forces and actual experimental forces are shown in **Figure 5.13** (b) and (d). With the exception of the oscillations caused by the spike forces, close agreements between the calculated (dashed line) and experimental (solid line) forces in both cases demonstrate the accuracy of the mathematical model of the inverse screw system with nylon adaptive flywheel.

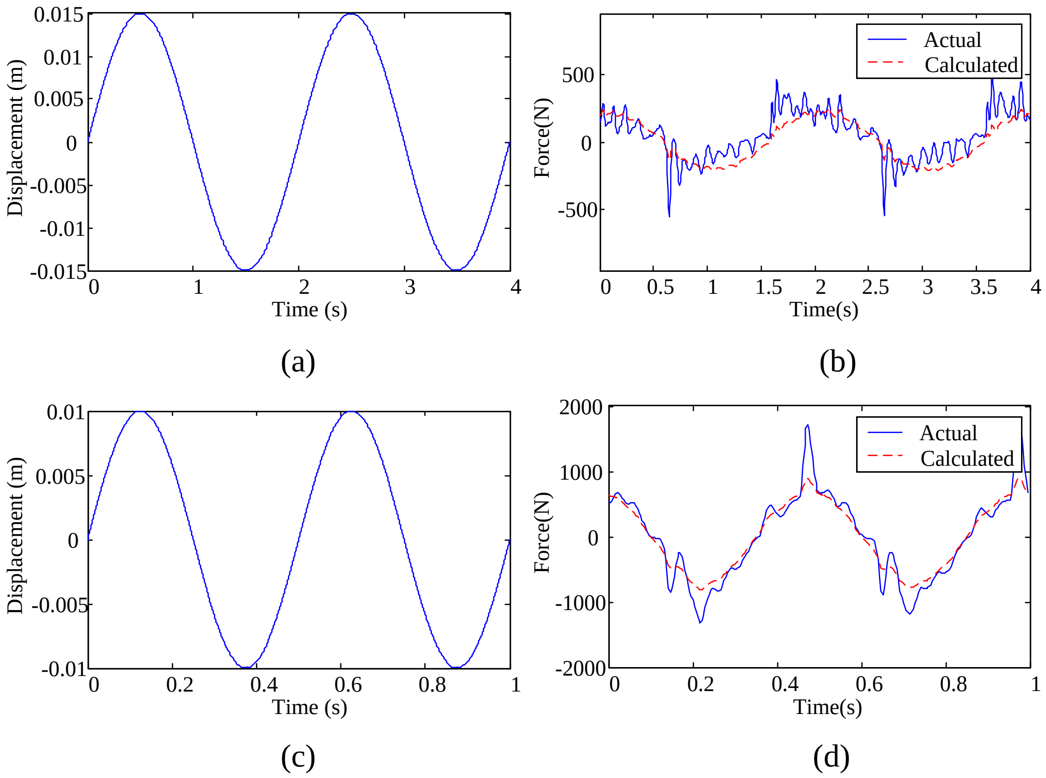

(a) (b)

(c) (d)

Figure 5.13. Comparison between the actual and calculated force, based on the mathematical model: (a) sinusoidal input with frequency 0.5Hz and amplitude 0.015m, (b) comparison between actual and calculated force corresponding to the sinusoidal input in (a), (c) sinusoidal input with frequency 2Hz and amplitude 0.01m, (d) comparison of the actual and calculated force corresponding to the sinusoidal input in (c)

To better observe the behavior of the nylon adaptive flywheel, two additional experiments were performed. First, experiments under three situations were carried out: maximum, minimum and variable (spring-driven) slider position, respectively. By using foamed plastic, the location of the sliders in the slots can be fixed at the maximum radius (the longest distance from the rotation center) and at the minimum radius (the shortest distance from the rotation center). The comparison is shown in **Figure 5.14** with sinusoidal input of frequency 1Hz and amplitude 0.005m.

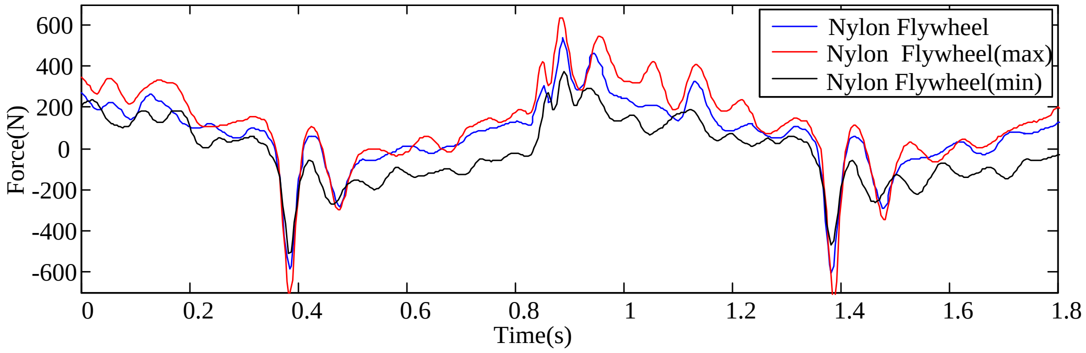

Figure 5.14 The comparison of three situations: variable, maximum, and minimum slider position

Based on the comparison of three configurations in **Figure 5.14**, it can be concluded that the adaptive nylon flywheel is capable of generating a variable inertia force, as predicted.

The relationship between the nylon adaptive flywheel with and without sliders was compared in another experiment. Instead of using the whole nylon adaptive flywheel, all the springs and sliders were removed. With a sinusoidal input of frequency 0.1Hz and amplitude 0.005m, the corresponding force vs time curves of the two configurations are shown for comparison in **Figure 5.15**.

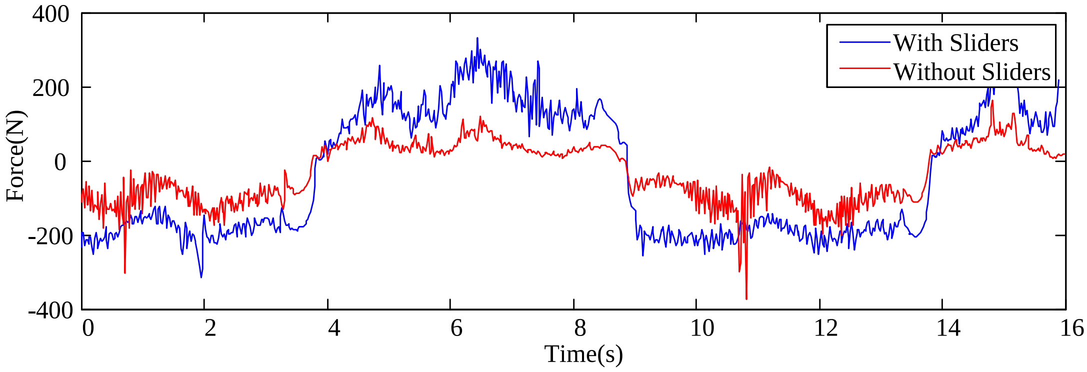

Figure 5.15 Comparison between nylon adaptive flywheel with and without sliders

As is shown in **Figure 5.15**, without all the sliders, the weight of the flywheel is reduced which eventually causes the decay of the inertia force. Another phenomenon that can be observed from the 8th to the 14th second in **Figure 5.15** is that the adaptive flywheel shows a certain ability to suppress the spike force which is caused by the hydraulic station and transmission backlash in the inverse screw.

5.3. Two-terminal hydraulic system with rectifier

In this chapter, experiments are carried out to verify the mathematical model of two-terminal devices. The close agreement between the experimental results and the calculated results based on the model indicates that the model is accurate. However, in all these experiments, there is always the inevitable problem of spike in the measured force. In the previous experiments, some key parameters were identified through experimental data. Even if most of the spikes in the data were eliminated during identification, the results will still be affected by the presence of the spikes. By reducing the spikes in the experiments, the accuracy of the key parameters will be improved, which leads to a more accurate mathematical model for the two-terminal hydraulic system.

As mentioned before, the spikes in the experiments are mainly caused by the hydraulic station and backlash in the two-terminal system. For a hydraulic station, the characteristics of the system are fixed after manufacture and calibration, which implies that it is almost impossible to eliminate the spikes by adjusting the hydraulic station. The only feasible way to reduce the spikes is to minimize the effect caused by backlash. Through improving the manufacturing precision, the transmission backlash in the inverse-screw system can be reduced. However, the cost of this two-terminal system will then increase dramatically.

For a hydraulic system, due to air in the hydraulic oil, the existence of backlash is inevitable. The air in the hydraulic system can be reduced by multiple ways, but they usually require an auxiliary device and a lot of time. Therefore, when the air in the hydraulic system reaches a relative low level, it will be much more difficult to minimize the backlash by further reducing the air in the hydraulic system. In the experiments performed herein, the spike force always appears when there is a change in movement direction. By adding a hydraulic rectifier to force the hydraulic motor to rotate in a single direction instead of constantly changing direction, the spike force can be reduced effectively. The prototype of the two-terminal hydraulic system with rectifier is shown in **Figure 5.16**.

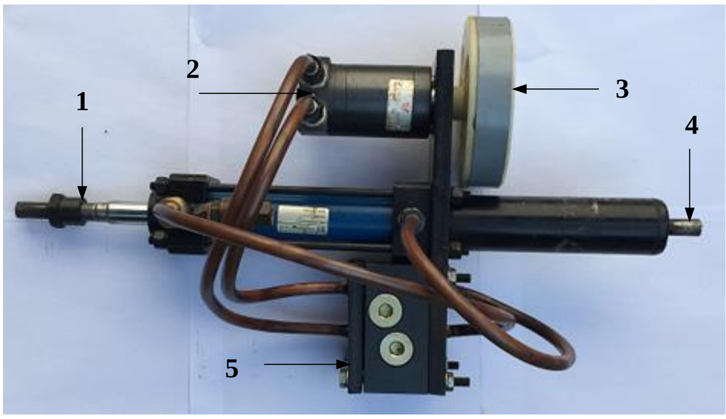

Figure 5.16 prototype of two-terminal hydraulic system with rectifier (Note: 1-terminal one 2- hydraulic motor 3-flywheel 4-terminal two 5-hydraulic rectifier)

The parameters of the new two-terminal hydraulic system with rectifier can be found in **Table 5.3**

Table 5.3 Specific parameters of the new two-terminal hydraulic system

No	Name	Notation	Specification
1	Travel of the piston		0.3 m
2	Maximum pressure		8 MPa
3	Cross-section area of the cylinder	A	0.00146 m^2
4	Displacement of the motor	H	1.1072×10^{-6} m^3/rad

As mentioned in chapter 3, in order to obtain a higher changing ratio, a light-density, high-strength material, nylon in this case, is used to manufacture the adaptive flywheel. However, due to its light weight, it will eventually lead to an insufficient inertial force in future applications with a two-terminal hydraulic system.

By re-designing the parameters of the nylon adaptive flywheel, the flywheel can generate enough inertial force for the two-terminal hydraulic system with rectifier. The schematic diagram of new nylon adaptive flywheel is shown **Figure 5.17**. The design of the new adaptive flywheel is identical to the design in Chapter 3. The only difference between these two designs is the actual value of those key parameters.

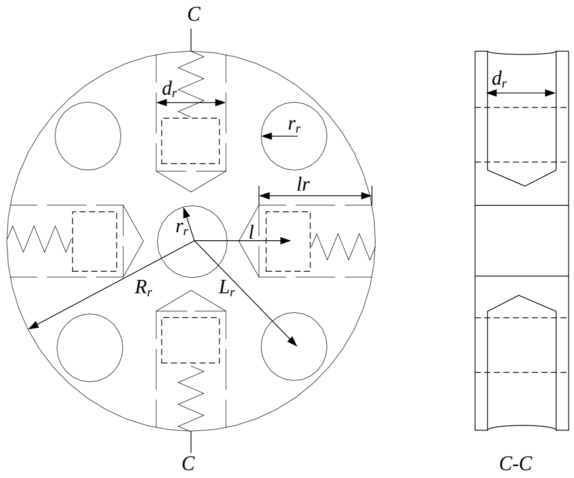

Figure 5.17 Schematic diagram of new nylon adaptive flywheel

The key parameters of this new adaptive flywheel can be found in **Table 5.4**

Table 5.4 Specific parameters of the new nylon adaptive flywheel

Name	**Notation**	**Specification**
Outer radius of flywheel	R_r	0.075m
Thickness of nylon disk	T_r	0.033m
Distance between hole and rotation center	L_r	0.056m
Radius of inner circle	r_{r1}	0.01m
Radius of holes in flywheel	r_{r2}	0.013m
Diameter of slots in flywheel	d_r	0.025m
Length of slots	l_{r1}	0.053m

Radius of sliders	r_{r3}	0.012m
Length of sliders	l_{r2}	0.022m
Mass of slider	m_{sr}	0.078kg
Density of PA66	ρ	1150kg/m^3
Stiffness of spring	k_{sr}	120N/m

The Letry electro hydraulic servo fatigue test machine PLN-20 was again used in the experiments. The experimental rig of the two-terminal hydraulic system with rectifier is shown in **Figure 5.18**. The specific parameters of this test machine can be found in **Table 5.2**.

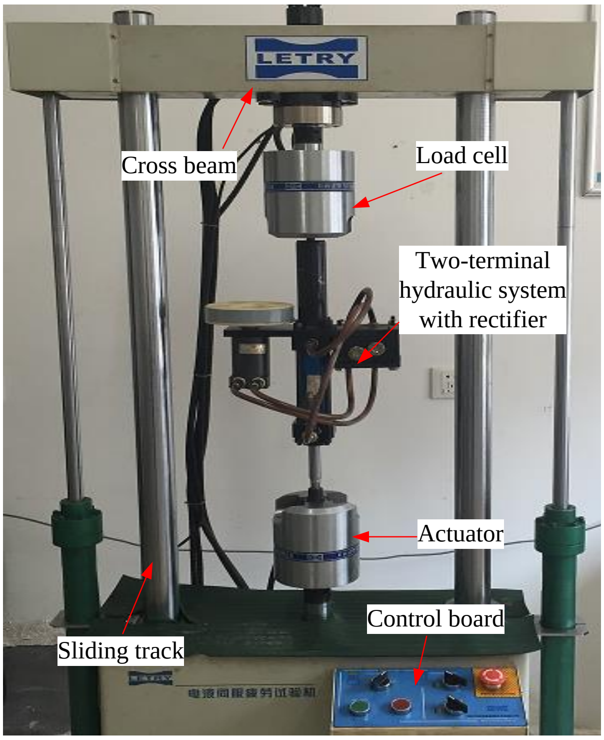

Figure 5.18 Experimental rig of two-terminal hydraulic system with rectifier

The first two sets of experiments were conducted without the adaptive flywheel.

The only difference in operating condition is with or without the hydraulic rectifier. Through these experiments, the effect caused by the rectifier can be isolated and verified. The results are shown in **Figure 5.19**. Additional experimental data can be found in Appendix B.

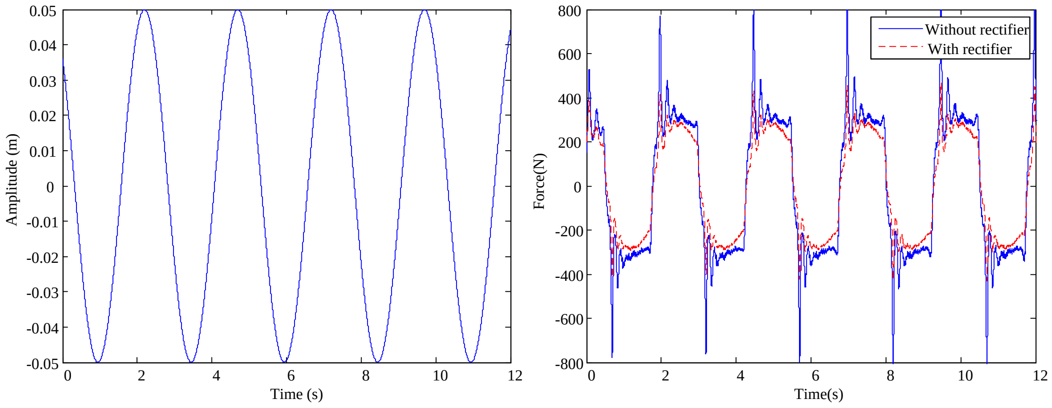

(a) (b)

Figure 5.19 Comparison of two-terminal hydraulic system with and without rectifier: (a) Sinusoidal input (frequency = 0.4Hz, and amplitude = 0.05m), and (b) Measured force of two-terminal hydraulic system with and without rectifier.

Figure 5.19 shows the comparison between the two-terminal hydraulic system with and without rectifier, and shows that the spike forces are smaller when the rectifier is applied. The results validate the effectiveness of rectifier in spike reduction.

By substituting equations (3.19)-(3.24) with the specific parameters given in **Table 5.4**, the moment of inertia of the new adaptive nylon flywheel I_{afr} can be calculated. Based on equation (3.11) and **Table 5.3**, the equivalent mass of the new adaptive nylon flywheel m_{er} can also be determined.

The same identification strategy as outlined in section 4.1 and 4.2 was applied to identify the key parameters for the new hydraulic system with rectifier. The three key parameters can be identified by:

$$\{f_r, c_r, k_r\} = \arg\min\left(\sqrt{\frac{1}{t_{er}-t_{sr}}\sum_{t=t_{sr}}^{t_{er}}\left(F_{mr}(t)-F_{tr}(t)\right)^2}\right) \tag{5.12}$$

where f_r is the force of friction of two-terminal hydraulic system, c_r represents the damping ratio, k_r is the stiffness of whole system, $F_{mr}(t)$ is the measured force, $F_{cr}(t)$ is the theoretically calculated force, t_{sr} is the start time of data recording, and t_{er} is the end time. Since the data are discrete, the above criterion can be rewritten as:

$$\{f_r, c_r, k_r\} = \arg\min\left(\sqrt{\frac{1}{n_{er}-1}\sum_{n=1}^{n_{er}}\left(F_{mr}(n) - F_{tr}(n)\right)^2}\right) \qquad (5.13)$$

where $F_{mr}(n)$ is the measured force and $F_{cr}(n)$ is the theoretically calculated force using equation (5.13) at sampling point n, and n_{er} is the last sampling point of the dataset. By using 15 datasets of sinusoidal inputs with frequency range from 0.1Hz to 5Hz and amplitude range from 0.005m to 0.015mm, parameters, f_r, k_r and c_r can be estimated as

$$c_r = 8100\,\text{Ns/m},\quad f_r = 240\,\text{N},\quad k_i = 9.89\times 10^5\,\text{N/m} \qquad (5.14)$$

After the determination of all four key parameters (equivalent mass m_{er}, friction of two-terminal hydraulic system f_r, damping ratio c_r and stiffness of whole system k_r respectively), the behavior of the new two-terminal hydraulic system with rectifier and nylon flywheel can be predicted. Two sinusoidal inputs with frequency 1Hz, amplitude 0.05m and frequency 0.2Hz, amplitude 0.15m are applied, the corresponding comparison of actual measured force and theoretical calculated force are shown in **Figure 5.20**.

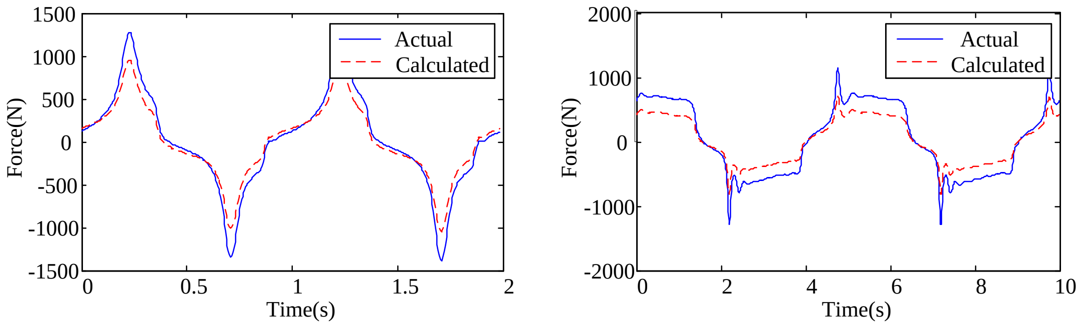

(a) (b)

Figure 5.20 Comparison between actual measured force and theoretically calculated force: (a) Force corresponding to sinusoidal inputs with frequency 1Hz, amplitude 0.05m, and (b) Force corresponding to sinusoidal inputs with frequency 0.2Hz, amplitude 0.15m.

Compared to the two-terminal hydraulic system without rectifier, the new mathematical model obtained with the two-terminal hydraulic system with rectifier (**Figure 5.20**) shows better agreement with the experimental data, which indicates that the identified key parameters are more accurate.

5.4. Conclusion

In this chapter, key parameters for both the two-terminal hydraulic system and inverse screw system were identified via experimental studies. Additional experiments were also carried out to verify the accuracy of these parameters and mathematical models. The close agreement between theoretical and measured forces validates the accuracy of both systems. In both experiments, spike forces were observed, which are caused by the backlash. In order to minimize the spike forces during the experiments, a hydraulic rectifier was required in the experiments. By adding the hydraulic rectifier, the spike forces in two-terminal hydraulic system was reduced, which led to more accurate key parameters and mathematical model.

6. Application of hydraulic two-terminal device with adaptive flywheel to suspension system

In Chapter 4, three different suspension systems were evaluated under ideal conditions. In this chapter, instead of an ideal hydraulic two-terminal device, a modified model of the hydraulic two-terminal device (referred to as an “actual” hydraulic two-terminal device) is applied to the suspension system. The reason for this approach is to be able to understand the factors that affect the performance of the proposed designed systems. The key parameters of the hydraulic system have been identified in Chapter 5. Therefore, another two suspension systems are introduced, which are the suspension system consisting of a two-terminal device without adaptive flywheel (suspension system A) and suspension system consisting of a two-terminal device with adaptive flywheel (suspension system B). Performance criteria are applied to evaluate these two suspension systems, and comparisons are carried out between them and a traditional suspension system with no flywheel. Finally, the performance of suspension system B with different changing ratio is discussed, and an optimal changing ratio is determined under certain circumstances.

6.1. Mathematical models for the suspension systems

In this chapter, rather than the two-terminal inverse screw system, the two-terminal hydraulic system is chosen for two reasons. First, since the ideal two-terminal hydraulic system was chosen for simulation in chapter 4, a two-terminal hydraulic system is also chosen here for consistence and fair comparison. The second reason is the application environment. For application to a suspension system, the frequency of the vibrations can be quite high, which will lead to abrasion of a screw transmission. Under this situation, the inverse screw system can be damaged in a short period of time.

To isolate the behavior of the adaptive flywheel, a new suspension system model is required. Therefore, as shown in **Figure 6.1**, suspension system A is introduced. Compared to a traditional suspension system, a hydraulic two-terminal system must also be added between the tire and vehicle body in suspension system A.

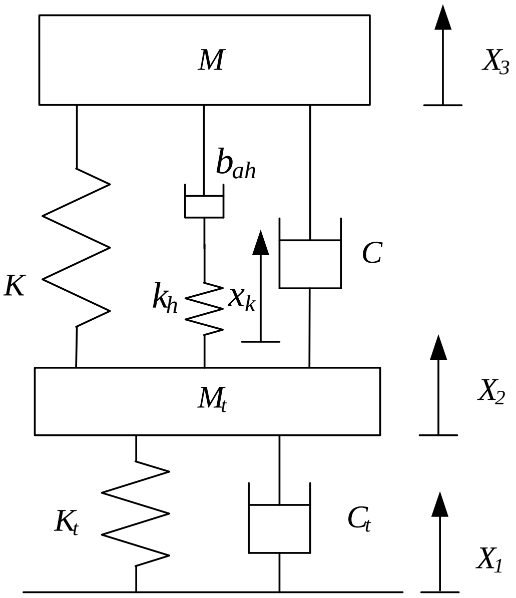

Figure 6.1 Suspension system A

From **Figure 6.1**, the mathematical model of suspension system A can be written as:

$$\begin{cases} M\ddot{X}_3 + K(X_3 - X_2) + C(\dot{X}_3 - \dot{X}_2) + b_{ah}(\dot{X}_3 - \dot{X}_2 - \dot{x}_k) = 0 \\ M_t\ddot{X}_2 + K_t(X_2 - X_1) + C_t(\dot{X}_2 - \dot{X}_1) - K(X_3 - X_2) - C(\dot{X}_3 - \dot{X}_2) - k_h x_k = 0 \\ k_h x_k = b_{ah}(\dot{X}_3 - \dot{X}_2 - \dot{x}_k) + F_{fh}\,\mathrm{sgn}(X_3 - X_2) \end{cases} \tag{6.1}$$

In equation (6.1), M is the weight of quarter car and one passenger, K represents the stiffness of suspension system, C is the damping ratio of suspension system, b_{ah} is the damping ratio of two-terminal hydraulic system, k_h is the stiffness of the two-terminal hydraulic system, and x_k is the elastic deformation of the two-terminal hydraulic system, K_t is the stiffness of the tire, C_t is the damping coefficient of the tire, X_1 is the road vertical displacement, X_2 is the displacement of the unsprung mass (mass not supported by the suspension), X_3 represents the displacement of the sprung mass (all combined masses that are supported by the suspension).

In **Figure 6.2**, suspension system B is shown. Compared to suspension system A, an adaptive flywheel is mounted on a hydraulic two-terminal system in this suspension system. The performance evaluation of this suspension system will indicate the relative advantage of the hydraulic two-terminal system with an adaptive flywheel.

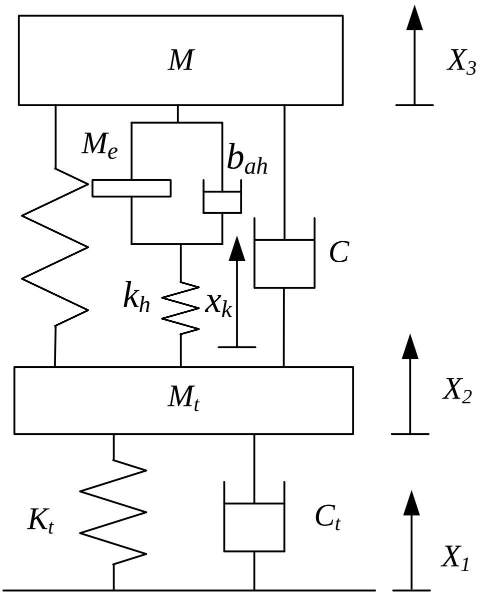

Figure 6.2 Suspension system B

Based on **Figure 6.2**, the mathematical model of suspension system B can be presented as:

$$\begin{cases} M\ddot{X}_3 + M_e(\ddot{X}_3 - \ddot{X}_2 - \ddot{x}_k) + K(X_3 - X_2) + C(\dot{X}_3 - \dot{X}_2) + b_{ah}(\dot{X}_3 - \dot{X}_2 - \dot{x}_k) = 0 \\ M_t\ddot{X}_2 + K_t(X_2 - X_1) + C_t(\dot{X}_2 - \dot{X}_1) - K(X_3 - X_2) - C(\dot{X}_3 - \dot{X}_2) - k_h x_k = 0 \\ k_h x_k = M_e(\ddot{X}_3 - \ddot{X}_2 - \ddot{x}_k) + b_{ah}(\dot{X}_3 - \dot{X}_2 - \dot{x}_k) + F_{fh} \end{cases} \tag{6.2}$$

6.2. Performance evaluation

As indicated earlier, due to the non-linearity of the adaptive flywheel, the transfer function of suspension system B cannot be obtained in closed form. Therefore, the same performance criteria will be introduced to evaluate suspension system A and suspension system B as previously used, which are riding comfort, tire grip and vehicle body deflection. The same simulation strategy as used in Chapter 4 is applied to the performance evaluation, which implies that the static moment of inertia of the nylon adaptive flywheel is still set at $I_{afn,\min} = 2.231 \times 10^{-4} kg.m^2$ and the other key parameters of these two suspension systems can be obtained from equation (4.16). The parameters of the hydraulic two-terminal system were identified in Chapter 5.

6.2.1. Riding comfort

Riding comfort is one of the most important performance criteria for a suspension system. Due to the non-linearity of suspension system B, equation (4.12) cannot be applied to evaluate the riding comfort of suspension system B. However, weighted root mean square acceleration is considered as a key index to judge the riding comfort when the velocity of the car is fixed, and this is expressed in meters per second squared (m/s^2) for translational vibrations. Based on equation (4.15), the weighted root mean square acceleration of suspension system A and B can be determined.

Similar to Chapter 4, three different excitations are applied to simulate the road surface, which are zero input, impulse input and sinusoidal input, respectively.

6.2.1.1. Zero input

An initial displacement of 0.05m is applied to the three suspension systems, which are traditional suspension system, suspension system A and suspension system

B. Through the combination of equation (4.1), (4.15), (6.1) and (6.2), the numerical solution of the weighted root mean square acceleration for each suspension system in the time-domain can be calculated through Matlab. The results of this simulation are shown in **Table 6.1** as the vehicle body mass is varied.

Table 6.1 Weighted root mean square acceleration with zero input

Vehicle body mass M_v (kg)	**Weighted accelerations of traditional suspension system a_w(m/s^2)**	**Weighted accelerations of suspension system A a_w(m/s^2)**	**Weighted accelerations of suspension system B a_w(m/s^2)**
340	0.4656	0.3749	0.2879
350	0.4524	0.3643	0.2847
360	0.4397	0.3571	0.2813
370	0.4288	0.3493	0.2779
380	0.4154	0.3425	0.2741
390	0.3996	0.3359	0.2707
400	0.3878	0.3187	0.2671

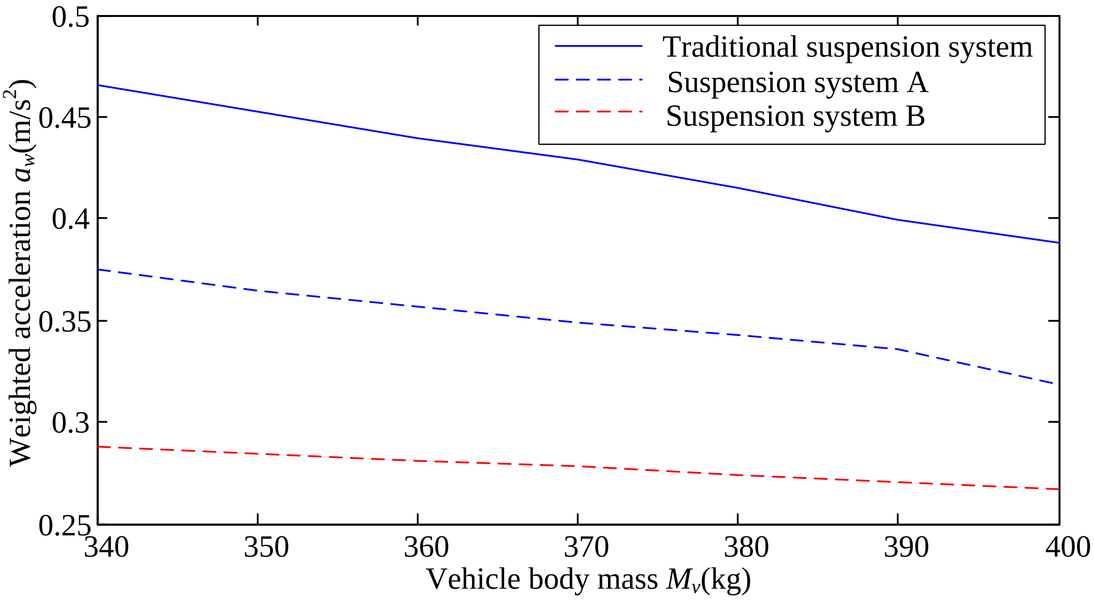

Figure 6.3 Weighted root mean square acceleration with zero input

Figure 6.3 shows the weighted root mean square acceleration of three suspension systems under zero input. The weighted root mean square acceleration of suspension system B is smaller than other two suspension systems under the same vehicle body mass, which implies that the suspension system B outperforms both traditional suspension system and suspension system A. Compared to results in **Table 4.1,** the same trends can be found in **Table 6.1**, with the increasing of vehicle body mass, the riding comfort improves. However, suspension system B shows better performance than the AFW suspension system in chapter 4 for riding comfort. Since the weighted root mean square acceleration of suspension system A is smaller than the traditional suspension system, which means, in addition to the adaptive flywheel, the two-terminal hydraulic system also improves riding comfort.

6.2.1.2. Impulse input

An impulse input with amplitude of 0.05m is applied to each suspension system. Using the same mathematical model, the results can be determined by Matlab and are shown in **Table 6.2**.

Table 6.2 Weighted root mean square acceleration with impulse input

Vehicle body mass M_v (kg)	**Weighted accelerations of traditional suspension system**	**Weighted accelerations of suspension system A a_w(m/s^2)**	**Weighted accelerations of suspension system B a_w(m/s^2)**
340	0.4878	0.3728	0.2589
350	0.4684	0.3614	0.2557
360	0.4546	0.3519	0.2521
370	0.4398	0.3432	0.2487

380	0.4264	0.3353	0.2459
390	0.4112	0.3281	0.2427
400	0.3986	0.3216	0.2384

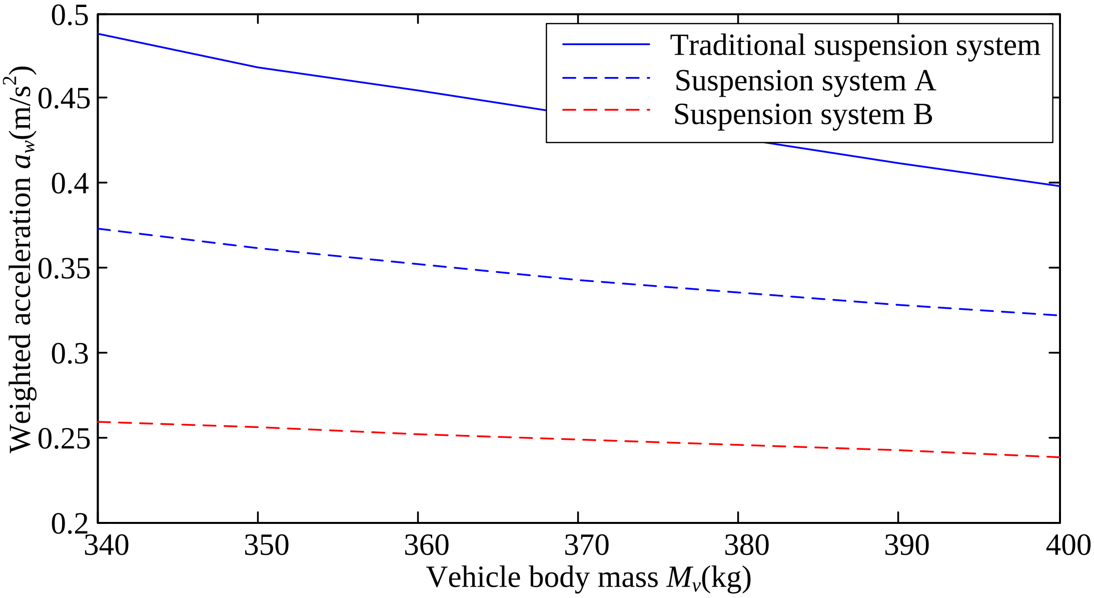

Figure 6.4 Weighted root mean square acceleration with impulse input

Figure 6.4 shows the weighted root mean square acceleration of the three suspension systems under impulse input. The weighted root mean square acceleration of suspension system B is the smallest of the three suspension systems under the same vehicle body mass, which indicates that suspension system B shows better performance than the other two suspension systems. By comparing results between **Table 4.2** and **Table 6.2**, the results are similar to the results under zero input. That is, with the increase in vehicle body mass, the riding comfort improves in both the AFW suspension system and suspension system B. However, with the two-terminal hydraulic system, suspension system B out-performs the AFW suspension system in riding comfort.

6.2.1.3. Sinusoidal input

To simulate a rough road situation, a sinusoidal input with wave length of 4m, amplitude 0.05m and frequency 5Hz is applied to each suspension system. The results of simulation can be found in **Table 6.3**

Table 6.3 Weighted root mean square acceleration with sinusoidal input

Vehicle body mass M_v (kg)	**Weighted accelerations of traditional suspension system**	**Weighted accelerations of suspension system A a_w(m/s^2)**	**Weighted accelerations of suspension system B a_w(m/s^2)**
340	1.9786	1.7453	1.8497
350	1.8498	1.6231	1.7549
360	1.7249	1.5107	1.6643
370	1.6256	1.3891	1.4989
380	1.5143	1.2797	1.3658
390	1.3983	1.1789	1.2873
400	1.2964	1.0813	1.1847

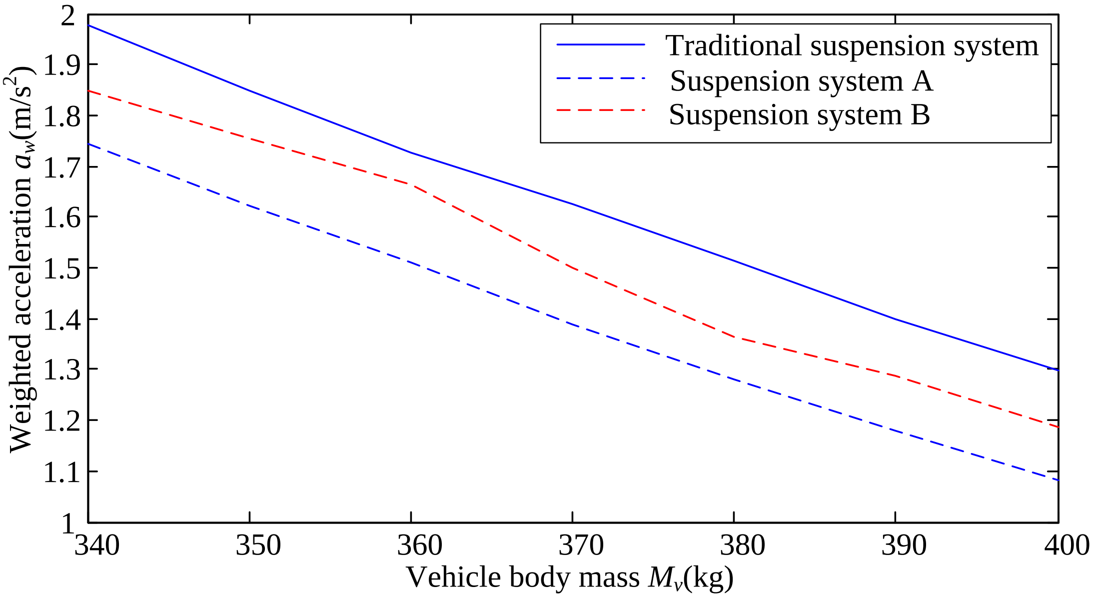

Figure 6.5 Weighted root mean square acceleration with sinusoidal input

As shown in **Figure 6.5**, with sinusoidal input, the results of the three suspension systems in this case are different than with the two other inputs. Here, the weighted root mean square acceleration of suspension system B is larger than suspension system A, but smaller than with the traditional suspension. This result implies that suspension system B gives the middle performance of the three chosen suspension systems under the case of a sinusoidal input. The results in **Table 4.3** show that suspension system B is better than the AFW suspension system in riding comfort. However, based on **Table 6.3**, suspension system A out-performs suspension system B. Therefore, the better riding comfort of suspension system B is due to the two-terminal hydraulic system.

6.2.2. Tire grip

As a key criterion to indicate the ride safety of a vehicle, tire grip index is another important factor to evaluate the performance of a suspension system. Due to the non-linearity of suspension system B, the tire grip index is defined as the ratio between static and dynamic loads, which can be calculated via equation (4.21). The same simulation strategy as used in Chapter 4 is applied to these comparison simulations.

6.2.2.1. Zero input

An initial displacement 0.05m is applied to the three suspension systems. The results can be found in **Table 6.4**.

Table 6.4 Weighted root mean square tire grip index with zero input

Vehicle body mass M_v (kg)	**Weighted tire grip index of traditional suspension system M_{wtg}**	**Weighted tire grip index of suspension system A M_{wtg}**	**Weighted tire grip index of suspension system B M_{wtg}**

340	0.3156	0.2892	0.0642
350	0.3012	0.2817	0.0627
360	0.2874	0.2743	0.0611
370	0.2756	0.2655	0.0596
380	0.2649	0.2574	0.0583
390	0.2551	0.2496	0.0570
400	0.2462	0.2427	0.0556

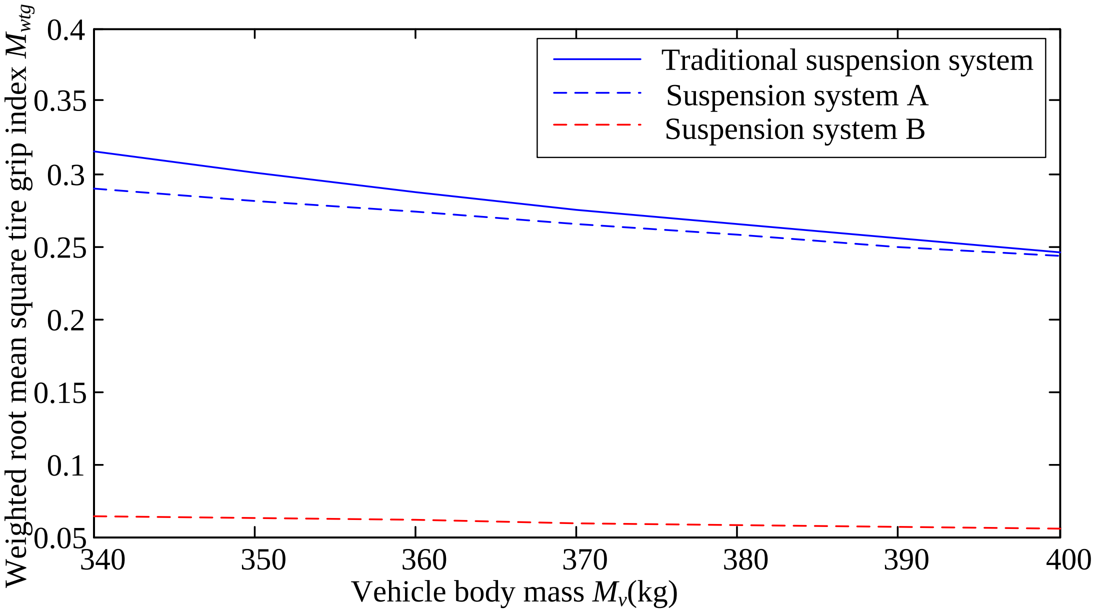

Figure 6.6 Weighted root mean square tire grip index with zero input

In **Figure 6.6**, weighted root mean square tire grip index of the three suspension systems under zero input are shown. Compared to the other two suspension systems, the weighted root mean square tire grip index of the suspension system B is the smallest. According to equation (4.20) the smaller weighted root mean square tire grip index implies a higher vehicle safety, therefore suspension system B shows a better outcome than both the other suspension systems under this condition. Based on **Table 4.4** and **Table 6.4,** the difference of the weighted root mean square tire grip index between suspension system B and AFW suspension system is small, suspension system B shows a slight improvement due to the presence of the two-terminal hydraulic system.

6.2.2.2. Impulse input

An impulse input with amplitude of 0.05m is applied to each suspension system. The results are shown in **Table 6.5**.

Table 6.5 Weighted root mean square tire grip index with impulse input

Vehicle body mass M_v **(kg)**	**Weighted tire grip index of traditional suspension system** M_{wtg}	**Weighted tire grip index of suspension system A** M_{wtg}	**Weighted tire grip index of suspension system B** M_{wtg}
340	0.3879	0.3774	0.1139
350	0.3624	0.3541	0.1085
360	0.3412	0.3307	0.1027
370	0.3208	0.3119	0.0959
380	0.3001	0.2907	0.0897
390	0.2814	0.2716	0.0851
400	0.2628	0.2546	0.0804

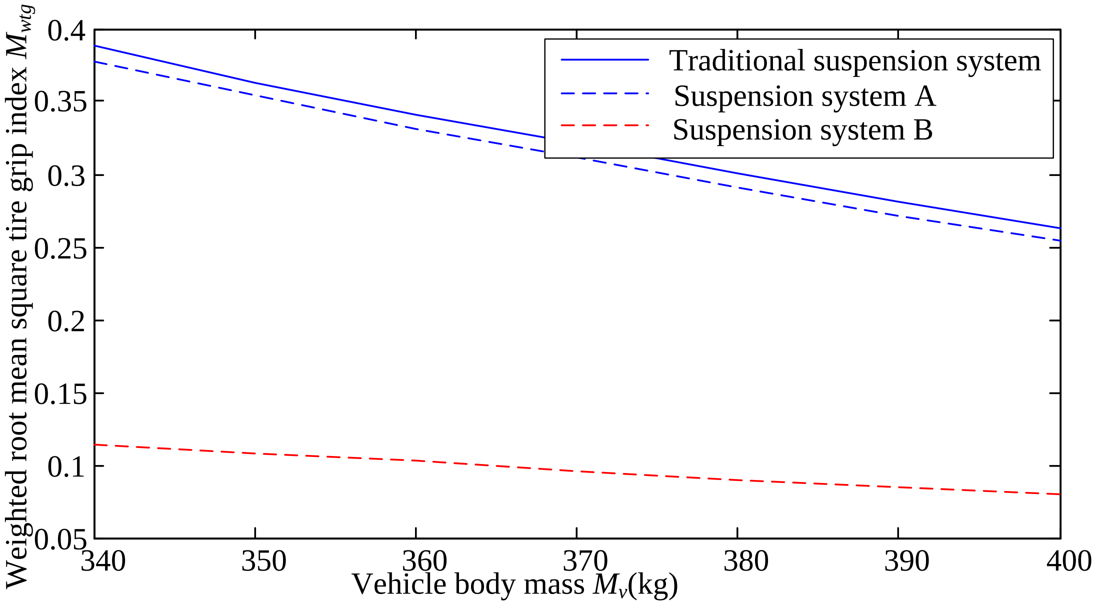

Figure 6.7 Weighted root mean square tire grip index with impulse input

Figure 6.7 shows the weighted root mean square tire grip index of three suspension systems with an impulse input. Since the weighted root mean square tire grip index of suspension system B is still the smallest of all three suspension systems under same vehicle body mass, it follows that it out-performs the suspension system A and the traditional suspension system. From **Table 4.5** in chapter 4 and **Table 6.5**, the same results as zero input can be found, suspension system B also shows a slight improvement over the AFW suspension system due to the two-terminal hydraulic system.

6.2.2.3. Sinusoidal input

A sinusoidal input with wave length of 4m, amplitude of 0.05m and a frequency of 5Hz is applied to each suspension system. The results are shown in **Table 6.6**.

Table 6.6 Weighted root mean square tire grip index with sinusoidal input

Vehicle body	**Weighted**	**Weighted tire**	**Weighted tire**

mass M_v (kg)	**tire grip index of traditional suspension system M_{wtg}**	**grip index of suspension system A M_{wtg}**	**grip index of suspension system B M_{wtg}**
340	0.8458	0.8334	0.4423
350	0.8014	0.7915	0.4178
360	0.7624	0.7525	0.3804
370	0.7256	0.7147	0.3489
380	0.6929	0.6709	0.3197
390	0.6614	0.6327	0.2917
400	0.6319	0.6103	0.2685

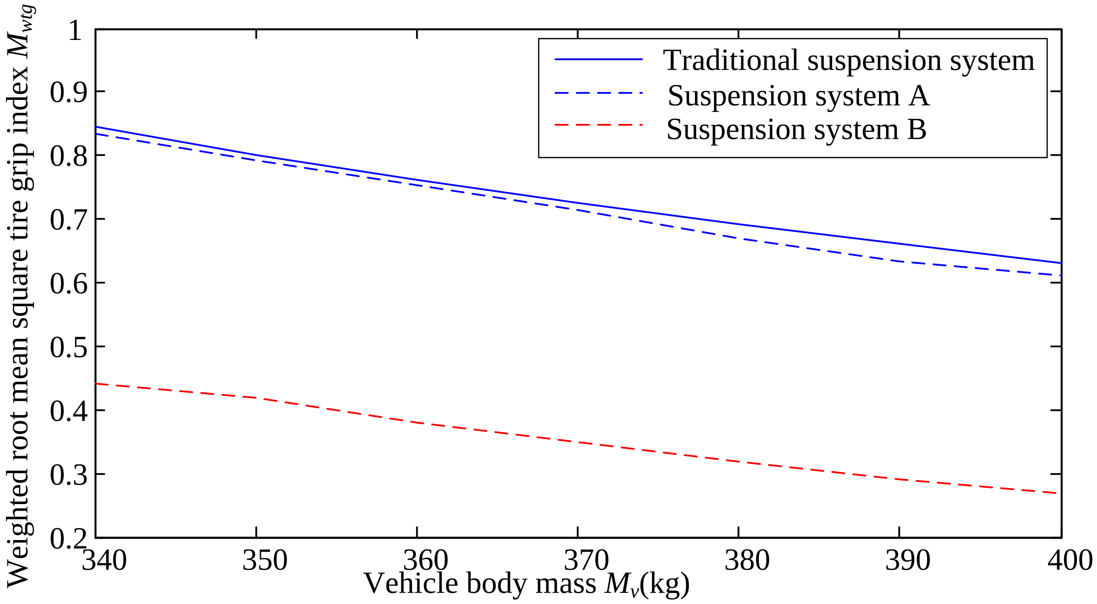

Figure 6.8 Weighted root mean square tire grip index with sinusoidal input

From **Figure 6.8**, under the same road conditions with the same velocity, and for the same vehicle body mass, suspension system B provides the smallest weighted root mean square tire grip index. Based on this, suspension system B provides higher safety performance than both the traditional suspension system and suspension system A. By comparing results in **Table 4.6** and **Table 6.6**, because of the application of two-terminal hydraulic system, suspension system B shows better performance than the AFW suspension system. However, the improvement of the suspension system performance is quite small.

6.2.3. Vehicle body deflection

The last performance criterion is the vehicle body deflection. Because of the non-linearity of suspension system B, equation (4.26) is introduced to calculate weighted root mean square vehicle body deflection for each suspension system. Similar to the simulations of riding comfort and tire grip index, three excitations will be applied to simulate different road situations.

6.2.3.1. Zero input

An initial displacement 0.05m is applied on the three suspension systems. The results are shown in **Table 6.7**.

Table 6.7 Weighted root mean square vehicle body deflection with zero input

Vehicle body mass M_v (kg)	**vehicle body deflections of traditional suspension system D_{fw}(m)**	**Weighted vehicle body deflections of suspension system A D_{fw}(m)**	**Weighted vehicle body deflections of suspension system B D_{fw}(m)**
340	0.0035	0.0021	0.0021
350	0.0035	0.0021	0.0021
360	0.0035	0.0021	0.0021
370	0.0035	0.0021	0.0020
380	0.0034	0.0020	0.0020
390	0.0034	0.0020	0.0020
400	0.0034	0.0020	0.0020

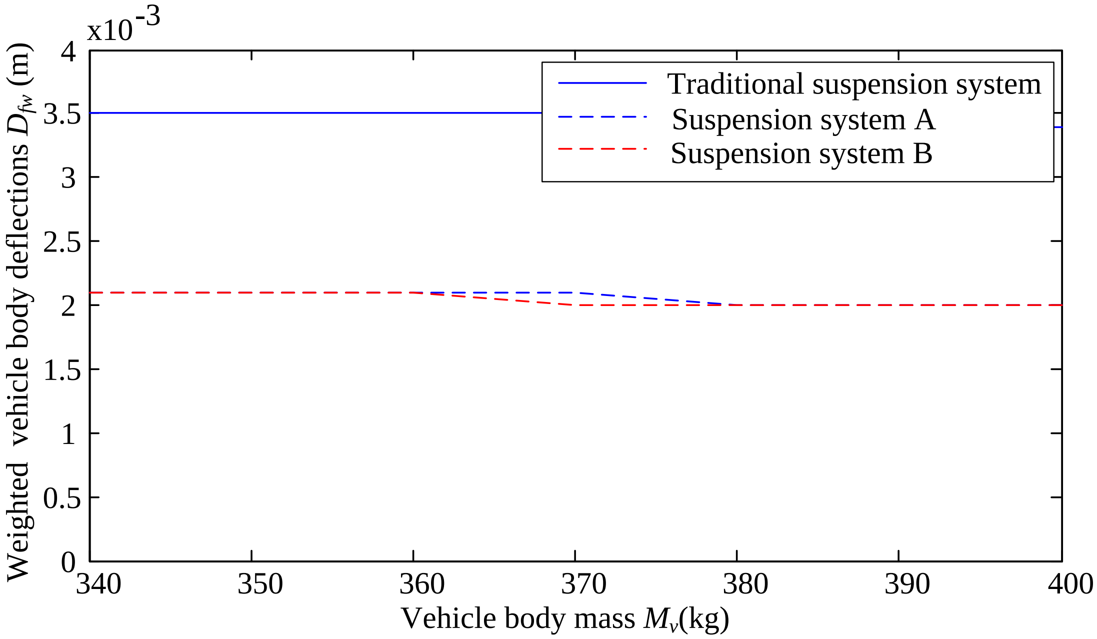

Figure 6.9 Weighted root mean square vehicle body deflection with zero input

Based on **Figure 6.9**, suspension system A and B show a smaller weighted root mean square vehicle body deflection than the traditional suspension system under zero input. However, the weighted root mean square vehicle body deflection of suspension system A and B are almost identical. This result implies that the proposed suspension system B shows no improvement compared to suspension system A, which also indicates that the adaptive flywheel shows no effect on the vehicle body deflection. Based on **Table 4.7** in chapter 4 and **Table 6.7**, suspension system B out-performs the AFW suspension system. However, suspension system A and suspension system B show almost identical results. Therefore, the improvement of suspension system B in vehicle body deflection is due to the two-terminal hydraulic system.

6.2.3.2. Impulse input

An impulse input with amplitude 0.05m is applied to each suspension system. The results are shown in **Table 6.8**.

Table 6.8 Weighted root mean square vehicle body deflection with impulse input

Vehicle body mass M_v (kg)	**vehicle body deflections of traditional suspension system D_{fw}(m)**	**Weighted vehicle body deflections of suspension system A D_{fw}(m)**	**Weighted vehicle body deflections of suspension system B D_{fw}(m)**
340	0.0031	0.0017	0.0017
350	0.0031	0.0017	0.0017
360	0.0031	0.0017	0.0017
370	0.0031	0.0016	0.0017
380	0.0031	0.0016	0.0016
390	0.0031	0.0016	0.0016
400	0.0031	0.0016	0.0016

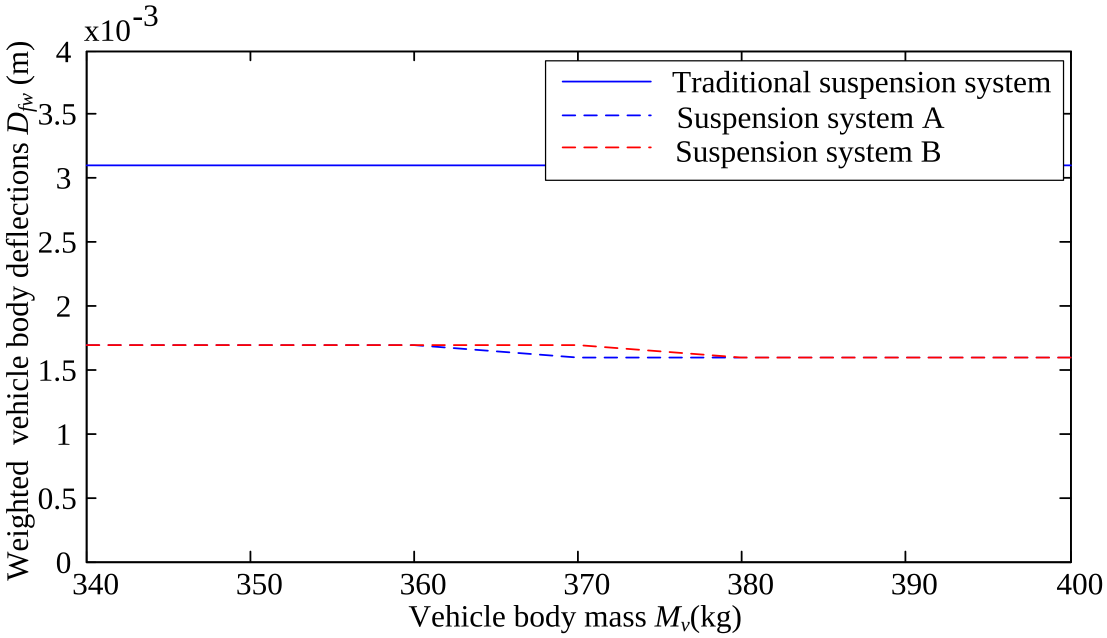

Figure 6.10 Weighted root mean square vehicle body deflection with impulse input

From **Figure 6.10**, the same results can be found as for the case of zero input. The weighted root mean square vehicle body deflection of suspension system A and B are almost identical, which is smaller than for the traditional suspension system. This result indicates that there is almost no performance difference for suspension system A and B; the adaptive flywheel shows no effect on vehicle body deflection under impulse input. By comparing **Table 4.8** in chapter 4 and **Table 6.8**, the same results under zero input can be found. Because of the application of the two-terminal hydraulic system, Suspension system B shows better performance than the traditional suspension system.

6.2.3.3. Sinusoidal input

A sinusoidal input with wave length 4m, amplitude 0.05m and frequency 5Hz is applied to each suspension system. The results are shown in **Table 6.9**.

Table 6.9 Weighted root mean square vehicle body deflection with sinusoidal input

Vehicle body mass M_v (kg)	**vehicle body deflections of traditional suspension system D_{fw}(m)**	**Weighted vehicle body deflections of suspension system A D_{fw}(m)**	**Weighted vehicle body deflections of suspension system B D_{fw}(m)**
340	0.0096	0.0077	0.0137
350	0.0095	0.0076	0.0132
360	0.0093	0.0074	0.0128
370	0.0091	0.0071	0.0122
380	0.0090	0.0071	0.0118
390	0.0088	0.0070	0.0113
400	0.0087	0.0069	0.0109

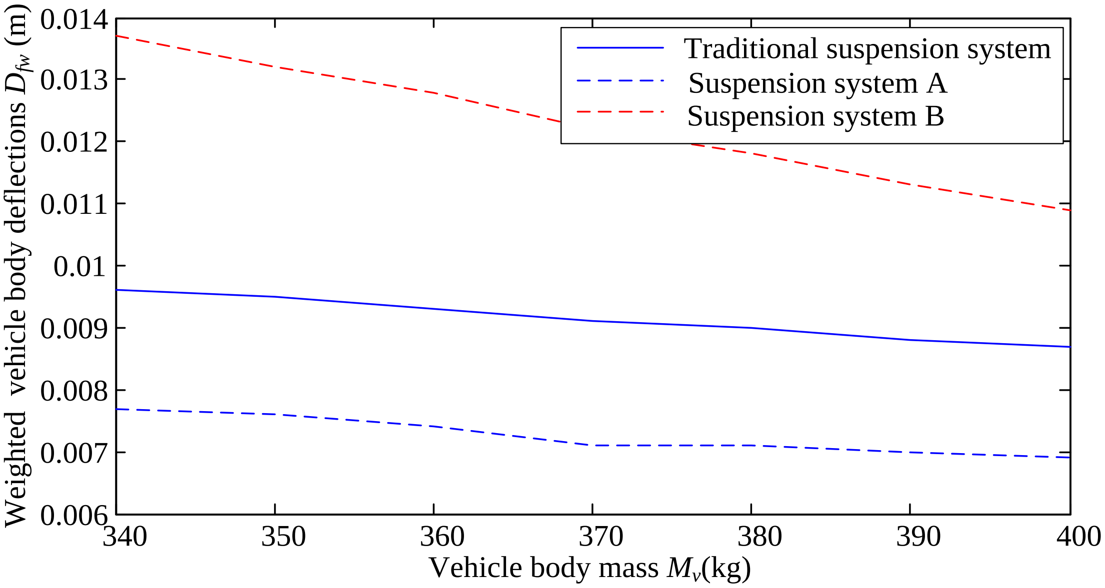

Figure 6.11 Weighted root mean square vehicle body deflection with sinusoidal input

Figure 6.11 shows the weighted root mean square vehicle body deflection of the three different suspension systems with sinusoidal input. The weighted root mean square vehicle body deflection of suspension system B is bigger than other two suspension systems, which implies that in this case, the traditional suspension system and the suspension system A show better results than the suspension system B.

Based on the results of chapter 4 and **Table 6.9**, the same trend can be found in all the suspension systems. With a higher vehicle body mass, the weighted root mean square vehicle body deflection is smaller. Suspension system B shows slightly better performance than the AFW suspension system, but worse performance than the traditional suspension systems. Therefore, the two-terminal hydraulic system provides better results in the weighted root mean square vehicle body deflection for suspension system B.

Comparing the results in **Table 6.1** to **Table 6.9** to those in chapter 4, despite the actual difference in numerical values; the trends with variable vehicle body mass in **Table 6.1** to **Table 6.9** remain generally the same.

6.3. Performance evaluation under different changing ratio

Based on the simulations in the previous subsection, suspension system B shows better performance under most road situations. To fully analyze the characteristics of suspension system B, more simulations need to be considered.

Similar to chapter 4, the changing ratio of the adaptive flywheel is the only variable in this simulation. The range of the changing ratio is varied from 5% to 55%, and vehicle body mass is kept at 370kg. Based on same initial conditions, three different excitations are applied as input, which are zero input, impulse input and sinusoidal input, respectively.

6.3.1. Zero input

Assume an initial displacement 0.05m is applied to the suspension system B, then the only variable is the changing ratio of the adaptive flywheel. The results of simulation for various changing ratios are shown in **Table 6.10**.

Table 6.10 Performance with different changing ratio under zero input

Changing ratio of moment of inertia (%)	Weighted accelerations of suspension system B a_w(m/s^2)	Weighted tire grip index of suspension system B M_{wtg}	Weighted vehicle body deflections of suspension system B D_{fw}(m)
Index value of traditional suspension system	0.4288	0.2756	0.0035
5	0.3197	0.1665	0.0021
10	0.3125	0.1584	0.0022
15	0.3038	0.1277	0.0020
20	0.2940	0.1060	0.0020
25	0.2831	0. 0822	0.0021
30	0.2708	0.0569	0.0020
35	0.2581	0.0451	0.0021
40	0.2467	0.0392	0.0020
45	0.2371	0.0361	0.0022
50	0.2284	0.0335	0.0021
55	0.2211	0.0319	0.0021

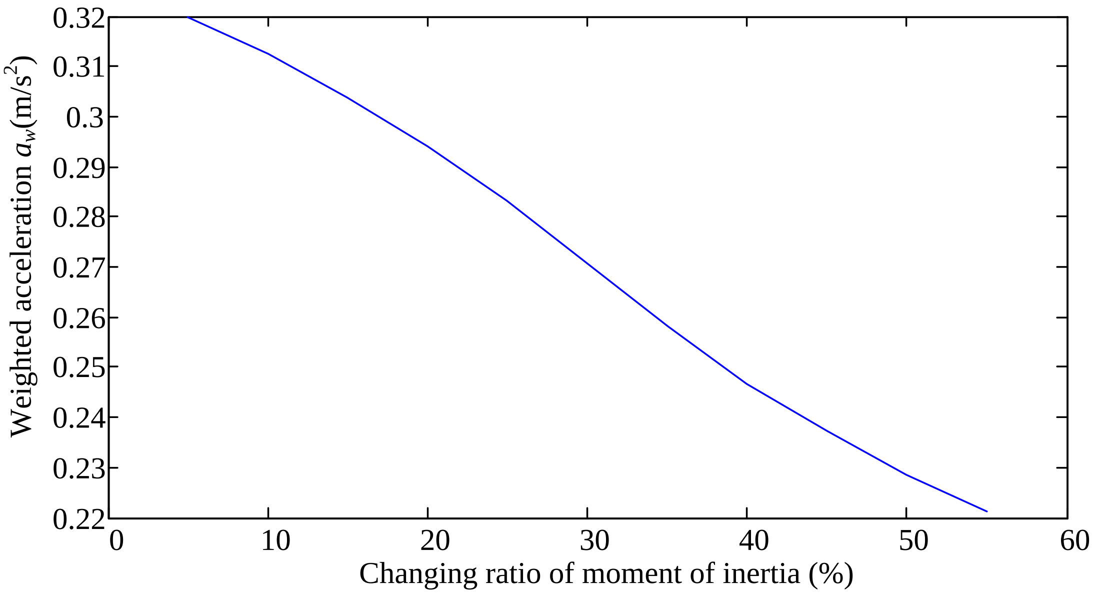

Figure 6.12 Weighted accelerations of suspension system B with different changing ratio under zero input

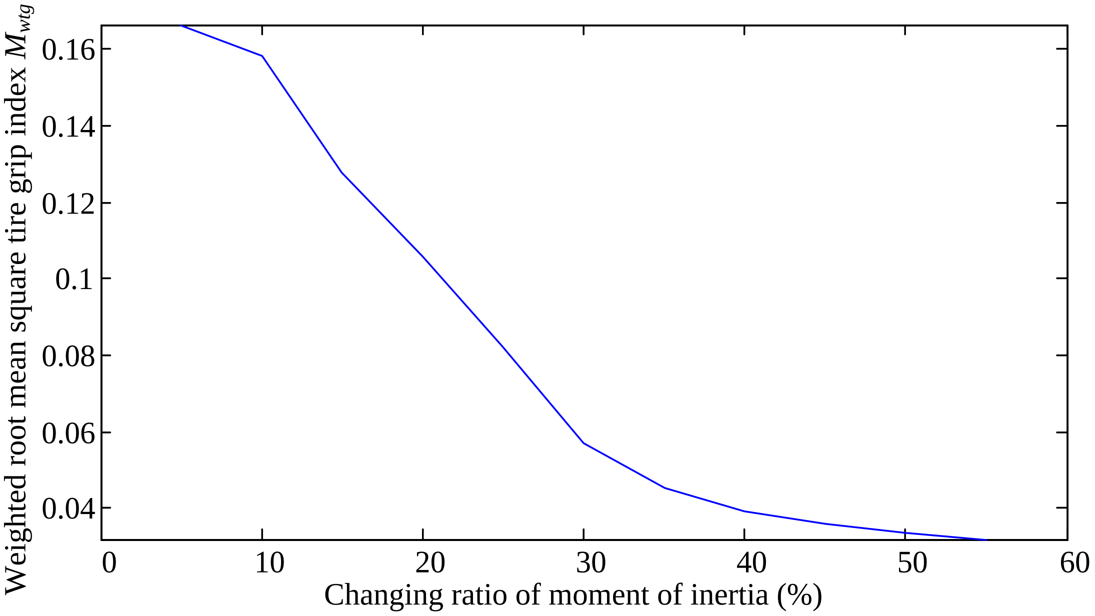

Figure 6.13 Weighted tire grip index of suspension system B with different changing ratio under zero input

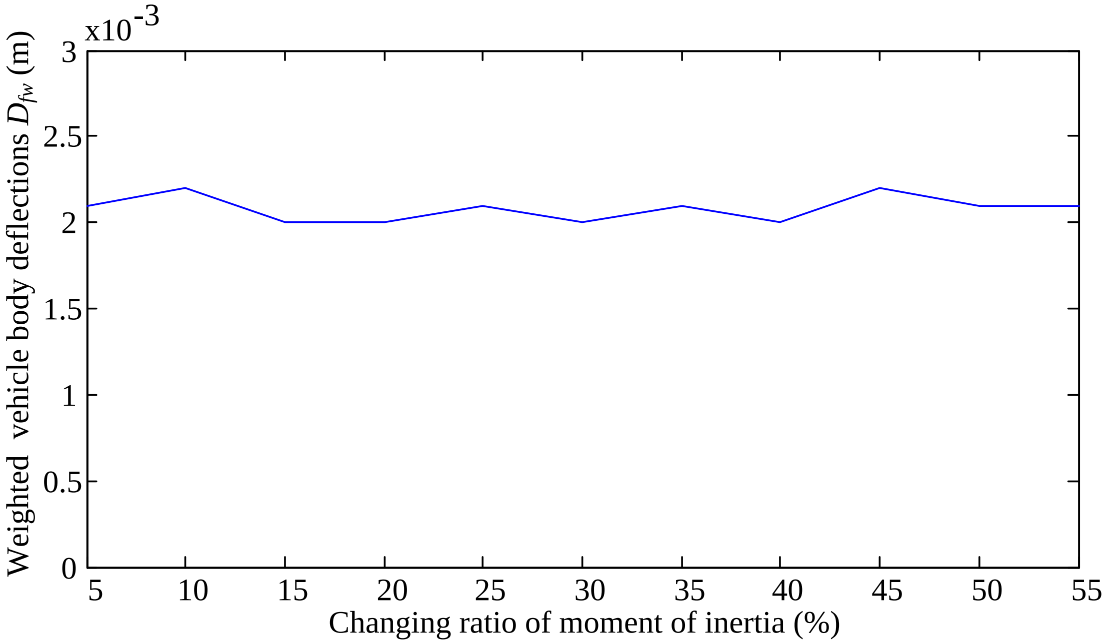

Figure 6.14 Weighted vehicle body deflections of suspension system B with different changing ratio under zero input

Figure 6.12 shows the weighted accelerations of suspension system B with different changing ratio under zero input and shows that the weighted accelerations will decrease when the changing ratio of the adaptive flywheel increases. This implies that with higher changing ratio, the riding comfort will also improve. **Figure 6.13** shows the weighted tire grip index of suspension B system with different changing ratio under zero input. With higher changings ratio, the index will decrease, which also implies an improvement of vehicle safety. **Figure 6.14** is the weighted vehicle body deflections of AFW suspension system with different changing ratio under zero input. Based the results of **Figure 6.14**, the weighted vehicle body deflections of AFW suspension system, are not affected by the increasing changing ratio of the adaptive flywheel. The trends in **Table 6.10** is the same as **Table 4.10.**

By comparing **Table 4.10** in chapter 4 and **Table 6.10**, under the same changing ratio of adaptive flywheel, suspension system B shows better performance than AFW suspension system in all three performance criteria, which are riding comfort, tire grip and vehicle body deflection respectively. Based on the discussion mentioned above, the improvement of suspension system B is due to the application of two-terminal hydraulic system.

6.3.2. Impulse input

In this simulation, an impulse input with amplitude 0.05m is applied, the results of simulation for various changing ratios are shown in **Table 6.11**.

Table 6.11 Performance with different changing ratio under impulse input

Changing ratio of moment of inertia (%)	Weighted accelerations of suspension system B a_w(m/s^2)	Weighted tire grip index of suspension system B M_{wtg}	Weighted vehicle body deflections of suspension system B D_{fw}(m)
Index value of traditional suspension system	0.4398	0.3208	0.0031
5	0.2975	0.1673	0.0017
10	0.2877	0.1567	0.0017
15	0.2769	0.1451	0.0018
20	0.2657	0.1299	0.0018
25	0.2539	0.1152	0.0018
30	0.2409	0.0938	0.0017
35	0.2258	0.0796	0.0019
40	0.2109	0.0675	0.0019
45	0.1963	0.0573	0.0017

50	0.1846	0.0495	0.0017
55	0.1739	0.0279	0.0017

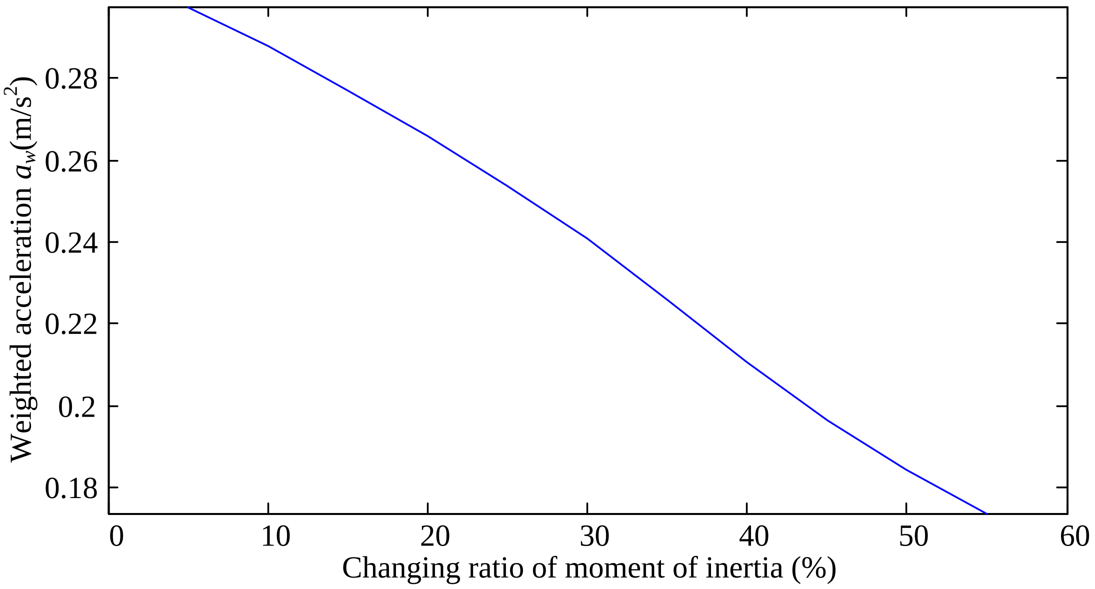

Figure 6.15 Weighted accelerations of suspension system B with different changing ratio under impulse input

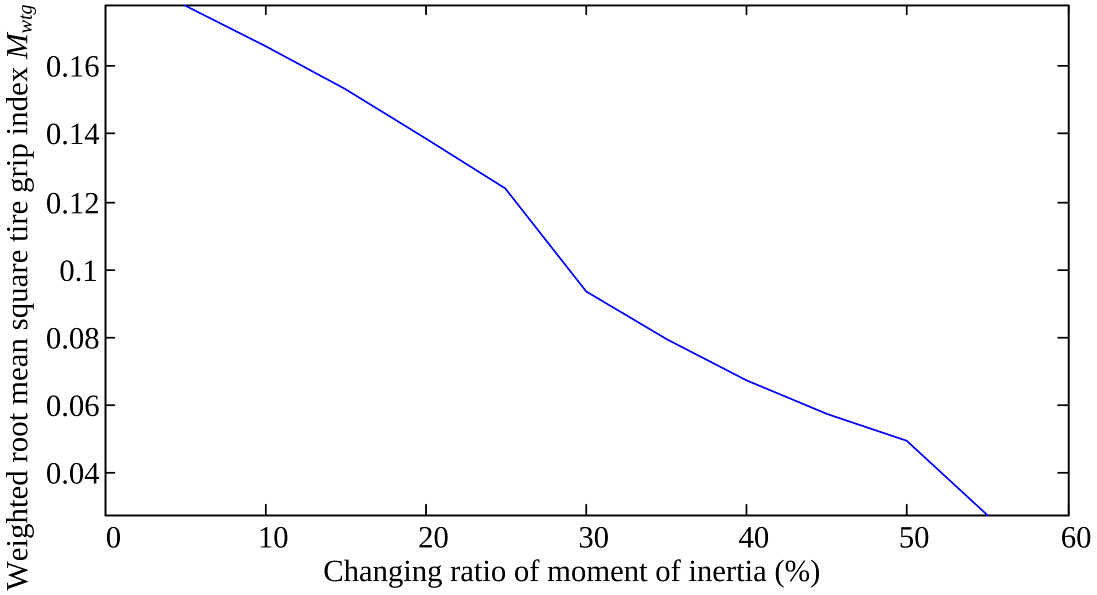

Figure 6.16 Weighted tire grip index of suspension system B with different changing ratio under impulse input

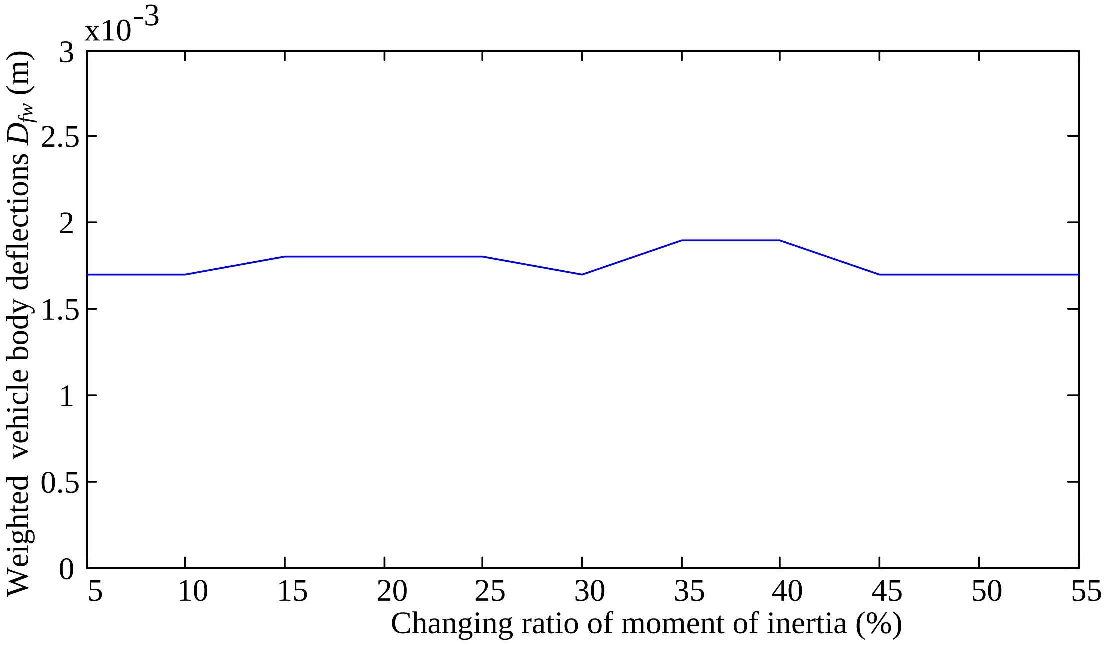

Figure 6.17 Weighted vehicle body deflections of suspension system B with different changing ratio under impulse input

Figure 6.15 shows the relationship between the weighted accelerations of the suspension system B and different changing ratios of the adaptive flywheel under an impulse input. With an increase in the changing ratio of the adaptive flywheel, the weighted acceleration will decrease. This result indicates that a higher changing ratio of the adaptive flywheel will improve riding comfort. **Figure 6.16** is the weighted tire grip index of suspension system B with different changing ratio under impulse input. This shows that the weighted tire grip index will decrease with increasing the changing ratio, which implies that vehicle safety improves under increasing changing ratio. **Figure 6.17** is the weighted vehicle body deflections of suspension system B with different changing ratio under impulse input. With the variable changing ratio, the weighted vehicle body deflections of suspension system B is almost the same. Based on this, the changing ratio of the adaptive flywheel does not affect the weighted vehicle body deflections of suspension system B. The same results as for zero input can be found between **Table 4.11** in chapter 4 and **Table 6.11**. Due to the application of two-terminal hydraulic system, suspension system B out-performs AFW suspension system for all three performance criteria.

6.3.3. Sinusoidal input

A sinusoidal input with amplitude 0.05m and frequency 5Hz is applied as excitation similar to the last simulation. Results about this simulation are shown in **Table 6.12**.

Table 6.12 Performance with different changing ratio under sinusoidal input

Changing ratio of moment of inertia (%)	Weighted accelerations of suspension system B a_w(m/s^2)	Weighted tire grip index of suspension system B M_{wtg}	Weighted vehicle body deflections of suspension system B D_{fw}(m)
Index value of traditional suspension system	1.6256	0.7256	0.0091
5	1.0377	0.5351	0.0121
10	1.2476	0.4946	0.0121
15	1.2689	0.4607	0.0121
20	1.3011	0.4246	0.0123
25	1.3446	0.3899	0.0123
30	1.4087	0.3379	0.0122
35	1.4623	0.2320	0.0122
40	1.5089	0.1101	0.0122
45	1.5477	0.0816	0.0121

50	1.5746	0.0608	0.0121
55	1.5973	0.0551	0.0121

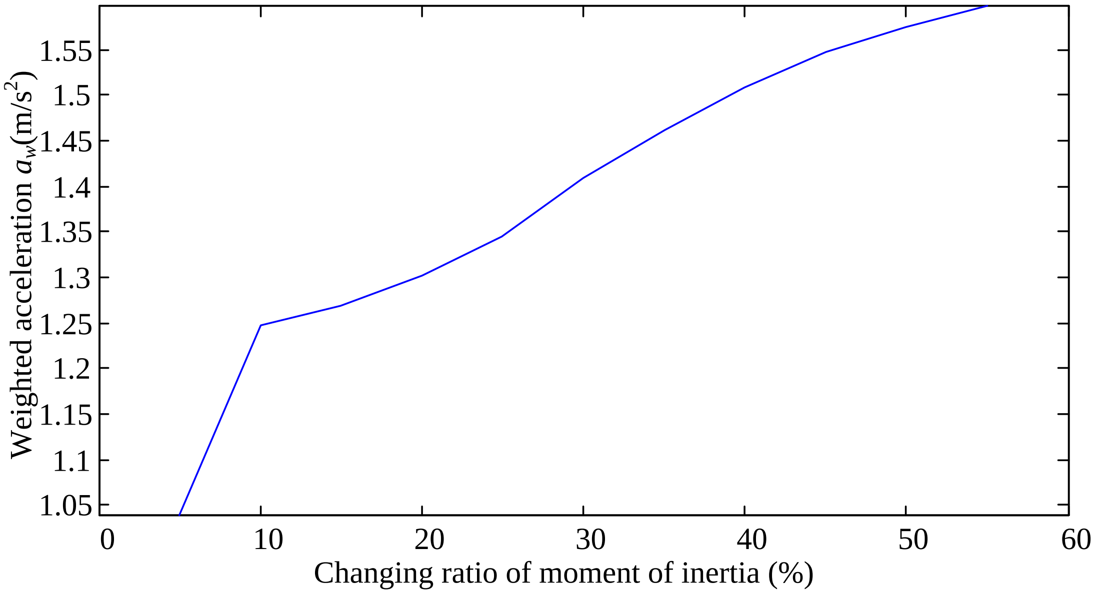

Figure 6.18 Weighted accelerations of suspension system B with different changing ratio under sinusoidal input

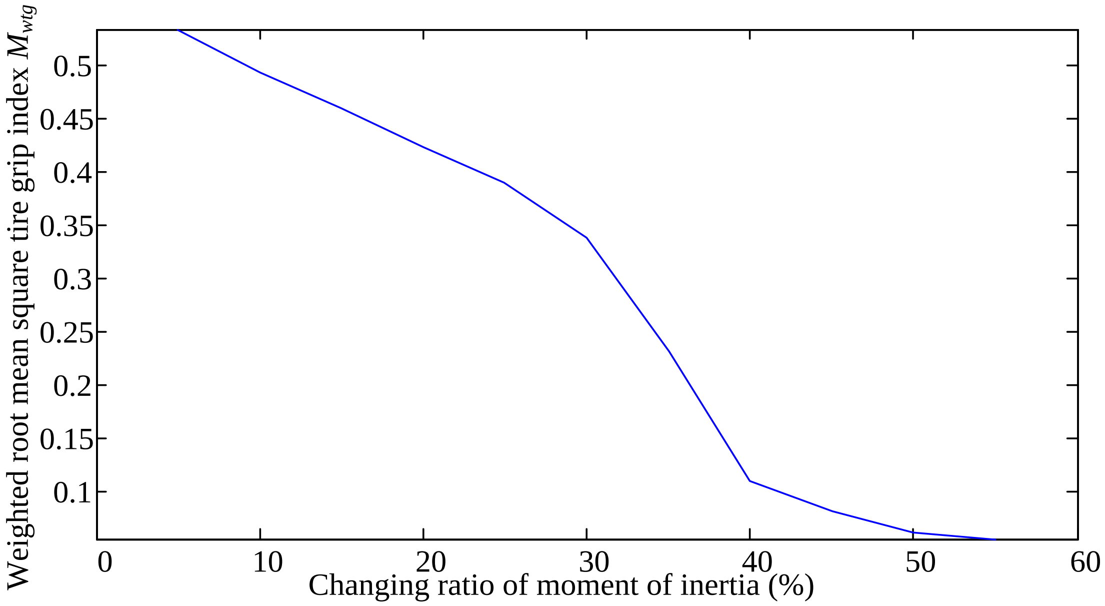

Figure 6.19 Weighted tire grip index of suspension system B with different changing ratio under sinusoidal input

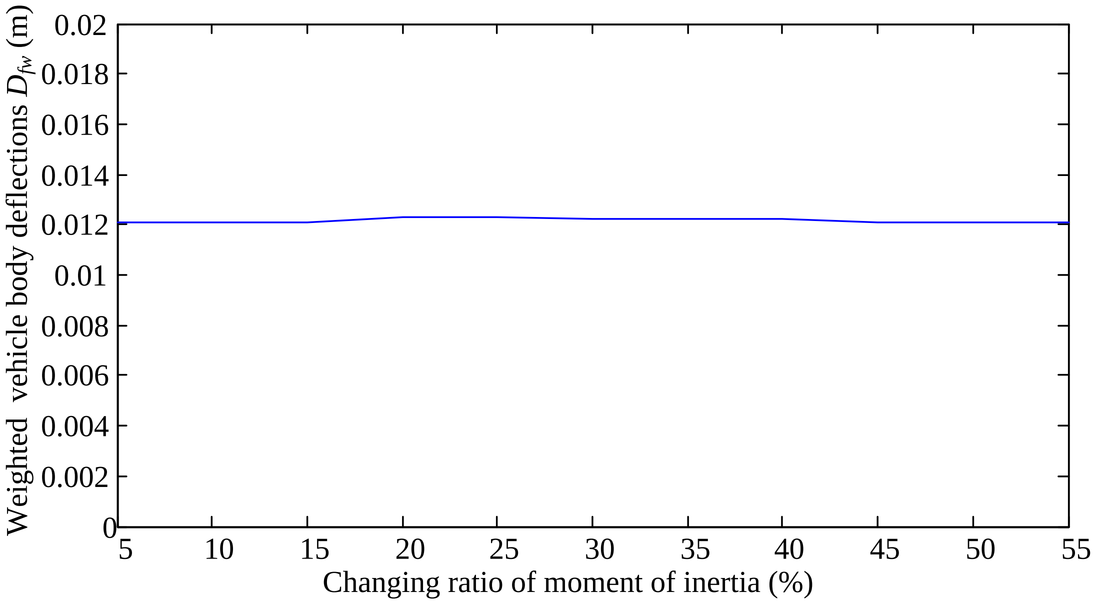

Figure 6.20 Weighted vehicle body deflections of suspension system B with different changing ratio under sinusoidal input

Figure 6.18 is the weighted accelerations of the suspension system B with different changing ratio. However, the results of the simulation are different from both prior simulation results and show that with an increasing changing ratio of the adaptive flywheel, the weighted accelerations of suspension system B also increase, which implies that the riding comfort worsens. **Figure 6.19** is the weighted tire grip index of AFW suspension system with different changing ratio under sinusoidal input, the results of the simulation are similar to the prior simulations under zero and impulse input, which indicates that the weighted tire grip index of suspension system B will decrease when the changing ratio increases. Eventually, with the decrease of weighted tire grip index of suspension system B, the safety of the vehicle will improve. **Figure 6.20** shows the weighted vehicle body deflections of suspension system B with different changing ratio. The results in this case are the same as for the former simulation; the variable changing ratio does not affect the weighted vehicle body deflections of suspension system B.

From **Table 4.12** in chapter 4 and **Table 6.12**, different results can be found compared to zero input and impulse input. Under the same changing ratio of the adaptive flywheel, suspension system B out-performs the AFW suspension system in both riding comfort and vehicle body deflection due to the application of the two-terminal hydraulic system. However, the AFW suspension system shows slight improvement than suspension system B for tire grip.

6.3.4. Optimal changing ratio for adaptive flywheel

6.3.4.1. Determination of optimal changing ratio for adaptive flywheel

Based on the previous section, with different inputs and different changing ratios of the adaptive flywheel, the performance of the suspension system B is also quite different. As for chapter 4, under specific conditions, the optimal ratio of suspension system B can be calculated.

In this simulation, three criteria are considered to optimize the changing ratio for the adaptive flywheel. These are cost of manufacture, desired proportion of performance and the proportion of inputs. To compare the AFW suspension system (ideal two-terminal hydraulic device) and suspension system B (actual two-terminal device), all three criteria are chosen to be identical, which means equation (4.27)to equation (4.39) are applied to determine the optimal changing ratio. The performance proportion of riding comfort x_1 and safety x_2, and the proportion of zero input x_3, impulse input x_4 and sinusoidal input x_5 are 0.35, 0.65, 0.1, 0.5 and 0.4, which are the same as chosen in chapter 4.

From the results in **Table 6.10** to **Table 6.12**, the optimal changing ratio can be determined through the same Chebyshev goal programming, which is 0.316. This optimal changing ratio of adaptive flywheel for suspension system B is obtained under the specific choices of x_1 to x_5 selected above, which are a function of cost, performance proportion and the proportion of inputs. Any change of these conditions implies that the optimal changing ratio will then also be different.

With this optimal changing ratio, the performance of this suspension system with different inputs can be found in **Table 6.13**.

Table 6.13 Performance of suspension system B with different input under optimal changing ratio

Input	Weighted accelerations of suspension system B a_w(m/s^2)	Weighted tire grip index of suspension system B M_{wtg}	Weighted vehicle body deflections of suspension system B D_{fw}(m)
Zero input	0.2667	0.0531	0.0021
Impulse input	0.2357	0.0891	0.0019
Sinusoidal input	1.4264	0.3028	0.0122

Table 6.13 shows the performance of the suspension system B with different inputs under optimal changing ratio. Compared to the traditional suspension system:

1) Under zero input, the weighted accelerations of suspension system B decreases 37.8%, the weighted tire grip index of suspension system B decreases 68.1% and the weighted vehicle body deflections of suspension system B decreases 40%.
2) Under impulse input, the weighted accelerations of suspension system B decrease 46.4%, the weighted tire grip index of suspension system B weighted decreases 72.2% and the vehicle body deflections of suspension system B decreases 38.7%.
3) Under sinusoidal input, the weighted accelerations of suspension system B decrease 12%, the weighted tire grip index of suspension system B decrease 58.3% and the weighted vehicle body deflections of suspension system B increase 34.1%.

By comparing these results with chapter 4, the optimal changing ratio for adaptive flywheel in suspension system B is higher than for the AFW suspension system under the same conditions, as was predicted. Since the two-terminal hydraulic system is applied, the converting ratio of equivalent mass will decrease, which implies that a higher changing ratio for adaptive flywheel is required in order to maintain the same performance as for an ideal two-terminal system. With the actual two-terminal device in suspension system B, the performances of all evaluations are better than the ideal two-terminal device in AFW suspension system, except for the weighted tire grip index under sinusoidal input.

6.3.4.2. Optimal changing ratio for adaptive flywheel with different performance and inputs proportion

By adjusting the performance proportion or the proportion of inputs, or choosing different function of cost, the optimal changing ratio of adaptive flywheel for suspension system B will also be different. Based on same reasons mentioned in chapter 4, two different situations will be discussed, which are different proportion of performance and different proportion of inputs.

Through fixing the proportion of inputs, the relationship between optimal changing ratio and performance proportion can be investigated as shown in **Table 6.14**.

Table 6.14 Optimal changing ratio with different performance proportion

Riding comfort x_1	0.2	0.4	0.5	0.6	0.8
Safety x_2	0.8	0.6	0.5	0.4	0.2
Optimal changing ratio x	0.418	0.337	0.293	0.261	0.243

Table 6.14 is the relationship between the optimal changing ratio and the

performance proportion and shows that with an increasing proportion of riding comfort (or equivalently a decreasing proportion of safety), the optimal changing ratio will decrease.

For the same reason mentioned in chapter 4, the proportion of zero input is fixed at 0.1, and the variables varied are the proportion of impulse input and sinusoidal input. The relationship between optimal changing ratio and proportion of inputs is shown in **Table 6.15**.

Table 6.15 Relationship between optimal changing ratio and proportion of inputs

Proportion of impulse input x_4	0.1	0.3	0.45	0.6	0.8
Proportion of sinusoidal input x_5	0.8	0.6	0.45	0.3	0.1
Optimal changing ratio x	0.221	0.253	0.297	0.358	0.427

Table 6.15 is the relationship between optimal changing ratio and proportion of inputs, and shows that a high proportion of impulse input (or equivalently low proportion of sinusoidal input), the optimal changing ratio will increase.

From **Table 6.14** and **Table 6.15**, the results show the same trends as in chapter 4. However, with the same proportion of performance and proportion of input, the optimal changing ratio of adaptive flywheel for suspension system B is higher than for the AFW suspension system.

6.4. Conclusion

In this chapter, three different suspension systems were evaluated, which are the traditional suspension system, suspension system A and suspension system B. Three performance criteria were applied, namely, riding comfort, tire grip index and vehicle body deflection. Zero input, impulse input and sinusoidal input were applied to simulate different road conditions.

With zero input, suspension system B outperforms both the traditional suspension system and suspension system A on riding comfort and tire grip. For vehicle body suspension, suspension system B and suspension system A show almost the same results, which are both better than the traditional suspension system. Under an impulse input, the same results as for zero input are obtained. When the excitation is sinusoidal, the suspension system B out-performs other suspension systems in tire grip. However, in vehicle body deflection, suspension system B gives the worst results. For riding comfort, suspension system B performs middle results, which is better than the traditional suspension system, but worse than suspension system A.

The performance of the suspension system B is different when the changing ratio of the adaptive flywheel is variable. Under zero input, both riding comfort and tire grip are better with an increasing changing ratio of the adaptive flywheel. However, the weighted vehicle body deflections are not affected. Under impulse input, the same results can be found as zero input. With a sinusoidal input, riding comfort decreases when the changing ratio of the adaptive flywheel increases, but the tire grip improves. Vehicle body deflections are still not affected by the variable changing ratio of the adaptive flywheel. The trends of these results are the same as those found in chapter 4.

The optimal changing ratio of adaptive flywheel for suspension system B was obtained under the same specific choices as chapter 4, which are a function of cost, performance proportion and the proportion of inputs. With the optimal changing ratio of the adaptive flywheel for suspension system B, the performances of all evaluations were better than the ideal two-terminal device in AFW suspension system, except for the weighted tire grip index under sinusoidal input.

Optimal changing ratio will be variable with different conditions. The trends shown by the optimal changing ratio of the adaptive flywheel for suspension system B is the same as for the AFW suspension system. With increasing proportion of riding comfort (or equivalently a decreasing proportion of safety), the optimal changing ratio will decrease. For a high proportion of impulse input (or equivalently low proportion of sinusoidal input), the optimal changing ratio will increase. However, with the same proportion of performance and proportion of input, the optimal changing ratio of the adaptive flywheel for suspension system B is higher than the AFW suspension system as we predicted. Since the two-terminal hydraulic system is applied, the converting ratio of equivalent mass will decrease, which implies a higher changing ratio for the adaptive flywheel is required in order to maintain the same performance as that of the ideal two-terminal system.

7. Steady state frequency response of two-terminal device with adaptive flywheel

In the previous chapters, a new two-terminal device with an adaptive flywheel was proposed. Simulations were carried out to verify the performance of this new device as a potential suspension component. The results illustrate that a traditional suspension system with this new component shows better performance under most circumstances. However, due to the non-linearity of the device, the analysis of the response of the system is much more difficult than for a linear system. In particular, the nonlinearity of the system introduces difficulty in the analysis of the steady-state frequency response of the system. The method chosen to analyze the steady-state frequency response of the system is one of the most important tools for the design and analysis of a system since this tool is used to determine the frequency response of the system. The lack of an appropriate analysis method for the determination of the steady state frequency response of a two-terminal device with adaptive flywheel is a potential impediment to the implementation of the adaptive flywheel. Therefore, to address this problem, this Chapter applies several methods for the analysis of the steady state frequency response of a two-terminal device with adaptive flywheel. The methods presented here are the single harmonic balance method, the multi-harmonic balance method and the scanning iterative multi-harmonic balance method, respectively.

7.1. Differential equation of motion for two-terminal device with adaptive flywheel

An ideal two-terminal hydraulic system with adaptive flywheel is applied to a suspension system, as shown in **Figure 7.1**. This suspension system is the quarter car model without tire, as presented in chapter 4, which consists of a mass, damper and spring. All the parameters are the same as in chapter 4.

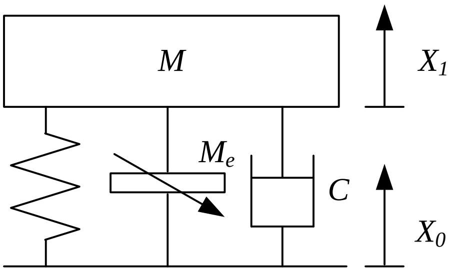

Figure 7.1 two-terminal device with adaptive flywheel

Based on **Figure 7.1**, the differential equation of motion for this system can be written as:

$$M\ddot{X}_1(t)+M_e(\ddot{X}_1(t)-\ddot{X}_0(t))+K(X_1(t)-X_0(t))+C(\dot{X}_1(t)-\dot{X}_0(t))=0 \qquad (7.1)$$

In equation (7.1), the equivalent mass M_e is determined by the inputs. Based on equation (3.6), (3.9) and (3.12), the equivalent mass M_e (m_{em} in equation (3.12)) can be expressed as:

$$M_e=\left[8.83\times10^{-4}+0.14\left(\frac{k_{sm}l_{m,\min}}{k_{sm}-m_{sm}\omega_m{}^2}\right)\right]\frac{A^2}{h^2} \qquad (7.2)$$

Since $\omega_m=vA/h$, and $v=\dot{X}_1(t)-\dot{X}_0(t)$, equation (7.2) can be represented as:

$$M_e=\left[8.83\times10^{-4}+0.14\left(\frac{k_{sm}l_{m,\min}}{k_{sm}-m_{sm}\left(\dot{X}_1(t)-\dot{X}_0(t)\right)^2\frac{A^2}{h^2}}\right)\right]\frac{A^2}{h^2} \qquad (7.3)$$

Substituting equation (7.3) into equation (7.1), the differential equation of motion for this system is given by

$$\begin{aligned}&M\ddot{X}_1(t)+\left[8.83\times10^{-4}+0.14\left(\frac{k_{sm}l_{m,\min}}{k_{sm}-m_{sm}\left(\dot{X}_1(t)-\dot{X}_0(t)\right)^2\frac{A^2}{h^2}}\right)\right]\frac{A^2}{h^2}\left(\ddot{X}_1(t)-\ddot{X}_0(t)\right) \\ &+K\left(X_1(t)-X_0(t)\right)+C\left(\dot{X}_1(t)-\dot{X}_0(t)\right)=0\end{aligned} \qquad (7.4)$$

For equation (7.4), the initial conditions of the system are considered to be zero, which implies that

$$\begin{cases} X_1(0) = X_0(0) = 0 \\ \dot{X}_1(0) = \dot{X}_0(0) = 0 \end{cases} \tag{7.5}$$

The displacement of the base of this system, $X_0(t)$, is assumed to be simple harmonic motion with amplitude B_s and frequency f_s:

$$X_0(t) = B_s \sin\left(2\pi f_s t\right) \tag{7.6}$$

From equation (7.6), the differential equation of motion for the system can be rewritten as:

$$M\ddot{X}_1(t) + \left[8.83\times10^{-4} + 0.14\left(\frac{k_{sm} l_{m,\min}}{k_{sm} - m_{sm}\left(\dot{X}_1(t) - 2\pi f_s B_s \cos\left(2\pi f_s t\right)\right)^2 \dfrac{A^2}{h^2}} \right) \right] \frac{A^2}{h^2}\left(\ddot{X}_1(t)\right.$$
$$\left. + 4\pi^2 f_s^2 B_s \sin\left(2\pi f_s t\right)\right) + K\left(X_1(t) - B_s \sin\left(2\pi f_s t\right)\right) + C\left(\dot{X}_1(t) - 2\pi f_s B_s \cos\left(2\pi f_s t\right)\right) = 0$$

(7.7)

7.2. Steady state harmonic response analysis by single harmonic balance method

The harmonic balance method is one of the most commonly used analysis methods for solving for the response of a non-linear system [189–191]. The fundamental concept of this method assumes that the system response is periodic, which implies that the response of the system can be represented as a Fourier series. By substituting the Fourier series representation of the response back into the differential equation of motion, a new equation for the different harmonic components can be obtained. Through equalizing the coefficients of each harmonic component, a set of equations can be determined. The solution of this set of equations is the response of the system.

The harmonic balance method is accurate for both weak nonlinear systems and strong nonlinear systems, and has been applied to many engineering fields [192–194]. However, in most cases, the harmonic balance method always involves a large number of equations, which makes the method computationally expensive. To simplify the calculation, the solution for the system may be assumed as a first order harmonic. This approach is referred to as the single harmonic balance method.

Assume that the solution for equation (7.7) can be represented as

$$X_1(t) = B_{s1}\sin\left(2\pi f_s t\right) + B_{s2}\cos\left(2\pi f_s t\right) \tag{7.8}$$

In equation (7.8), by calculating B_{s1} and B_{s2}, the solution for the suspension system of a two-terminal device with adaptive flywheel can be determined. Combining equations (7.7) and (7.8), a new equation can be written as:

$$\begin{aligned}
&M\left(-4\pi^2 f_s^2 B_{s1}\sin\left(2\pi f_s t\right) - 4\pi^2 f_s^2 B_{s2}\cos\left(2\pi f_s t\right)\right) + \Big[8.83\times10^{-4} + \\
&0.14\left(\frac{k_{sm} l_{m,\min}}{k_{sm} - m_{sm}\left(2\pi f_s B_{s1}\cos\left(2\pi f_s t\right) - 2\pi f_s B_{s2}\sin\left(2\pi f_s t\right) - 2\pi f_s B_s\cos\left(2\pi f_s t\right)\right)^2 \dfrac{A^2}{h^2}}\right)\Bigg] \\
&\frac{A^2}{h^2}\left(\left(-4\pi^2 f_s^2 B_{s1}\sin\left(2\pi f_s t\right) - 4\pi^2 f_s^2 B_{s2}\cos\left(2\pi f_s t\right)\right) + 4\pi^2 f_s^2 B_s\sin\left(2\pi f_s t\right)\right) + \\
&K\left(\left(B_{s1}\sin\left(2\pi f_s t\right) + B_{s2}\cos\left(2\pi f_s t\right)\right) - B_s\sin\left(2\pi f_s t\right)\right) \\
&+C\left(2\pi f_s B_{s1}\cos\left(2\pi f_s t\right) - 2\pi f_s B_{s2}\sin\left(2\pi f_s t\right) - 2\pi f_s B_s\cos\left(2\pi f_s t\right)\right) = 0
\end{aligned} \tag{7.9}$$

From equation (7.9), after expanding, there are terms such as $\sin\left(2\pi f_s t\right)\cos\left(2\pi f_s t\right)$ or $\left(\cos 2\pi f_s t\right)^2 - \left(\sin 2\pi f_s t\right)^2$, which can be rewritten as

$$\begin{cases}
\sin\left(2\pi f_s t\right)\cos\left(2\pi f_s t\right) = \dfrac{1}{2}\sin\left(2\pi f_s t\right) \\
\left(\cos 2\pi f_s t\right)^2 = \dfrac{1+\cos\left(4\pi f_s t\right)}{2} \\
\left(\sin 2\pi f_s t\right)^2 = \dfrac{1-\cos\left(4\pi f_s t\right)}{2}
\end{cases} \tag{7.10}$$

As mentioned above, the assumption that the solution is only first order harmonic implies that the higher order harmonic response will be neglected. Therefore, equation (7.9) can be simply rewritten as:

$$C_1 \sin\left(2\pi f_s t\right) + C_2 \cos\left(2\pi f_s t\right) = 0 \tag{7.11}$$

In equation (7.11),

$$\begin{cases} C_1 = f_1(B_{s1}, B_{s2}, B_s) \\ C_2 = f_2(B_{s1}, B_{s2}, B_s) \end{cases} \tag{7.12}$$

Equation (7.12) states that C_1 and C_2 are functions of B_{s1}, B_{s2} and B_s. To have a solution for equation (7.11), C_1 and C_2 have to be zero, which implies that

$$\begin{cases} f_1(B_{s1}, B_{s2}, B_s) = 0 \\ f_2(B_{s1}, B_{s2}, B_s) = 0 \end{cases} \tag{7.13}$$

Since the input is given, the amplitude of the input B_s is also known. Equation (7.13) will eventually become two equations in two unknowns B_{s1} and B_{s2}, which implies that B_{s1} and B_{s2} can be found. Due to the complexity of B_{s1} and B_{s2}, the solutions are simplified as:

$$\begin{cases} B_{s1} = f_1(M, K, C, k_{sm}, l_{m,\min}, A, h, m_{sm}, B_s, f_s) \\ B_{s2} = f_2(M, K, C, k_{sm}, l_{m,\min}, A, h, m_{sm}, B_s, f_s) \end{cases} \tag{7.14}$$

7.3. Numerical solution for the system response

Numerical solutions are one of the most important methods to analyze the dynamic response of a non-linear system. This approach is based on using numerical methods to solve the system differential equation of motion, such as the Newmark-beta method or Runge-Kutta method. Numerical methods can be applied to the analysis of both linear and non-linear systems. Moreover, these methods can also show accurate results for analyzing both weak and strong non-linear system.

Numerical simulations have become the most widely used analysis method for non-linear systems. However, by using numerical simulations to directly solve the system differential equation of motion, the solutions are in the time-domain, which is better suited for analysis of the transient response. In most engineering circumstances, the steady state harmonic response is often also of great interest. Therefore, using the numerical simulation of the differential equation of motion as a method to find the frequency response of a non-linear system implies long computational times. The system response of several periods must be considered for a steady state response, and then the amplitude of the response is the amplitude of the steady state response.

In the numerical simulation of this chapter, the system response in the time-domain is calculated under for a given frequency and then the simulation is repeated for another frequency and so forth until enough steady-state amplitude/frequency pairs are computed to obtain a frequency response curve.

In order to ensure that the system reaches a steady state, the calculation duration of the time-domain system response for each frequency excitation is 500 periods, and the system response of the last two periods are considered to be the steady state response. As described in previous chapters, inputs with different amplitudes and frequencies will affect the equivalent mass M_e, which eventually leads to a change in the resonance frequency. In the simulations, the frequency interval is 0.05Hz, the relationship between amplitude and frequency is determined as:

$$B_{sa} = E(f_{va}) \tag{7.15}$$

where B_{sa} is the amplitude of the system response, and $E(f_{va})$ is a function with variable f_{va}. If $E(f_{va0}) > E(f_{va0} + 0.05)$, the interval frequency will become 0.001Hz. When $E(f_{va0} + M_i * 0.001) > E(f_{va0} + (M_i + 1) * 0.001)$, the resonance frequency will be $(f_{va0} + M_i * 0.001)Hz$. The comparison between the simulated (brute-force) steady-state frequency response and the frequency response obtained via the single harmonic balance method under different amplitude inputs is shown in **Figure 7.2**.

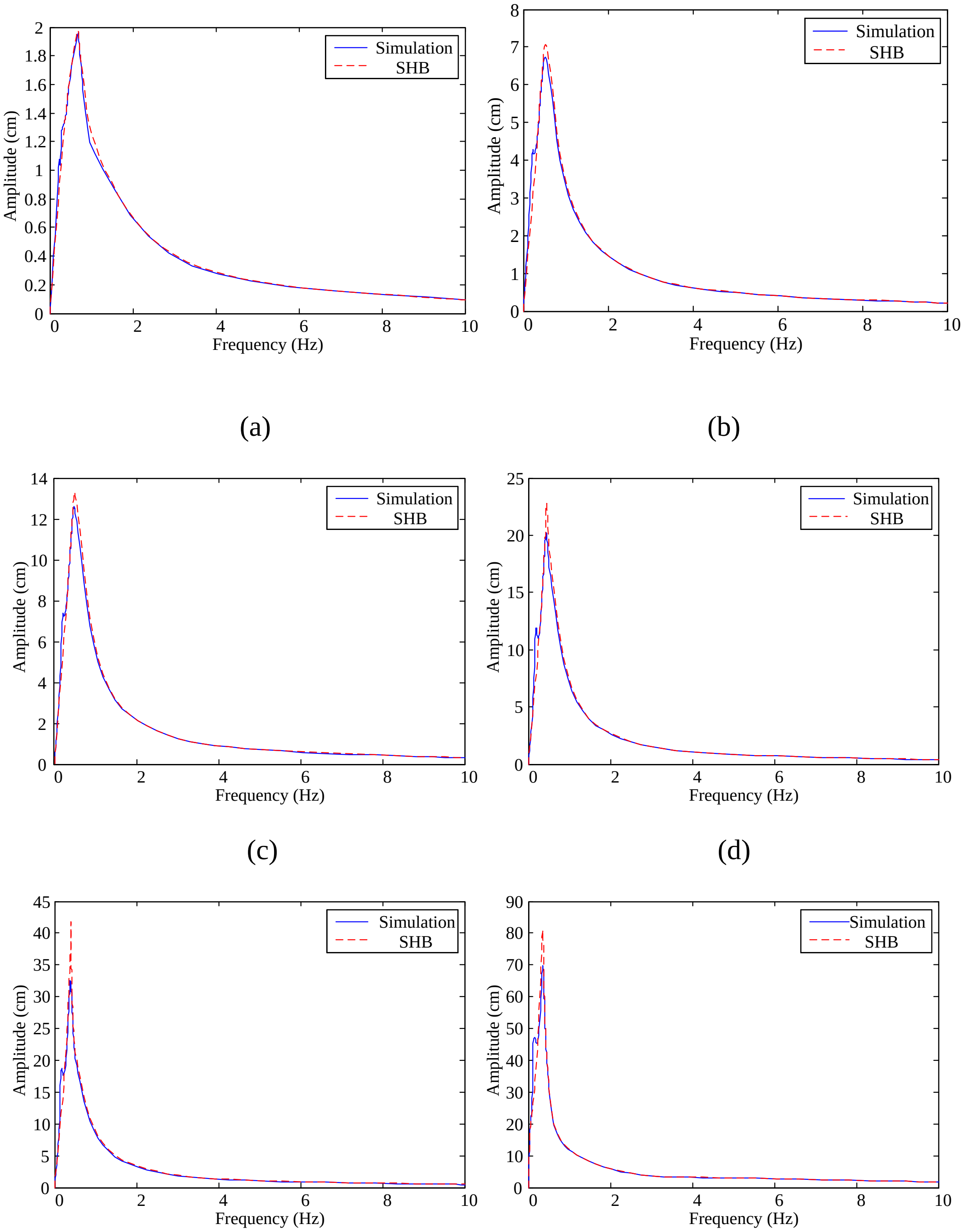

(a) (b)

(c) (d)

(e) (f)

Figure 7.2 Comparisons between simulation solution and single harmonic balance method frequency response under different amplitude inputs a) $B_s = 1cm$. b) $B_s = 3cm$. c) $B_s = 5cm$. d) $B_s = 7cm$. e) $B_s = 10cm$. f) $B_s = 20cm$.

Figure 7.2 show the comparison between the simulation solution and the frequency response solution obtained via the single harmonic balance method, under different amplitude inputs. In **Figure 7.2**, the response results obtained by numerical simulation and single harmonic balance method are compared. The results show close agreement between the two methods. However, when the inputs frequency reaches the resonance frequency of the system, the response results between the two methods start to differ. From **Figure 7.2**, it can be observed that under a small amplitude input, close agreement of the response results between the two methods, and still show good agreement even at the resonance frequency. With an increase of amplitude for the inputs, the difference of response results also increases, which implies that the error of the single harmonic balance method is increasing with increasing amplitude of the input.

Table 7.1 Resonance frequency and max amplitude of response under inputs with different amplitudes

Amplitude of input	Resonance Frequency	Max amplitude of response
1cm	0.680Hz	1.9934cm
3cm	0.535Hz	7.0943cm
5cm	0.505HZ	12.7923cm
7cm	0.450Hz	20.3555cm
10cm	0.395Hz	32.5353cm
20cm	0.350Hz	72.4034cm

Table 7.1 shows the resonance frequency and maximum amplitude of the response under inputs with different amplitudes, ranging from 1cm to 20cm. Based on

Table 7.1, with higher amplitude inputs, the maximum amplitude of the response is also higher, but the transmissibility is also larger, which can be represented as the ratio between maximum amplitude of response and the amplitude of the input. Another phenomenon can be observed from **Table 7.1**; with increasing amplitude of the input, the resonance frequency decreases. The reason for this phenomenon is caused by the change in the equivalent mass. Under the same frequency, higher amplitude inputs will lead to larger equivalent masses, which cause the natural frequency of the system to drift lower.

By enlarging the view of each figure in **Figure 7.2**, from frequency 0 to 0.25Hz, this system shows slight super-harmonic response under different inputs, which can also be called super harmonic resonance. This is shown in **Figure 7.3**.

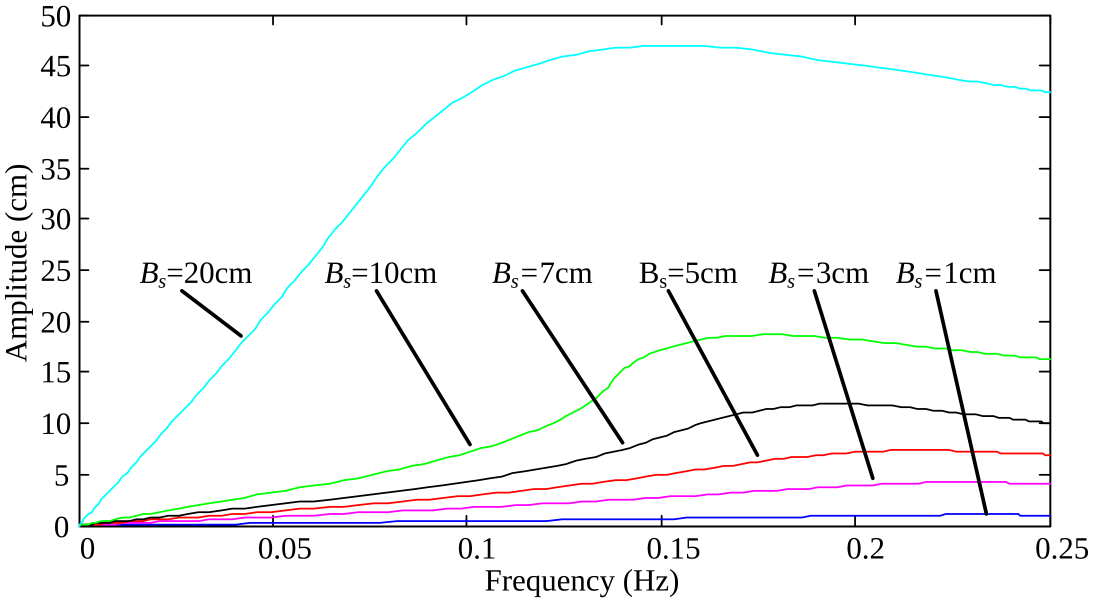

Figure 7.3 Enlarged view of super-harmonic responses under different inputs

Figure 7.3 shows the super-harmonic responses under different inputs. However, with the single harmonic balance method, these super-harmonic responses cannot be captured. In order to verify the accuracy of the single harmonic balance method, the normalized root mean square errors between the numerical solution and the single harmonic balance method are calculated via

$$E_{nrm} = \sqrt{\frac{\sum_{i=1}^{2000}(A_1(f(0.005i)) - A_2(f(0.005i)))^2}{\sum_{i=1}^{2000} A_2(f(0.005i))^2}} \tag{7.16}$$

In equation (7.16), $A_1(f(0.005i)$ is the amplitude of the numerical solution under frequency $0.005i$ where i is an integer, and $A_2(f(0.005i))$ is the amplitude of the single harmonic balance solution under frequency $0.005i$. The results can be found in **Table 7.2**

Table 7.2 Normalized root mean square errors between numerical simulation and single harmonic balance method

Sinusoidal input Amplitude (cm)	Normalized root mean square error
1	2.8%
2	4.7%
5	8.1%
7	12.9%
10	17.8%
20	36.9%

Table 7.2 shows the normalized root mean square errors under different amplitudes of the sinusoidal input. With the higher amplitude of inputs, the normalized root mean square error increases. **Table 7.2** supports the previous statement about **Figure 7.2**, which is that the difference in results between the numerical solution and the single harmonic balance method increases with higher amplitudes of the input.

7.4. Multi-harmonic balance method for steady state harmonic response analysis

As mentioned in the last sub-section, the accuracy of the solution for the single harmonic balance method will decrease with an increase of amplitude of the input. Moreover, the single harmonic balance method cannot capture super-harmonic or sub-harmonic responses.

By using the multi-harmonic balance method, all the above-mentioned problems can be addressed. The basic concept of the multi-harmonic balance method is the assumption that the response of the system contains more than the first order harmonic. Assume that the steady state response for the system in **Figure 7.1** can be presented as:

$$X_1(t) = \frac{1}{2}B_{m0} + \sum_{i=1}^{N_m}\left[B_{m1i}\sin\left(2\pi f_s it\right) + B_{m2i}\cos\left(2\pi f_s it\right)\right] \tag{7.17}$$

In equation (7.17), B_{m0} is the coefficient of constant, N_m is the highest order harmonic of the system response, B_{m1i} and B_{m2i} are coefficients of each order harmonic of the system response. Equation (7.17) can be rewritten as:

$$X_1(t) = \begin{bmatrix} \frac{1}{2}B_{m0} & B_{m11} & B_{m21} & B_{m12} & B_{m22} & \cdots & B_{m1N_m} & B_{m2N_m} \end{bmatrix} \begin{bmatrix} 1 \\ \sin\left(2\pi f_s t\right) \\ \cos\left(2\pi f_s t\right) \\ \sin\left(2\pi f_s 2t\right) \\ \cos\left(2\pi f_s 2t\right) \\ \vdots \\ \sin\left(2\pi f_s N_m t\right) \\ \cos\left(2\pi f_s N_m t\right) \end{bmatrix}$$

(7.18)

By substituting equation (7.18) into equation (7.7), a new equation can be obtained, which is similar to equation (7.9). Due to the complexity of this new equation, a simplified version of this equation can be presented as:

$$\begin{bmatrix} C_{m0} & C_{m11} & C_{m21} & C_{m12} & C_{m22} & \cdots & C_{m1N_m} & C_{m2N_m} \end{bmatrix} \begin{bmatrix} 1 \\ \sin\left(2\pi f_s t\right) \\ \cos\left(2\pi f_s t\right) \\ \sin\left(4\pi f_s t\right) \\ \cos\left(4\pi f_s t\right) \\ \vdots \\ \sin\left(2\pi f_s N_m t\right) \\ \cos\left(2\pi f_s N_m t\right) \end{bmatrix} = 0$$

(7.19)

In equation (7.19), the new coefficients can be presented as:

$$\begin{cases} C_{m0} = f_0\left(\frac{1}{2}B_{m0} \quad , B_{m11} \quad , B_{m21} \quad , B_{m12} \quad , B_{m22} \quad \cdots \quad B_{m1N_m} \quad , B_{m2N_m}\right) \\ C_{m11} = f_{11}\left(\frac{1}{2}B_{m0} \quad , B_{m11} \quad , B_{m21} \quad , B_{m12} \quad , B_{m22} \quad \cdots \quad B_{m1N_m} \quad , B_{m2N_m}\right) \\ C_{m21} = f_{21}\left(\frac{1}{2}B_{m0} \quad , B_{m11} \quad , B_{m21} \quad , B_{m12} \quad , B_{m22} \quad \cdots \quad B_{m1N_m} \quad , B_{m2N_m}\right) \\ C_{m12} = f_{12}\left(\frac{1}{2}B_{m0} \quad , B_{m11} \quad , B_{m21} \quad , B_{m12} \quad , B_{m22} \quad \cdots \quad B_{m1N_m} \quad , B_{m2N_m}\right) \\ C_{m22} = f_{22}\left(\frac{1}{2}B_{m0} \quad , B_{m11} \quad , B_{m21} \quad , B_{m12} \quad , B_{m22} \quad \cdots \quad B_{m1N_m} \quad , B_{m2N_m}\right) \\ \vdots \\ C_{m1N_m} = f_{1N_m}\left(\frac{1}{2}B_{m0} \quad , B_{m11} \quad , B_{m21} \quad , B_{m12} \quad , B_{m22} \quad \cdots \quad B_{m1N_m} \quad , B_{m2N_m}\right) \\ C_{m2N_m} = f_{1N_m}\left(\frac{1}{2}B_{m0} \quad , B_{m11} \quad , B_{m21} \quad , B_{m12} \quad , B_{m22} \quad \cdots \quad B_{m1N_m} \quad , B_{m2N_m}\right) \end{cases}$$

(7.20)

Based on equation (7.20), the new coefficients are functions of coefficients of equation (7.18). For a solution of equation (7.19) to exist, all the coefficients must be zero, which implies

$$
\begin{cases}
f_0\left(\frac{1}{2}B_{m0}\quad ,B_{m11}\quad ,B_{m21}\quad ,B_{m12}\quad ,B_{m22}\quad \ldots B_{m1N_m}\quad ,B_{m2N_m}\right) = {}_2 \\
f_{11}\left(\frac{1}{2}B_{m0}\quad ,B_{m11}\quad ,B_{m21}\quad ,B_{m12}\quad ,B_{m22}\quad \ldots B_{m1N_m}\quad ,B_{m2N_m}\right) = {}_2 \\
f_{21}\left(\frac{1}{2}B_{m0}\quad ,B_{m11}\quad ,B_{m21}\quad ,B_{m12}\quad ,B_{m22}\quad \ldots B_{m1N_m}\quad ,B_{m2N_m}\right) = {}_2 \\
f_{12}\left(\frac{1}{2}B_{m0}\quad ,B_{m11}\quad ,B_{m21}\quad ,B_{m12}\quad ,B_{m22}\quad \ldots B_{m1N_m}\quad ,B_{m2N_m}\right) = {}_2 \\
f_{22}\left(\frac{1}{2}B_{m0}\quad ,B_{m11}\quad ,B_{m21}\quad ,B_{m12}\quad ,B_{m22}\quad \cdots\quad B_{m1N_m}\quad ,B_{m2N_m}\right) = 0 \\
\vdots \\
f_{1N_m}\left(\frac{1}{2}B_{m0}\quad ,B_{m11}\quad ,B_{m21}\quad ,B_{m12}\quad ,B_{m22}\quad \cdots\quad B_{m1N_m}\quad ,B_{m2N_m}\right) = 0 \\
f_{1N_m}\left(\frac{1}{2}B_{m0}\quad ,B_{m11}\quad ,B_{m21}\quad ,B_{m12}\quad ,B_{m22}\quad \cdots\quad B_{m1N_m}\quad ,B_{m2N_m}\right) = 0
\end{cases}
\tag{7.21}
$$

In equation (7.21), there are $2N_m+1$ unknown coefficients, these are B_{m0}, B_{m1i} and B_{m2i} for $i=1..N$, respectively. However, there are also $2N_m+1$ equations, which means all the coefficients can be determined as:

$$
\begin{cases}
B_{m0} = f_{m0}(M,K,C,k_{sm},l_{m,\min},A,h,m_{sm},B_s,f_s) \\
B_{m11} = f_{m11}(M,K,C,k_{sm},l_{m,\min},A,h,m_{sm},B_s,f_s) \\
B_{m21} = f_{m21}(M,K,C,k_{sm},l_{m,\min},A,h,m_{sm},B_s,f_s) \\
B_{m12} = f_{m12}(M,K,C,k_{sm},l_{m,\min},A,h,m_{sm},B_s,f_s) \\
B_{m22} = f_{m22}(M,K,C,k_{sm},l_{m,\min},A,h,m_{sm},B_s,f_s) \\
\vdots \\
B_{m1N_m} = f_{m1N_m}(M,K,C,k_{sm},l_{m,\min},A,h,m_{sm},B_s,f_s) \\
B_{m2N_m} = f_{m2N_m}(M,K,C,k_{sm},l_{m,\min},A,h,m_{sm},B_s,f_s)
\end{cases}
\tag{7.22}
$$

Using the same numerical simulation approach, comparison of the results between the numerical solution and the results of the multi-harmonic balance method is shown in **Figure 7.4**.

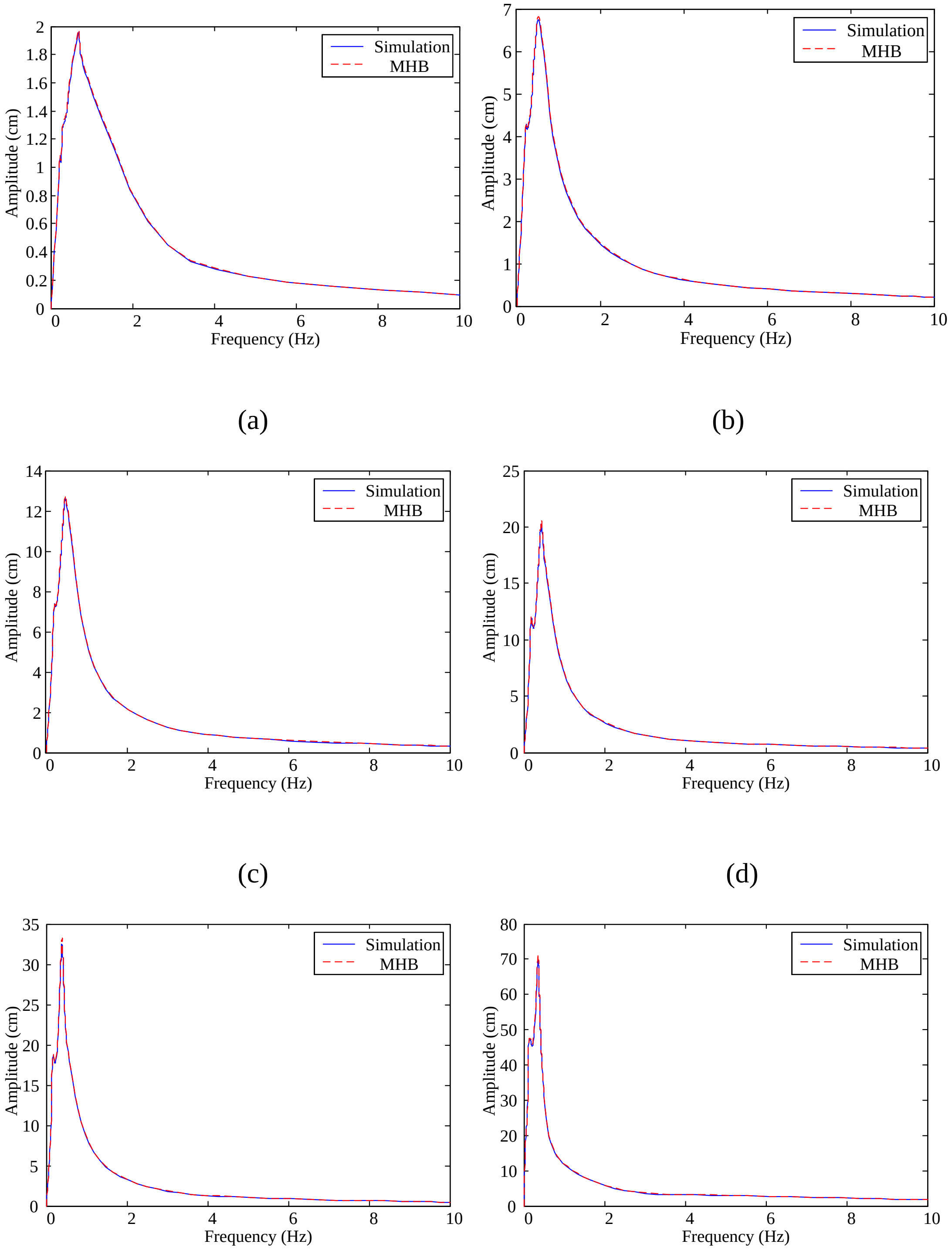

(a) (b)

(c) (d)

(e) (f)

Figure 7.4 Comparisons between simulation solution and multi-harmonic balance method under different amplitude inputs a) $B_s = 1cm$. b) $B_s = 3cm$. c) $B_s = 5cm$. d) $B_s = 7cm$. e) $B_s = 10cm$. f) $B_s = 20cm$.

Figure 7.4 shows the comparison of the results between the simulation solution and the multi-harmonic balance method under different amplitude inputs. The close agreement between the two curves implies the accuracy of the multi-harmonic balance method. The solution of the multi-harmonic balance method captures the super-harmonic responses of each input. Moreover, when the frequency of inputs reaches the resonance frequency, the solution of the multi-harmonic balance method is still accurate even under high amplitude.

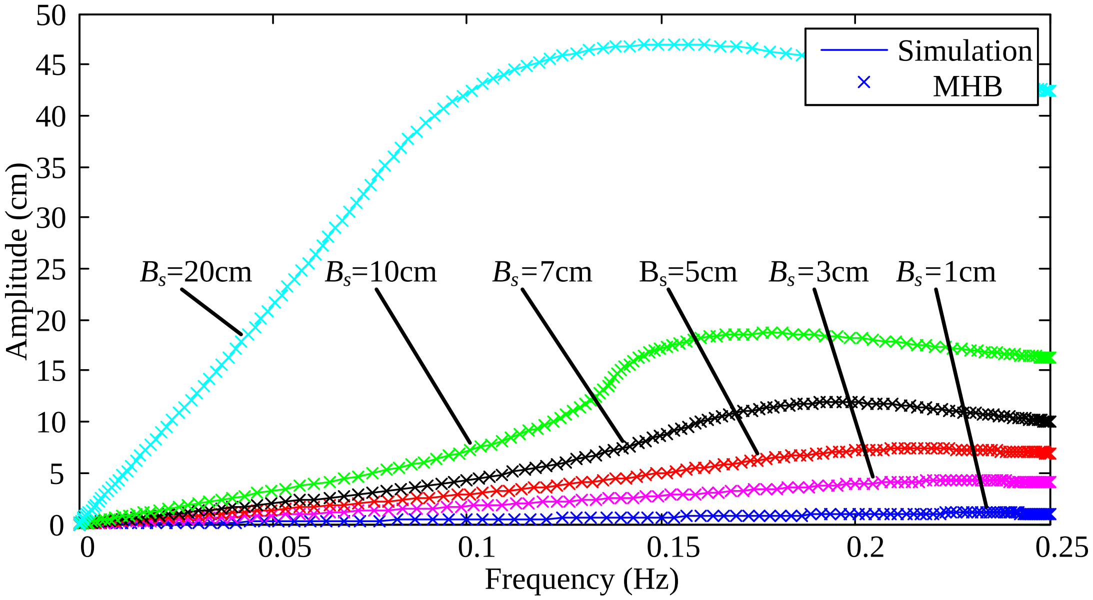

Figure 7.5 Enlarged view of super-harmonic responses comparison between numerical simulation and multi-harmonic balance method under different inputs

Figure 7.5 shows the enlarged view of the comparison of the super-harmonic responses between the numerical simulation and the multi-harmonic balance method under different inputs. The close agreement between the numerical simulation and the multi-harmonic balance method implies that the multi-harmonic balance method can accurately capture the super-harmonic response of the system.

By calculating the normalized root mean square errors between the numerical simulation and the multi-harmonic balance method, the accuracy of the multi-harmonic balance method can be verified. The results can be found in **Table 7.3**

Table 7.3 Normalized root mean square errors between numerical simulation and multi-harmonic balance method

Sinusoidal input Amplitude (cm)	Weighted root mean square error
1	0.08%
2	0.29%
3	0.67%
5	1.18%
7	1.89%
10	5.12%
20	12.94%

Table 7.3 shows the normalized root mean square errors between the numerical simulation and the multi-harmonic balance methods, and shows that the results are much more accurate than for the single harmonic balance method. Even under the highest amplitude of inputs, the normalized root mean square error is still under 15%.

7.5. Scanning iterative multi-harmonic balance method

In the previous sub-section, the single harmonic balance method and the multi-harmonic balance method were both applied to analyze the steady state response of this system in **Figure 7.1**. The results show that the single harmonic balance method can be used to analyze the steady state response of this system under small amplitude inputs without super-harmonic or sub-harmonic response. On the other hand, the multi-harmonic balance method can not only be applied to analyze high amplitude inputs to the system, but it can also accurately capture the super-harmonic response of the system. However, due to the complexity of the differential equation of motion for this system, the calculation process for the harmonic balance method is cumbersome. Based on equation (7.9), even for a single harmonic balance method, the determination of the coefficients is quite complicated.

To simplify the process of calculation, researchers have proposed semi-analytical methods based on the harmonic balance method [193,195]. One of the classical methods is the incremental harmonic balance method [196]. This method combines the Newton-Raphson method with the harmonic balance method. Tamura and Wei proposed a new method named the harmonic balance-Newton Raphson method, which has proven to be another incremental harmonic balance method [197]. However, by using these methods to analyze the adaptive flywheel system, a lengthy calculation process is still required, which can be difficult to apply. In this section, a new scanning iterative multi-harmonic balance method is proposed to analyze the steady state response of the adaptive flywheel.

It is assumed that there are constant terms and super-harmonic terms (same as for the multi-harmonic balance method) in the system response, which can be represented as:

$$X_1(t)=\frac{1}{2}B_{h0}+\sum_{i=1}^{N_s}B_{h1i}\sin(2\pi i f_s t)+B_{h2i}\cos(2\pi i f_s t) \qquad (7.23)$$

In equation (7.23), B_{h0} is a constant coefficient, constants B_{h1i} and B_{h2i} are coefficients for the different order harmonics, and N_h is the highest order of harmonic. All the coefficients can be written as an unknown vector B_h

$$B_h=[\frac{1}{2}B_{h0},B_{h11},B_{h21},B_{h12},B_{h22},\cdots B_{h1N_h},B_{s2N_h}] \qquad (7.24)$$

Based on the differential equation of motion for this system, an error function $E_h(t)$ can be applied to equation (7.7)

$$M\ddot{X}_1(t)+\left[8.83\times10^{-4}+0.14\left(\frac{k_{sm}l_{m,\min}}{k_{sm}-m_{sm}(\dot{X}_1(t)-2\pi f_sB_s\cos\left(2\pi f_st\right))^2\dfrac{A^2}{h^2}}\right)\right]\frac{A^2}{h^2}\left(\ddot{X}_1(t)\right.$$

$$\left.+4\pi^2 f_s{}^2B_s\sin\left(2\pi f_st\right)\right)+K\left(X_1(t)-B_s\sin\left(2\pi f_st\right)\right)+C\left(\dot{X}_1(t)-2\pi f_sB_s\cos\left(2\pi f_st\right)\right)=E_h(t)$$

(7.25)

From the assumption in equation (7.23), $X_1(t)$ is a periodic function with period $\frac{1}{f_s}$, which implies that the differential equation of motion for this system is also a periodic function with period $\frac{1}{f_s}$. The error function $E_h(t)$ can be presented as a Fourier series:

$$E_h(t)=\frac{1}{2}E_{h0}+\sum_{i=1}^{N_s}E_{h1i}\sin\left(2\pi f_sit\right)+E_{h2i}\cos\left(2\pi f_sit\right) \tag{7.26}$$

E_{h0} is the constant coefficient, E_{h1i} and E_{h2i} are coefficients for the different order harmonics, and N_h is the highest order harmonic. All the coefficients can be written as an error vector E_h:

$$E_h=[\frac{1}{2}E_{h0},E_{h11},E_{h21},E_{h12},E_{h22},\cdots,E_{h1N_h},E_{h2N_h}] \tag{7.27}$$

The error vector can be determined using Fast Fourier Transform. First, the time vector T_h is needed, which can be represented as:

$$T_h=\left[0,\frac{1}{2\pi N_{hf}},\frac{2}{2\pi N_{hf}},\cdots,\frac{N_{hf}-1}{2\pi N_{hf}}\right] \tag{7.28}$$

In equation (7.28), N_{hf} is the number of time points, which has to satisfy two requirements: 1) satisfy the data length for a Fast Fourier Transform and 2) should be able to avoid frequency overlap. In order to meet the first requirement, N_{hf} must be determined by

$$N_{hf}=2^{L_h} \tag{7.29}$$

In equation (7.29), L_h is positive integer. To satisfy the second requirement, the following condition must hold:

$$N_{hf} > 2N_h \tag{7.30}$$

Substituting all the time points in the time vector T_h into equation (7.25), the value of the error function in the time domain can be calculated. By using the Fast Fourier Transform and the value of the error function in the time domain, the error vector E_h can be determined.

When the unknown vector B_h is the accurate system response, the error function should be zero, which implies that

$$\left\|E_h\right\|^2 = 0 \tag{7.31}$$

To obtain the accurate system response, the solution of the differential equation of motion for this system can be converted into a non-linear optimization problem, which can be presented as:

$$\min E_h(B_h) = E_h E_h^T \tag{7.32}$$

Equation (7.32) can be solved by many non-linear optimization iterative algorithms. The flow diagram of the scanning iterative multi-harmonic balance method is shown in **Figure 7.6**.

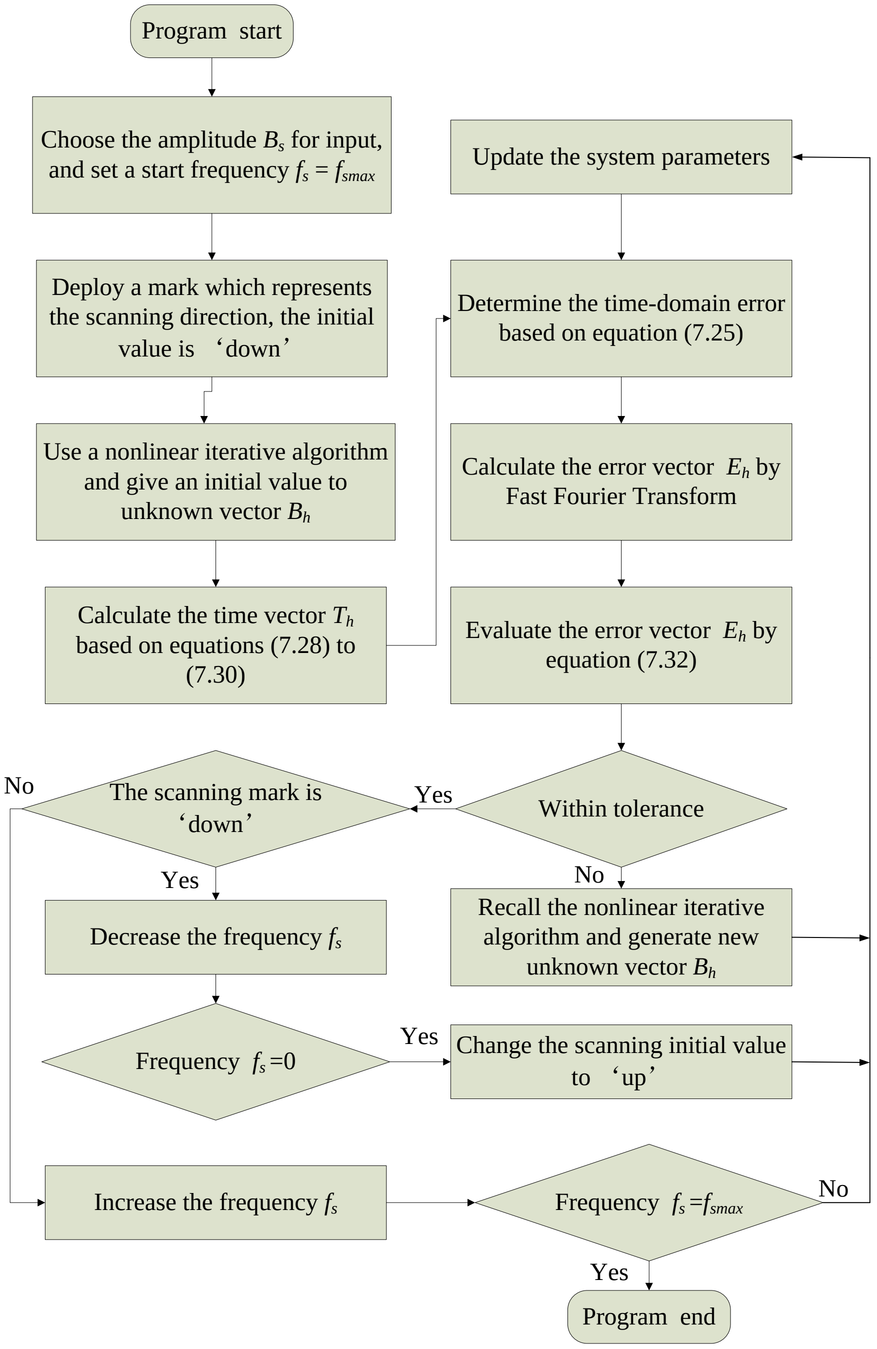

Figure 7.6 Flow diagram of the scanning iterative multi-harmonic balance method

Figure 7.6 Shows the flow diagram of the scanning iterative multi-harmonic balance method. By using this method to analyze the system response, the starting scanning frequency is needed, which is $f_s = f_{s\max}$ in this simulation. The initial value of the unknown vector B_h can be calculated under frequency $f_{s\max}$, which will be the iterative initial value for the next iterative frequency response calculation. Setting the calculation frequency as $f_s = f_s - \Delta f$, then the former frequency response calculation is repeated until the frequency $f_s = 0$.

Since the steady state harmonic response for a nonlinear system is related to the initial state of the system - even under the same amplitude and frequency input - the system response will be different when the frequency increases or decreases. To obtain a more accurate system response, the scanning direction has to be both up and down. When the frequency f_s reaches zero, the scanning direction will change to ‘up’, which means that the calculation frequency will be $f_s = f_s + \Delta f$. The whole calculation process is repeated until the frequency reaches $f_{s\max}$.

Several numerical simulations are performed to compare the results between the numerical solution and the multi-harmonic balance method. These are shown in **Figure 7.7**.

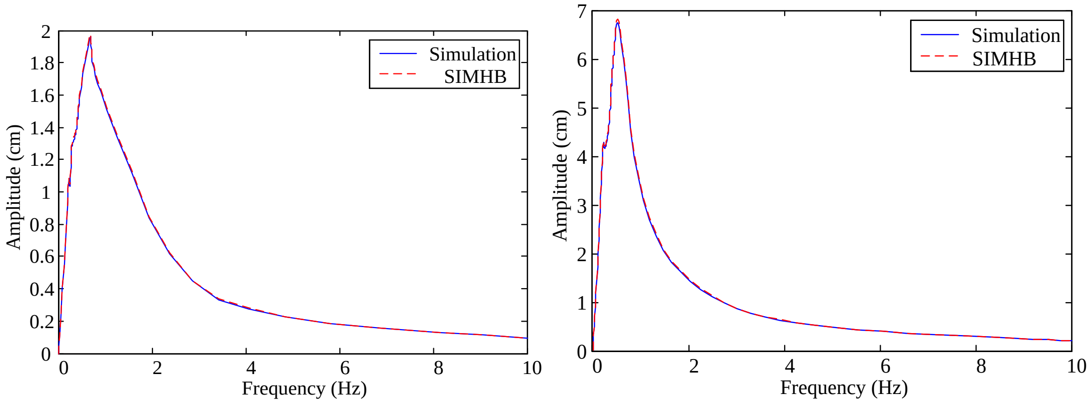

(a) (b)

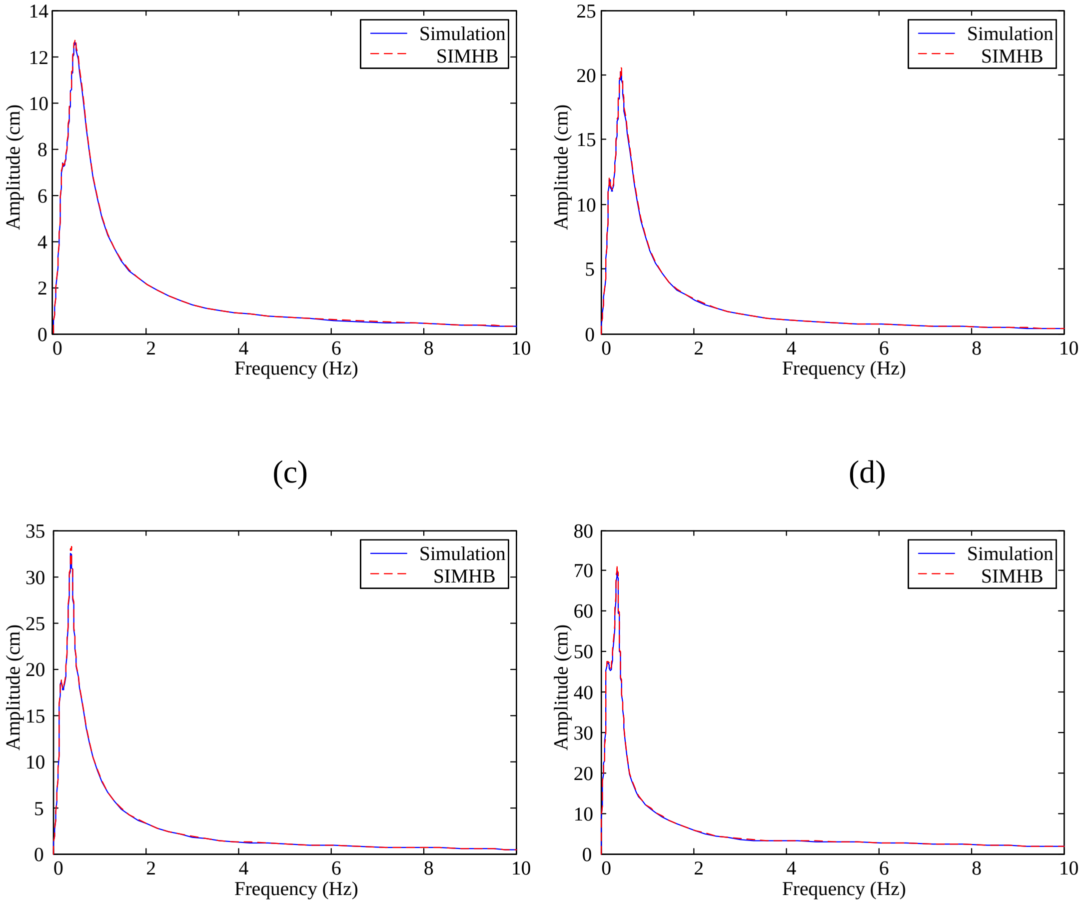

(c) (d)

(e) (f)

Figure 7.7 Comparison between simulation solution and single harmonic balance method for different amplitude inputs a) $B_s = 1cm$. b) $B_s = 3cm$. c) $B_s = 5cm$. d) $B_s = 7cm$. e) $B_s = 10cm$. f) $B_s = 20cm$.

Figure 7.7 shows the comparison of the results between the simulation solution and the scanning iterative multi-harmonic balance method for different amplitude inputs. The close agreement between the two curves demonstrates the accuracy of the scanning iterative multi-harmonic balance method. Similar to the multi-harmonic balance method, the scanning iterative multi-harmonic balance method also captures the super-harmonic responses of each input.

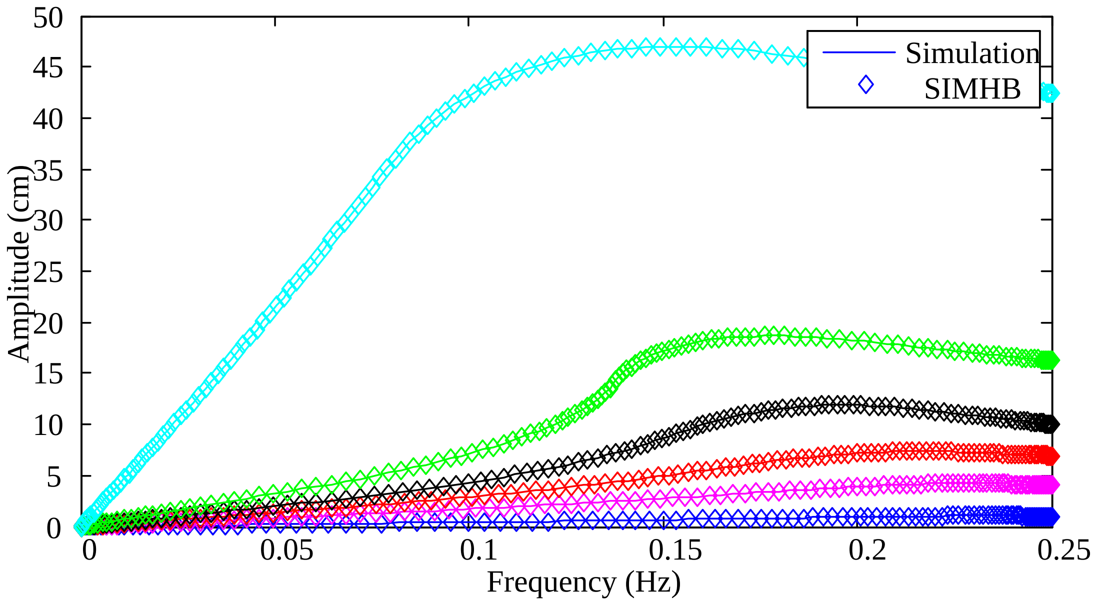

Figure 7.8 Enlarged view of super-harmonic responses comparison between numerical simulation and scanning iterative multi-harmonic balance method under different inputs

Figure 7.8 shows the enlarged view of the comparison of the super-harmonic responses between the numerical simulation and the scanning iterative multi-harmonic balance method associated with different inputs. The close agreement between the numerical simulation and the scanning iterative multi-harmonic balance method implies that the scanning iterative multi-harmonic balance method can accurately capture the super-harmonic response of this system.

Figure 7.5 and **Figure 7.8** show that there are almost no differences between the results of the multi-harmonic balance method and scanning iterative multi-harmonic balance method. By calculating the normalized root mean square errors between numerical simulation and multi-harmonic balance method, the differences are shown in **Table 7.4**.

Table 7.4 Normalized root mean square errors between numerical simulation and scanning iterative multi-harmonic balance method

Sinusoidal input Amplitude (cm)	Weighted root mean square error ()
1	0.075%
2	0.253%
3	0.599%
5	1.013%
7	1.67%
10	4.78%
20	11.07%

Table 7.4 shows the normalized root mean square errors between the numerical simulation and the scanning iterative multi-harmonic balance method. The results indicate that the scanning iterative multi-harmonic balance method provides a more accurate system response than multi-harmonic balance method.

As mentioned above, due to the complexity of the differential equation of motion for the system, the calculation based on the multi-harmonic balance method can be extremely difficult. For this system, the calculation involves several dozen equations, which leads to a large computational load. However, by using the scanning iterative multi-harmonic balance method, the time for programming is significantly reduced. In the case presented here, the time for programming the scanning iterative multi-harmonic balance method was a quarter of that for the multi-harmonic balance method (results may be different depending on programming skill). Moreover, once the program frame is built, this method can be used for analyzing different non-linear systems with minor changes.

From the scanning iterative multi-harmonic balance method, a comparison can be made between a traditional suspension system and a suspension system with a two-terminal device with adaptive flywheel, which is shown in **Figure 7.9**.

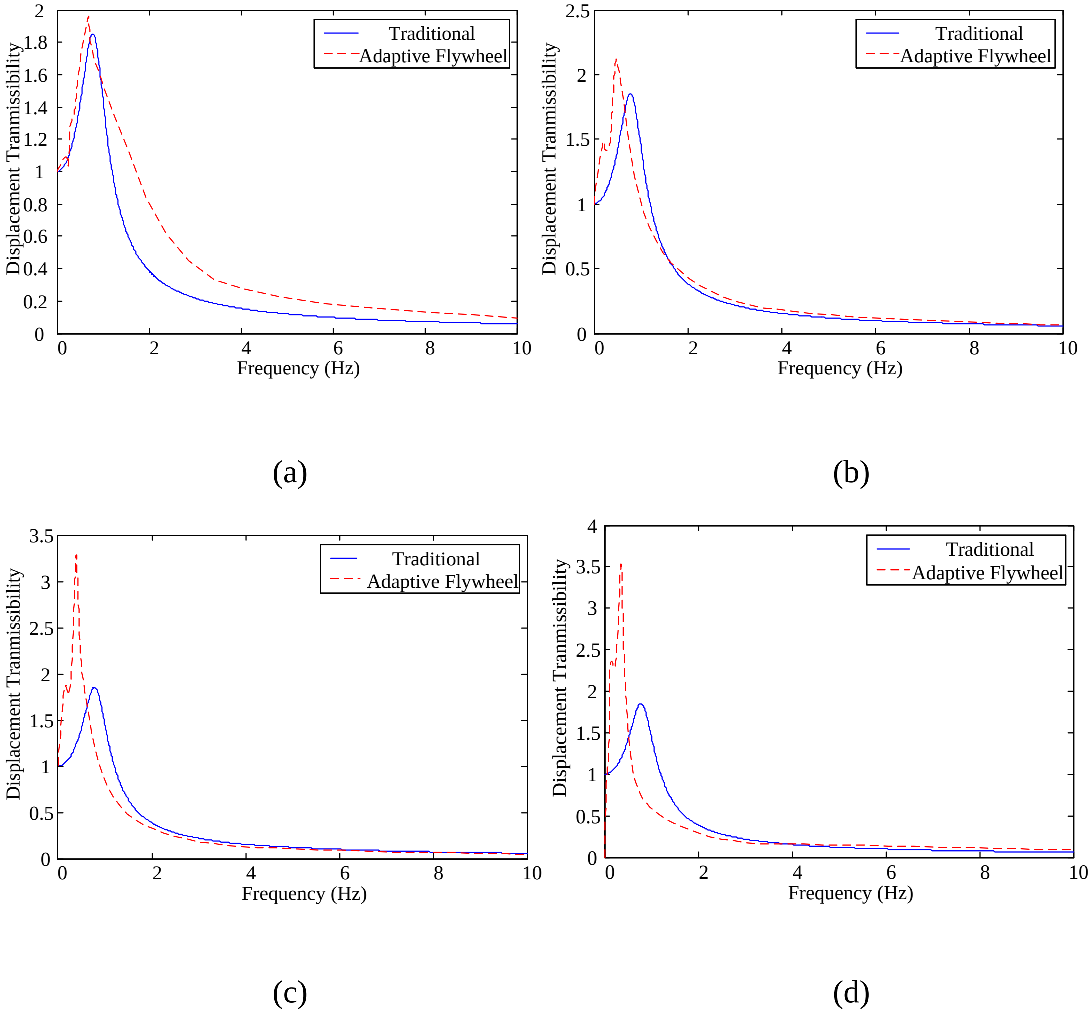

Figure 7.9 Comparison between the traditional suspension system and suspension system of two-terminal device with adaptive flywheel under different amplitude inputs: a) $B_s = 1cm$, b) $B_s = 5cm$, c) $B_s = 10cm$, and d) $B_s = 20cm$.

Figure 7.9 shows the comparison between the traditional suspension system and suspension system with a two-terminal device with adaptive flywheel, under different amplitude inputs. The results imply that the displacement transmissibility of the traditional suspension system out-performs the suspension system of the two-terminal device with the adaptive flywheel, which agrees with the results of the analysis of the suspension deflection in chapter 4. The situation becomes worse when the frequency reaches the resonance frequency. However, based on **Figure 7.9**, the resonance frequency of the suspension system with the two-terminal device with the adaptive flywheel is much lower than that of the traditional suspension system. For example, from **Figure 7.9** (d), the resonance frequency is only 0.35Hz, which implies that in order to reach the resonance frequency, the velocity of the vehicle must be around 8 km/hr. Under most circumstances, the velocity of a vehicle is much faster than this speed, which means that the peak in the displacement transmissibility will not correspond to normal operating conditions.

Another phenomenon can be observed in **Figure 7.9**. Unlike the traditional suspension system, the resonance frequency of the suspension system with a two-terminal device with adaptive flywheel changes with the amplitude of the input. As previously mentioned, this is caused by the equivalent mass generated by the adaptive flywheel. By using the scanning iterative multi-harmonic balance method, the resonance frequency of the suspension system of the two-terminal device with adaptive flywheel can be observed directly, which can help to redesign the flywheel to avoid a certain frequency. For example, if the situation requires a lower resonance frequency, some weight can be added to the frame of the adaptive flywheel, or the stiffness of the spring can be reduced, which allows the slider to reach the maximum displacement even under a relatively small input.

7.6. Conclusions

In this chapter, in order to analyze the steady state response, three different methods were proposed to analyze the steady state response of the two-terminal device with adaptive flywheel. These methods are the single harmonic balance method, the multi-harmonic balance method and the scanning iterative multi-harmonic balance method, respectively.

The single harmonic balance method can be used to analyze the steady state response of the system under small amplitude input without super-harmonic or sub-harmonic responses. However, the accuracy of the solution of single harmonic balance method will decrease with an increase in the amplitude of the inputs.

Moreover, the single harmonic balance method cannot capture super-harmonic or sub-harmonic responses.

For the multi-harmonic balance method, the solution captures the super-harmonic responses of each input. Additionally, when the frequency of inputs reaches the resonance frequency, the solution of the multi-harmonic balance method is still accurate even under high input amplitude. Due to the complexity of the differential equation of motion for this system, the computation to obtain all the coefficients for the multi-harmonic balance method is difficult.

In view of the difficulties with the multi-harmonic balance method, a new scanning iterative multi-harmonic balance method was proposed to analyze the steady state frequency response of the adaptive flywheel. The results indicate that the scanning iterative multi-harmonic balance method provides a more accurate system response than the multi-harmonic balance method with much less computational effort.

At the end of the chapter, a comparison of the displacement transmissibility between the traditional suspension system and a suspension system with a two-terminal device with adaptive flywheel under different amplitude inputs was carried out. The results show that the traditional suspension system out-performs the suspension system of the two-terminal device with the adaptive flywheel when the frequency is around the resonance frequency. However, in order to be at the resonance frequency, the velocity of the vehicle needs to be extremely low.

8. Conclusion

8.1. Concluding remarks

In this thesis, adaptive flywheels made of two different materials are proposed, and the corresponding mathematical models for the adaptive flywheels are developed. Two-terminal hydraulic device and two-terminal inverse screw device are introduced to analyze these adaptive flywheels. The mathematical models for both two-terminal devices are also formulated. Experiments are carried out to identify key parameters for both the two-terminal hydraulic system and inverse screw system. More experiments are applied to verify the accuracy of these parameters and mathematical models, and the close agreement between theoretical and measured forces indicates the accuracy of both systems. In both experiments, spike forces are discovered, which are caused by backlash. In order to minimize the spike forces during experiments, a hydraulic rectifier is proposed in the experiments. Through adding the hydraulic rectifier, the spike forces in the two-terminal hydraulic system are reduced, which eventually leads to improved accuracy of key parameters and the mathematical model.

By applying the adaptive flywheel to an ideal two-terminal device, three different suspension systems are introduced and evaluated by three of the most commonly used performance criteria. The results indicate that a suspension system with a two-terminal device with adaptive flywheel out-performs the other two suspension systems in most cases, suggesting promising potential of the adaptive flywheel for use in vehicle suspension system. The relationship between changing ratio of adaptive flywheel and suspension performance was discussed. By determining the optimal changing ratio, the optimal design of the adaptive flywheel can be calculated, which provides a guiding design principle under certain conditions.

Through introducing a real two-terminal hydraulic system with identified parameters, two different suspension systems are proposed. The results of performance evaluation demonstrate that the suspension system consisting of a two-terminal device with adaptive flywheel performs better than both the traditional system and the suspension system consisting of a two-terminal device without adaptive flywheel. These results imply that the suspension system provides better performance with an adaptive flywheel under a real two-terminal hydraulic system. Therefore, such a suspension system could be applied to a vehicle suspension system. The optimal changing ratio is higher than for the ideal two-terminal hydraulic system even under the same conditions.

To analyze the steady state response, three different methods were applied to analyze the steady state response of the two-terminal device with adaptive flywheel. These methods are the single harmonic balance method, the multi-harmonic balance method and the scanning iterative multi-harmonic balance method, respectively.

Compared to the single harmonic balance method, the multi-harmonic balance method provides a much more accurate system response. However, the multi-harmonic balance method is computationally intensive. With complex mathematical system models, it can be difficult to obtain the system response with this method. To simplify the calculation process for the frequency response, a new scanning iterative multi-harmonic balance method was proposed. Results indicate that this method provides a more accurate system response than the single harmonic balance method with much less computational effort.

8.2. Future work

Some examples of further research directions based on the proposed approach are:

1. Although the system models were evaluated experimentally, the performance evaluation of the suspension response in this thesis is based on simulation. In the future, a prototype of a two-terminal device with adaptive flywheel can be built and installed on a suspension system of a car. By recording the vibration signal, the real performance of the proposed suspension system can be experimentally

verified.

2. In this thesis, the proposed two-terminal device with adaptive flywheel is too big to be installed on a suspension system of car. Therefore, the design of this system should be improved to reduce the size of the two-terminal device.
3. Further research on reducing the components of the adaptive flywheel and increasing the reliability also needs to be performed.

References

[1] Kareem, A., Kijewski, T., and Yukio, T., 1999, “Mitigation of Motions of Tall Buildings with Specific Examples of Recent Applications,” Wind and Structures, (2), pp. 201–251.

[2] Scott, R., 2001, *In the Wake of Tacoma: Suspension Bridges and the Quest for Aerodynamic Stability*, Amer Society of Civil Engineers, Reston, Va.

[3] Hu, H., 2005, *Fundamentals of Mechanical Vibration*, Beihang University Press, Beijing.

[4] Grapis, O., Tamužs, V., Andersons, N.-G., and Ohlson, J., 2006, “Overcritical High-Speed Rotor Systems, Full Annular Rub and Accident,” Journal of Sound and Vibration, **290**(3–5), pp. 910–927.

[5] Christopher B. Best, 2010, “Putter with Vibration Isolation,” The Journal of the Acoustical Society of America, **128**, p. 960.

[6] Simmons, R., and Simmons, R., 2007, “Vibration Isolation,” ASHRAE Journal, **49**(8), pp. 30–40.

[7] Filipović, D., and Schröder, D., 1998, “Band Vibration Absorber,” Journal of Sound and Vibration, **214**(3), pp. 553–566.

[8] Barbara Tiseo, Antonio Concilio, Antonio Gianvito, and Gary Koopmann, 2007, “An Adaptive Tunable Dynamic Vibration Absorber,” The Journal of the Acoustical Society of America, **122**, p. 3085.

[9] Arcidiacono, G., Capitani, R., and Vianello, M., 2001, “Simulated Experimental Design Used to Define the Characteristic Curves of Car Shock‐absorbers,” Quality and Reliability Engineering International, **17**(2), pp. 71–84.

[10] Calvo, J. A., López-Boada, B., Román, J. L. S., and Gauchía, A., 2009, “Influence of a Shock Absorber Model on Vehicle Dynamic Simulation,” Proceedings of the Institution of Mechanical Engineers, Part D: Journal of Automobile Engineering, **223**(2), pp. 189–203.

[11] "Shock Absorber.jpg (450×267)" [Online]. Available: http://www.agosto.com.tw/images/car/dic/shock%20absorber.jpg. [Accessed: 30-Sep-2015].

[12] Rahmat A. Shoureshi, 1997, "Adaptive-Passive Vibration Control System," The Journal of the Acoustical Society of America, **102**, p. 2476.

[13] Behrens, S., Fleming, A. J., and Moheimani, S. O. R., 2005, "Passive Vibration Control via Electromagnetic Shunt Damping," IEEE/ASME Transactions on Mechatronics, **10**(1), pp. 118–122.

[14] Sales, T. P., Rade, D. A., and De Souza, L. C. G., 2013, "Passive Vibration Control of Flexible Spacecraft Using Shunted Piezoelectric Transducers," Aerospace Science and Technology, **29**(1), p. 403.

[15] Sean G. C. Sutcliffe, Graham P. Eatwell, and Stephen M. Hutchins, 1992, "Active Control of Vibration," The Journal of the Acoustical Society of America, **92**, p. 627.

[16] Mark F. L. Harper, 1996, "Active Control of Vibration," The Journal of the Acoustical Society of America, **99**, p. 643.

[17] P. Micheau, and A. Berry, 2005, "Stability Conditions in Decentralized Active Vibration Control of a Flexible Plate," The Journal of the Acoustical Society of America, **118**, p. 1950.

[18] Larry Watkins, 2013, "Active Vibration Control for Subterranean Drilling Operations," The Journal of the Acoustical Society of America, **134**, p. 2373.

[19] Veres, S. M., 2002, *Active Sound and Vibration Control: Theory and Applications*, IET.

[20] Fuller, C. R., Elliott, S., and Nelson, P. A., 1997, *Active Control of Vibration*, Academic Press, London; San Diego.

[21] Huyanan, S., and Sims, N. D., 2007, "Vibration Control Strategies for Proof-Mass Actuators," Journal of Vibration and Control, **13**(12), pp. 1785–1806.

[22] Braghin, F., Cinquemani, S., and Resta, F., 2011, "A Model of Magnetostrictive Actuators for Active Vibration Control," Sensors and Actuators A: Physical, **165**(2), pp. 342–350.

[23] Preumont, A., 2011, *Vibration Control of Active Structures: An Introduction*, Springer, Berlin.

[24] Kimihiko Nakano, M. O., 2010, “Feasibility Study on Self-Powered Active Vibration Control Using a Piezoelectric Actuator.”

[25] Liu, Y., Matsuhisa, H., and Utsuno, H., 2008, “Semi-Active Vibration Isolation System with Variable Stiffness and Damping Control,” Journal Of Sound And Vibration, **313**(1–2), pp. 16–28.

[26] Caruso, G., Ben Mekki, O., and Bourquin, F., 2009, “Modeling and Experimental Validation of a New Electromechanical Damping Device,” Journal of Vibroengineering, **11**(4), p. 9p.

[27] Kasemi, B., Muthalif, A. G. A., Rashid, M. M., and Fathima, S., 2012, “Fuzzy-PID Controller for Semi-Active Vibration Control Using Magnetorheological Fluid Damper.”

[28] Ishida, Y., 2012, “Recent Development of the Passive Vibration Control Method,” Mechanical Systems and Signal Processing, **29**, pp. 2–18.

[29] Ming-Lai Lai, 1997, “Tuned Mass Damper,” The Journal of the Acoustical Society of America, **102**, p. 678.

[30] Weber, F., Boston, C., and Maslanka, M., 2011, “An Adaptive Tuned Mass Damper Based on the Emulation of Positive and Negative Stiffness with an MR Damper,” Smart Materials & Structures, **20**(1).

[31] Michael E. McGuire, 2011, “Spare Tire Tuned Mass Damper,” The Journal of the Acoustical Society of America, **130**, p. 1083.

[32] Smith, M. C., 2002, “Synthesis of Mechanical Networks: The Inerter,” IEEE Transactions on Automatic Control, **47**(10), pp. 1648–1662.

[33] Rivin, E. I., 2003, *Passive Vibration Isolation*, ASME Press, New York.

[34] Wang, F.-C., and Wu, S.-Y., 2014, “Vibration Control of an Optical Table Employing Mechatronic Inerter Networks,” Journal of Vibration and Control, **1**, pp. 56–78.

[35] Li, C., Wang, S., Kang, L., Lei, S., and Yu, Q., 2010, “Two-Terminal Manipulation of Masses: Application to Vibration Isolation of Passive Suspensions,” Journal of Vibroengineering, **12**(2).

[36] Li, C., Liang, M., Wang, Y., and Dong, Y., 2011, “Vibration Suppression Using Two-Terminal Flywheel. Part II: Application to Vehicle Passive Suspension,” Journal of Vibration and Control, pp. 1353–1365.

[37] Li, C., and Liang, M., 2012, “Characterization and Modeling of a Novel Electro-Hydraulic Variable Two-Terminal Mass Device,” Smart Mater. Struct., **21**(2), pp. 1–12.

[38] Li, C., Liang, M., Wang, Y., and Dong, Y., 2012, “Vibration Suppression Using Two-Terminal Flywheel. Part I: Modeling and Characterization,” Journal of Vibration and Control, **18**(8), pp. 1096–1105.

[39] Xu, T., Liang, M., Li, C., Yang, S.,“Design and Analysis of a Shock Absorber with a Variable Moment of Inertia Flywheel for Passive Vehicle Suspension.” submitted to Journal of Sound and Vibration, 2017.

[40] Shenhar, J., 1983, “Application of Control Theory to Large Flexible Structures Using the Independent Modal-Space Control Method.”

[41] Baz, A., and Poh, S., 1990, “Experimental Implementation of the Modified Independent Modal Space Control Method,” Journal of Sound and Vibration, **139**(1), pp. 133–149.

[42] Gbur, G. J., 2011, *Mathematical Methods for Optical Physics and Engineering*, Cambridge University Press, Cambridge.

[43] Pai, M. A., 1989, *Energy Function Analysis for Power System Stability*, Springer US, Boston, MA.

[44] Battilotti, S., *Noninterracting Control with Stability for Nonlinear Systems*, Springer Berlin / Heidelberg.

[45] De Silva, C. W., 2009, *Modeling and Control of Engineering Systems*, CRC Press, Boca Raton.

[46] Bueno De Araujo, P., and Zanetta Jr., L. C., 2001, “Pole Placement Method Using the System Matrix Transfer Function and Sparsity,” International Journal of Electrical Power and Energy System, **23**(3), pp. 173–178.

[47] Zubov, N., Mikrin, E., Misrikhanov, M. S., and Ryabchenko, V., 2013, “Modification of the Exact Pole Placement Method and Its Application for the Control of Spacecraft Motion,” Journal Of Computer And Systems Sciences International, **52**(2), pp. 279–292.

[48] Dyer, P., 1970, *Computation and Theory of Optimal Control*, Elsevier.

[49] Speyer, J. L., 2010, *Primer on Optimal Control Theory*, Society for Industrial and Applied Mathematics.

[50] Tiba, D., 1990, *Optimal Control of Nonsmooth Distributed Parameter Systems*.

[51] 1993, *Optimal Control*.

[52] Pavel, N. H., Corduneanu, C., and International Conference on Optimal Control of Differential Equations : Athens, O., 1994, *Optimal Control of Differential Equations*, MDekker, New York.

[53] Oborn, J., Bertilsson, H., and Rigdahl, M., 2001, “Styrene-Ethylene/Butylene-Styrene Blends for Improved Constrained-Layer Damping,” Journal Of Applied Polymer Science, **80**(14), pp. 2865–2876.

[54] Liya Bochkareva, and Maksim Kireitseu, 2006, “Metal‐polymer‐ceramic Constrained Layer Damping System,” The Journal of the Acoustical Society of America, **119**, p. 3299.

[55] Cao, X., Zhang, Z., and Hua, H., 2011, “Free Vibration of Circular Cylindrical Shell with Constrained Layer Damping,” Applied Mathematics and Mechanics, **32**(4), pp. 495–506.

[56] Xie, Z., Wong, P. K., and Lo, K. H., 2012, “Optimal Vibration Control of a Rotating Plate with Self-Sensing Active Constrained Layer Damping.”

[57] Liang, Y.-J., and Wu, S.-L., 2013, “Optimal Vibration Control for Tracked Vehicle Suspension Systems,” Mathematical Problems in Engineering, **2013**.

[58] Lewis, F. L., 2014, *Cooperative Control of Multi-Agent Systems : Optimal and Adaptive Design Approaches,* Springer, London.

[59] I. P. Priban, and W. F. Fincham, 1965, “Self-Adaptive Control and the Respiratory System,” Nature, **208**(5008), p. 339.

[60] Li, F., and Xie, J., 1998, “Practical Realization of a Self-Adaptive Feed-Forward Control System for RF Gun Beam-Loading Compensation,” Nuclear Inst. and Methods in Physics Research, A, **407**(1), pp. 332–337.

[61] Qi, C., Pan, H., and Wang, Y., 2012, “Design and Realization of Two-Axis Horizontal Stabilized Platform Based on Self-Correction Control Method.”

[62] Dones, I., Manenti, F., Preisig, H., and Buzzi-Ferraris, G., 2010, “Nonlinear Model Predictive Control: A Self-Adaptive Approach,” Industrial & Engineering Chemistry Research, **49**(10), pp. 4782–4791.

[63] Valoor, M. T., Chandrashekhara, S., and Agarwal, S., 2001, “Self-Adaptive Vibration Control of Smart Composite Beams Using Recurrent Neural Architecture,” International Journal of Solids and Structures, **38**(44–45), pp. 7857–7874.

[64] Hammond, P. H., Society of Instrument Technology, National Physical Laboratory, and International Federation of Automatic Control, 1966, *Theory of Self-Adaptive Control Systems; Proceedings.*, New York, Plenum Press.

[65] Mackenroth, U., 2004, *Robust Control Systems : Theory and Case Studies*, Springer, Berlin ; New York.

[66] Sun, W., Gao, H., and Yao, B., 2013, “Adaptive Robust Vibration Control of Full-Car Active Suspensions With Electrohydraulic Actuators,” Ieee Transactions On Control Systems Technology, **21**(6), pp. 2417–2422.

[67] Nguyen, V., and Choi, S. B., 2011, “A Robust Vibration Control for a Multi-Active Mount System Subjected to Broadband Excitation,” Smart Materials & Structures, **20**(5).

[68] Ayyub, B. M., Guran, A., and Haldar, A., 1997*, Uncertainty Modeling in Vibration, Control and Fuzzy Analysis of Structural Systems*, World Scientific, Singapore ; River Edge, NJ.

[69] Li, D., and Xu, R., 2013, “Autonomous Decentralized Intelligent Vibration Control for Large Split-Blanket Solar Arrays,” Science China Technological Sciences, **56**(3), pp. 703–712.

[70] Selected, peer reviewed papers from the I. C. on I. S. and V. C. (ISVC), 2011, *Intelligent Structure and Vibration Control : Selected, Peer Reviewed Papers from the International Conference on Intelligent Structure and Vibration Control (ISVC) 2011, January 14-16, 2011, Chongqing, China*, Trans Tech Publications Ltd, Switzerland.

[71] Muradova, A. D., and Stavroulakis, G. E., 2013, “Fuzzy Vibration Control of a Smart Plate,” International Journal of Computational Methods in Engineering Science and Mechanics, **14**(3), pp. 212–220.

[72] Gordon, T. J., Marsh, C., and Wu, Q. H., 1993, “Stochastic Optimal Control of Active Vehicle Suspensions Using Learning Automata,” Proceedings of the Institution of Mechanical Engineers. Part I, Journal of systems and control engineering, **207**(3), pp. 143–152.

[73] Valavanis, K. P., 2009, *Applications of Intelligent Control to Engineering Systems*.

[74] Moretti, P. M., 2000, *Modern Vibrations Primer*, CRC Press, Boca Raton, Fla.

[75] Nwokah, O. D. I., and Hurmuzlu, Y., 2002, *The Mechanical Systems Design Handbook : Modeling, Measurement, and Control*, CRC Press, Boca Raton, Fla.

[76] Preumont, A., 2008, *Active Control of Structures*.

[77] Yalla, S. K., Kareem, A., and Kantor, J. C., 2000, “Semi-Active Variable Damping Liquid Column Dampers,” Proceedings of SPIE - The International Society for Optical Engineering, **3988**, pp. 75–83.

[78] Zhang, Y., 2001, “Semi-Active Control of Dynamically Excited Structures Using Active Interaction Control.”

[79] Sahasrabudhe, S., 2002, “Semi-Active Control of Sliding Isolated Buildings and Bridges with Variable Stiffness and Damping Systems.”

[80] Guglielmino, E., 2008, *Semi-Active Suspension Control*.

[81] Guglielmino, E., 2008, *Semi-Active Suspension Control Improved Vehicle Ride and Road Friendliness*, Springer, London.

[82] Savaresi, S. M., 2010, *Semi-Active Suspension Control Design for Vehicles*, Elsevier ; Kidlington, Oxford, UK; Burlington, Mass, Amsterdam ; Boston.

[83] Liu, H. (Professor of I. S., Gao, H., Li, P., and Institution of Engineering and Technology, publisher, 2013, *Handbook of Vehicle Suspension Control Systems*, The Institution of Engineering and Technology, ©2014, London.

[84] 2014, "Hydraulic Shock Absorber," Mena Report.

[85] Shih, M. C., and Wang, T., 2008, "Active Control of Electro-Rheological Fluid Embedded Pneumatic Vibration Isolator," Integrated Computer-Aided Engineering, **15**(3), pp. 267–276.

[86] Jiang, Z., and Christenson, R., 2012, "A Fully Dynamic Magneto-Rheological Fluid Damper Model," Smart Materials And Structures, **21**(6).

[87] Suh, M. S., and Yeo, M. S., 1999, "Development of Semi-Active Suspension Systems Using ER Fluids for the Wheeled Vehicle," Journal Of Intelligent Material Systems And Structures, **10**(9), pp. 743–747.

[88] Dogruer, U., Gordaninejad, F., Evrensel, C. A., and Gordaninejad, F., 2003, "A New Magneto-Rheological Fluid Damper for High-Mobility Multi-Purpose Wheeled Vehicle (HMMWV)."

[89] Dogruer, U., Gordaninejad, F., Evrensel, C., Dogruer, U., Gordaninejad, F., and Evrensel, C., 2004, "A Magneto-Rheological Fluid Damper for High-Mobility Multi-Purpose Wheeled Vehicle (HMMWV)."

[90] Karakas, E. S., Gordaninejad, F., Evrensel, C. A., Yeo, M.-S., Liu, Y., Sahin, H., Karakas, E. S., Gordaninejad, F., Evrensel, C. A., Liu, Y., Sahin, H., and Yeo, M.-S., 2004, "Control of a Quarter HMMWV Suspension System Using a Magneto-Rheological Fluid Damper."

[91] Mead, D. J., 1998, *Passive Vibration Control*, Wiley, Chichester ; New York.

[92] Krysinski, T., 2007, *Mechanical Vibrations Active and Passive Control*, ISTE, London ; Newport Beach, CA.

[93] Rees, D. W. A., 2009, *Mechanics of Optimal Structural Design : Minimum Weight Structures*, Chichester John Wiley & Sons, Ltd.

[94] Hagedorn, P., and Spelsberg-Korspeter, G., 2014, *Active and Passive Vibration Control of Structures*, Springer, Wien.

[95] Parker, P., 2000, “Wind Tunnel Model System Dynamic Analysis and Simulation with Application to Model System Vibration Suppression.”

[96] Stein, G. J., and Múčka, P., 2011, “Study of Simultaneous Shock and Vibration Control by a Fore-and-Aft Suspension System of a Driver’s Seat,” International Journal of Industrial Ergonomics, **41**(5), pp. 520–529.

[97] Wen, P., and Li, Y., 2011, “Twin Rotor System Modeling, de-Coupling and Optimal Control.”

[98] Khalili, S. M. R., Shokuhfar, A., and Ghasemi, F. A., 2007, “Effect of Smart Stiffening Procedure on Low-Velocity Impact Response of Smart Structures,” Journal of Materials Processing Tech., **190**(1), pp. 142–152.

[99] Keane, A. J., and Bright, A. P., 1996, “PASSIVE VIBRATION CONTROL VIA UNUSUAL GEOMETRIES: EXPERIMENTS ON MODEL AEROSPACE STRUCTURES,” Journal of Sound and Vibration, **190**(4), pp. 713–719.

[100] Sarlin, E., Liu, Y., Vippola, M., Zogg, M., Ermanni, P., Vuorinen, J., and Lepistö, T., 2012, “Vibration Damping Properties of Steel/Rubber/Composite Hybrid Structures,” Composite Structures, **94**(11), pp. 3327–3335.

[101] Soong, T. T., Costantinou, M. C., and International Centre for Mechanical Sciences, 1994, *Passive and Active Structural Vibration Control in Civil Engineering*, Springer-Verlag, Wien ; New York.

[102] Syngellakis, S., 2013, *Seismic Control Systems : Design and Performance Assessment*, WIT, Southampton, England.

[103] Beskos, D. E., and Anagnostopoulos, S. A., 1997, *Computer Analysis and Design of Earthquake Resistant Structures : A Handbook*, Computational Mechanics Publications, Southampton, UK ; Boston.

[104] Nishimura, H., and Kojima, A., 1999, “Seismic Isolation Control for a Building-like Structure,” Control Systems, IEEE, **19**(6), pp. 38–44.

[105] 2014, *Integrated Seismic Design of Structure and Control Systems*, Springer International Publishing.

[106] Chen, W.-F., and Duan, L., 2003, *Bridge Engineering : Seismic Design*, CRC Press, Boca Raton, FL.

[107] Dai, H., Liu, Z., and Wang, W., 2012, "Structural Passive Control on Electromagnetic Friction Energy Dissipation Device," Thin-Walled Structures, **58**, pp. 1–8.

[108] Curadelli, O., 2011, "Seismic Reliability of Spherical Containers Retrofitted by Means of Energy Dissipation Devices," Engineering Structures, **33**(9), pp. 2662–2667.

[109] Sahoo, D. R., and Rai, D. C., 2010, "Seismic Strengthening of Non-Ductile Reinforced Concrete Frames Using Aluminum Shear Links as Energy-Dissipation Devices," Engineering Structures, **32**(11), pp. 3548–3557.

[110] Gajan, S., and Saravanathiiban, D. S., 2011, "Modeling of Energy Dissipation in Structural Devices and Foundation Soil during Seismic Loading," Soil Dynamics and Earthquake Engineering, **31**(8), pp. 1106–1122.

[111] Kitada, T., Matsumura, M., and Otoguro, Y., 2003, "Seismic Retrofitting Techniques Using an Energy Absorption Segment for Steel Bridge Piers," Engineering Structures, **25**(5), pp. 621–635.

[112] Shim, C. S., Chung, C.-H., and Kim, H. H., 2008, "Experimental Evaluation of Seismic Performance of Precast Segmental Bridge Piers with a Circular Solid Section," Engineering Structures, **30**(12), pp. 3782–3792.

[113] Sabouri-Ghomi, S., Ahouri, E., Sajadi, R., Alavi, M., Roufegarinejad, A., and Bradford, M. A., 2012, "Stiffness and Strength Degradation of Steel Shear Walls Having an Arbitrarily-Located Opening," Journal of Constructional Steel Research, **79**, pp. 91–100.

[114] Edalath, S., Kukreti, A. R., and Cohen, K., 2013, "Enhancement of a Tuned Mass Damper for Building Structures Using Fuzzy Logic," Journal of Vibration and Control, **19**(12), pp. 1763–1772.

[115] Novo, T., Varum, H., Teixeira-Dias, F., Rodrigues, H., Silva, M., Costa, A., and Guerreiro, L., 2014, "Tuned Liquid Dampers Simulation for Earthquake Response Control of Buildings," Bulletin of Earthquake Engineering, **12**(2), pp. 1007–1024.

[116] Setareh, M., Ritchey, J. K., Baxter, A. J., and Murray, T. M., 2006, "Pendulum Tuned Mass Dampers for Floor Vibration control.(Author Abstract)," Journal of Performance of Constructed Facilities, **20**(1), p. 64.

[117] Weng, F., and Mao, W., 2012, "Parameter-Dependent Vibration-Attenuation Controller Design for Electro-Hydraulic Actuated Linear Structural Systems," Earthquake Engineering and Engineering Vibration, **11**(1), pp. 73–82.

[118] Brebbia, C. A., 2005, *Earthquake Resistant Engineering Structures V*, WIT Press, Southampton, UK ; Boston.

[119] Lin, C.-C., Lu, L.-Y., Lin, G.-L., and Yang, T.-W., 2010, "Vibration Control of Seismic Structures Using Semi-Active Friction Multiple Tuned Mass Dampers," Engineering Structures, **32**(10), pp. 3404–3417.

[120] Steinbuch, R., 2011, "Bionic Optimisation of the Earthquake Resistance of High Buildings by Tuned Mass Dampers," Journal of Bionic Engineering, **8**(3), pp. 335–344.

[121] Ribeiro, E. A., Pereira, J. T., and Alberto Bavastri, C., 2015, "Passive Vibration Control in Rotor Dynamics: Optimization of Composed Support Using Viscoelastic Materials," Journal of Sound and Vibration, **351**, pp. 43–56.

[122] Bompos, D. A., and Nikolakopoulos, P. G., 2015, "Rotordynamic Analysis of a Shaft Using Magnetorheological and Nanomagnetorheological Fluid Journal Bearings," Tribology Transactions, pp. 00–00.

[123] Sinha, A., 2010, *Vibration of Mechanical Systems*, Cambridge University Press, Cambridge.

[124] Newland, D. E., 2006, *Mechanical Vibration Analysis and Computation*, Dover Publications, Mineola, NY.

[125] A, T., 1971, "Vibrations and Their Dampers of Shaft Systems Supported by Ball Bearings," Lubrication, **16**, pp. 1–8.

[126] Adams, M. L., 2010, *Rotating Machinery Vibration from Analysis to Troubleshooting*, CRC Press/Taylor & Francis, Boca Raton Fla.

[127] Zhou, W. J., Yang, Y. C., Xing, G. K., and Wang, L. Q., 2013, “Numerical Investigation of Nonlinear Vibration for Rotor-Seal System of Centrifugal Pump,” IOP Conference Series: Materials Science and Engineering, **52**(3), p. 5.

[128] Zhang, W., Yang, J., Gao, Q., and Li, J., 2014, “Reducing the Influence of Partial Admission on Unstable Synchronous Vibration of Turbines by Bearing Elevation Optimization,” Proceedings of the Institution of Mechanical Engineers, Part C: Journal of Mechanical Engineering Science, **228**(1), pp. 56–66.

[129] Ishida, Y., and Liu, J., 2010, “Elimination of Unstable Ranges of Rotors Utilizing Discontinuous Spring Characteristics: An Asymmetrical Shaft System, an Asymmetrical Rotor System, and a Rotor System With Liquid,” Journal Of Vibration And Acoustics-Transactions Of The Asme, **132**(1).

[130] Cai, K., Yin, H., Qin, Q., and Li, Y., 2014, “Self-Excited Oscillation of Rotating Double-Walled Carbon Nanotubes,” Nano Letters, **14**(5), pp. 2558–2562.

[131] Zhang, L., Li, X., Yao, Y., and Yang, L., 2010, “Study on Cascaded Whole-Leaf Spring Oscillation Mechanism for Mould in Continuous Casting,” Ironmaking & Steelmaking, **37**(3), pp. 204–210.

[132] Tuplin, W. A., 1966, *Torsional Vibration.*, Pitnam, London.

[133] Hidehiko Kuroda, 2007, “Torsional Vibration Measuring Instrument,” The Journal of the Acoustical Society of America, **121**, p. 1281.

[134] Inman, D. J., 2001, *Engineering Vibration*, Prentice Hall, Englewood Cliffs, NJ.

[135] Walker, D. N., 2004, *Torsional Vibration of Turbomachinery*, McGraw-Hill, New York.

[136] Janusz Walkowc, 1997, “Active Torsional Vibration Damper,” The Journal of the Acoustical Society of America, **102**, p. 3248.

[137] Reimpell, J., 2001, *The Automotive Chassis Engineering Principles : Chassis and Vehicle Overall, Wheel Suspensions and Types of Drive, Axle Kinematics and*

Elastokinematics, Steering, Springing, Tyres, Construction and Calculations Advice., Butterworth Heinemann, Oxford.

[138] Sandin, P. E., 2003, *Robot Mechanisms and Mechanical Devices Illustrated*, McGraw-Hill, New York.

[139] Chen, Y. W., 2014, *Structural Genomics : General Applications*, Humana Press, New York.

[140] Qiu, J. S., and Meng, J., 2011, "Nonlinear Finite Element Analysis and Experimental Study of Leaf Spring Suspension."

[141] N. Lavanya, and P. Sampath Rao, 2014, "Design and Analysis of A Suspension Coil Spring For Automotive Vehicle," International Journal of Engineering Research and Applications, **4**(9), p. 151.

[142] 2006, "Design Engineering - Air Spring Suspension: Air of Intelligence," The Engineer, pp. 47–48.

[143] Matschinsky, W., 2000, *Road Vehicle Suspensions*, Professional Engineering Pub, London, UK.

[144] Le, K. C., and Pieper, A., 2014, "Damping of Roll Vibrations of Vehicle Suspension," Vehicle System Dynamics, pp. 1–18.

[145] Society of Automotive Engineers, and SAE World Congress : Detroit, M.), 2007, *Reliability and Robust Design in Automotive Engineering, 2007.*, Society of Automotive Engineers, Warrendale, Pa.

[146] Blundell, M., 2004, *Multibody Systems Approach to Vehicle Dynamics*, Burlington Butterworth-Heinemann.

[147] Arikere, A., Saravana Kumar, G., and Bandyopadhyay, S., 2010, "Optimisation of Double Wishbone Suspension System Using Multi-Objective Genetic Algorithm."

[148] Uchida, T., and Mcphee, J., 2012, "Driving Simulator with Double-Wishbone Suspension Using Efficient Block-Triangularized Kinematic Equations," Multibody System Dynamics, **28**(4), pp. 331–347.

[149] Cheng, X., and Lin, Y., 2014, “Multiobjective Robust Design of the Double Wishbone Suspension System Based on Particle Swarm Optimization,” Scientific World Journal.

[150] Blanco, J. C., and Munoz, L. E., 2014, “Multi-Objective Optimization of the Geometry of a Double Wishbone Suspension System,” Vibroengineering Procedia, **3**, p. 70.

[151] Balike, K., Rakheja, S., and Stiharu, I., 2011, “Development of Kineto-Dynamic Quarter-Car Model for Synthesis of a Double Wishbone Suspension,” Vehicle System Dynamics, **49**(1–2), pp. 107–128.

[152] Shi, C. H., Kang, S. H., Li, C. H., Huang, L., Shi, C. H., Zhang, X. Z., and Hu, J. Z., 2014, “Design and Analysis of Double Wishbone Suspension Module with Wheel-Track Variant Wheels.”

[153] Dhir, A., and Sankar, S., 1995, “Dynamics of off-Road Tracked Vehicles Equipped with Trailing Arm Suspension,” Proceedings Of The Institution Of Mechanical Engineers Part D-Journal Of Au, **209**(3), pp. 195–215.

[154] Wang, W., Li, Y., Zhang, S., and Wang, B., 2014, “Research on the Ride Comfort of Electric Drive System Based on Double Trailing Arm Suspension.”

[155] Zhao, J.-S., Li, L., Chen, L., and Zhang, Y., 2010, “The Concept Design and Dynamics Analysis of a Novel Vehicle Suspension Mechanism with Invariable Orientation Parameters,” Vehicle System Dynamics, **48**(12), pp. 1495–1510.

[156] Kang, H. Y., and Suh, C. H., 1994, “Synthesis and Analysis Spherical-Cylindrical (SC) Link in the McPherson Strut Suspension Mechanism,” Journal of Mechanical Design, **116**(2), p. 599.

[157] Habibi, H., Shirazi, K. H., and Shishesaz, M., 2008, “Roll Steer Minimization of McPherson-Strut Suspension System Using Genetic Algorithm Method,” Mechanism and Machine Theory, **43**(1), pp. 57–67.

[158] Kang, D.-O., Heo, S.-J., and Kim, M.-S., 2010, “Robust Design Optimization of the McPherson Suspension System with Consideration of a Bush Compliance

Uncertainty," Proceedings of the Institution of Mechanical Engineers, Part D: Journal of Automobile Engineering, **224**(6), pp. 705–716.

[159] Anderson, B. D. O., 1973, *Network Analysis and Synthesis: A Modern Systems Theory Approach*, Englewood Cliffs, NJ: Prentice-Hall.

[160] Storer, J. E., 1957, *Passive Network Synthesis.* --, McGraw-Hill, New York.

[161] Chen, W.-K., and ScienceDirect, 2005, *The Electrical Engineering Handbook*, Elsevier Academic Press, Boston.

[162] Ulrich, R. K., and Schaper, L. W., 2003, *Integrated Passive Component Technology*, IEEE Press ; Hoboken, NJ, Piscataway, NJ.

[163] Uhlig, S., 2007, *Passive and Active Network Measurement*.

[164] Zobrist, G. W., 1965, *Digital Computer Analysis of Passive Networks Using Topological Formulas* \, Deptof Electrical Engineering, University of Missouri, Columbia.

[165] Anderson, B., and Kailath, T., 1979, "Passive Network Synthesis via Dual Spectral Factorization," Circuits and Systems, IEEE Transactions on, **26**(10), pp. 866–873.

[166] Guillemin, E. A., 1957, *Synthesis of Passive Networks; Theory and Methods Appropriate to the Realization and Approximation Problems.*, New York, Wiley 1957.

[167] Smith, M. C., and Walker, G., 2000, "Performance Limitations and Constraints for Active and Passive Suspensions: A Mechanical Multi-Port Approach," Vehicle System Dynamics, **33**(3), pp. 137–168.

[168] Hu, Y., and Chen, M. Z. Q., 2015, "Performance Evaluation for Inerter-Based Dynamic Vibration Absorbers," International Journal of Mechanical Sciences.

[169] Wang, F., Hong, M., and Lin, T. C., 2011, "Designing and Testing a Hydraulic Inerter," Proceedings Of The Institution Of Mechanical Engineers Part C-Journal Of Me, **225**(C1), pp. 66–72.

[170] Lazar, I. F., Neild, S. A., and Wagg, D. J., 2014, "Using an Inerter‐based Device for Structural Vibration Suppression," Earthquake Engineering & Structural Dynamics, **43**(8), pp. 1129–1147.

[171] Smith, M. C., 2002, “Synthesis of Mechanical Networks: The Inerter,” Ieee Transactions On Automatic Control, **47**(10), pp. 1648–1662.

[172] Chen, M. Z. Q., Hu, Y., Li, C., and Chen, G., 2015, “Performance Benefits of Using Inerter in Semiactive Suspensions,” Control Systems Technology, IEEE Transactions on, **23**(4), pp. 1571–1577.

[173] Li, C., Liang, M., Wang, Y., and Dong, Y., 2012, “Vibration Suppression Using Two-Terminal Flywheel. Part I: Modeling and Characterization,” Journal Of Vibration And Control, **18**(8), pp. 1096–1105.

[174] Anderson, T. J., Anderson, M. J., Hocut, C., Zornik, W., and Blotter, J. D., 2000, “Passive Vibration Suppression Using Nonlinear Electromechanical Coupling,” The Journal of the Acoustical Society of America, **108**(5), pp. 2478–2478.

[175] Guyomar, D., and Badel, A., 2006, “Nonlinear Semi-Passive Multimodal Vibration Damping: An Efficient Probabilistic Approach,” Journal of Sound and Vibration, **294**(1), pp. 249–268.

[176] Peng, Z., Lang, Z., and Meng, G., 2012, “Evaluation of Transmissibility for a Class of Nonlinear Passive Vibration Isolators,” Frontiers of Mechanical Engineering, **7**(4), pp. 401–409.

[177] Nordin, M., Galic’, J., and Gutman, P.-O., 1997, “New Models for Backlash and Gear Play,” Int. J. Adapt. Control Signal Process., **11**(1), pp. 49–63.

[178] Wang, X., ed., 2010, *Vehicle Noise and Vibration Refinement*, Woodhead Publishing, Boca Raton, Fla.

[179] Sun, X., Chen, L., Wang, S., Zhang, X., and Yang, X., 2016, “Performance Investigation of Vehicle Suspension System with Nonlinear Ball-Screw Inerter,” International Journal of Automotive Technology, **17**(3), pp. 399–408.

[180] Rath, J. J., Veluvolu, K. C., and Defoort, M., 2014, “Adaptive Super-Twisting Observer for Estimation of Random Road Excitation Profile in Automotive Suspension Systems,” TheScientificWorldJournal, **2014**, p. 203416.

[181] Čorić, M., Deur, J., Xu, L., Tseng, H. E., and Hrovat, D., 2016, “Optimisation of Active Suspension Control Inputs for Improved Vehicle Ride Performance,” Vehicle System Dynamics, **54**(7), pp. 1004–1030.

[182] Devdutt, M., and Aggarwal, M., 2015, “Fuzzy Control of Passenger Ride Performance Using MR Shock Absorber Suspension in Quarter Car Model,” International Journal of Dynamics and Control, **3**(4), pp. 463–469.

[183] Lee, H.-G., Sung, K.-G., Choi, S.-B., Park, M.-K., and Park, M.-K., 2011, “Performance Evaluation of a Quarter-Vehicle MR Suspension System with Different Tire Pressure,” International Journal of Precision Engineering and Manufacturing, **12**(2), pp. 203–210.

[184] Nguyen, L., Hong, K.-S., and Park, S., 2010, “Road-Frequency Adaptive Control for Semi-Active Suspension Systems,” International Journal of Control, Automation and Systems, **8**(5), pp. 1029–1038.

[185] Naraghi, M., 1996, *Dynamics and Control of Fast Automated Guided Vehicles for High Load Applications.*, 1996.

[186] Jae-Hoon Lee, Changwan Han, Dongsu Ahn, Jin Kyoo Lee, Sang-Hu Park, and Seonghun Park, 2013, “Design and Performance Evaluation of a Rotary Magnetorheological Damper for Unmanned Vehicle Suspension Systems,” The Scientific World Journal, **2013**.

[187] Zhu, J.-Y., 2009, “Empirical Analysis of the Effect of Rural Education on Income Distribution of Rural Labor Force - A Case of Yongchuan District, Chongqing,” Asian Agricultural Research, **1**.

[188] Kang, L., and Peng, F., 2013, “Cost Competitiveness Comparisons and Convergence in China,” National Institute Economic Review, (223), p. 49.

[189] García-Saldaña, J. D., and Gasull, A., 2015, “The Period Function and the Harmonic Balance Method,” Bulletin des sciences mathématiques, **139**(1), pp. 33–60.

[190] Razzak, M. A., 2016, “A Simple Harmonic Balance Method for Solving Strongly Nonlinear Oscillators,” Journal of the Association of Arab Universities for Basic and Applied Sciences, **21**, pp. 68–76.

[191] Mohammadian, M., and Shariati, M., 2017, “Approximate Analytical Solutions to a Conservative Oscillator Using Global Residue Harmonic Balance Method,” Chinese Journal of Physics, **55**(1), pp. 47–58.

[192] Weisheit, K., and Marburg, S., 2016, “Calculation of the Response of a Periodically Excited Beam with Frictional Contact Using Harmonic Balance Method,” Procedia IUTAM, **19**, pp. 282–288.

[193] Shen, Y.-J., Wen, S.-F., Li, X.-H., Yang, S.-P., and Xing, H.-J., 2016, “Dynamical Analysis of Fractional-Order Nonlinear Oscillator by Incremental Harmonic Balance Method,” Nonlinear Dynamics, **85**(3), pp. 1457–1467.

[194] Molla, M. H. U., Razzak, M. A., and Alam, M. S., 2016, “Harmonic Balance Method for Solving a Large-Amplitude Oscillation of a Conservative System with Inertia and Static Non-Linearity,” Results in Physics, **6**, pp. 238–242.

[195] Liu, J. K., Chen, F. X., and Chen, Y. M., 2012, “Bifurcation Analysis of Aeroelastic Systems with Hysteresis by Incremental Harmonic Balance Method,” Applied Mathematics and Computation, **219**(5), pp. 2398–2411.

[196] Chen, Y. M., Liu, J. K., and Meng, G., 2011, “Incremental Harmonic Balance Method for Nonlinear Flutter of an Airfoil with Uncertain-but-Bounded Parameters,” Applied Mathematical Modelling.

[197] Celik, M., Atalar, A., and Tan, M. A., 1996, “A New Method for the Steady-State Analysis of Periodically Excited Nonlinear Circuits,” Circuits and Systems I: Fundamental Theory and Applications, IEEE Transactions on, **43**(12), pp. 964–972.

Appendix A – Signals used in Model Validation

Table of part experimental data for section 4.1

	Signal type	Frequency	Amplitude	Recording length	purpose
1	Triangular	0.1Hz	0.05m	100 seconds	Identification
2	Triangular	0.1Hz	0.1m	100 seconds	Identification
3	Triangular	0.2Hz	0.05m	50 seconds	Identification
4	Triangular	0.2Hz	0.1m	50 seconds	Identification
5	Triangular	0.5Hz	0.05m	20 seconds	Identification
6	Triangular	0.5Hz	0.1m	20 seconds	Validation
7	Triangular	0.5Hz	0.15m	20seconds	Identification
8	Triangular	1Hz	0.05m	10 seconds	Identification
9	Triangular	1Hz	0.1m	10 seconds	Validation
10	Triangular	1Hz	0.15m	10 seconds	Identification
11	Sinusoidal	0.1Hz	0.01m	100 seconds	Validation
12	Sinusoidal	0.1Hz	0.02m	100 seconds	Identification
13	Sinusoidal	0.1Hz	0.03m	100 seconds	Validation
14	Sinusoidal	0.1Hz	0.05m	100 seconds	Validation
15	Sinusoidal	0.1Hz	0.08m	100 seconds	Validation
16	Sinusoidal	0.1Hz	0.10m	100 seconds	Identification
17	Sinusoidal	0.1Hz	0.12m	100 seconds	Validation
18	Sinusoidal	0.1Hz	0.15m	100 seconds	Identification
19	Sinusoidal	0.2Hz	0.01m	50 seconds	Validation
20	Sinusoidal	0.2Hz	0.02m	50 seconds	Identification
21	Sinusoidal	0.2Hz	0.03m	50 seconds	Validation
22	Sinusoidal	0.2Hz	0.05m	50 seconds	Identification
23	Sinusoidal	0.2Hz	0.08m	50 seconds	Validation

24	Sinusoidal	0.2Hz	0.10m	50 seconds	Identification
25	Sinusoidal	0.2Hz	0.12m	50 seconds	Validation
26	Sinusoidal	0.2Hz	0.15m	50 seconds	Identification
27	Sinusoidal	0.4Hz	0.01m	25 seconds	Validation
28	Sinusoidal	0.4Hz	0.02m	25 seconds	Identification
29	Sinusoidal	0.4Hz	0.03m	25 seconds	Identification
30	Sinusoidal	0.4Hz	0.05m	25 seconds	Validation
31	Sinusoidal	0.4Hz	0.08m	25 seconds	Identification
32	Sinusoidal	0.4Hz	0.10m	25 seconds	Validation
33	Sinusoidal	0.4Hz	0.12m	25 seconds	Identification
34	Sinusoidal	0.4Hz	0.15m	25 seconds	Validation
35	Sinusoidal	0.5Hz	0.01m	20 seconds	Identification
36	Sinusoidal	0.5Hz	0.02m	20 seconds	Validation
37	Sinusoidal	0.5Hz	0.03m	20 seconds	Identification
38	Sinusoidal	0.5Hz	0.05m	20 seconds	Validation
39	Sinusoidal	0.5Hz	0.08m	20 seconds	Validation
40	Sinusoidal	0.5Hz	0.10m	20 seconds	Validation
41	Sinusoidal	0.5Hz	0.12m	20 seconds	Validation
42	Sinusoidal	0.5Hz	0.15m	20 seconds	Identification
43	Sinusoidal	1Hz	0.01m	10 seconds	Validation
44	Sinusoidal	1Hz	0.02m	10 seconds	Validation
45	Sinusoidal	1Hz	0.03m	10 seconds	Identification
46	Sinusoidal	1Hz	0.05m	10 seconds	Validation
47	Sinusoidal	1Hz	0.08m	10 seconds	Identification
48	Sinusoidal	1Hz	0.10m	10 seconds	Validation
49	Sinusoidal	1Hz	0.12m	10 seconds	Identification
50	Sinusoidal	1Hz	0.15m	10 seconds	Validation
51	Sinusoidal	2Hz	0.01m	5 seconds	Validation n

52	Sinusoidal	2Hz	0.02m	5 seconds	Validation
53	Sinusoidal	2Hz	0.03m	5 seconds	Identification
54	Sinusoidal	2Hz	0.05m	5 seconds	Validation
55	Sinusoidal	2Hz	0.08m	5 seconds	Identification
56	Sinusoidal	2Hz	0.10m	5 seconds	Validation
57	Sinusoidal	2Hz	0.12m	5 seconds	Identification
58	Sinusoidal	2Hz	0.15m	5 seconds	Validation
59	Sinusoidal	5Hz	0.01m	2 seconds	Validation
60	Sinusoidal	5Hz	0.02m	2 seconds	Identification
61	Sinusoidal	5Hz	0.03m	2 seconds	Identification
62	Sinusoidal	5Hz	0.05m	2 seconds	Validation
63	Sinusoidal	5Hz	0.08m	2 seconds	Validation
64	Sinusoidal	10Hz	0.01m	1 seconds	Validation
65	Sinusoidal	10Hz	0.02m	1 seconds	Identification
66	Sinusoidal	10Hz	0.03m	1 seconds	Validation
67	Sinusoidal	10Hz	0.05m	1 seconds	Identification
68	Sinusoidal	10Hz	0.08m	1 seconds	Validation

Table of part experimental data for section 4.2 and section 4.3

	Signal type	Frequency	Amplitude	Recording length	purpose
1	Sinusoidal	0.1Hz	0.01m	100 seconds	Validation
2	Sinusoidal	0.1Hz	0.02m	100 seconds	Identification
3	Sinusoidal	0.1Hz	0.03m	100 seconds	Validation
4	Sinusoidal	0.1Hz	0.05m	100 seconds	Validation
5	Sinusoidal	0.1Hz	0.08m	100 seconds	Validation
6	Sinusoidal	0.1Hz	0.10m	100 seconds	Identification

7	Sinusoidal	0.1Hz	0.12m	100 seconds	Validation
8	Sinusoidal	0.1Hz	0.15m	100 seconds	Identification
9	Sinusoidal	0.1Hz	0.18m	100 seconds	Validation
10	Sinusoidal	0.1Hz	0.20m	100 seconds	Validation
11	Sinusoidal	0.2Hz	0.01m	50 seconds	Validation
12	Sinusoidal	0.2Hz	0.02m	50 seconds	Identification
13	Sinusoidal	0.2Hz	0.03m	50 seconds	Validation
14	Sinusoidal	0.2Hz	0.05m	50 seconds	Identification
15	Sinusoidal	0.2Hz	0.08m	50 seconds	Validation
16	Sinusoidal	0.2Hz	0.10m	50 seconds	Identification
17	Sinusoidal	0.2Hz	0.12m	50 seconds	Validation
18	Sinusoidal	0.2Hz	0.15m	50 seconds	Identification
19	Sinusoidal	0.2Hz	0.18m	50 seconds	Validation
20	Sinusoidal	0.2Hz	0.20m	50 seconds	Validation
21	Sinusoidal	0.4Hz	0.01m	25 seconds	Validation
22	Sinusoidal	0.4Hz	0.02m	25 seconds	Identification
23	Sinusoidal	0.4Hz	0.03m	25 seconds	Identification
24	Sinusoidal	0.4Hz	0.05m	25 seconds	Validation
25	Sinusoidal	0.4Hz	0.08m	25 seconds	Identification
26	Sinusoidal	0.4Hz	0.10m	25 seconds	Validation
27	Sinusoidal	0.4Hz	0.12m	25 seconds	Identification
28	Sinusoidal	0.4Hz	0.15m	25 seconds	Validation
29	Sinusoidal	0.4Hz	0.18m	25 seconds	Validation
30	Sinusoidal	0.4Hz	0.20m	25 seconds	Validation
31	Sinusoidal	0.5Hz	0.01m	20 seconds	Identification
32	Sinusoidal	0.5Hz	0.02m	20 seconds	Validation
33	Sinusoidal	0.5Hz	0.03m	20 seconds	Identification
34	Sinusoidal	0.5Hz	0.05m	20 seconds	Validation

35	Sinusoidal	0.5Hz	0.08m	20 seconds	Validation
36	Sinusoidal	0.5Hz	0.10m	20 seconds	Validation
37	Sinusoidal	0.5Hz	0.12m	20 seconds	Validation
38	Sinusoidal	0.5Hz	0.15m	20 seconds	Identification
39	Sinusoidal	0.5Hz	0.18m	20 seconds	Validation
40	Sinusoidal	0.5Hz	0.20m	20 seconds	Validation
41	Sinusoidal	1Hz	0.01m	10 seconds	Validation
42	Sinusoidal	1Hz	0.02m	10 seconds	Validation
43	Sinusoidal	1Hz	0.03m	10 seconds	Identification
44	Sinusoidal	1Hz	0.05m	10 seconds	Validation
45	Sinusoidal	1Hz	0.08m	10 seconds	Identification
46	Sinusoidal	1Hz	0.10m	10 seconds	Validation
47	Sinusoidal	1Hz	0.12m	10 seconds	Identification
48	Sinusoidal	1Hz	0.15m	10 seconds	Validation
49	Sinusoidal	1Hz	0.18m	10 seconds	Validation
50	Sinusoidal	1Hz	0.20m	10 seconds	Validation
51	Sinusoidal	2Hz	0.01m	5 seconds	Validation n
52	Sinusoidal	2Hz	0.02m	5 seconds	Validation
53	Sinusoidal	2Hz	0.03m	5 seconds	Identification
54	Sinusoidal	2Hz	0.05m	5 seconds	Validation
55	Sinusoidal	2Hz	0.08m	5 seconds	Identification
56	Sinusoidal	2Hz	0.10m	5 seconds	Validation
57	Sinusoidal	2Hz	0.12m	5 seconds	Identification
58	Sinusoidal	2Hz	0.15m	5 seconds	Validation
59	Sinusoidal	5Hz	0.01m	2 seconds	Validation
60	Sinusoidal	5Hz	0.02m	2 seconds	Identification
61	Sinusoidal	5Hz	0.03m	2 seconds	Identification
62	Sinusoidal	5Hz	0.05m	2 seconds	Validation

63	Sinusoidal	5Hz	0.08m	2 seconds	Validation
64	Sinusoidal	5Hz	0.1m	2 seconds	Validation
65	Sinusoidal	5Hz	0.12m	2 seconds	Validation
66	Sinusoidal	5Hz	0.15m	2 seconds	Validation
67	Sinusoidal	10Hz	0.01m	1 seconds	Validation
68	Sinusoidal	10Hz	0.02m	1 seconds	Identification
69	Sinusoidal	10Hz	0.03m	1 seconds	Validation
70	Sinusoidal	10Hz	0.05m	1 seconds	Identification
71	Sinusoidal	10Hz	0.12m	1 seconds	Validation
72	Sinusoidal	10Hz	0.15m	1 seconds	Validation

Appendix B - Code

Code of simulation:

```
t = cell(size(Freqs));
Resp = t;
Ft = t;
RespAmp = Freqs;
tSeg = zeros(size(t));
StartPnt = [];
N = length(nCycles);
t1 = cell(N,1);
Resp1 = t1;
Ft1 = t1;
for i = 1:N
    ExParas.A = Amps(i); ExParas.Omega = 2 * pi * Freqs(i);
    SysParas = fnUpdateSys(ExParas,SysParas,BWParas);
    if ~isempty(StartPnt)
        StartPnt(1) = StartPnt(1) / SysParas.L;
        StartPnt(2) = SysParas.T / SysParas.L * StartPnt(2);
    end
    [~,f0] = fnExcite(SysParas,[]);
    [t{i},Resp{i}] =
fnNumSim(SysParas,BWParas,fnExcite,f0,nCycles(i),StartPnt);
    Ft{i} = fnExcite(SysParas,t{i});
    [t{i},Resp{i}] = fnTransResult(t{i},Resp{i},SysParas);
    [~,Ft{i}] = fnTransResult(t{i},Ft{i},SysParas);
    RespAmp(i) = GetAmp(t{i},Resp{i}(:,1) + Ft{i},Freqs(i),false);
    if i > 1
        t1{i} = t1{i - 1}(end) + t{i}(2:end);
        Resp1{i} = Resp{i}(2:end,1);
        Ft1{i} = Ft{i}(2:end);
        tSeg(i) = t1{i - 1}(end);
    else
        t1(i) = t(i);
        Resp1{i} = Resp{i}(:,1);
        Ft1{i} = Ft{i};
        tSeg(i) = 0;
    end
    if ~isempty(hFigs)
        if i > idxTurningPnt
            bSweepUp = false;
```

```
            else
                bSweepUp = true;
            end

UpdatePlot(t1{i},Ft1{i},Resp1{i},Freqs(i),hFigs,bSweepUp,2);
        end
        StartPnt = [Resp{i}(end,:)]';
    end
        for i = 1:N
    end
    t1 = cell2mat(t1);
    Resp1 = cell2mat(Resp1);
    Ft1 = cell2mat(Ft1);
end
function Amp = GetAmp(t,x,f0,bIncludeDC)
    T = 2 / f0;
    tStart = t(end) - T;
    xStart = interp1(t,x,tStart,'pchip');
    idx = find(t > tStart,1);
    tAmp = [tStart;t(idx:end)];
    Resp = [xStart;x(idx:end)];
    DC = mean(Resp);
    Amp = (max(Resp) - min(Resp)) / 2;
    if bIncludeDC
        Amp = Amp + DC;
    end
end
function UpdatePlot(t,xg,x,f0,hFigs,bSweepUp,nPhaseCyclesCnt)
    hFigx = []; hFigPhase = [];
    if ~isempty(hFigs)
        hFigx = hFigs(1);
        if length(hFigs) == 2
            hFigPhase = hFigs(2);
        end
    end
    if bSweepUp
        szStyle = 'y';
    else
        szStyle = 'g';
    end
    if ~isempty(hFigx)
        figure(hFigx);
        plot(t,x,szStyle);
```

```
        plot(t,xg,'c--');
        tmp = axis;
        plot([t(1),t(1)],[tmp(3),tmp(4)],'r--');
    end
    if ~isempty(hFigPhase)
        figure(hFigPhase);
        tSpan = nPhaseCyclesCnt / f0;
        idxStart = find(t <= t(end) - tSpan,1,'last');
        plot(xg(idxStart:end),xg(idxStart:end) +
x(idxStart:end),szStyle);
    end
end

function dz=fQCI(t,z)%quarter car impulse input
%z(1)=x3, z(2)=x3', z(3)=x2,
z(4)=x2',z(5)=x3e,z(6)=x3e',z(7)=x2e,z(8)=x2e',
mt=30;
m=320;
ct=700;
c=7000;
kt=100000;
k=80000;
dz=zeros(8,1);
t1=0;
t2=0.001;
dz(1)=z(2);
dz(2)=-k/m*(z(1)-z(3))-c/m*(z(2)-z(3));
dz(3)=z(4);
dz(4)=-kt/mt*(z(3)-(stepfun(t,t1)-stepfun(t,t2)))-ct/mt*z(4)+k/mt*(z(
1)-z(3))+c/mt*(z(2)-z(3));
dz(5)=z(6);
me=(0.000883+0.14*(2.025/(90-32368*(dz(6)-dz(8)).^2)).^2)*924797;
dz(6)=me/m*(dz(6)-dz(8))-k/m*(z(5)-z(7))-c/m*(z(6)-z(8));
dz(7)=z(8);
dz(8)=-me/mt*(dz(6)-dz(8))-kt/mt*(z(7)-(stepfun(t,t1)-stepfun(t,t2)))
-ct/mt*z(8)+k/mt*(z(5)-z(7))-c/mt*(z(6)-z(8));
end

function dz=fQCs(t,z)%quarter car sinusoidal input
%z(1)=x3, z(2)=x3', z(3)=x2,
z(4)=x2',z(5)=x3e,z(6)=x3e',z(7)=x2e,z(8)=x2e',
mt=30;
m=320;
```

```
ct=700;
c=7000;
kt=100000;
k=80000;
Ip=10*sin(2*t);
Ip1=20*cos(2*t);
dz=zeros(8,1);
dz(1)=z(2);
dz(2)=-k/m*(z(1)-z(3))-c/m*(z(2)-z(3));
dz(3)=z(4);
dz(4)=-kt/mt*(z(3)-Ip)-ct/mt*(z(4)-Ip1)+k/mt*(z(1)-z(3))+c/mt*(z(2)-z
(3));
dz(5)=z(6);
me=(0.000883+0.14*(2.025/(90-32368*(dz(6)-dz(8)).^2)).^2)*924797;
dz(6)=me/m*(dz(6)-dz(8))-k/m*(z(5)-z(7))-c/m*(z(6)-z(8));
dz(7)=z(8);
dz(8)=-me/mt*(dz(6)-dz(8))-kt/mt*(z(7)-Ip)-ct/mt*(z(8)-Ip1)+k/mt*(z(5
)-z(7))-c/mt*(z(6)-z(8));
end

function dz=fQCZ(t,z)%quarter car zero inout
%z(1)=x3, z(2)=x3', z(3)=x2,
z(4)=x2',z(5)=x3e,z(6)=x3e',z(7)=x2e,z(8)=x2e',
mt=30;
m=320;
ct=700;
c=7000;
kt=100000;
k=80000;
dz=zeros(8,1);
dz(1)=z(2);
dz(2)=-k/m*(z(1)-z(3))-c/m*(z(2)-z(3));
dz(3)=z(4);
dz(4)=-kt/mt*z(3)-ct/mt*z(4)+k/mt*(z(1)-z(3))+c/mt*(z(2)-z(3));
dz(5)=z(6);
me=(0.000883+0.14*(2.025/(90-32368*(dz(6)-dz(8)).^2)).^2)*924797;
dz(6)=me/m*(dz(6)-dz(8))-k/m*(z(5)-z(7))-c/m*(z(6)-z(8));
dz(7)=z(8);
dz(8)=-me/mt*(dz(6)-dz(8))-kt/mt*z(7)-ct/mt*z(8)+k/mt*(z(5)-z(7))-c/m
t*(z(6)-z(8));
end

x=[0  0.15 0.23 0.25 ];
```

```
y=[0  0.64  1.12  1 ];
values = spcrv([[x(1) x x(end)];[y(1) y y(end)]],3);
 plot(values(1,:),values(2,:));
 hold on;
 x=[0  0.15 0.23 0.25 ];
y=[0  0.64  1.12  1 ];
values = spcrv([[x(1) x x(end)];[y(1) y y(end)]],3);
 plot(values(1,:),values(2,:),'d');
 hold on;
x=[ 0  0.125 0.22    0.2500];
y=[  0  2.111 4.44    4.0379];
values = spcrv([[x(1) x x(end)];[y(1) y y(end)]],3);
 plot(values(1,:),values(2,:),'m');
 hold on;
 x=[ 0  0.125 0.22    0.2500];
y=[  0  2.111 4.44    4.0379];
values = spcrv([[x(1) x x(end)];[y(1) y y(end)]],3);
 plot(values(1,:),values(2,:),'md');
 hold on;
x=[ 0  0.125 0.2    0.2500];
y=[ 0  3.5  7.7  6.9504  ];
values = spcrv([[x(1) x x(end)];[y(1) y y(end)]],3);
 plot(values(1,:),values(2,:),'r');
 hold on;
 x=[ 0  0.125 0.2    0.2500];
y=[ 0  3.5  7.7  6.9504  ];
values = spcrv([[x(1) x x(end)];[y(1) y y(end)]],3);
 plot(values(1,:),values(2,:),'rd');
 hold on;
x=[ 0  0.125  0.18   0.2500];
y=[0   5  12.96  10.0414];
values = spcrv([[x(1) x x(end)];[y(1) y y(end)]],3);
 plot(values(1,:),values(2,:),'k');
 hold on;
 x=[ 0  0.125  0.18   0.2500];
y=[0   5  12.96  10.0414];
values = spcrv([[x(1) x x(end)];[y(1) y y(end)]],3);
 plot(values(1,:),values(2,:),'kd');
 hold on;
x=[0   0.125  0.15   0.2500];
y=[ 0    8.1   20.12 16.2462];
values = spcrv([[x(1) x x(end)];[y(1) y y(end)]],3);
 plot(values(1,:),values(2,:),'g');
```

```
 hold on;
 x=[0    0.125  0.15    0.2500];
y=[ 0     8.1    20.12 16.2462];
values = spcrv([[x(1) x x(end)];[y(1) y y(end)]],3);
 plot(values(1,:),values(2,:),'gd');
 hold on;
x=[ 0    0.0500     0.11  0.2500];
y=[  0   20.9996     50  42.4126];
values = spcrv([[x(1) x x(end)];[y(1) y y(end)]],3);
 plot(values(1,:),values(2,:),'c');
 hold on;
 x=[ 0    0.0500     0.11  0.2500];
y=[  0   20.9996     50  42.4126];
values = spcrv([[x(1) x x(end)];[y(1) y y(end)]],3);
 plot(values(1,:),values(2,:),'cd');
 hold on;
xlabel('Frequency (Hz)');
ylabel('Amplitude (cm)');
legend('Simulation','SIMHB')

clear all% on degree freedom with zero input

z0=[0.1;0;0.1;0];
%z0=[0;0;0;0]


[t,z]=ode45(@F11,[0,10],z0);
plot(t,z(:,3),'--');
hold on;
[t,z]=ode45(@F12,[0,10],z0);
plot(t,z(:,3),'--');
hold on;
[t,z]=ode45(@F1,[0,10],z0);
plot(t,z(:,1),t,z(:,3),'--');
hold on;
xlabel ('T');
ylabel ('Displacement');
legend ('Traditional','Flywheel')

clear all% on degree freedom with sinusoidal input

%z0=[0.1;0;0.1;0];
z0=[0;0;0;0];
```

```
[t,z]=ode45(@F31,[0,30],z0);
plot(t,z(:,3),'--r');
hold on;
[t,z]=ode45(@F32,[0,30],z0);
plot(t,z(:,3),'--');
hold on;
[t,z]=ode45(@F3,[0,30],z0);
plot(t,z(:,1),t,z(:,3),'--k');
hold on;
xlabel ('T');
ylabel ('Displacement');
legend ('Min','Max','Traditional','Flywheel')

clear all% on degre freedom with impulse input

%z0=[0.1;0;0.1;0];
z0=[0;0;0;0];

[t,z]=ode45(@F2,[0,10],z0);
plot(t,z(:,1),t,z(:,3),'--');

xlabel ('T');
ylabel ('Displacement');
legend ('Traditional','Flywheel')

[t,z]=ode45(@F41,[0,30],z0);%0.05
a=max(z(:,3));
E=zeros(2,21);
E(:,2)=[0.05,a];
[t,z]=ode45(@F42,[0,30],z0);%0.1
a=max(z(:,3));
E(:,3)=[0.1,a];
[t,z]=ode45(@F43,[0,30],z0);%0.25
a=max(z(:,3));
E(:,4)=[0.25,a];
[t,z]=ode45(@F44,[0,30],z0);%0.35
a=max(z(:,3));
E(:,5)=[0.35,a];
[t,z]=ode45(@F45,[0,30],z0);%0.375
a=max(z(:,3));
E(:,6)=[0.375,a];
```

```
[t,z]=ode45(@F46,[0,30],z0);%0.38
a=max(z(:,3));
E(:,7)=[0.38,a];
[t,z]=ode45(@F47,[0,30],z0);%0.385
a=max(z(:,3));
E(:,8)=[0.385,a];
[t,z]=ode45(@F48,[0,30],z0);%0.39
a=max(z(:,3));
E(:,9)=[0.39,a];
[t,z]=ode45(@F49,[0,30],z0);%0.395
a=max(z(:,3));
E(:,10)=[0.395,a];
[t,z]=ode45(@F5,[0,30],z0);%0.4
a=max(z(:,3));
E(:,11)=[0.4,a];
[t,z]=ode45(@F51,[0,30],z0);%0.405
a=max(z(:,3));
E(:,12)=[0.405,a];
[t,z]=ode45(@F52,[0,30],z0);%0.41
a=max(z(:,3));
E(:,13)=[0.41,a];
[t,z]=ode45(@F53,[0,30],z0);%0.415
a=max(z(:,3));
E(:,14)=[0.415,a];
[t,z]=ode45(@F54,[0,30],z0);%0.42
a=max(z(:,3));
E(:,15)=[0.42,a];
[t,z]=ode45(@F55,[0,30],z0);%0.425
a=max(z(:,3));
E(:,16)=[0.425,a];
[t,z]=ode45(@F56,[0,30],z0);%0.45
a=max(z(:,3));
E(:,17)=[0.45,a];
[t,z]=ode45(@F57,[0,30],z0);%0.5
a=max(z(:,3));
E(:,18)=[0.5,a];
[t,z]=ode45(@F58,[0,30],z0);%1
a=max(z(:,3));
E(:,19)=[1,a];
[t,z]=ode45(@F59,[0,30],z0);%2.5
a=max(z(:,3));
E(:,20)=[2.5,a];
[t,z]=ode45(@F6,[0,30],z0);%5
```

```
a=max(z(:,3));
E(:,21)=[5,a];
d=max(E(2,:))
E(2,:)=E(2,:)/10;
plot(E(1,:),E(2,:));
xlabel('Frequency (Hz)');
ylabel('Amplitude (Cm)');
```

Appendix C – Accepted Manuscripts

1. Shuai Yang, Tongyi Xu, Chuan Li, Ming Liang and Natalie Baddour, ‘Design, modeling and testing of a two-terminal mass device with an adaptive flywheel’, *Journal of Mechanical Design,* 138(9), 2016.
2. Shuai Yang, Ming Liang and Natalie Baddour, ’Design, Modeling and Evaluation of Nylon Adaptive Flywheel’, Proceedings of the Canadian Society for Mechanical Engineering International Congress, Kelowna, Canada, 2016.